Design and evaluation of a GMR-biosensor for magnetic characterization of biological medium

Hamidreza Shirzadfar

Ecole doctorale IAEM
Département de formation Doctorale
Electronique Electrotechnique

THÈSE

Pour l'obtention du titre de :

DOCTEUR de L'UNIVERSITÉ DE LORRAINE

Spécialité: *Systèmes électroniques*

Présentée par :

Hamidreza SHIRZADFAR

CONCEPTION ET REALISATION D'UN BIOCAPTEUR A GMR POUR LA CARACTERISATION DE MILIEUX BIOLOGIQUES

Thèse soutenue publiquement le 23 juin 2014 à Nancy devant le jury composé de :

François BURET	Professeur, Université de Lyon	Rapporteur
Laurent BERQUEZ	Professeur, Université de Toulouse	Rapporteur
Jean Marie BILBAULT	Professeur, Université de Bourgogne	Examinateur
Sotoshi YAMADA	Professeur, Université de Kanazawa	Examinateur
Djilali KOURTICHE	Professeur, Université de Lorraine	Co-directeur de thèse
Mustapha NADI	Professeur, Université de Lorraine	Directeur de thèse

Institut Jean Lamour ; Université de Lorraine –CNRS ; UMR 7198 ;
Faculté des Sciences et Technologies
Pôle M4 : matière, matériaux, métallurgie, mécanique

Ce travail a été réalisé grâce à la collaboration et au soutien du Pr Sotoshi YAMADA du laboratoire "Division of Biological Measurement and Applications" de l'Université de Kanazawa au Japon

This work was made possible thanks to Professor Sotoshi YAMADA's collaboration and support from "Division of Biological Measurement and Applications", University of Kanazawa in Japan

本研究は、金沢大学 山田外史教授の協力と、金沢大学環日本海域環境研究センター生体機能計測研究部門の支援によって可能となりました。

Acknowledgements

First and foremost, I am deeply grateful to all members of the jury, Pr. Laurent Berquez of Université Paul Sabatier Toulouse III and Pr. François Buret of École Centrale de Lyon for accepting to be the reviewers of my thesis and agreeing to devote their valuable time to evaluate the manuscript. I would also like to express my deep thanks to Pr. Jean Marie Bilbault from Université de Bourgogne for accepting to be examiner in the jury.

I am especially indebted to Professor Sotoshi Yamada from Kanazawa University for having collaborate on this PhD thesis and also for accepting to be examiner of the jury. It has been a real pleasure for me to visit him and his laboratory during the summer 2011. I will not forget those enjoyable and illuminating discussions with him and all members of Division of Biological Measurement and Applications during this traineeship in Kanazawa University. Hours spending there have highlighted my way as a researcher and were a good start for my investigation. During my PhD at Université de Lorraine and Kanazawa University I feel deeply indebted to many great people who provided me with a tremendous intellectual and scientific support and gave me an unforgettable experience.

I would like to thank my co-director, Professor Djilali Kourtiche, for his continuous advices, assistance and help in the development of my PhD process. I learned a lot from him how to solve experimental problems.

I am also deeply grateful to my first advisor Professor Mustapha Nadi for accepting me as a PhD student and for his guidance, patience, motivation and encouragement throughout my PhD study. His guidance helped me all the time during thesis research and scientific challenges.

I also want to thank Patrice Roth, our excellent assistant engineer for his technical support. This thesis would not have finished without his help. I would like to thank Pierre Schmitt, research engineer and Christine Daudens, secretary of our department in the Institut Jean Lamour-laboratory.

I have had the great pleasure of working on my project with Professor Stéphane Mangin and Dr. Thomas Hauet and I very appreciate their scientific help during all these years. With them we organized a wonderful collaboration with the Ukrainian colleagues.

I am particularly thankful to Dr. Julien Claudel, not only my colleague during my stay in France but also my best friend. I have enjoyed notably the opportunity of friendship and work

with him. He was very helpful in teaching French language and gave me a great support for my experiments.

In additional, I would also like to thank all the members and colleagues of Institute Jean Lamour in Université de Lorraine.

Я хотел бы выразить признательность моей Дашке за многие часы, которые она провела корректируя мою работу, а так же за её безоговорочную поддержку. В течение нашей жизни во Франции мы делили все печали и радости и без нее мне было бы очень сложно.

Finally, I dedicate this thesis to my lovely parents who, unfortunately have both passed away but I feel that they are always with me in my heart; my family and dear friends for their constant support and unconditional encouragement.

Hamidreza Shirzadfar

June 2014

List of Figures

List of Tables

Contents

List of Symbols

Unit Symbol	Name	Unit
R	Resistance	Ω
R_{AP}	Antiparallel resistance	Ω
R_P	Parallel resistance	Ω
θ	Angle of magnetization	–
μ_0	Permeability of free space	H/m
π	Pi	–
H	Magnetic field	A/m
M	Magnetization	A/m
W	Energy	J
t, d	Thickness of magnetic layer	m
M_S, B_S	Saturation magnetization	A/m
I	Current	A
L	Length	m
W	Width	m
Δρ/ρ	Magnetoresistivity ratio	%
U_{out}	Sensor's output voltage	V
H_X	Measured magnetic field	A/m
H_d	Demagnetizing field	A/m
H_P	Bias field	A/m
H_K	Anisotropy field	A/m
J	Current density	$A.m^{-2}$
β	Bulk spin coefficient	–
γ	Interfacial spin coefficient	–
r_b	Interfacial resistance	Ω
ρ_F^*	Ferromagnetic multilayer resistivity	Ω.m
$\rho_F^{\uparrow}$, $\rho_F^{\downarrow}$	Bulk resistivity	Ω.m
ρ	Electrical resistivity	Ω.m
δ	Skin depth	m
f	Frequency	Hz
μ	Permeability	$H \cdot m^{-1}$
Z	Impedance	Ω
χ_m	Magnetic susceptibility	–
μ_r	Relative permeability	–
H_S	Saturation field	A/m
B_r	Residual magnetization	T
H_C	Coercive force	A/m
B	Magnetic flux density	T
R	Radius	m
N	Number of the turn on the each coil	–
A	Cross sectional area	m^2
V_S	Voltage in secondary coil	V
V_P	Voltage in primary coil	V
N_S, N_P	Number of turns in secondary and primary coils	–
I_S, I_P	Current of turns in secondary and primary coils	–

R_G	Gain resistance	Ω
G	Gain value	dB
C	Capacitance	F
ΔR	Change in resistance	Ω
V_{sup}	Voltage of power supply	V
k	Variation the sensing element	Ω/T
R_{GMR}	Resistance value of GMR element	Ω
D_W	Weight density	mgFe/ml
D_V	Volume density	%
ρ	Density	kg/cm^3
γ_f	Specific gravity	–
rh	Height of magnetic nanoparticle	m
rp	Radius of magnetic nanoparticle	m
P_b, P_g	Magnetic path	m
Φ_b, Φ_g	Magnetic flux	Wb
S	Surface of magnetic path	m^2
B_0	Magnetic flux density outside the cavity	T
B_1	Magnetic flux density inside the cavity	T
h_S	Space factor of cluster	–
S	Aspect ratio	–
N	Demagnetizing factor	–
χ^*	Relative susceptibility	–
χ_i	Initial magnetic susceptibility	–
μ_{ri}	Initial relative permeability	–
ϕ	Volume section of magnetic solid to carrier liquid	m^2
Md	Magnetic domain magnetization	–
d	Diameter of magnetic particle	m
k	Boltzmann's constant	J/K
m	Magnetic moment	$A.m^2$
T	Temperature	K
δ	Variations of the magnetic flux density	%

List of Abbreviations

GMR	Giant magnetoresistance
FM	Ferromagnetic
NM	Nonmagnetic
bcc	Body centered cubic
SQUID	Superconducting quantum interference device
AMR	Anisotropic magnetoresistivity
MR	Magnetoresistance ratio
SNR, S/N	Signal-to-noise ratio
CIP	Current in plane
CPP	Current perpendicular to plane
SV-GMR	Spin valve giant magnetoresistance
MTJ	Magnetic tunnel junction
GMI	Giant magnetoimpedance
DM	Diamagnetic
PM	Paramagnetic
SPM	Superparamagnetic
MRI	Magnetic resonance imaging
FPC	Flexible printed circuit
PCB	Printed circuit board
AD	Analog device
NEP	Noise equivalent power
FFT	Fast Fourier transform
CST	Simulation technology program
VSM	Vibrating sample magnetometer
MAG-D	Magnetic fluid-D
EHEC	Enterohemorrhagic Escherichia coli
HUS	Uremic syndrome
STEC	Shiga toxin-producing Escherichia coli
PDMS	Polydimethylsiloxane

Synthèse francophone du mémoire

Introduction et objectifs de l'étude

Au cours des dernières années, la recherche et le développement de nouveaux capteurs ont connu une très forte croissance dans certaines disciplines scientifiques, et en particulier dans le domaine biomédical.

L'effet de magnétorésistance géante a été décrit indépendamment en 1988 par le Professeur Albert Fert, chercheur à l'Université de Paris-11, et par le Professeur Peter Grunberg de l'Institut de physique de l'état solide du Centre de recherche de Jülich (Allemagne). Pour ces travaux, ils ont reçu le prix Nobel de physique en 2007 pour leurs travaux dans ce domaine. La nature de l'effet magnétorésistif est une variation importante de la résistance (10-20 %) de structures multicouches de métaux magnétiques et non magnétiques, sous l'effet d'un champ magnétique externe, même faible. La base de ce phénomène est due à la propriété du moment quantique ou du «spin» de l'électron.

L'effet de base du phénomène GMR est de réduire de façon significative la résistance des couches alternées de la structure multicouche de l'échantillon, lorsque celles-ci sont exposées à un champ magnétique externe.

Grâce à leurs petites tailles, faible consommation d'énergie, grande robustesse dans des conditions sévères et un coût relativement faible, les capteurs GMR sont de plus en plus utilisés dans les systèmes électroniques industriels, notamment informatiques ou automobiles, ainsi que dans l'équipement médical de diagnostic. Les capteurs GMR ont une grande sensibilité et une capacité de détection pour la mesure de faibles champs.

Notre manuscrit étant rédigé en anglais avec l'autorisation du Présidant de l'Université de Lorraine, cette synthèse en français en reprend l'essentiel sous forme descriptive des différents chapitres. Afin de ne pas alourdir l'ensemble du mémoire, nous avons choisi d'éviter de reprendre systématiquement les figures dans cette partie.

Dans cette thèse, nous utilisons les GMR pour caractériser des milieux biologiques. Dans un premier temps, différents modèles de capteurs GMR en fonction de leur conception sont présentés. La méthode de caractérisation pour chaque capteur GMR en vue de trouver la valeur de sensibilité maximale est également décrite.

Une fois ces étapes accomplies, nous avons utilisés les GMR pour mesurer les propriétés magnétiques, telles que la perméabilité relative et de la susceptibilité, de fluides magnétiques (ferrofluides) pour de très faibles concentrations.

Les fluides magnétiques sont des solutions colloïdales de matériaux magnétiques de tailles infimes. Les fluides magnétiques sont uniques parce qu'ils combinent une mobilité et une aimantation plus élevée que les liquides ordinaires. Chaque particule est revêtue d'une fine couche de protection qui empêche l'adhérence d'autres particules. Ces particules répandues dans le volume entier du liquide peuvent absorber une charge positive et produire des forces électrostatiques répulsives.

Quand un champ magnétique est appliqué à un ferrofluide, les moments magnétiques des particules s'alignent sur le champ presque instantanément. L'aimantation d'un fluide magnétique répond instantanément à des changements dans le champ magnétique appliqué, et lorsque celui-ci est enlevé, le dipôle magnétique de chaque particule se réoriente de façon aléatoire.

Aujourd'hui, les ferrofluides ont un grand panel d'utilisations et sont proposés pour diverses applications telles que la médecine, le génie mécanique, les appareils électroniques, l'exploitation minière et les applications militaires.

A titre d'application, nous avons étudié la possibilité de caractériser par GMR une bactérie de type Escheri Coli, l'objectif étant à terme le développement d'un biocapteur associer à une électronique embarquée pour du diagnostic in situ.

Chapitre 1 : Eléments de base de la magnétorésistance géante

1.1 Introduction

Notre travail vise à une application des magnétorésistances géantes, nous n'avons pas prétention à leur développement, des rappels de base sont donc nécessaires pour notre communauté d'électroniciens du biomédical. Ce premier chapitre expose les principes théoriques de base des effets de la magnétorésistance géante (GMR) et présente plusieurs types de magnétorésistance.

L'effet de magnétorésistance géante est observé dans les matériaux multicouches possédant une alternance de couches minces de métaux ferromagnétiques et non magnétiques. L'épaisseur d'une couche ultra-mince individuelle peut être seulement de quelques nanomètres. La résistance de l'échantillon atteint son maximum lorsque les champs magnétiques locaux dans les matériaux ferromagnétiques se trouvent dans des directions opposées et son minimum quand les directions sont les mêmes. Ce phénomène a été appelé magnétorésistance géante, car la valeur de résistance était beaucoup plus grande que celle des magnétorésistances connues.

Depuis sa description en 1988, de nombreux capteurs ont été et sont développés ou conçus sur la base de l'effet GMR pour être utilisés dans diverses applications parmi lesquelles la plus connue est la lecture des disques durs de stockage informatique mais aussi les détecteurs de mouvements, les biocapteurs, etc.

Ce chapitre donne un aperçu général des propriétés et de la classification des matériaux magnétiques. Il traite ensuite de l'utilisation de liquides magnétiques, notamment dans les bio-applications.

1.2 Aperçu historique et bases de l'effet GMR

L'effet de base du phénomène GMR est de façon significative la résistance des couches alternées de la structure multicouche de l'échantillon, lorsque celles-ci sont exposées à un champ magnétique externe (voir Figure a). Cet effet a été décrit en 1988 par Albert Fert et Peter Grünberg.

Le développement de méthodes de fabrication de composants de dimensions nanométriques ont permis de créer des dispositifs utilisant avec succès cette propriété de l'électron. Ce fut le début d'un nouveau domaine scientifique; la spintronique. L'émergence de capteurs basés sur l'effet GMR a surtout permis une forte augmentation de la densité d'enregistrement des disques durs d'ordinateurs. Mais de nos jours, il ne s'agit plus du seul domaine d'application.

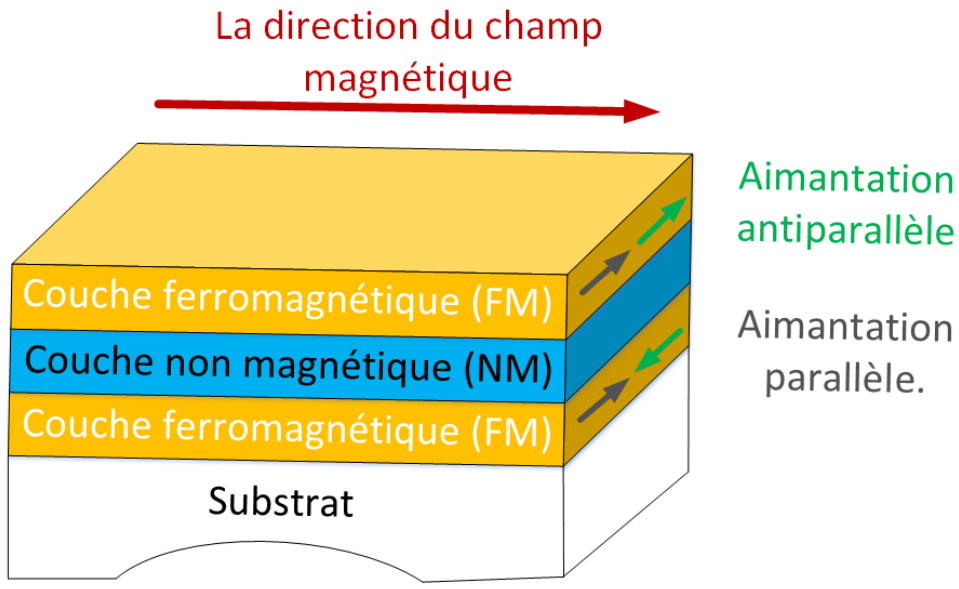

Figure a. Structure de la GMR.

L'effet GMR est engendré par les propriétés quantiques des électrons, qui ont des caractéristiques telles que le spin d'électron. Les électrons peuvent présenter seulement deux directions possibles: vers le haut ou vers le bas. La conduction des électrons dont la direction d'orientation de leurs spins est la même que celle du champ magnétique dans la GMR rencontre moins de résistance dans leur mouvement que les électrons orientés dans le sens opposé, qui eux présentent une plus grande résistance cinétique en entrant plus souvent en collision avec des atomes présents dans leur environnement.

La magnétorésistance est observée lorsqu'un courant électrique circule dans un matériau ferromagnétique à basse température. Ceci peut s'expliquer par le fait que, sous certaines conditions, il y a une forte différence entre la résistivité $\rho \uparrow$ pour les électrons dont les spins sont parallèles à la direction de l'aimantation et de la résistivité $\rho \downarrow$ pour des électrons avec des spins pointés dans la direction antiparallèle.

1.3 Classes de magnétorésistances géantes

1.3.1 Vannes de spin (SV-GMR)

Le principe de fonctionnement dépend du fait qu'une partie est très sensible au champ extérieur et que l'autre, qui sert de système de référence magnétique, ne l'est pas. Cette structure fournit un signal bipolaire avec une grande sensibilité dans un dispositif optimisé.

De plus, la couche antiferromagnétique employée dans cette structure peut être influencée par le champ magnétostatique de la couche libre.

1.3.2 Courant dans le plan (CIP) et le courant perpendiculaire au plan (CPP)

L'effet de magnétorésistance géante dans une grille multicouche de métal ferromagnétique et normal se manifeste au niveau du courant perpendiculaire au plan (CPP) et du courant dans le plan (CIP). Dans la structure CIP, le courant est parallèle aux plans des couches magnétiques et dans la structure CPP le courant circule perpendiculairement au plan du film.

Les mécanismes des effets de la GMR dans les géométries CPP et CIP sont similaires et ont des caractéristiques semblables. Les valeurs de la magnétorésistance obtenues pour le premier effet, sont environ deux fois supérieures à celles de la seconde. Cependant, la résistance absolue des super-réseaux métalliques, avec une épaisseur totale de l'ordre de quelques dizaines de nanomètres mesurée dans la géométrie du CPP, est très petite et difficile à mesurer. Par conséquent, les applications pratiques de l'effet GMR en géométrie CPP sont beaucoup moins attractives.

1.3.3 Structure de jonction tunnel magnétique (JTM)

Dans d'autres générations de la spintronique, des structures basées sur le phénomène de la jonction tunnel magnétique (JTM) avaient été inclues. Le JTM se compose de deux couches de matériaux ferromagnétiques séparées par une couche ultra - mince d'isolant. De plus, si l'épaisseur de l'isolant est plus petite que 2 nm, l'électron peut traverser la barrière. Ce processus est appelé effet tunnel, et cela est dû à la nature ondulatoire des électrons. La probabilité d'effet tunnel dépend de la longueur d'onde ou de l'énergie de l'électron.

Dans un matériau ferromagnétique, l'énergie d'un électron dépend de l'orientation de son «spin» -vers le haut ou vers le bas. Cela conduit à un effet tunnel dépendant du spin. Si les moments magnétiques des couches adjacentes sont parallèles, la conductivité de la jonction tunnel magnétique est grande, et si l'aimantation est anti-parallèle, la probabilité de l'effet tunnel est faible.

1.3.4 Structure Magnétoimpédance géante (MIG)

L'effet de magnétoimpédance géante (MIG) a été découvert il y a quelques années dans les alliages amorphes. L'effet de magnéto-impédance géante est un phénomène qui implique d'importantes variations de l'impédance d'un conducteur métallique magnétique

(ferromagnétique) lorsqu'il est placé dans un champ magnétique continu, en présence d'un courant à haute fréquence (de quelques dizaines de kHz à quelques centaines de MHz.

1.4 Les matériaux magnétiques

1.4.1 Classification

a. Diamagnétisme

Le diamagnétisme est l'une des propriétés fondamentales de toute substance, quand celle-ci est magnétisée dans la direction opposée à celle du champ magnétique appliqué. Un grand nombre de composés organiques et inorganiques en interaction avec le champ magnétique se comportent comme un diamagnétique.

b. Paramagnétisme

Le paramagnétisme concerne les substances dont les particules possèdent un moment magnétique intrinsèque. En l'absence d'un champ extérieur, ces moments sont orientés de manière aléatoire (pas d'aimantation) et sont orientés, lors de l'application d'un champ extérieur, le long de celui-ci (aimantation paramagnétique). En général, le paramagnétisme est faible par rapport au ferromagnétisme.

c. Ferromagnétisme

Le ferromagnétisme concerne les substances qui ont une perméabilité magnétique bien supérieure à 1. Celles-ci comprennent le fer, le nickel, le cobalt, et de nombreux alliages d'entre eux. La caractéristique de ces substances est une valeur de sensibilité exceptionnellement élevée. Les matériaux ferromagnétiques ont une susceptibilité magnétique extrêmement élevée et fortement dépendante du précédent champ appliqué.

d. Ferrimagnétisme

Le ferrimagnétisme est une propriété magnétique de la matière dans laquelle les moments magnétiques des atomes ou des ions voisins sont orientés antiparallèlement les uns des autres. Dans les matériaux ferrimagnétiques l'aimantation perdure, même après la suppression d'un champ magnétique externe. Un matériau ferrimagnétique peut montrer, en dépit de l'orientation antiparallèle de ses moments magnétiques, un grand moment magnétique total, dans au moins un domaine.

e. Antiferromagnétisme

L'antiferromagnétisme est l'un des états magnétiques d'une substance, où les aimantations élémentaires (atomique ou ionique) dans les particules adjacentes de la matière sont orientées dans des directions antiparallèles (à l'opposé du ferromagnétisme). L'aimantation globale est donc très faible. De plus, la sensibilité de l'antiferromagnétisme est faible et positive, contrairement au ferromagnétisme, où la même orientation d'aimants élémentaires conduit à une forte aimantation.

1.4.2 Propriétés et applications des matériaux magnétiques

Depuis ces dernières années, les matériaux magnétiques font partis des domaines de développement les plus rapides des micro-nanosciences modernes. Ils captent l'attention des chercheurs pour diverses applications dans des domaines comme la chimie, la physique, la biologie et les usages médicaux qui nécessitent chaque année d'avantage de nouveaux matériaux présentant de nouvelles propriétés qualitatives.

Actuellement, les fluides magnétiques sont utilisés dans diverses applications technologiques telles que l'industrie chimique (comme lubrifiants magnétiques dans les systèmes de refroidissement), la médecine (séparation magnétique des cellules, traitement du cancer , administration de médicaments magnétiques et immunologiques), en génie mécanique (Projets de recherche de la NASA sur l'utilisation d'un fluide ferromagnétique dans un anneau fermé, comme base pour un système de stabilisation de vaisseau spatial dans l'espace; ainsi dans le secteur de l'imprimerie et l'industrie du pétrole), les appareils électroniques, l'industrie minière et militaire (colmatage de brèches et isolation entre elles de pièces en mouvement, réduction de frottement).

Une autre utilisation importante des ferrofluides est présente en médecine. Comme nous le savons, les médicaments anticancéreux sont nocifs pour les cellules saines. Cependant en les mélangeant avec un fluide magnétique avant de les injecter dans le sang, il est possible de les canaliser vers une tumeur sans endommager les tissus environnants. Des particules de magnétite magnétiques sont utilisées pour traiter le cancer par hyperthermie. Cette méthode de traitement repose sur le fait que, sous l'influence d'un champ magnétique, l'alternance des particules de magnétite provoque leur échauffement et inhibe la croissance de cellules

cancéreuses. La thérapie hyperthermie en utilisant ferrofluide est présenté en Figure b.

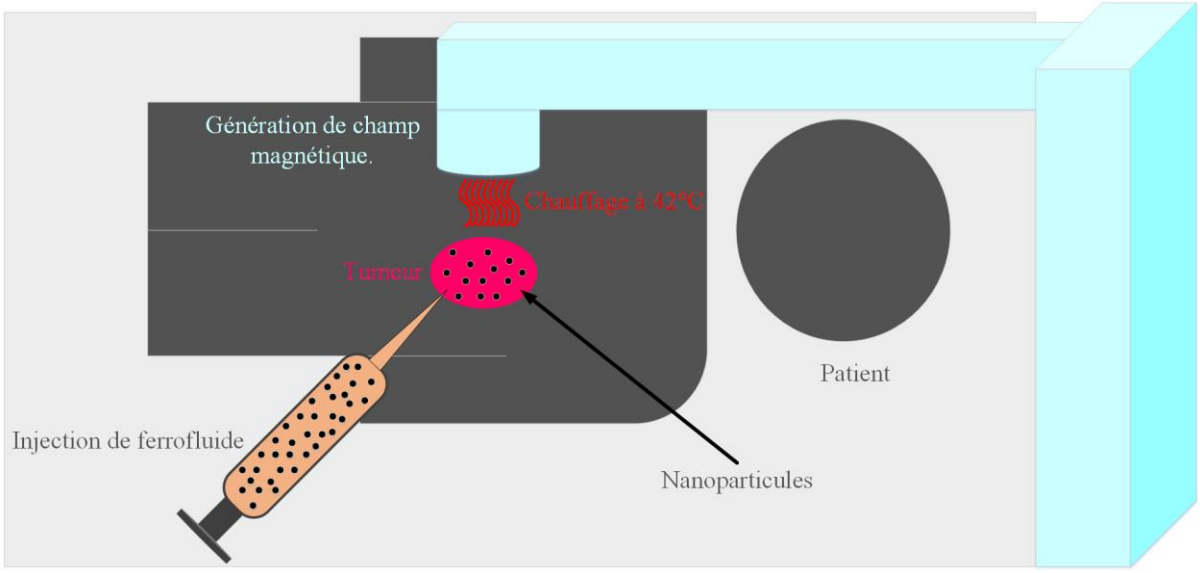

Figure b. Thérapie hyperthermie.

Un fluide magnétique peut aussi être utilisé comme agent de contraste pour rayons X. Les diagnostics habituels par radioscopie des voies gastro-intestinales sont basés sur l'utilisation du sulfate de baryum (bouillie barytée). Une autre bio-application majeure des fluides magnétiques est en chirurgie. Un fluide magnétique peut être injecté dans une veine ou une artère, puis positionnée à l'aide d'un aimant afin de réaliser un bouchon pour obturer une veine après une ablation. Finalement, nous pouvons mentionner un autre rôle vital des fluides magnétiques, celui de son utilisation en orthopédie et traumatologie où il est utilisé pour lubrifier les articulations (pour les prothèses des membres inférieurs). Le traitement local de l'arthrite ou l'arthrose avec l'injection de ferrofluide dans le joint est présenté en Figure c.

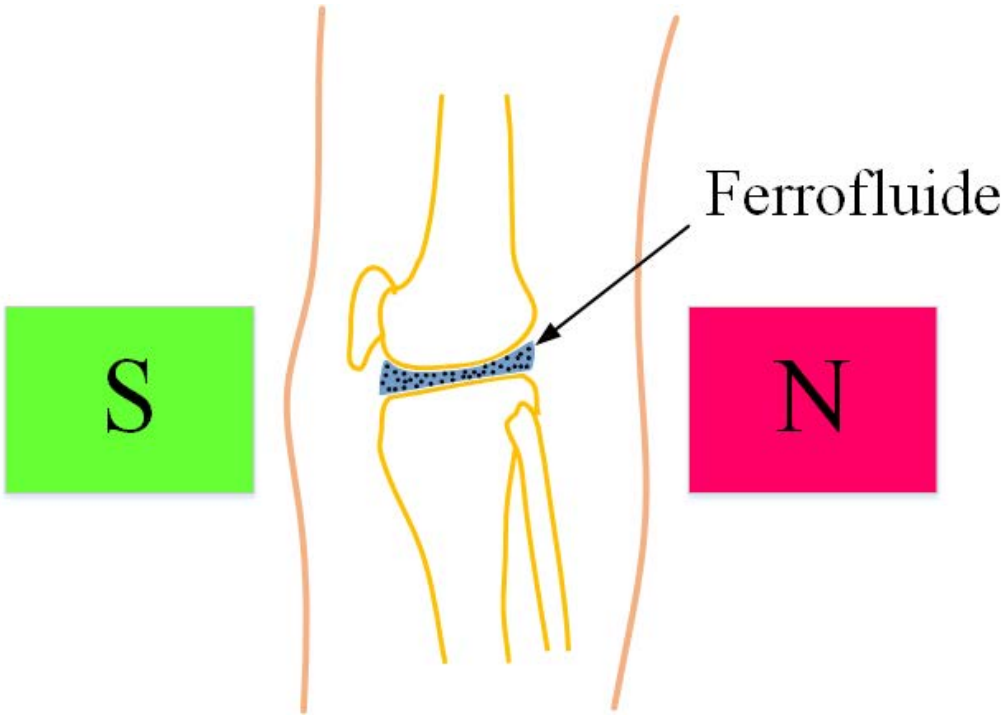

Figure c. Traitement local de l'arthrose en utilisant un liquide magnétique.

1.5 Conclusion

Le début du premier chapitre contient un résumé de l'histoire de la découverte de l'effet de magnétorésistance géante (GMR) et décrit les premières expérimentations de cet effet sur les multicouches Fe/Cr antiferromagnétiquement couplé (AFC) en 1988.

Par la suite, la comparaison du capteur GMR et d'autres types de capteurs de champ magnétique, en fonction leurs puissances, leurs coûts et leurs aptitudes à détecter le champ magnétique dans plusieurs gammes ont été exposés. Nous avons décrit les caractéristiques fondamentales pour comprendre l'effet GMR en multicouches et présenté les structures les plus importantes de la magnétorésistance géante.

Par ailleurs, nous avons pris connaissance du comportement de l'ensemble des matériaux magnétiques placés dans un champ magnétique ou lorsque le champ magnétique est supprimé. Nous pouvons en conclure que tous les matériaux peuvent être classés dans différentes catégories en fonction de leur susceptibilité magnétique.

A la fin de ce chapitre, un bref historique et les principales applications des fluides magnétiques dans divers domaines, en particulier en médecine, ont été examinés.

Chapitre 2: Caractérisation de capteurs GMR de type aiguille

2.1 Introduction

Un biocapteur est un dispositif dédié à la détection ou la quantification des propriétés physiques associant un élément biologique avec un composant de détection physico-chimique ou physique. La fabrication des biocapteurs basés sur l'effet GMR constitue une nouvelle façon de détecter et caractériser les propriétés des molécules biologiques magnétiques. Le principe de mesure est la variation de la résistance électrique de l'élément GMR lorsqu'il est soumis à un champ magnétique, suivant la présence ou non de micro ou nanoparticules. Sous cet effet, même en présence d'un faible champ magnétique, la résistance change.

Ce deuxième chapitre traite plus spécifiquement de la fabrication et la caractérisation des différents types de capteurs utilisés, soit les capteurs dénommés GMR I et GMR II conçus à l'Université de Kanazawa et le capteur GMR III développé dans notre laboratoire. Nous avons déterminé la valeur de la sensibilité de chaque capteur GMR et calculé les variations de résistances ΔR des éléments selon la densité du flux magnétique (B).

2.2 Structures et conceptions des sondes GMR à aiguille

2.2.1 Premier modèle de capteur

Dans ce type de capteur GMR, l'aiguille du capteur comporte deux éléments de détection, placés en début et au bout de l'aiguille. Chaque élément de détection présente des dimensions de 75 µm × 75 µm.

La configuration en demi-pont de Wheatstone du capteur GMR permet de mesurer les variations de tension induites par le champ magnétique, en supprimant en grande partie la composante continue de la tension de polarisation du pont de mesure. Les résistances du pont de Wheatstone doivent avoir approximativement les mêmes valeurs que les éléments GMR, de façon à avoir la même valeur de tension sur chaque partie de la sortie différentielle. Cette configuration permet d'amplifier directement les variations du signal, sans utiliser de filtre passe-haut pour éliminer la composante continue.

La longueur de l'aiguille à injecter dans la cavité pour la mesure dans les fluides magnétiques est de 3 cm, avec un diamètre d'environ 300 µm. L'aiguille est réalisée en carbure de titane-aluminium (AlTiC), un matériau dur réalisé par frittage de l'oxyde d'aluminium (Al_2O_3) et du carbure de titane (TiC). Les éléments de détection sont sensibles à la présence d'un champ magnétique. Pour ce type de capteur GMR, le courant maximal admissible est de 9,7 mA.

Les éléments de détection voient leurs résistances changées en présence du champ magnétique. Le premier élément GMR détermine la densité de flux magnétique (B_1) dans le récipient contenant le liquide et la seconde la densité de flux magnétique extérieur (B_0). Le sens de détection du capteur GMR est perpendiculaire à l'aiguille.

2.2.2 Deuxième modèle de capteur

Le deuxième capteur est constitué de deux parties principales: la première est une aiguille et la seconde est un pont de Wheatstone.

Le type de capteur à aiguille SV-GMR (à valve de spin) est constitué de quatre éléments de détection. Le premier élément de détection (GMR1) se situe à la pointe de l'aiguille et les autres (GMR2, GMR3 et GMR4) se situent à l'autre extrémité de l'aiguille. Chaque élément de détection présente des dimensions de 75 µm × 40 µm (voir Figure d). Ils sont tous les quatre interconnectés avec une configuration en pont de Wheatstone.

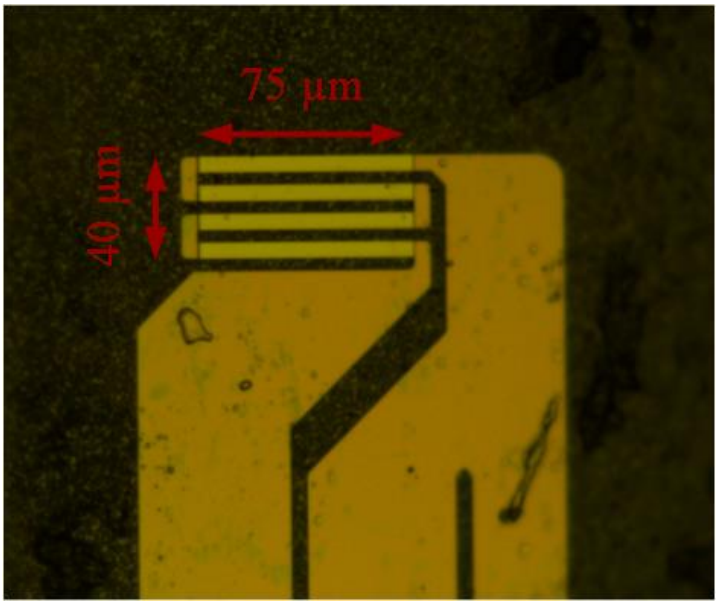

Figure d. Zone active pour chaque élément de détection.

Comme nous l'avions mentionné précédemment pour le premier modèle du capteur GMR, le premier élément de détection, à la pointe du capteur, est en contact avec le liquide magnétique dans la cavité et les autres éléments de détection sont placés de telle façon à détecter la densité de flux magnétique à l'extérieur du ferrofluide de la cavité.

La longueur de l'aiguille est de 17 mm avec une section carré de 300 × 300 µm et le matériau utilisé pour sa fabrication est le même que celui utilisé pour le premier modèle. La direction de détection de ce capteur GMR est parallèle à l'aiguille. Il convient de noter que le courant maximum admissible pour ce type de capteur GMR est 5 mA.

2.2.3 Troisième modèle de capteur

Le modèle GMRIII se compose de deux éléments de détection GMR, placés dans une micro-puce. Ces deux éléments de détection sont situés l'un en face de l'autre, tête-bêche. Cette configuration des deux éléments GMR permet d'augmenter la sensibilité, la détection précise du champ magnétique dans les deux sens est améliorée. La mini-puce possède trois broches qui sont connectées à une alimentation électrique.

La longueur de l'aiguille du capteur est de 30 mm, les éléments GMR sont placés à la pointe de l'aiguille et interconnectés à deux résistances de référence présentes à l'autre bout, le tout formant une configuration en demi-pont de Wheatstone.

Le sens de détection du capteur GMR de type III est colinéaire à l'aiguille. Ce capteur est fourni avec une connectique mini-B USB placée à l'extrémité du capteur et connectée à l'alimentation en courant continu par le biais d'une carte d'interface. De plus, le courant maximum de ce type de capteur GMR est de 5 mA.

2.3 Caractérisation des capteurs à magnétorésistance géante

2.3.1 Caractérisation du premier capteur

L'objectif principal de cette partie est de caractériser le capteur GMR I. Pour cela, nous devons créer une densité de flux magnétique uniforme uniquement au niveau de l'élément sensible, car pour calculer précisément la sensibilité, elle ne doit être en contact qu'avec le premier capteur GMR placé au bout de l'aiguille. Celui-ci est placé au centre des bobines avec une densité de flux magnétique (B_1) et le deuxième élément GMR devrait rester complètement en dehors du champ (B_0).

À cette fin, nous avons fabriqué des bobines de Helmholtz de petites tailles, composé de deux bobines de diamètre 18 mm et de 9 enroulements. La distance entre les bobines est juste suffisante pour laisser passer l'aiguille du capteur.

Pour faciliter l'utilisation et assurer la protection de l'aiguille contre les chocs, nous avons utilisé un système de déplacement. Celui-ci est commandé par le contrôleur PCON-CG-42PI qui nous permet de sauvegarder jusqu'à 512 positions préréglées en utilisant le logiciel fourni.

Grâce au système de déplacement, nous avons la possibilité d'insérer minutieusement et progressivement la fine aiguille au centre de la petite bobine de Helmholtz, générant le champ magnétique uniforme.

Le banc de mesure est contrôlé par deux outils : le premier pour piloter le système de déplacement, et le second pour contrôler le spectromètre d'impédance HF2IS et stocker les données de mesure obtenues avec le capteur GMR.

Le capteur GMR I est connecté à l'alimentation en courant continu (± 6 V) par le biais d'une carte d'interface, sur laquelle est placée une résistance pour limiter le courant. Le signal différentiel (Vout-Vref) est envoyé vers un préamplificateur (AD 620) pour y être amplifié 1200 fois (gain de 62 dB) avant son acquisition par l'impédance mètre HF2IS. Les données de sortie (Vrms, déphasage [deg]) du signal GMR sont sauvegardées sur l'ordinateur.

La petite bobine de Helmholtz est alimentée par un amplificateur à gain variable. Grace aux générateurs de signaux de sortie du HF2IS, nous pouvons directement générer le signal d'alimentation des bobines de Helmholtz. Un multimètre de contrôle placé entre l'amplificateur de puissance et la bobine de Helmholtz permet de mesurer le courant traversant la bobine. La fréquence de travail utile de la bobine de Helmholtz est de 60 Hz. En fonction de la valeur de la tension d'entrée (en mV), nous pouvons obtenir une densité de flux magnétique (B) variant 5 µT à 410 µT. La mesure du champ a été obtenue à l'aide d'un Gaussmètre/Teslamètre 3D.

Différentes valeurs de résistances ont été testées au niveau de la carte d'interface pour obtenir la sensibilité la plus grande possible. La meilleure sensibilité a été obtenue en utilisant deux résistances supplémentaires de 809 Ω chacune, et avec une densité de flux magnétique d'environ 9 µT. De plus, selon les résultats obtenus, nous pouvons en conclure que la variation de la valeur de l'élément sensible (GMR) en fonction de la densité de flux magnétique (B) est environ égale à 0,34 $\%mT^{-1}$.

2.3.2 Caractérisation du deuxième capteur

Nous avons utilisé la même configuration que pour le premier modèle afin de caractériser ce capteur. La différence concerne le positionnement de la petite bobine Helmholtz, compte tenu de la direction de la sensibilité du modèle de capteur 2 (colinéaire à l'aiguille).

La fréquence de travail utile de la bobine de Helmholtz est de 75 Hz. En fonction de la valeur de la tension d'entrée (en mV), nous avons pu obtenir une gamme de densité de flux magnétique (B) de 6 µT à 309 µT. Les résultats expérimentaux de caractérisation du gain de la sonde à aiguille ont permis de déterminer la configuration donnant la meilleure sensibilité pour ce capteur. Celle-ci a été obtenue par l'utilisation d'une seule résistance de 2.128 kΩ pour la carte d'interface, avec une densité de flux magnétique d'environ 130 µT.

Avec les résultats du second modèle de capteur, nous pouvons en conclure que la variation de la valeur de l'élément sensibilité en fonction de la densité de flux magnétique vaut à 0.71 $\%mT^{-1}$ dans la partie linéaire. La sensibilité de l'élément maximale (1,46 $\%mT^{-1}$) est atteinte avec une résistance 2.128 kΩ à 130 µT.

2.3.3 Caractérisation du troisième capteur

La bobine de Helmholtz réalisée au sein de notre laboratoire, pour cette étape de caractérisation, se compose de deux bobines circulaires de douze enroulements avec un conducteur de 16 mm^2 (cuivre multibrins). Chaque bobine possède un diamètre de 52 cm et la distance entre les bobines est égale au rayon des bobines (26 cm).

Le capteur GMR III est connecté à l'alimentation en courant continu (± 6 V) à travers la carte d'interface. Le signal différentiel Vout-Vref (sans préamplificateur) est envoyé à l'impédance mètre HF2IS. Les données de sortie du signal du capteur GMR sont ensuite sauvegardées.

La bobine de Helmholtz est alimentée par un amplificateur de puissance. Les fréquences de travail utiles de la bobine de Helmholtz sont de 60, 75 et 100 Hz. En changeant la valeur de tension d'entrée (mV), la densité de flux magnétique (B) a pu être régulée jusqu'à 750 µT.

Les valeurs de sensibilité les plus élevées en fonction de la densité de flux magnétique, pour les différentes fréquences, sont approximativement égale à 245 µV/µT. De plus, selon les résultats obtenus, nous pouvons conclure que la valeur de la sensibilité de l'élément GMR en fonction de la densité de flux magnétique (B) est approximativement égale à 4% mT^{-1}.

2.4 Conclusion

Dans ce chapitre, nous avons présenté la conception et les spécifications de chaque capteur GMR. Les capteurs possèdent deux parties principales, la première est l'aiguille du capteur, spécialement conçue pour s'insérer au milieu d'une cavité de faibles dimensions, contenant un ferrofluide. Sur l'aiguille de chaque capteur, les éléments de détection sont placés pour mesurer la densité de flux magnétique à l'intérieur et à l'extérieur du fluide magnétique (en tant que référence).

Le deuxième élément important des sondes est la configuration en pont de Wheatstone afin de mesurer les variations de tension induites par le champ magnétique, tout en supprimant la majeure partie de la tension continue de polarisation de la GMR. Cette configuration est idéale pour maximiser la sensibilité de mesure. A la fin de ce chapitre, nous avons mené les

étapes de caractérisation des capteurs, et les sensibilités de tous les capteurs ont été déterminées.

Chapitre 3: Détection des propriétés des fluides magnétiques par capteurs GMR

3.1 Introduction

Les propriétés magnétiques de la matière biologique restent encore un champ d'investigation largement étudié dans le cadre des travaux de recherche liés aux applications en nanomédecine. Les variations de susceptibilité ou de perméabilité en fonction de la fréquence sont une base pour le développement de nouvelles applications biomédicales. Les GMRs sont particulièrement bien adaptées pour la détection des particules magnétiques, car elles offrent une haute sensibilité et une capacité de détection à l'échelle micrométrique et nanométrique.

Les ferrofluides et les liquides magnétiques comportent des particules en matériaux magnétiques tels que le fer, le nickel et le cobalt de très faibles tailles. Ils ont actuellement une grande importance dans les technologies militaires, mécaniques ou électroniques ainsi que dans les différents domaines d'applications médicaux.

L'objectif du troisième chapitre est d'estimer par la mesure les propriétés magnétiques telles que la perméabilité relative et la susceptibilité de fluides magnétiques par un capteur GMR. Afin de valider les résultats expérimentaux obtenus avec les capteurs, nous allons les comparer à ceux obtenus par d'autres méthodes classiques comme le magnétomètre à échantillon vibrant (VSM : Vibrating Sample Magnetometer) ou des calculs théoriques.

3.2 Méthodologie expérimentale de ferrofluide

3.2.1 Préparation de plusieurs concentrations de ferrofluide et montage expérimental

Plusieurs expériences ont été réalisées afin de préparer les différents fluides magnétiques avec plusieurs valeurs de densité relative (D_W) qu'on peut calculer avec l'équation (3.1). Une concentration initiale (de référence) de fluide magnétique (Fe_2O_3), avec des particules magnétiques de 16 nm a été réalisée à partir de 40 % de fluide magnétique mélangé avec 60 % d'eau distillée. Dans cette partie, le ferrofluide a été dilué avec de l'eau distillée pour obtenir plusieurs fluides magnétiques ayant des densités de poids égales à 0,09 %, 0,3 %, 0,4 % et 1 % (Densité volumique de 1:50 , 1:120 , 1:160 , 1:600). La Figure e représente la vue de quatre échantillons de fluide magnétique de différentes densités.

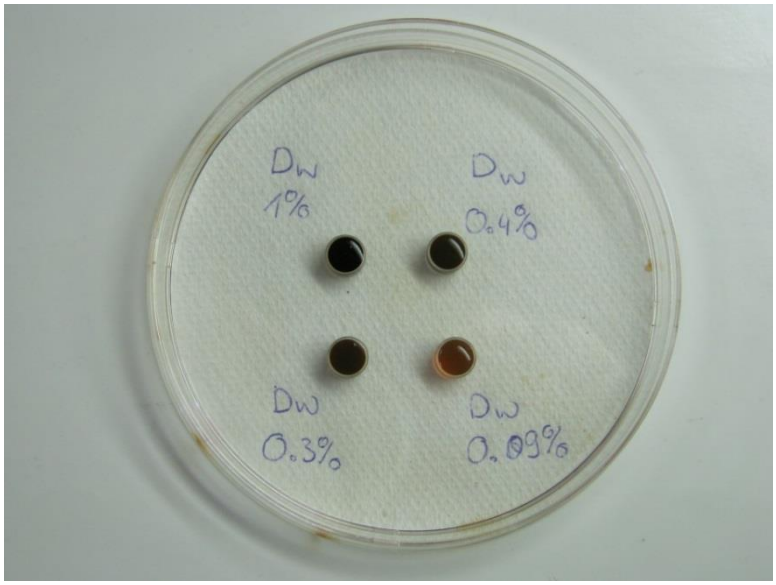

Figure e. Différentes concentrations de ferrofluide.

78,5 µl de chaque fluide magnétique ont été déposés à tour de rôle dans une cavité cylindrique de dimensions 5 mm × 4 mm à l'aide d'une micro pipette. Puis, les quatre ferrofluides sont placés au centre de la bobine de Helmholtz, où le champ magnétique est le plus uniforme.

Le dispositif expérimental pour la mesure se compose de deux parties principales. La première partie correspond au capteur GMR à aiguille et la deuxième partie représente l'élément la bobine de Helmholtz pour générer un champ magnétique uniforme.

Le capteur de type SV-GMR à aiguille utilisé dans cette étude est constitué de deux éléments de détection GMR connectés dans une configuration en pont de Wheatstone. La dimension de chaque élément de détection est de 150 µm par 150 µm. La longueur de l'aiguille est égale à 3cm pour une section de 300 µm × 300 µm. L'aiguille de détection est placée avec précaution dans le ferrofluide, au centre de la cavité. Après chaque mesure de ferrofluide, l'aiguille du capteur GMR a été nettoyée avec soin.

Le signal de sortie est amplifié en utilisant un circuit amplificateur (AD524: Dispositif analogique avec un gain de 40 dB). Les signaux différentiels Vout-Vref du capteur GMR ont été acquis par amplificateur à verrouillage de phase numérique multifonction (NF Li 5640). Afin de réduire le pourcentage d'erreur des mesures du capteur GMR, nous avons mesuré l'amplitude du signal et de la phase moyennée 5 fois pour chaque échantillon par le biais d'un programme MATLAB® pilotant l'amplificateurs à verrouillage. Par la suite, nous avons calculé une moyenne des données obtenues pour chaque échantillon.

Le signal de la bobine de Helmholtz est amplifié par un amplificateur de puissance alimenté par un signal sinusoïdal provenant d'un générateur d'onde (Wave factory 1965 NF electronic instruments multifonction), l'amplitude du courant de la bobine de Helmholtz est observée par un oscilloscope (oscilloscope Iwatsu DS-8814 Bringo). La fréquence expérimentale d'excitation de la bobine de Helmholtz est de 100 Hz, le courant d'entrée de la bobine est de 200 mA, avec un champ d'excitation (H) d'environ 121 A/m et une densité de flux magnétique (B) de 153 μT. La fréquence de mesure est de 100 Hz.

3.2.2 Méthode expérimentale et résultats obtenus par VSM

Le centre de compétences (CC) Magnétisme de l'Institut Jean Lamour regroupe des appareils permettant d'effectuer diverses mesures physiques entre autres en fonction d'un champ magnétique et/ou de la température (http://ijl.univ-lorraine.fr/la-recherche/centre-decompetences/magnetisme/equipements.html). Le magnétomètre à échantillon vibrant ou VSM (Vibrating Sample Magnetometer) est un instrument utilisé pour caractériser et mesurer les propriétés magnétiques de matériaux en fonction du champ magnétique, de la température et du temps. Le VSM a été inventé par Simon Foner au laboratoire Lincoln en 1955. Un VSM peut être utilisé pour la caractérisation de liquide, poudre ou films minces. Parmi les propriétés qui peuvent être mesurées, on peut notamment citer les moments magnétiques (aimantation) et champ coercitif.

Le principe de la mesure du VSM repose sur la détermination de la variation d'une induction magnétique produite par le mouvement oscillant vertical de l'échantillon à travers les bobines. Dans cette méthode, l'échantillon est placé sous un champ magnétique uniforme.

Le champ magnétique alternatif provoque un champ électrique dans les bobines d'exploration (selon la loi de Faraday), leurs signaux sont mesurés par un détecteur synchrone. En outre, la fréquence et l'amplitude du VSM sont constantes.

3.2.3 Comparaison des résultats obtenus par le capteur GMR et par le VSM

Les résultats (voir Figure 3.18) sont présentés sous forme de rapport entre perméabilité relative (μ_r) et susceptibilité (χ) en fonction de différentes gammes de densités (D_W %), avec les résultats obtenus par le capteur GMR de type aiguille et ceux obtenus à partir du VSM.

On peut observer que les résultats pour μ_r et χ sont proportionnels à D_W et que les résultats du capteur GMR et du VSM sont cohérents entre eux.

3.3 Estimation de la densité de poids de fluide magnétique, de la perméabilité relative et de la susceptibilité magnétique du fluide-D

3.3.1 Spécification et préparation des différentes concentrations de fluide MAG-D

Le fluide magnétique-D (MAG-D) est utilisé comme marqueur de contraste spécifique aux résonances magnétiques (IRM), qui contient une dispersion aqueuse d'un grand nombre de nanoparticules superparamagnétiques d'oxyde de fer ayant des diamètres hydrodynamiques de 100 à 200 nm. Ses particules superparamagnetiques ont un noyau de magnétite (Fe_3O_4= $Fe^{II}(Fe^{III})_2O_4$). Le fluide magnétique-D peut être injecté sous forme intraveineuse, pour réduire le temps de diffusion et réaliser une imagerie immédiate du foie. La densité de poids et la densité de volume de fluide pur MAG-D peuvent être déterminées à partir des équations 3.1 et 3.2.

Le fluide MAG-D est également appliqué dans d'autres applications telles que la séparation des cellules et des médicaments magnétiques ciblant.

A partir du fluide MAG-D de base (200 nm), nous avons préparé plusieurs concentrations en le mélangeant avec de l'eau distillée, afin de mesurer avec le capteur GMR les paramètres des fluides magnétiques tels que la perméabilité et la susceptibilité relative en fonction de leurs différentes dilutions. Dans cette étape de l'expérience, une micro pipette a été utilisée pour réduire au maximum la marge d'erreurs des dilutions.

Nous avons réalisé plusieurs dilutions telles que 1:1, 1:3, 1:6, 1:10, 1:20 et 1:40 du fluide pur MAG-D.

3.3.2 Description de la méthode expérimentale et de la configuration de mesure

La bobine de Helmholtz utilisée est alimentée par un amplificateur à gain variable relié à deux transformateurs série adaptateurs d'impédance. Par ailleurs, la fréquence d'utilisation de la bobine de Helmholtz est de 75 Hz et la tension d'entrée générée par l'impédance mètre HF2IS est de 180 mV. La valeur de la densité de flux magnétique (B) produite au centre de la bobine de Helmholtz est de 185,7 µT.

Au début, l'aiguille du capteur était précautionneusement placée au centre de la bobine de Helmholtz pour enregistrer à titre de référence les données du capteur sans présence de fluide magnétique (seulement de l'air). Ces données sont utilisées comme référence pour calculer les changements de densité de flux magnétique pour différentes concentrations. Ensuite, 450 µl de fluide pur MAG-D ont été versés dans la cavité cylindrique de dimensions 8×8 mm à

l'aide d'une micropipette. La cavité est placée au centre de la bobine de Helmholtz, puis l'aiguille du capteur insérée avec beaucoup d'attention au milieu de la cavité. Nous avons ensuite sauvegardé les données de sortie du capteur par le programme d'interface du HF2IS. Après chaque mesure, l'aiguille du capteur GMR a été prudemment sortie de la cavité de liquide magnétique pour être nettoyée très méticuleusement à l'eau distillée avec éponge douce, afin de réduire le pourcentage d'erreurs de test par contamination.

Cette méthode de mesure a été utilisée pour les autres fluides de différentes concentrations (densités de poids variant de 2,45 %, 1,23 %, 0,62 %, 0,35 % et 0,22 %).

En outre, il faut souligner que la cavité a été réalisé au laboratoire en polydiméthylsiloxane (PDMS), substance biocompatible et très résistante à de nombreux solvants.

3.3.3 Analyse des résultats du capteur GMR et comparaison avec les résultats expérimentaux et théoriques

Dans cette partie, nous présentons les résultats expérimentaux obtenus avec le deuxième modèle de capteur GMR. Au début, nous avons calculé la relation entre les variations de la densité de flux magnétique (δ %) et la densité de poids de fluide magnétique (D_W %) pour les faibles concentrations de fluides magnétiques.

Ensuite, les résultats expérimentaux obtenus par le capteur GMR à aiguille, montrant la relation entre la perméabilité relative et la susceptibilité en fonction de différentes densités de poids de fluide MAG-D sont présentées et évalués dans la Figure 3.26 et la Figure 3.27. La comparaison entre les résultats théorique et expérimentaux montre une bonne concordance.

3.4 Conclusion

Dans ce chapitre, nous avons préparé différentes concentrations de fluides basés sur 2 liquides magnétiques différents. Ils diffèrent par la taille, le nombre et la densité des particules. Ensuite, nous avons mesuré leurs propriétés magnétiques telles que la perméabilité relative (μ_r) et la susceptibilité (χ) grâce à des capteurs GMR.

Afin de valider les résultats expérimentaux obtenus par capteur GMR sur de premiers liquides, nous avons utilisé le magnétomètre à échantillon vibrant (VSM). Pour le fluide MAG-D, les résultats expérimentaux ont été comparés avec les résultats théoriques. Les comparaisons montrent que les résultats sont proches et en accord.

Chapitre 4: Détection de la bactérie Escherichia coli par capteur GMR

4.1 Introduction

La première partie de ce chapitre se concentre sur les cellules bactériennes, et en particulier sur Escherichia coli. Nous y décrivons une des plus meurtrières et des plus connues, Escherichia coli O157:H7 (EHEC) et les maladies associées.

Nous exposerons la détection d'un marqueur magnétique composé de microbilles par capteur GMR. Ces microbilles sont largement utilisés dans le domaine médical pour séparer les bactéries Escherichia coli O157:H7 de la nourriture, l'alimentation, l'eau, etc… . L'estimation des propriétés magnétiques de ce marqueur constitue notre second objectif.

4.2 Résumé sur les Escherichia coli

4.2.1 Définition des Escherichia coli

La bactérie E. coli a été découverte en 1885 par le bactériologiste allemand Theodor Escherich. E. coli est une bactérie de la famille des entérobactéries en forme de bâtonnet à Gram négatif, et il est classé comme un procaryote. Les cellules des bactéries procaryotes, comprennent, à la différence des eucaryotes, une structure relativement simple. Dans la cellule procaryote, les noyaux organisés sont absents et l'ADN flotte au centre du liquide (le cytoplasme) de la cellule. Elle ne contient qu'un seul chromosome, qui n'est pas séparé du reste de la cellule par une membrane, et se trouve directement dans le cytoplasme. Le chromosome bactérien contenant très peu de protéine et un brin d'ADN, il ne peut être appelé conventionnellement chromosome. Contrairement aux procaryotes qui ont un ADN circulaire, l'ADN eucaryote est linéaire.

4.2.2 Spécification d'Escherichia coli

La taille de cette bactérie est très faible, autour de 0,5 µm de diamètre et 2-3 µm de long pour un volume cellulaire d'environ 0,6-0,7 μm^3. Escherichia coli coexiste fréquemment avec des micro-organismes qui consomment de l'hydrogène.

La croissance optimale d'E. coli est réalisée à 37°C, certaines souches peuvent vivre à des températures jusqu'à 49°C. La croissance peut être stimulée par la respiration aérobie ou anaérobie, différentes sortes d'agents oxydants et réducteurs, y compris l'oxydation du pyruvate, l'hydrogène, les acides aminés, la réduction de l'oxygène, le nitrate, etc… .

Le procédé de reproduction chez les bactéries peut expliquer cela, lors de l'augmentation de cellules procaryotes, qui augmente considérablement le nombre de composés chimiques.

La grande majorité des procaryotes sont caractérisés par une division transversale homographique binaire, ce qui conduit à la formation de deux cellules identiques. La division de la majorité des bactéries Gram-positive et la division des cellules de cyanobactéries filamenteuses se produisent par le biais de la synthèse des parois transversales, allant de la périphérie vers le centre. Par conséquent, dans le milieu de la cellule, il y a une invagination, accompagnée par la formation de différents mésosomes. Ils sont activement impliqués dans la synthèse du peptidoglycane et d'autres cellules composant la paroi.

4.2.3 Maladies causées par Escherichia coli

Une grande partie des maladies provoquées par Escherichia coli sont des infections des voies urinaires, d'autres infections courantes originaires des conduits biliaires du foie et de la cavité abdominale, de la peau et des poumons.

Les infections causées par Enterohemorrhagic Escherichia coli (EHEC) sont généralement produites par la voie fécale-orale, par ingestion de viande contaminée, de lait, de légumes, etc.

Certains types d'E. coli telles qu'E. coli O157 de souches H7 et E. coli O104 de souches H21 synthétisent des toxines potentiellement mortelles.

E. coli O157:H7 est un sérotype d'E. coli qui a la capacité de produire des toxines telles que des toxines de Shiga ou des vérotoxines. Bien que la plupart des souches d'E. coli soient des hôtes naturels de l'intestin des animaux, la souche O157:H7 provoque de graves dommages de l'épithélium et de l'endothélium du gros intestin. E. coli O157:H7 est trouvée dans les intestins des animaux en bonne santé, qui sont le réservoir de l'infection.

La bactérie E. coli O157:H7 provoque une diarrhée sanglante.

4.3 Détection d'Escherichia coli O157:H7 par des billes magnétiques

4.3.1 Dynabeads Max E. coli O157

Dynabeads® MAX E. coli O157 est un marqueur biomagnétique qui est produit avec des particules de polymère sphériques superparamagnetic de taille et forme uniformes. Ces billes magnétiques permettent la séparation rapide et sélective des E. coli O157:H7 à partir d'échantillons d'aliments, d'eau et environnementaux par application d'un champ magnétique.

Ce produit est conçu et fabriqué par Life Technologies Société et proposé en deux contenus différents.

Il faut signaler que les principales spécifications de Dynabeads telles que le poids de la densité de particules, la taille, le nombre et la nature du matériel de noyau magnétique des billes sont des informations confidentielles que n'avons pas pu obtenir de la part du fabricant.

Cependant, un microscope optique a été utilisé pour visualiser et mesurer les particules de Dynabeads et dont le diamètre de chacune est d'environ 1 µm.

De plus, il était aussi intéressant pour nous de faire une analyse du pH du marqueur Dynabeds avec un pH-mètre.

Après calibration du pH-mètre, nous avons dilué la solution pure de Dynabeads avec le tampon 10 X de façon à obtenir quatre concentrations différentes (1:1, 1:4, 1:8 et 1:16).

En général, le tampon est une solution qui peut être ajoutée à une quantité modérée d'acide ou de base, sans modification significative (approximativement ± 1) de son pH (acide ou alcalin). Typiquement, une solution tampon acide est constituée d'un mélange ; acide faible et sa base conjuguée. De même, un tampon alcalin est constitué d'une base faible et de son acide conjugué.

Par conséquent, nous pouvons dire que le comportement de la solution tampon dépend des propriétés acides ou basiques du premier matériau. Par conséquent, le pH de Dynabeads purs est de 7.48, soit une substance basique, et le tampon de 10 X joue un rôle d'acide.

4.3.2 Description des méthodes expérimentales pour l'estimation des propriétés magnétiques des Dynabeads

Pour commencer, la puce GMR du capteur III a été placée au centre de la bobine de Helmholtz par le système de déplacement pour enregistrer les données de la sonde (Vrms et phase) sans la présence du marqueur Dynabeads E. coli.

La fréquence de la bobine de Helmholtz est fixée à 75 Hz et la tension de commande générée par l'impédance mètre HF2IS est égale à 350 mV. De plus, la valeur de la densité de flux magnétique (B) produite dans le centre de la bobine de Helmholtz a été mesurée par mesureur de champ, avec une valeur de 212 µT. La bobine de Helmholtz est alimentée par un amplificateur à gain variable au travers d'un transformateur abaisseur (gamme 45-1000 Hz) qui nous permet de transmettre 150 VA aux bobines de Helmholtz.

Dans l'étape suivante, nous avons versé 350 µl de Dynabeads pur dans la cavité de forme cylindrique avec des dimensions de 8 mm × 8 mm à l'aide d'une micropipette. La cavité contenant le marqueur pour E. coli est placée sous une densité de flux magnétique uniforme

au centre de la bobine de Helmholtz. Ensuite, le capteur GMR III est injecté avec soin au milieu de la cavité de l'échantillon, où la densité de flux magnétique est la plus grande. De même, les autres échantillons de concentrations 1:1 , 1:4, 1:8 et 1:16 sont respectivement placés au centre de la bobine de Helmholtz.

Grâce au programme d'interface d'HF2IS, les données du capteur pour chaque échantillon sont enregistrées et moyennées 64 fois. De plus, la mesure de chaque concentration a été répétée au moins trois fois pour assurer la précision des résultats. La Figure f présente le montage de mesure de détection des propriétés magnétiques de Dynabeads.

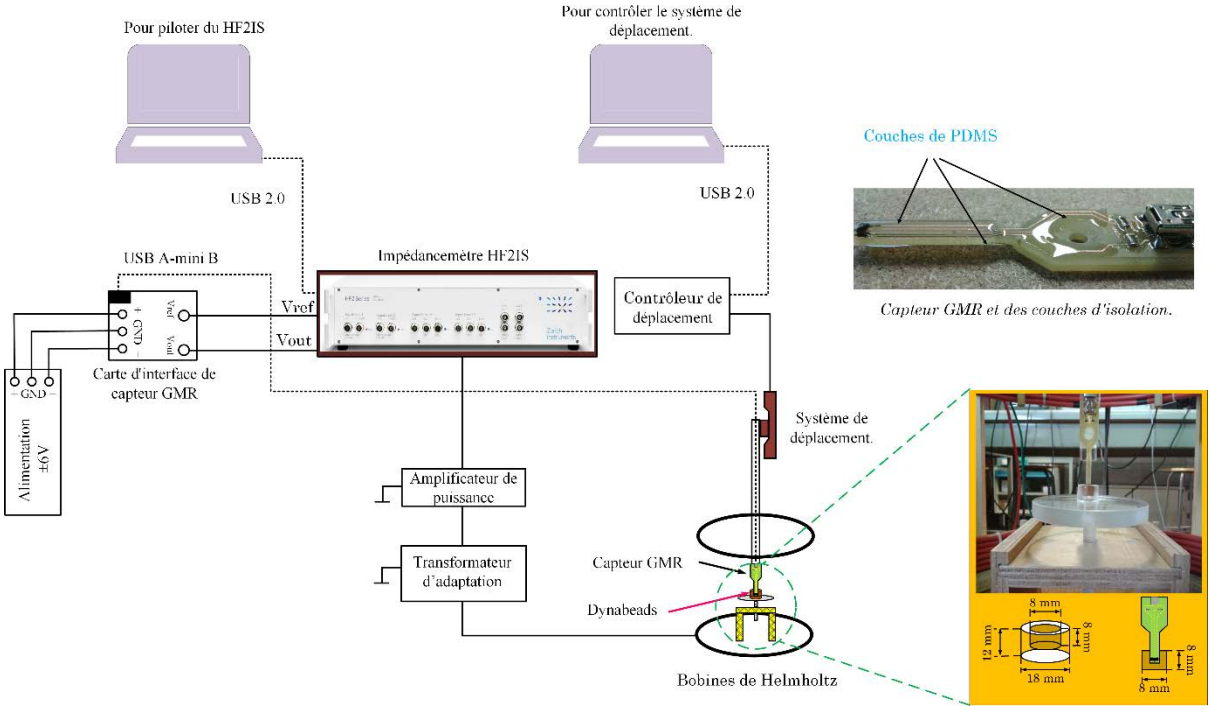

Figure f. Schéma de mesure pour la détection des propriétés magnétiques de Dynabeads.

Après chaque mesure, le capteur GMR ainsi que la cavité ont été rincées soigneusement à l'eau distillée et séchées avec un éponge douce au minimum deux fois, afin de réduire le pourcentage d'erreurs de test.

Finalement, nous avons étudié les propriétés magnétiques des marqueurs Dynabeads MAX E. Coli O157 et déterminé les résultats expérimentaux de la perméabilité relative (μ_r), et de la susceptibilité (χ) pour plusieurs concentrations (pur, 1:1, 1:4, 1:8, 1:16). Les résultats sont exposés dans la Figure 4.16 et Figure 4.17. Nous pouvons y voir que la perméabilité relative et la sensibilité sont proportionnelles à concentration.

4.4 Conclusion

La première partie de ce chapitre comprend un bref résumé d'un groupe très répandu de bactéries appelées Escherichia coli (E. coli). Nous avons revu les caractéristiques principales d'E. coli et de son processus de reproduction. Par la suite, nous nous sommes concentrés sur la bactérie E. coli O157:H7, une bactérie pathogène qui produit des toxines, telles que les toxines de Shiga ou des vérotoxines et peut provoquer une épidémie.

Dans la deuxième partie de ce chapitre, nous avons utilisé un marqueur magnétique de la marque Dynabeads MAX E. Coli O157, capable de détecter et séparer rapidement E. coli O157:H7 des environnements contaminés. La bonne capacité et la haute sensibilité du capteur GMR III nous donnent une estimation précise de ces micro-billes superparamagnétiques même à de faibles concentrations. Nous avons déterminé et mesuré la perméabilité relative (μ_r) et la sensibilité (χ) de plusieurs concentrations qui ont été préparés à partir du fluid Dynabeads pur.

Conclusion générale

L'objectif principal de cette thèse était de présenter une nouvelle méthode de mesure pour calculer et estimer les propriétés magnétiques des ferrofluides et des billes magnétiques, telles que la perméabilité relative et la susceptibilité grâce aux capteurs GMR. Cet objectif représente un intérêt scientifique et pratique concret pour les liquides magnétiques qui sont largement utilisés dans de nombreuses applications, en particulier dans le domaine biomédical. Peuvent être notamment cités le traitement de l'hyperthermie anticancéreuse, la séparation magnétique de cellules, la génération de vecteurs médicamenteux à base de nanoparticules, etc… .

Une autre application d'intérêt est la détection rapide, pratique et simple de bactéries telles qu'E. coli O157:H7 moyennant l'utilisation d'un marqueur magnétique.

Pour atteindre l'objectif principal de cette thèse, nous avons traité les étapes décrites ci-dessous.

Tout d'abord, nous avons présenté trois types de capteurs magnétiques conçus sur la base de l'effet de magnétorésistance géante. Un des soucis de ces capteurs est la fragilité de l'aiguille, complexe et coûteuse.

Dans un second temps, tous les composants de la chaîne de mesure, nécessaire pour caractériser les capteurs et mesurer les propriétés physiques des micro et nano particules ont été implémentés sous forme d'un banc expérimental. L'installation se compose de bobines de Helmholtz pour produire le champ magnétique uniforme au centre de celles-ci. De plus, nous avons conçu et réalisé plusieurs circuits électroniques jouant le rôle de carte d'interface afin de protéger chacun des capteurs GMR contre les surintensités, et réalisant les fonctions de pré-amplificateur pour amplifier le signal de sortie du capteur. D'autre part, un système de micro-déplacement et son panneau de contrôle ont été réalisés pour réduire les erreurs de positionnement et protéger l'aiguille du capteur contre dommages et erreurs de positionnement.

Ensuite, nous avons caractérisé chaque capteur pour déterminer sa sensibilité en fonction de la densité de flux magnétique (B).

Dans l'étape suivante, nous avons présenté les équations théoriques permettant de calculer la densité de poids et de volume de différentes concentrations de ferrofluides et d'autre part les

formules théoriques des changements de densité de flux magnétique, de la perméabilité relative et de la détection de sensibilité ont été exposés.

Puis, nous avons présenté d'autres mesures à titre comparatif effectuées sur un magnétomètre à échantillon vibrant (VSM).

Nous avons fabriqué des moules en téflon et en nylon avec des formes diverses pour réaliser les cavités. Celles-ci sont faites en polydiméthylsiloxane (PDMS), un matériau biocompatible et résistant à la corrosion et à l'encrassement.

A la fin de ces travaux de recherche, il convient de souligner que la méthode proposée par mesure magnétique grâce aux capteurs GMR a permis d'augmenter la vitesse, la précision et le confort de mesure comparé autres équipements similaires, comme SQUID ou VSM. Cela s'explique en raison de la taille microscopique du capteur, de la sensibilité adaptée et de la possibilité de mesure dans un faible champ magnétique.

Ces premiers travaux permettent d'envisager un développement de biocapteurs ou de dispositifs de mesure des propriétés magnétiques complémentaires de l'existant avec comme caractéristiques essentielles la possibilité de travailler à l'échelle microscopique et à large bande de fréquences en magnétospectroscopie.

Ecole doctorale IAEM
Département de formation Doctorale
Electronique Electrotechnique

THÈSE

Pour l'obtention du titre de :

DOCTEUR de L'UNIVERSITÉ DE LORRAINE

Spécialité: *Systèmes électroniques*

Présentée par :

Hamidreza SHIRZADFAR

DESIGN AND EVALUATION OF A GMR-BIOSENSOR FOR MAGNETIC CHARACTERIZATION OF BIOLOGICAL MEDIUM

Thèse soutenue publiquement le 23 juin 2014 à Nancy devant le jury composé de :

François BURET	Professeur, Université de Lyon	Rapporteur
Laurent BERQUEZ	Professeur, Université de Toulouse	Rapporteur
Jean Marie BILBAULT	Professeur, Université de Bourgogne	Examinateur
Sotoshi YAMADA	Professeur, Université de Kanazawa	Examinateur
Djilali KOURTICHE	Professeur, Université de Lorraine	Co-directeur de thèse
Mustapha NADI	Professeur, Université de Lorraine	Directeur de thèse

Institut Jean Lamour ; Université de Lorraine –CNRS ; UMR 7198 ;
Faculté des Sciences et Technologies
Pôle M4 : matière, matériaux, métallurgie, mécanique

Prologue

In various applications such as in medical, environmental and chemical analysis methods, there is a need to identify biological molecules. Our senses of smell and taste do exactly the same thing and our immune system identifies million kinds of molecules. Similarly to these amazing capabilities of biological systems, we may find ways to build new and efficient sensors.

In recent years, investigation and development of novel sensors and detecting technologies, which are appropriate and affordable, are major tasks in all scientific disciplines, particularly in biomedical research to save and treat patients.

The giant magnetoresistance effect (GMR) was established in 1988 at the University of Paris by Albert Fert and Peter Grünberg. In 2007 A. Fert and P. Grünberg were awarded the Nobel Prize in Physics for this work. The essence of the effect is a change in resistance (10−20%) of multilayer structures of magnetic and nonmagnetic metals, even with a slight change in the external magnetic field. The basis for this phenomenon is the property of quantum electron intrinsic angular momentum or spin.

The GMR effect significantly reduces the electrical resistance of a metallic multilayer structure composed of alternating layers of ferromagnetic metal with a thickness of several nanometers and nonmagnetic metal of the same thickness when exposed to a magnetic field.

Due to their small size, low power consumption, high robustness in adverse conditions and relatively low cost, GMR sensors are increasingly used in industrial and automotive electronic systems and in diagnostic medical equipment. GMR sensors have high sensitivity and detection capability for the measurement of magnetic fluids or magnetic markers in small fields.

Magnetic fluid or magnetic liquid are colloidal solutions of ultra-fine magnetic materials. Ferromagnetic materials consist of small nanoparticles of magnetic materials or some other compounds, containing iron, nickel or cobalt. Magnetic fluids are unique because they combine higher turnover and magnetization than ordinary liquids. Each particle is coated with a thin layer of protective membrane that prevents the adhesion of particles. These particles scatter throughout the entire volume of the liquid because they absorb positive charge and subsequently produce repulsive electrostatic forces.

Therefore, in contrast to conventional suspensions, the particles in a magnetic fluid do not settle to the bottom, and can maintain their performance over many years. Magnetic fluids have a unique combination of persistence and ability to interact with magnetic fields.

When a magnetic field is applied to a ferrofluid (ferromagnetic fluid), the magnetic moments of the particles align with the field almost instantly. The magnetization of a magnetic fluid responds rapidly to changes in the magnetic field, and unlike paramagnets the magnetism persists even after the external magnetic field is removed.

Nowadays, ferrofluids have a variety of uses and are proposed for several applications such as medicine (magnetic cell separation, cancer treatment, magnetic drug delivery etc.), mechanical engineering, electronic devices, mining and military.

This thesis project was carried out and supported by the team ‘‘Mesures et architectures électroniques’’, in the ‘‘Nanomatériaux Electronique et Vivant’’ department of Institute Jean Lamour (IJL) in University of Lorraine in a collaboration with Professor Sotoshi YAMADA at the Institute of Nature and Environmental Technology of Kanazawa University (Japan).

Plan of the thesis:

The **first chapter** of this thesis consists of two parts: first part refers and describes the giant magnetoresistance (GMR) effect in multilayers. It summarizes the several structures of GMR effect. It compares cost and ability to detect and identify the weak magnetic fields between GMR sensors and other kinds of magnetic field sensor. Second part mentions the different types of magnetic materials and their properties with presence or absence of the magnetic field. This chapter ends with a description of ferrofluid properties and their application domains.

Chapter two presents three different types of GMR sensor which have varied schemas and designs. This section introduces the system with requirements to protect the fragile needle of GMR sensors and also explains every component of measurement setup to characterize the GMR sensors. Finally, it presents the experimental results of values for maximum sensitivity of each GMR sensor.

In the **third chapter**, the GMR sensors with a good capability to detect and estimate the physical properties of magnetic fluid or ferrofluid in low concentrations were used. For this step, two various nanomagnetic fluids are suggested. First ferrofluid can be used for hyperthermia treatment and the second one is applied for MRI contrast agent and also for

magnetic drug targeting and cell separation applications. Additionally, this chapter validates our results with more classical instrument using vibrating sample magnetometer (VSM).

In the **fourth and last Chapter** of this thesis we start by a short bibliographic review of Escherichia coli bacteria and we particularly focus on the role and significance of Escherichia coli O157:H7 in the foodborne disease. Nowadays, many innovative methods have been developed for the detection and separation of Escherichia coli O157:H7 and one of these methods uses the special magnetic markers called Dynabeads Max E. coli O157. Most of these methods need few days to achieve the detection. In a second step, the GMR sensor III is used to detect these beads at different concentrations.

Chapter 1 : The principle of giant magnetoresistance and studies in magnetism

1.1 Introduction

This first Chapter introduces the basic theoretical principles of giant magnetoresistance (GMR) effect and explains several types of magnetoresistance.

A giant magnetoresistance is observed in multilayer materials with alternating thin layers of ferromagnetic and non-magnetic metals. An individual ultrathin layer's thickness may be only a few nanometers. The resistance of a sample reaches its maximum when local magnetic fields in ferromagnetic materials are in antiparallel and a minimum when they are in parallel. This phenomenon was named giant magnetoresistance, as resistance value was much greater than known magnetoresistance.

Currently, many sensors are being developed and designed on the basis of the GMR effect in order to be used in various applications such as in computer disc technology, motion sensor, biosensor etc.

This Chapter provides a general overview of properties and classification of magnetic materials. Then it discusses the usage of magnetic liquids in bio application and other domains.

1.2 Brief historical review of GMR effect

The giant magnetoresistance effect has been independently described in 1988 at the University of Paris 11 by Professor Albert Fert, and also by Professor Peter Grünberg [1] at the Institute of Solid State Physics in the Research Centre in Jülich (Germany). They were both honored with the Nobel prize in Physics in 2007.

The development of methods of manufacturing components with nanometer dimensions has allowed us to create devices that have successfully used this property of the electron. It was the beginning of a new scientific direction – so-called “spintronics”. The elements of apparatuses include spintronics and GMR sensors. The emergence of sensors based on the GMR-effect led to a sharp increase in the recording density of the hard disks of computers. But nowadays many applications were and are still developed.

Today, the GMR sensors are widely used in various industries and particularly in commercial electronics to measure several physical parameters, because of their high sensitivity, small size, low power consumption, large frequency response and low costs as compared to other magnetic sensors. The basic effect of the GMR phenomenon is to significantly reduce the

resistance of the alternating layers of multilayer structure composed of ferromagnetic (FM) and nonmagnetic (NM) when the layers of sample are exposed to an external magnetic field.

The GMR-effect is caused by the quantum properties of electrons, which have such characteristics as electron spin. Electrons can have only two directions – up and down. The conduction electrons of spin whose direction of spin is the same as the direction of the magnetic field inside the GMR encounter less resistance to their motion and have more freedom of movement than the electrons with spin oriented against the internal magnetic fields, which encounter greater resistance to their motion, and often collide with atoms in their environment. In the first case, the electrical resistance of the environment will be less than in the second one. Figure 1.1 presents several structures of GMR.

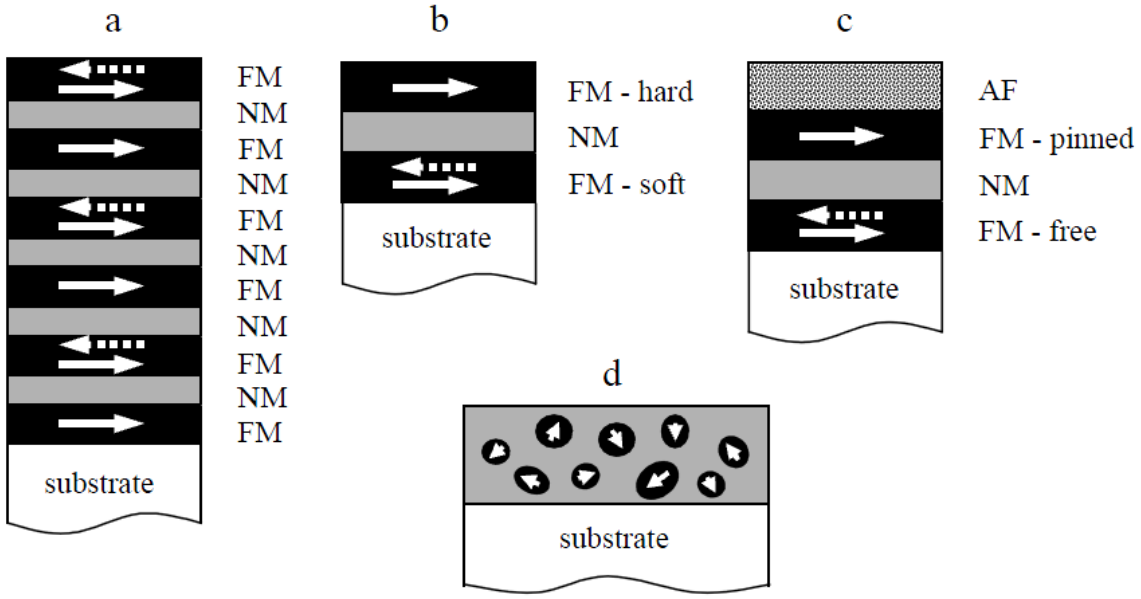

Figure 1.1 Various structures in which GMR can be observed: magnetic multilayer (a), pseudo spin valve as combine hard and soft magnetic (b), spin valve consists of a free layer (soft ferromagnetic layer), a non-magnetic metal spacer layer and pinned layer (ferromagnetic layer) (c), and granular thin film (d) [2].

The exchange of magnetic coupling between the magnetic films in the sandwich structure is the most important phenomenon observed in many GMRs. As shown in Figure 1.2 an antiferromagnetic coupling indicates that two nano magnetic films are magnetized antiparallel to each other. As discovered by Parkin et al. 1990 [3]: by varying the thickness of interlayers in the thin film multilayers, the magnetoresisatnce fluctuated within a certain period, as a periodic sequence from magnetizations of the films aligned from parallel to antiparallel (Figure 1.2).

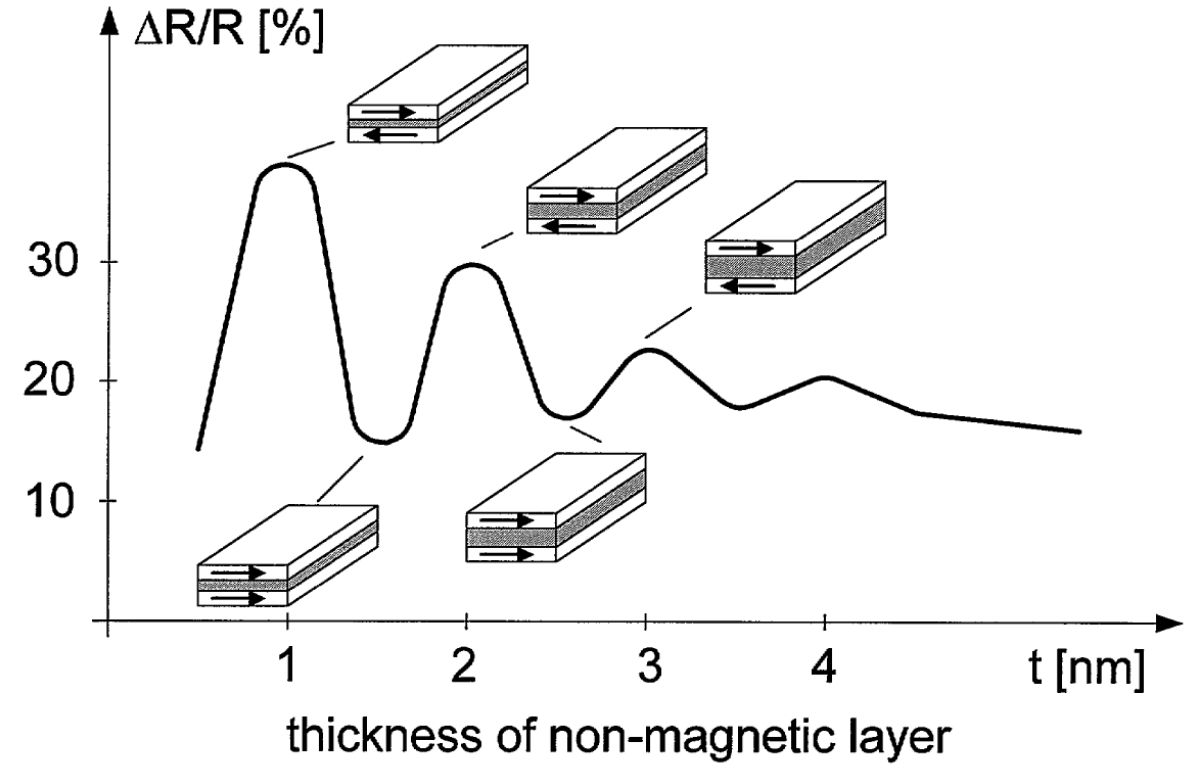

Figure 1.2 Evidence of oscillatory exchange coupling in thin film multilayers [3].

The results presented in Figure 1.3 indicate the variation in the resistances of a Body Centered Cubic (bcc) in (001)Fe/(001)Cr, the initial results that were obtained by Baibch et al. in 1988. In these experiments the highest magnitude of GMR was found at the level of ≈80 % at T=4.2 K for thickness of Fe 3nm/Cr 0.9nm. Furthermore, we observe from Figure 1.3 that with increasing thickness of the Cr the magnetoresistance is decreasing.

The first results of GMR (Baibich et al. 1988) were obtained on multilayers Fe/Cr antiferromagnetically coupled. Resistance drops abruptly when a field of applied magnetics is strong enough to overcome the antiferromagnetic coupling and to align the magnetizations of the layers. The arrows indicate the field saturation Hs needed to align all the magnetic layers. Furthermore, resistance in the antiparallel alignment is greater than in the parallel case.

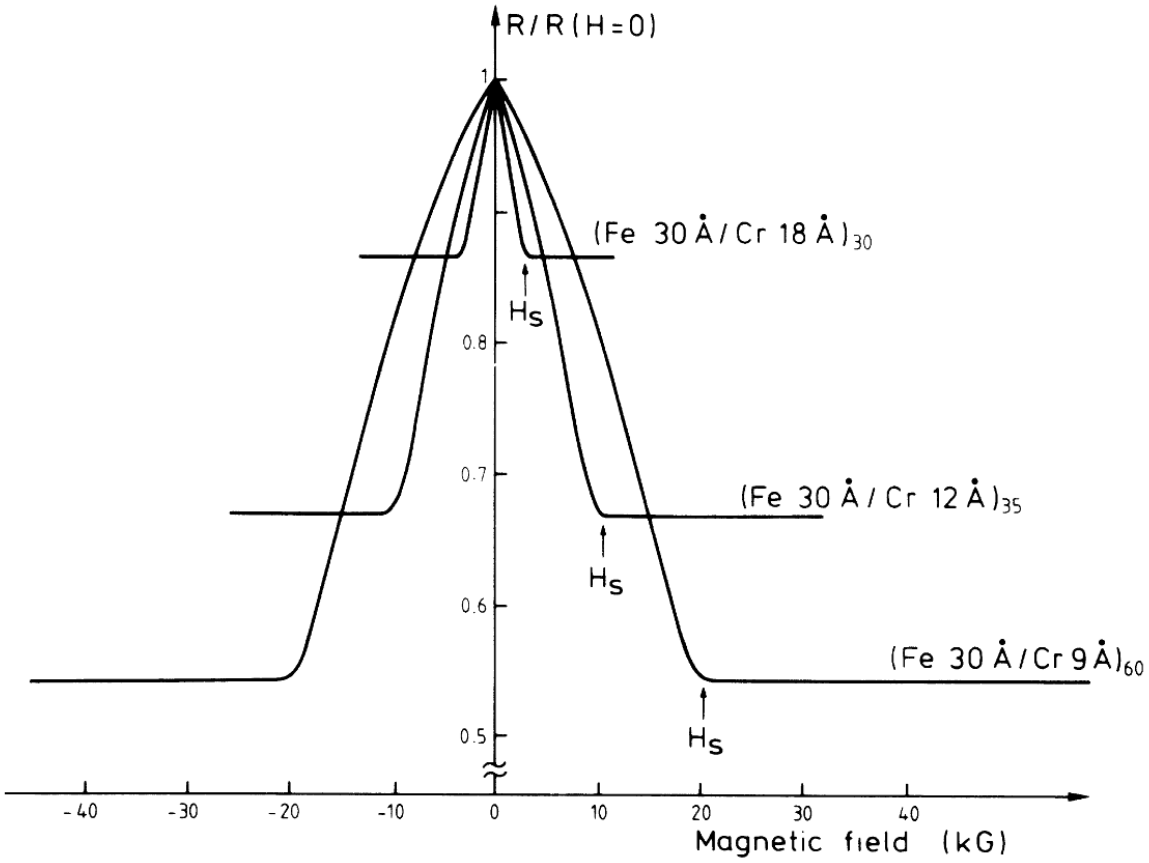

Figure 1.3 Magnetoresistance for several Fe/Cr multilayers at 4.2K [1].

Nowadays, there are many sensors that can be used in all applications for measuring magnetic field such as the GMR sensor, the superconducting quantum interference device (SQUID) sensor, the anisotropic magnetoresistive (AMR) sensor and etc. Figure 1.4 presents the comparison between several low-field sensors with the same minimum field resolution limited by thermal noise of 10^{-8} Oe/√Hz [4].

Sensors made of GMR materials are preferred for biomedical applications due to their high sensitive detection, quick response under low magnetic fields and lower cost as compared to sensors of comparable size. Figure 1.5 and Table 1.1 illustrate the differences between GMR and other magnetic field sensors [5, 6]. In addition, they provide comparison of basic specifications important to identifying sensors for individual applications. To summarize, GMR sensors have significant cost, usage advantages and performances.

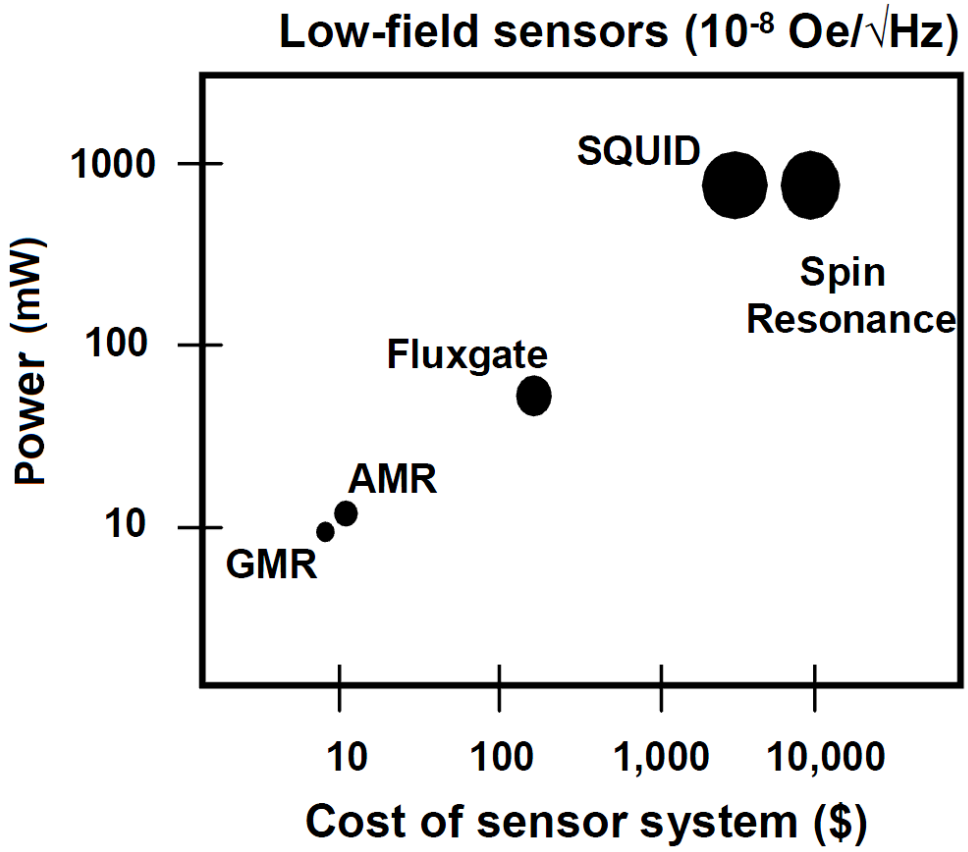

Figure 1.4 Comparison of power, price and size of several low magnetic field sensor technologies [4].

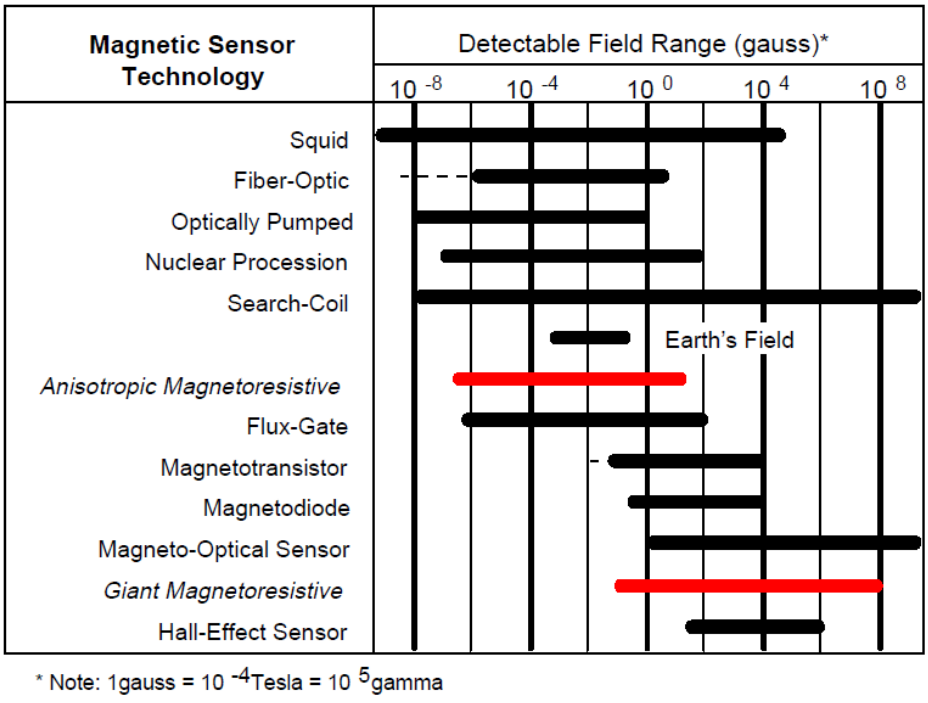

Figure 1.5 The field range comparison of several magnetic field sensors [5].

Table 1.1 Comparison of several magnetic field sensors [6].

	H range (T)	Sensitivity (V/T)	Response time	Power consumption	Sensor head size
GMR	10^{-12}-10^{-2}	120	1 MHz	10 mW	10-100μm
Hall	10^{-6}-10^{2}	0.65	1 MHz	10 mW	10-100μm
SQUID	10^{-14}-10^{-6}	10^{-14}	1 MHz	10 mW	10-100μm
Flux gate	10^{-12}-10^{-2}	3.2	5 kHz	1000 mW	10-20μm

1.3 Theoretical framework of giant magnetoresistance (GMR)

The magnetoresistance is observed when an electric current flows in a ferromagnetic material at low temperatures. This can be explained by the fact that, under certain conditions, there is a strong difference between the resistivity R↑ for electrons whose spins are parallel to the direction of the magnetization and the resistivity R↓ for electrons with spins pointed in the antiparallel direction. This can happen in transition metals due to electron valence s, p and d. The operating principles of giant magnetoresistance (GMR) are shown in Figure 1.6 (a, b).

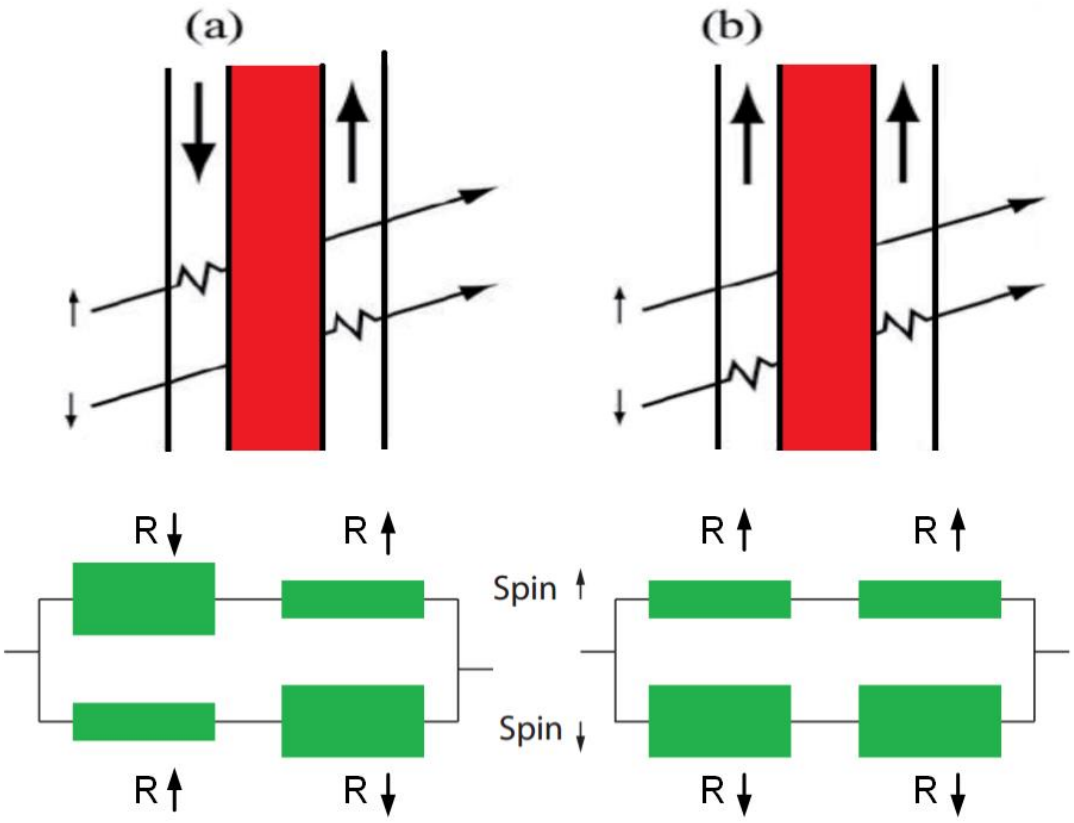

Figure 1.6 Schematic of giant magnetoresistance in a multilayer, two magnetic layers are polarized in the opposite directions (a) or in the same direction (b).

We can consider that a current is carried in two different channels (up and down) and in conventional conductive material, these two channels are equivalent.

In a ferromagnetic material, there is a huge difference between the two channels, but these two channels are equivalent in conductive materials [7]. The definition of the value of GMR is given by formula [8]:

$$GMR = \frac{R_{AP} - R_p}{R_p} = \frac{(R_\uparrow - R_\downarrow)^2}{4R_\uparrow R_\downarrow} \tag{1.1}$$

Where, R_{AP} and R_P are total resistances for the antiparallel and the parallel configuration.

The antiparallel alignment for both spin channel can be described by the following expression [9]:

$$R_{AP} = \frac{R_\uparrow + R_\downarrow}{2} \tag{1.2}$$

Where $R_\uparrow$ is the resistance for spin-up channel and $R_\downarrow$ is spin-down.

However, the total effective resistance of parallel alignment is [9]:

$$R_P = \frac{2(R_\uparrow \times R_\downarrow)}{R_\uparrow + R_\downarrow} \tag{1.3}$$

Also, the magnetoresistance ratio (MR) is given by equation 1.4 [10].

$$\frac{\Delta R}{R} = \frac{R_{AP} - R_P}{R_P} \tag{1.4}$$

Furthermore, by comparing between the parallel and antiparallel configurations of magnetic layers in the inverse GMR (different ferromagnetic materials FM1, FM2) and in normal GMR, we realize that in the inverse GMR the parallel magnetic configuration the resistance of spin value is greater than in antiparallel configuration ($R_P > R_{AP}$) and vice versa in normal GMR which has equivalent FM1 and FM2 ($R_{AP} > R_P$) [11, 12].

This is observed only in GMR where the interlayer coupling for the multilayer structure is antiferromagnetic, and just in these systems the relative orientation of magnetic moments in adjacent layers can vary significantly by the influence of an applied magnetic field.

Consequently, there are two states with different resistance. One can make a multilayer structure, called a superlattice, in which the magnetic and intermediate layers are repeated many times.

Figure 1.7 shows the characteristics of a typical GMR sensor with antiferromagnetic exchange coupling, interlayer thickness of Co 1.5 nm and Cu 0.9 nm at 4.2 K, with the strongest antiferromagnetic coupling. When the strength of the magnetic field is zero, the resistance is the highest, since all the Co-layers orient antiparallel, and the resistivity decreases with increasing field. The alignment of the spins with the field leads to saturation of resistance.

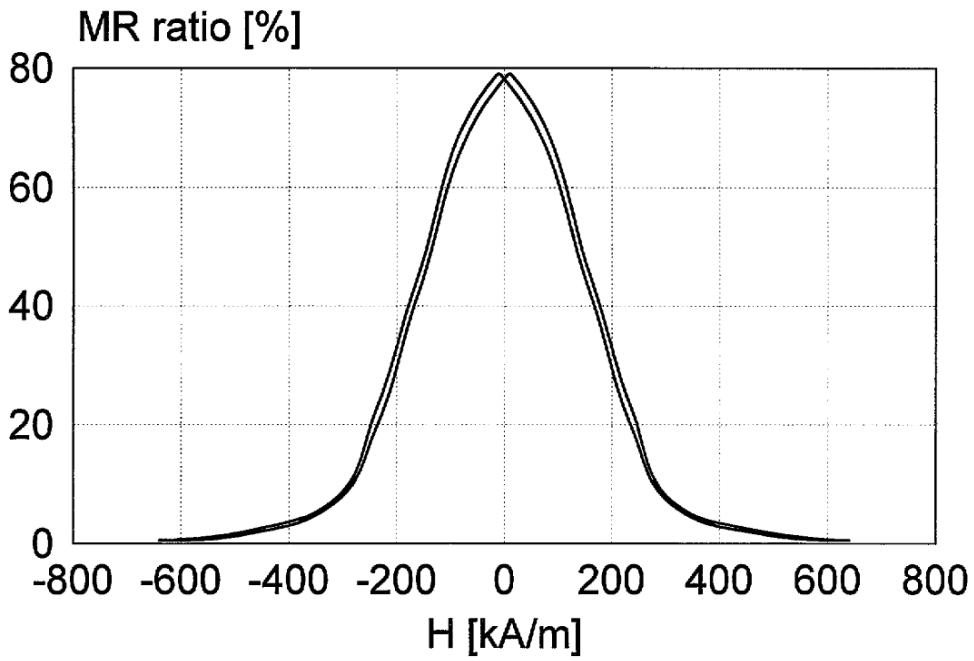

Figure 1.7 Characteristic of the GMR multilayer structure by (Co 1.5 nm/Cu 0.9 nm)×30 multilayer structure depends of magnetic fields [13, 14].

Resistance calculation of multilayers is determined by formula [14]:

$$R(H) = R_P + \frac{(R_{AP} - R_P)}{2}[1 - \cos(\theta_1 - \theta_2)] \tag{1.5}$$

Where R_P and R_{AP} are the resistances in the parallel and antiparallel magnetic configurations and θ_1, θ_2 present the angles of magnetization of the two magnetic layers.

1.4 Different types of giant magnetoresistive structures

1.4.1 Spin valve (SV-GMR) structures

As shown in Figure 1.8 the spin-valve structure consists of four different metallic layers where two ferromagnetic layers (FM) are separated by a nonmagnetic metallic layer (NM) and an antiferromagnetic layer (FM). The main principle of operation is that one of its parts (free layer) is very sensitive to the external field and other, which serves as the magnetic reference system, is not.

This structure provides a bipolar signal with a high sensitivity in an optimized device. Also the antiferromagnet employed in this structure can be influenced by the magnetostatic field from the free layer [15].

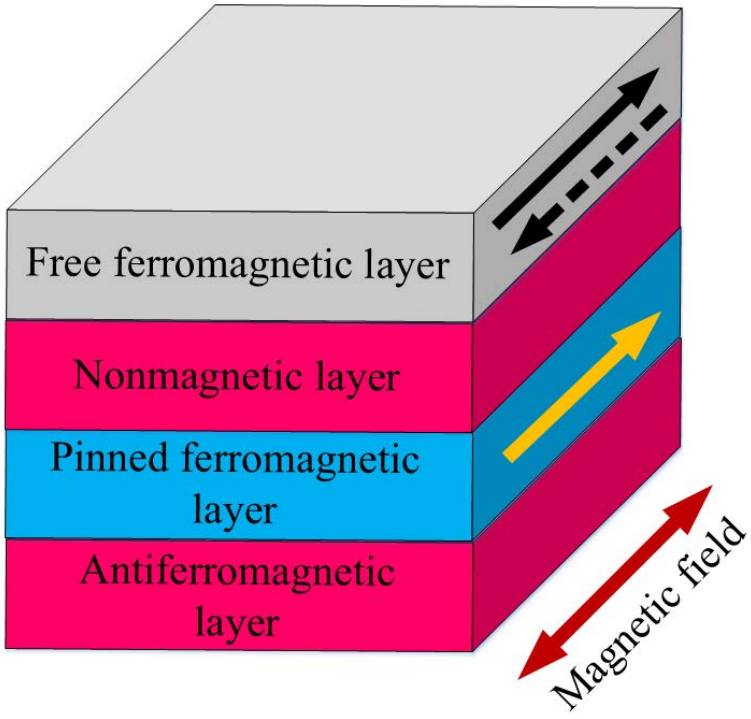

Figure 1.8 The structure of a spin-valve system.

Figure 1.9 (a, b) presents the typical characteristics of spin-valve sensors with configuration (8 nm FeMn (AF)/6 nm $Ni_{80}Fe_{20}$(free-F)/2.5 nm Cu (NM)/8 nm $Ni_{80}Fe_{20}$(F)) which consists of two hysteresis loops corresponding to the free ferromagnetic layer Figure 1.9 (a) and pinned ferromagnetic layer Figure 1.9 (b). This characteristics is obtained by Kools in 1996 [16].

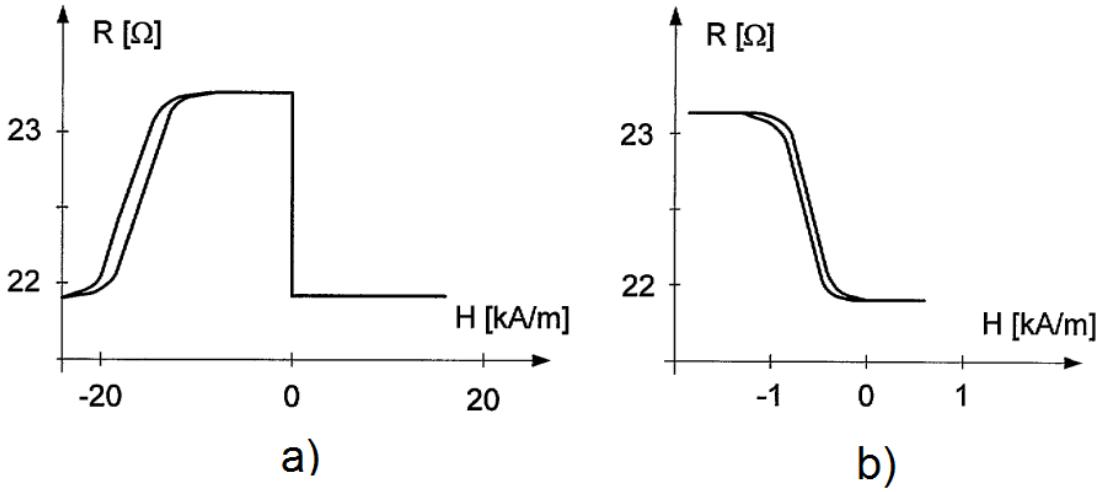

Figure 1.9 Hysteresis loops of the spin valve sensors [14].

Figure 1.10 shows the principle of the spin-valve sensor operation. Initially, the direction of the free layers magnetization changes when the magnetic field is decreased. In the pinned layer the direction of magnetization is changed by further reducing the magnetic field. The direction of the magnetization is parallel when both magnetic layers are placed in a large magnetic field. Additionally, the resistance of this construction is the largest during the replacement of the direction of magnetization (once both layers are magnetized antiparallel) [14].

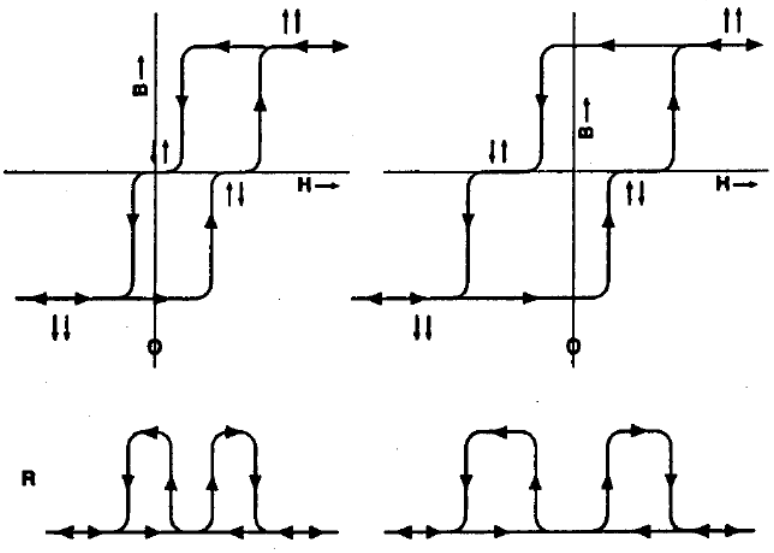

Figure 1.10 Principle of the spin-valve sensor [17].

Spin valves are of particular interest to developers of system memory on hard drives because their size can be much smaller than magnetic read heads with ferromagnetic, magnetic core and copper winding. Read heads based on the phenomenon of GMR spin valves are now

commonly applied in computer technology [18]. The main advantage of the spin valve is its ability to change resistance by 20 % in a magnetic field [19].

The results obtained by Miles and Parker for calculations of the magnetization distribution in free and pinned layers are presented in Figure 1.11. As can be seen for two layers (free and pinned) the change of magnetization in area between $-M_S$ and $+M_S$ is distributed outstandingly. Also the magnetized of free and pinned layers are non-uniformly at the edge of the stripe by inspiration of the magnetic field.

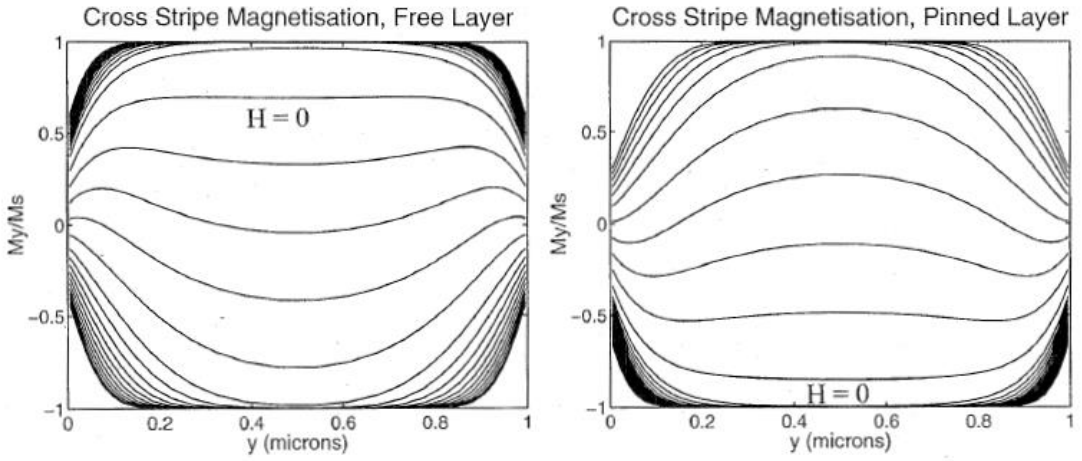

Figure 1.11 Calculations of the magnetization distribution of the spin-valve structure in pinned and free layers by [20].

The magnetization is necessary in order to create within the sensitive layer a stable single magnetic domain with a constant magnetic field for minimizing the noise domain. The noise domain is a crucial issue, very important for small magnetic GMR sensors and strongly related to structural properties and magnetic configuration.

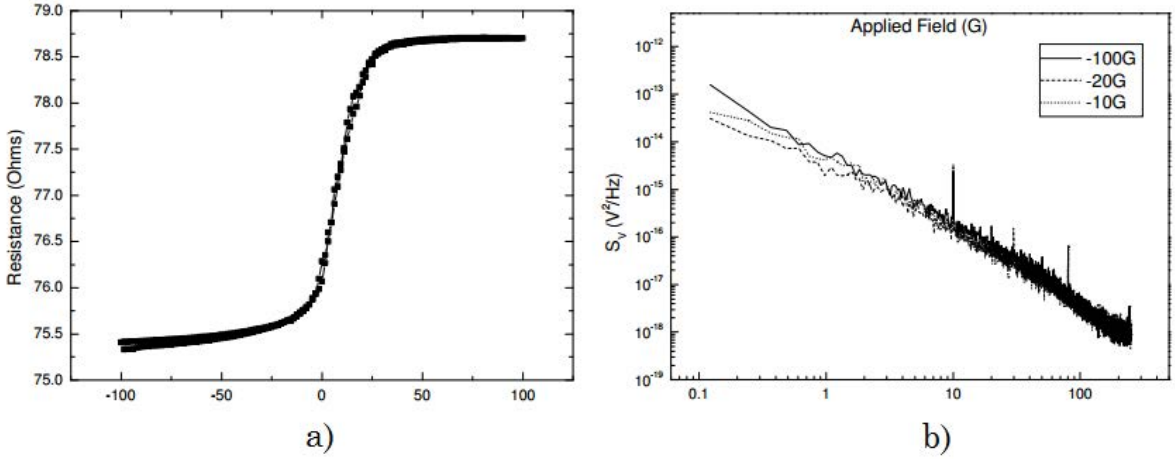

Figure 1.12 GMR characteristics as a function of the magnetic induction (a), 1/f noise in a yoke-type GMR (b) [21].

In Figure 1.12 presents results obtained by Pannetier et al. 2005, for 1/f noise (random telegraph noise) in a yoke-type GMR at room temperature with a sensing current of 3 mA for an external applied field of 100 G, 20 G and 10 G.

The output signal depends on the ratio length/width and can be determined by the equation [22]:

$$U_{out} = IR_{sq}\frac{L}{W}(\frac{\Delta\rho}{\rho})\frac{[\cos(\theta_{free}-\theta_{pinned})]}{2} \tag{1.6}$$

Where, I is a bias current, L is a length of thin film, W is a width of thin film, Δρ/ρ is a maximum value of the magnetoresistivity ratio. R_{sq} (resistance ohms per square) is the same for all square dimensions and depends only on thickness. In the spin-valve sensor expression the output signal can be rewritten as [14]:

$$U_{out} = IR_{sq}\frac{L}{W}(\frac{\Delta\rho}{\rho})\frac{H_X - H_P + H_{d2}}{H_K + H_{d1}} = J\rho L\frac{H_X - H_P + H_{d2}}{H_K + H_{d1}} \tag{1.7}$$

Where, H_x is a measured magnetic field, H_p=0.8–1.2 A/m, $H_{d1,2}$ is a demagnetizing field, H_k is an anisotropy field and J is a current density.

The sensitivity of a sensor depends on the width of thin film because the demagnetizing field relies on the thickness/width ratio. Nowadays, in several sensor applications, the resolution of the sensor is very important but the resolution is limited by noise. By Nor *et al.* 1998 it has been estimated that a signal-to-noise ratio (SNR or S/N) is proportional to the square root of the device area and can be determined using the following expression [14, 23]:

$$SNR = c\sqrt{LW} \tag{1.8}$$

where, c is a constant.

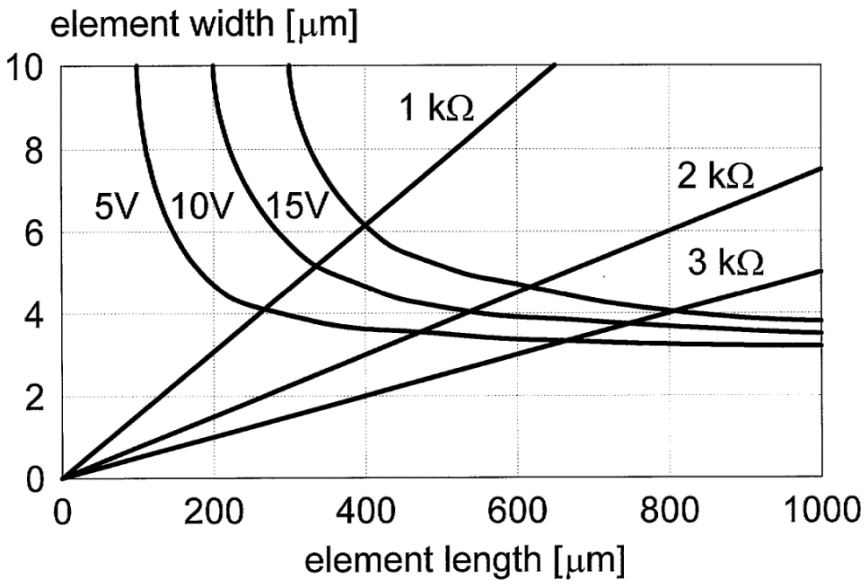

Figure 1.13 Relationship between design parameters of the spin-valve sensor [14, 24].

The relationship between the design parameters (width and length size element) have been developed by Spong et al. in 1996 as indicated Figure 1.13. Thereby, the supply voltage and sensor resistance for ideal and best width and length dimension can be determined.

1.4.2 Current in plane (CIP) and current perpendicular to plane (CPP) structures

Giant Magnetoresistance (GMR) effect was discovered while measuring the resistance of magnetic superlattices of current flowing in the plane of the system.

In 1991, the resistance change of magnetic metallic superlattices has been found by changing the relative orientation of the magnetic layers for the current flowing perpendicular to the plane of the layers.

In multilayergate heterostructures ferromagnetic metal and normal metal giant magnetoresistance effect appeared for the current perpendicular to plane (CPP) and the current in plane (CIP) geometry. In CIP structure current is parallel to the planes of the layered magnetic films and in CPP structure current flows perpendicular to the film plane as shown in Figure 1.14.

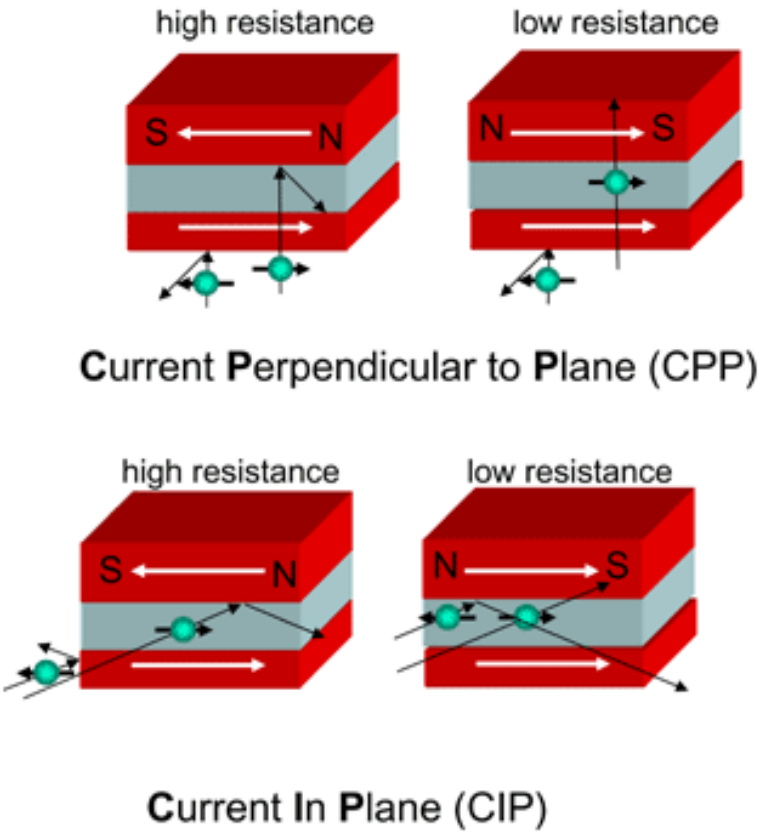

Figure 1.14 Schematic of current perpendicular to plane (CPP) and the current in plane (CIP) geometry [25].

The mechanisms of the effects of GMR in the CPP and CIP geometries are similar and possess main features [26]. The values of magnetoresistance obtained for the first effect are approximately two times greater than the second. However, the absolute resistance of metallic superlattices, the total thickness of the order of tens of nanometers as measured in the CPP geometry is very small and difficult to define. Therefore, practical applications of the GMR effect in CPP geometry are much less attractive. The analytical expression describing perpendicular giant magnetoresistance is presented below [27]:

$$\sqrt{(R_{AP}-R_P)R_{AP}} = \beta \frac{t_F}{t_F+t_N}\rho_F^* t + 2\gamma \times r_b^* M \tag{1.9}$$

Where, R_{AP} and R_P are resistances in antiparallel and parallel configurations of magnetization, M is the number of bilayers, β is the coefficient of bulk spin-dependent scattering or the difference between bulk resistivities $\rho_F^{\uparrow}, \rho_F^{\downarrow}$ and given by equation 1.10 [14, 28], t_F and t_N is the thickness of ferromagnetic and nonmagnetic layers respectively, t is the

thickness of the whole structure and γ is the coefficient of interface spin-dependent scattering or the difference between interface resistances $r_b^{\uparrow}$, $r_b^{\downarrow}$ and is described by the expression 1.11 [14, 28].

$$\begin{aligned} \rho_F^{\uparrow} &= 2\rho_F^{*}(1+\beta) \\ \rho_F^{\downarrow} &= 2\rho_F^{*}(1-\beta) \end{aligned} \tag{1.10}$$

$$\begin{aligned} r_b^{\uparrow} &= 2r_b^{*}(1+\gamma) \\ r_b^{\downarrow} &= 2r_b^{*}(1-\gamma) \end{aligned} \tag{1.11}$$

The samples made in the geometry of the current perpendicular to the planes (CPP), had a very low resistance. Therefore, for very accurate measurements of voltage one needs to use a DC SQUID voltmeter. The geometry of the sample and the superconducting measuring system of the CPP magnetoresistive effect were obtained by [29].

1.4.3 Magnetic tunnel junction (MTJ) structure

In other generations of spintronics, structures based on the phenomenon of the Magnetic Tunnel Junction (MTJ) had been included. The MTJ consists of two layers of ferromagnets, separated by an ultra-thin layer of insulator (see Figure 1.15).

Moreover, if the thickness of the insulator is smaller than 2 nm, the electron can leak through the barrier. This process is called tunneling due to the wave nature of electrons. The probability of tunneling depends on the wavelength or energy of the electron.

In a ferromagnetic material, the energy of an electron depends upon its spin orientation up or down. This leads to a spin-dependent tunneling effect. If the magnetic moments of adjacent layers are parallel, the conductivity of the magnetic tunnel junction is great, and if the magnetization is antiparallel, the tunneling probability is small. The maximum value of the magnetoresistive effect observed in the structures is approximately 50 % at room temperature.

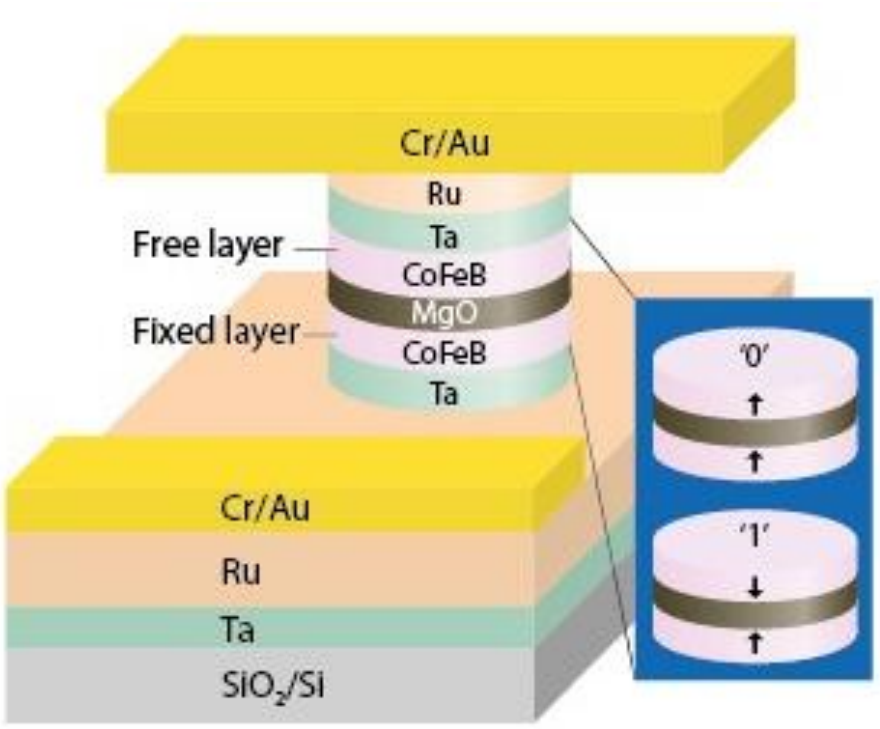

Figure 1.15 Structure representation of a magnetic tunnel junction (ferromagnetic layer fixed (CoFeB) and the other layer free to rotate in to each condition, low resistance ('0') or high resistance ('1'), MgO is a barrier layer [30].

1.4.4 Giant magnetoimpedance (GMI) structure

The giant magneto impedance (GMI) effect was discovered some years ago in the amorphous alloys [31]. The giant magnetoimpedance effect is a phenomenon that involves the large variation of the impedance from a metallic magnetic conductor (ferromagnetic) when submitted to a DC magnetic field in the presence of a high frequency current (from several tens of kHz to a few hundred MHz.

In recent year, the GMI has been extensively developed in magnetic thin nanowires, sandwiched and meandered ribbons and also in multilayered films due to its great potential for developing high sensitivity magnetic field sensors [32].

The impedance Z of thin film sample can be determined by the following equation [14, 33]:

$$|Z| = \frac{l\rho}{w}\frac{d}{\delta\sqrt{2}}\sqrt{\frac{\left(\cosh\frac{d}{\delta}+\cos\frac{d}{\delta}\right)}{\left(\cosh\frac{d}{\delta}-\cos\frac{d}{\delta}\right)}} \qquad (1.12)$$

where, l is the length, w is the width, d is the thickness of thin film sample, ρ is the electrical resistivity, h is the field and δ is the skin depth or penetration. The δ is given by the expression [14]:

$$\delta = \sqrt{\frac{\rho}{f \pi \mu}} \tag{1.13}$$

where, f is the frequency of the alternating current flowing along the sample, and μ is magnetic permeability.

Figure 1.16 (a, b) presents the oversimplified structure of giant magnetoimpedance configuration in single layered and in multilayered thin films. The GMI effect in multilayered clearly increases as compared with the single layered geometry. Briefly, it can be noted that in single layer structure by passing the AC current through the thin film a small AC magnetic field in the perpendicular direction is produced. The process of application an external DC magnetic field in the horizontal direction was described in [34].

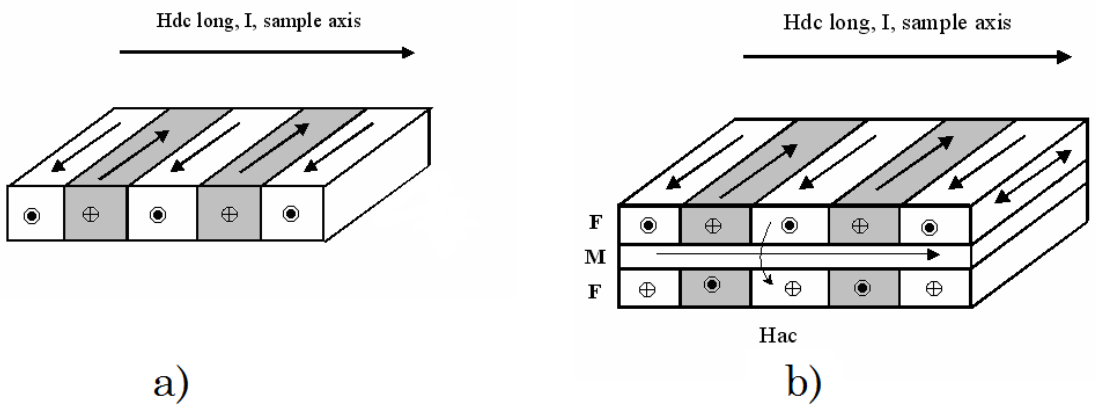

Figure 1.16 The giant magnetoimpedance configuration; in single layered (a) and in multilayered (b) thin films [34].

As displayed in Figure 1.16 (b) the schematic of multilayered structure is similar to sandwich ones, and consist of two ferromagnetic layers with one conductive layer (magnetic layer) in between. Multilayered structure consist on two ferromagnetic layers and a conductive metal located between them; the high variations in impedance can be achieved with large difference in the resistivity between ferromagnetic and conductive layers [34].

1.5 The basis of magnetism

Magnetism is a form of interaction between moving electric charges, carried out at a distance through a magnetic field. The world around us is large and diverse, filled with a variety of

objects and phenomena. Centuries of human activity has proved that objects and phenomena do not exist independently of each other, rather, between them there is a well-defined context. The role of science is reduced to the identification of these links, and creating instructions on how to use them for practical purposes.

There are special properties related to certain metals and minerals, such as the ability to attract pieces of steel or iron. This is a phenomenon of the magnetic field – the space in which occur the magnetic repulsive forces, or gravity. Faraday found that the magnetic properties are not only characteristic of steel and iron. However, changing the intensity of the magnetic phenomena is very easy and depends primarily on the substance itself. A group of substances, such as steel, nickel, iron, cobalt and various alloys have a strong intensity of the magnetic phenomena but in other cases it is small [35].

The quantitative characteristics of the magnetism of the particles are their orbital and spin magnetic moments. All the microstructural elements of materials such as electrons, protons and neutrons possess a magnetic moment, and any combination of the atomic nucleus and electron shells, as well as combinations of these combinations. Though atoms, molecules and macroscopic bodies may in principle be a source of magnetism, essentially some substances are magnetic.

1.5.1 Classification of magnetic materials

In general, all types of the observed magnetic behavior of materials can be classified into five types and presented below:

- Diamagnetism;
- Paramagnetism;
- Ferromagnetism;
- Ferrimagnetism;
- Antiferromagnetism.

Diamagnetism is a property of the substance which is magnetized opposite to the applied magnetic field [36]. A lot of organic and inorganic compounds in interaction with the magnetic field behave like diamagnetic.

At the diamagnetic moment of creating undamped microscopic electric currents induced by the magnetic field H (Lenz's rule). The magnitude of the induced magnetic moment is very small and the opposite of the direction of the applied field [36, 37] (Figure 1.17).

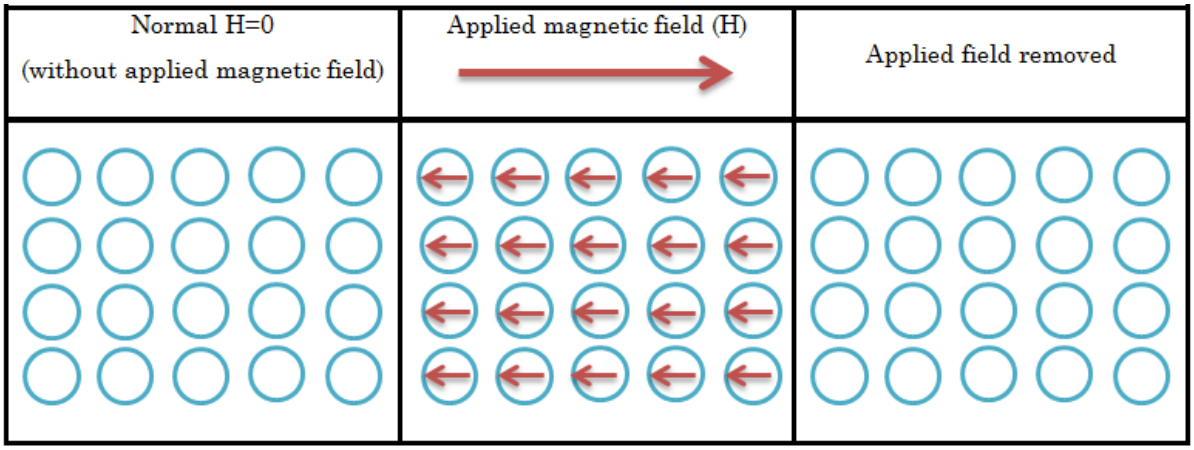

Figure 1.17 The configuration of atomic dipole for a diamagnetic material with and without applied magnetic field.

In the creation of the diamagnetic moment of the electrons of the atoms involved, as of the free charge carriers in metals and semiconductors.

Figure 1.17 presents the configuration of diamagnetic materials with and without an external magnetic field and also after remove a magnetic field. As observed, dipoles exist in diamagnetic materials only under presence of magnetic field.

Paramagnetism is substances whose particles possess an intrinsic magnetic moment, by the absence of an external field these moments are oriented randomly (magnetization is absent) and paramagnetism magnetized by the present external magnetic applied field along the field direction (Figure 1.18).

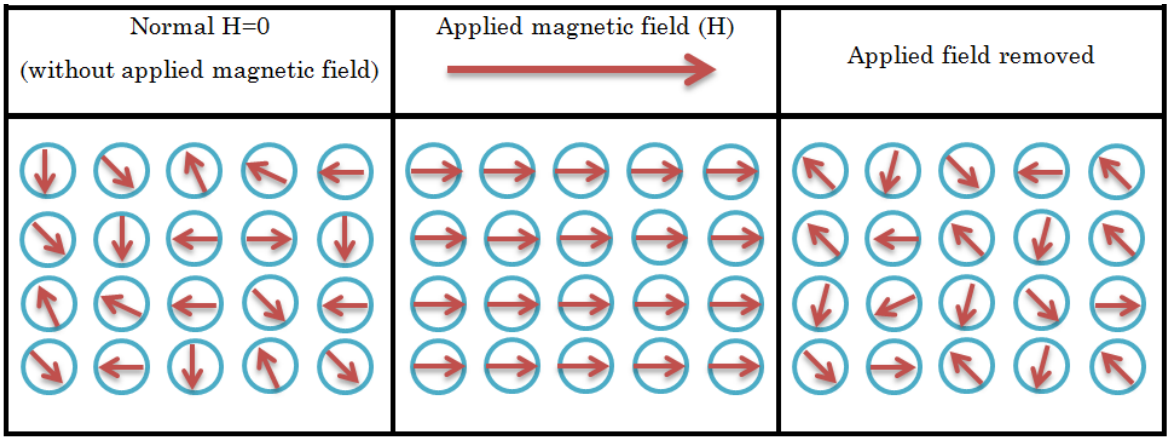

Figure 1.18 The configuration of atomic dipole for a paramagnetsim material.

In general, paramagnetism indicates weakness compared to the ferromagnetism. Paramagnetism usually is associated with the presence of unpaired electrons in an atom or molecule and has a positive magnetic susceptibility (χ_m) and relative magnetic permeability

(μ_r) greater than unity ($\mu_r = \mu / \mu_0 = (1 + \chi_m) > 1$, where $\mu_0 = 4\pi \times 10^{-7}$ H/m is vacuum permeability or magnetic constant in contrast to the diamagnetic ($\mu_r < 1$) [38].

In terms of relative permeability, the magnetic susceptibility (χ_m) is described by the expression:

$$\chi_m = \mu_r - 1 \tag{1.14}$$

Ferromagnetism is substances which have a magnetic permeability much greater than unity. These include iron, nickel, cobalt, and many alloys from them; the largest one is the magnetic permeability of iron [39]. A key feature of these substances (ferromagnetism) is unusually high value of sensitivity. Ferromagnetic materials have an extremely high magnetic susceptibility and strong dependence on the last field from the field [40]. Figure 1.19 presents the magnetic state of such materials and is defined by a magnetization curve (M) as a function of magnetic field (H) [41].

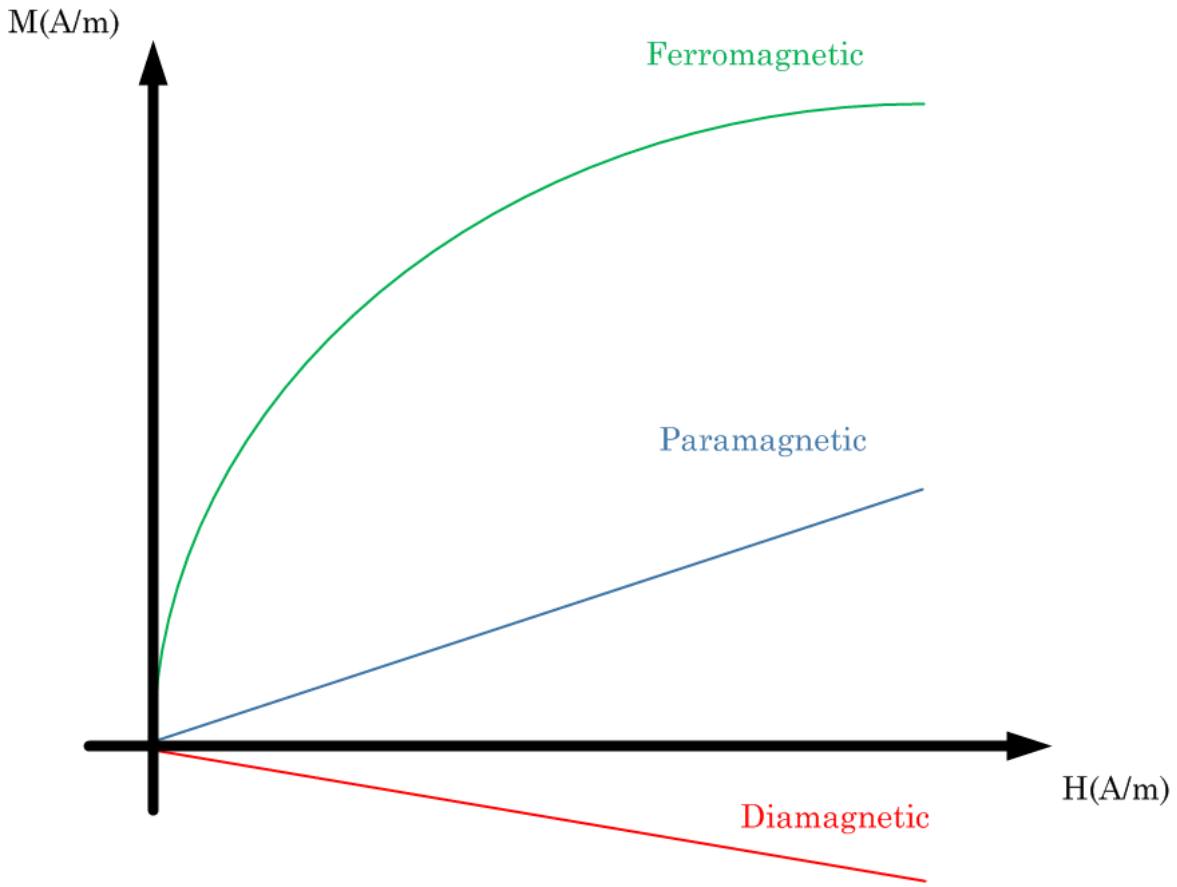

Figure 1.19 Comparison of magnetic behavior of the material.

When applied an external magnetic field (displacement of domain boundaries), the volume of domains oriented in the external field increases. And with the increase in the induction of the external field the magnetic induction of the magnetized material increases and after the phasing out of this field, the material retains a magnetization (Figure 1.20).

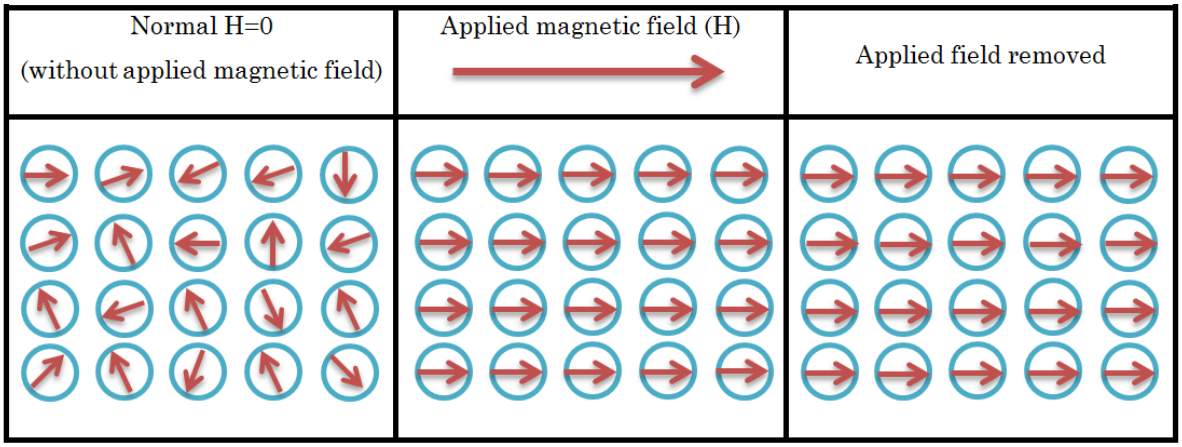

Figure 1.20 The configuration of atomic dipole for a ferromagnetism material with and without a magnetic field.

Ferromagnetic materials are characterized by a high degree of magnetization, which has a nonlinear dependence on the magnetic field. The basic magnetization curve of a ferromagnetic substance is shown schematically in Figure 1.21.

In addition to the nonlinear dependence of magnetization on the field, a ferromagnet shows hysteresis as the result of a lag in magnetization behind changes in the magnetic field. If you bring the magnetization to saturation and then decrease the intensity of the external magnetic field, the magnetization will not follow the original (primary) curve, but goes a little higher.

When the external magnetic field becomes zero, the induced magnetization does not disappear and remain at a level characterized by Br, called the residual induction [42].

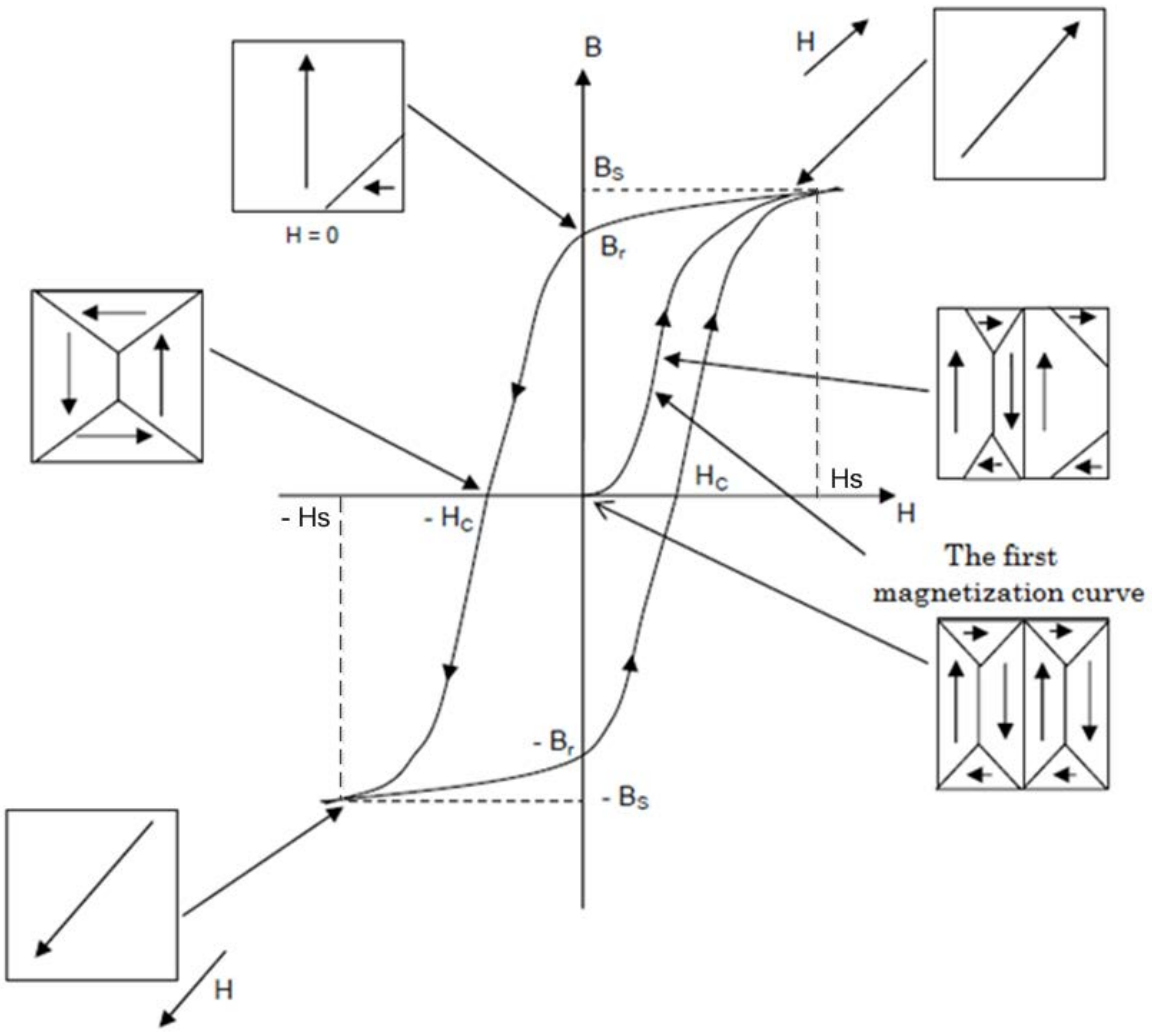

Figure 1.21 The basic magnetization curve and hysteresis loop of a ferromagnetic: B is refers to the magnetization of the particle; H is the magnetic field; B_S is saturation magnetization for H> Hs; H_S is saturation field corresponding to B_S; B_r is residual magnetization; H_C is coercive force or field necessary for the demagnetization of the particle [43].

If the initial state of the material is demagnetized, the constitutive law M (H) will describe the first magnetization curve as the field H is increasing. The magnetization of a ferromagnetic vanishes only under the influence of the magnetic field H having a direction opposite to the magnetizing field.

Ferromagnetic materials are used in permanent magnets and magnetic memory devices. If coercive force is high, it is called a hard ferromagnetic, characterized by a wide hysteresis loop. Ferromagnetic materials with a small coercive force (and thus a narrow hysteresis loop) are called soft [44].

Soft magnetic materials are used if there is a need of fast changes of the magnetic moment while applying a small magnetic field, such as in motors, magnetic head assembly (magnetic

heads), sensors, inductors and audio filters. Another type of ferromagnetic material is supper soft magnetic materials; these materials have a coercive force very close to zero [45]. The hysteresis loops that exist for ferromagnetic materials are shown in Figure 1.22.

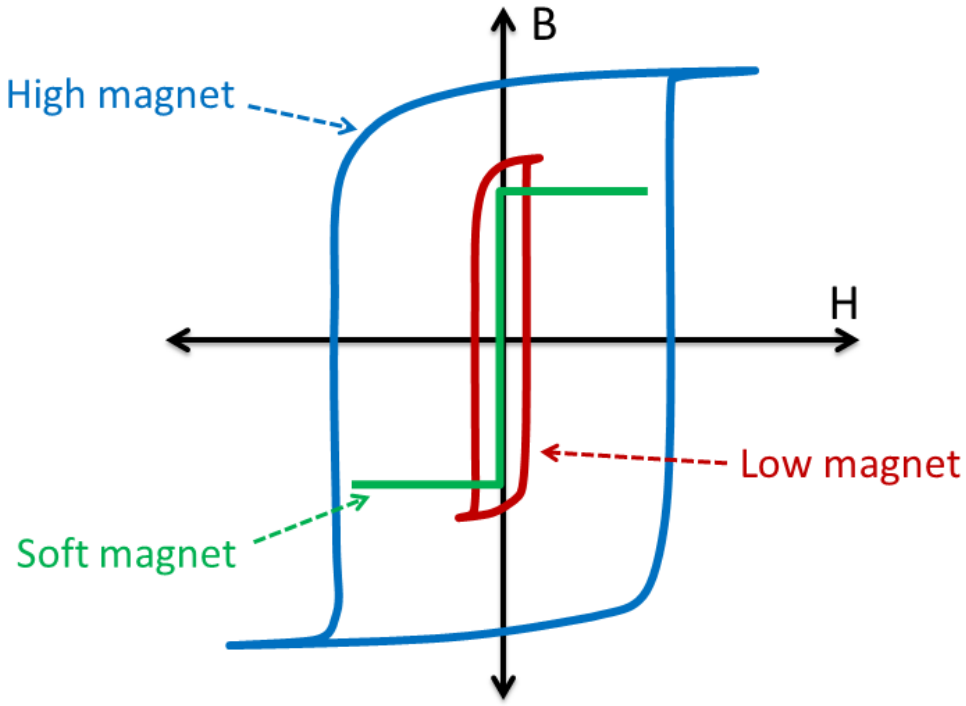

Figure 1.22 Typical Hysteresis curves for hard, low and soft magnetic materials.

Hysteresis loop is formed under cyclic reversal of the ferromagnetic, depending on the value of the magnetizing field H, and distinguish a particular cycle of maximum hysteresis loop. This implies that the magnetization of a ferromagnetic to a large extent depends on the prior history of his stay in the magnetic field.

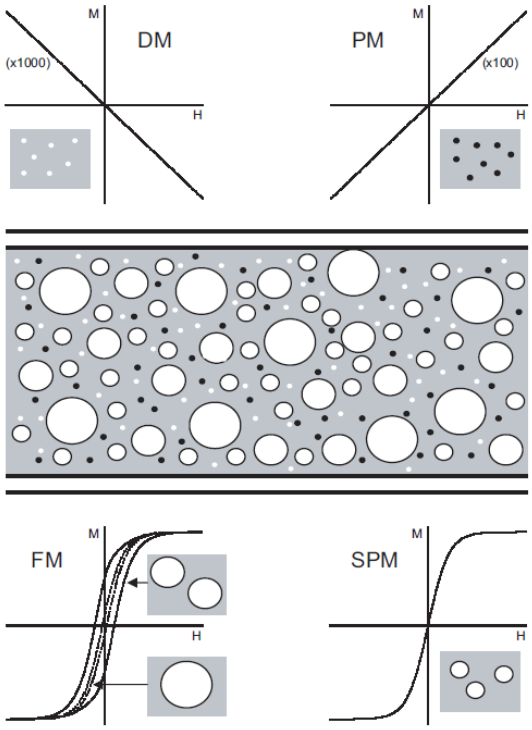

Figure 1.23 The schematic dependence of ferromagnetic particles injected into a blood vessel as function of their size. The biomaterials in the blood vessel are diamagnetic (DM) or paramagnetic (PM). The injected particles can be ferromagnetic (FM) or superparamagnetic (SPM) [46].

To understand the various schematics (hysteresis loop) of magnetic material we show the curve M-H (magnetization- external magnetic field). Presented results were reported by Pankhurst et al. 2003. These results obtained in biomedical category for blood vessel into which some magnetic nanoparticles have been injected (Figure 1.23).

Ferrimagnetism is a magnetic property of matter in which the magnetic moments of neighboring atoms or ions are oriented antiparallel (opposite directions) to each other. As shown in Figure 1.24, in ferrimagnetic materials the magnetization remains even after the removal of an external magnetic field. A ferrimagnetic material can show, in spite of the antiparallel orientation of its magnetic moments, a large total magnetic moment, at least within a domain.

Also in a ferrimagnetic material, an increase in the external magnetic field causes reorientation of sublattice magnetization ($_{\downarrow}\uparrow$) toward the direction of the external magnetic field ($_{\uparrow}\uparrow$) [47]. Ferrimagnetism occurs when the sublattices consist of ions with various numbers of unpaired electrons or ions of one element, but with varying degrees of oxidation.

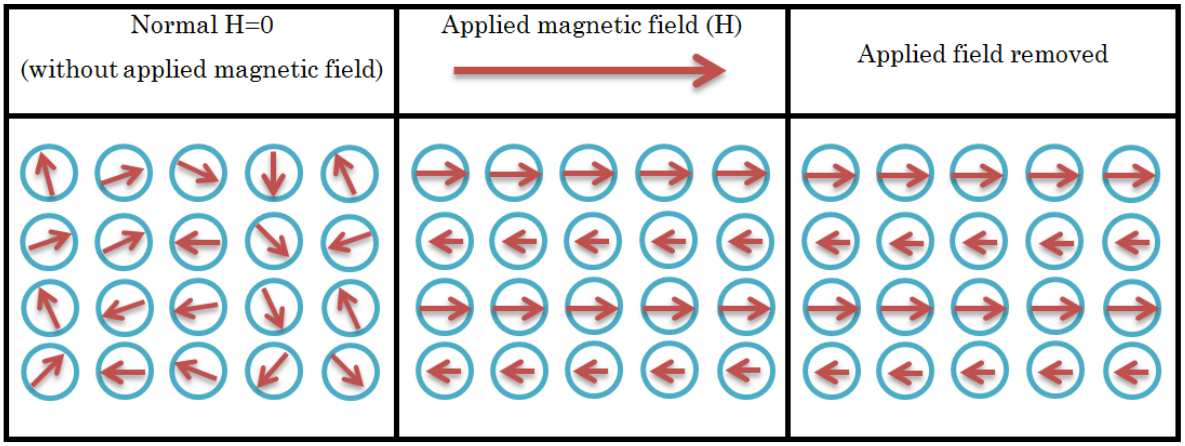

Figure 1.24 The configuration of atomic dipole for a ferrimagnetism.

Antiferromagnetism is one of the magnetic states of a substance, where the elementary (atomic or ionic) magnets in adjacent particles of matter are oriented in antiparallel directions (the opposite of ferromagnetism) [48], and therefore the magnetization as a whole is very small. In additional, the susceptibility of antiferromagnetism is weak and positive [49].

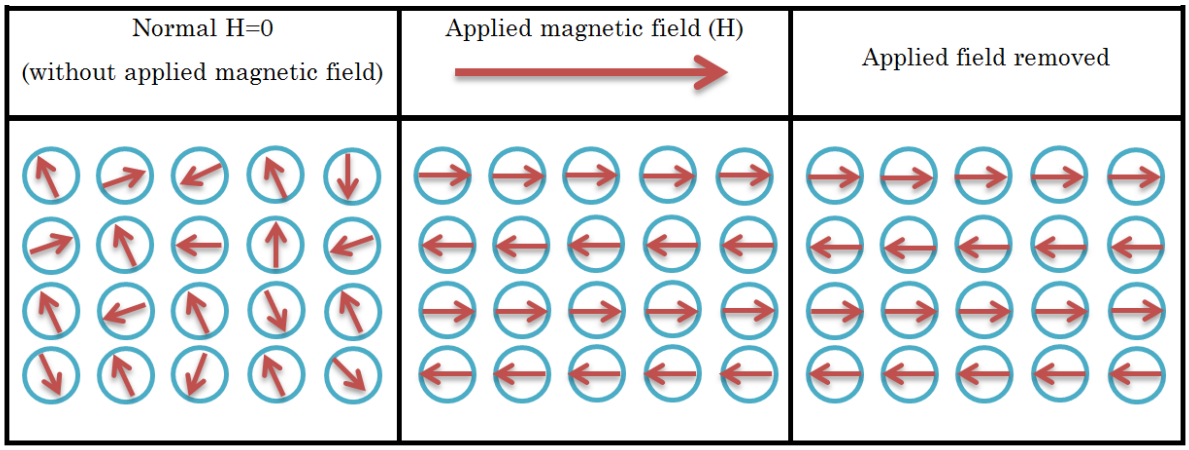

Figure 1.25 The configuration of atomic dipole for an antiferromagnetism.

Antiferromagnetism differs from ferromagnetism; the same orientation of elementary magnets leads to a high magnetization. The scheme of antiferromagnetic ordering is shown on Figure 1.25.

1.5.2 Properties of magnetic materials

Development of magnetic materials for micro and nanotechnologies increased these lasts years. Increasing attention is given by researchers to various applications in fields including chemistry, physics, and biology and in medical uses which every year require more and more new materials with new qualitative properties.

The size of these particles is essential, in order to determine the magnetic properties of these materials. By changing the size, shape, composition and structure of the nanoparticles the magnetic properties of materials based on them can be controlled to a certain extent. One of the main causes of the physical and chemical properties of small particles is found with a decrease in their size is the increase in the relative share of the atoms. Due to the energy point, reducing the particle size leads to an increase in the amount of energy.

The methods used to produce the magnetic materials (nanoparticles) can be summarized as following [50]:

- By conversion of nanoparticles of the same composition into nanoparticles of different composition,
- From chemical compounds by targeted changes in composition [51],
- Composition by utilizing the different methods with compact different materials (same or other).

For the production of magnetic materials based on nanoparticles there is often a need for their insertion into a chemically inert, nonmagnetic base, which would have little effect on the magnetic properties of isolated nanoparticles.

1.5.3 Bioapplication of magnetic nanoparticles

Nanometer is a unit of measurement equal to 10^{-9} m and an average of 3 to 6 atoms (depends on kind of atom) together to make a nanometer. All objects and creatures that range in size from 1 to 100 nm called the nanoscale. Nanomaterials are significant in medicine due to the many biological agents such as viruses, bacteria, antibodies and proteins are classified in nanoscale [52]. Figure 1.26 reports the nanoscale and other small scale.

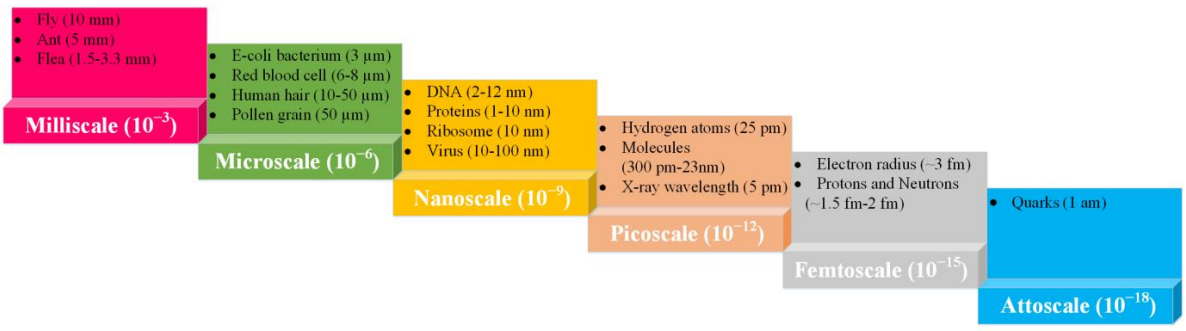

Figure 1.26 The scale from millimeter to meter dimensions.

In recent years, magnetic nanoparticle materials have received great interest in many different applications; especially, magnetic particles show great potential for use in biomedical

research, in clinical applications and in biological research. Furthermore, the methods developed for exploring and detecting the magnetic nanoparticles have provided investigators with a wide range of opportunities for diagnosis and treatment of these materials *in vivo.*

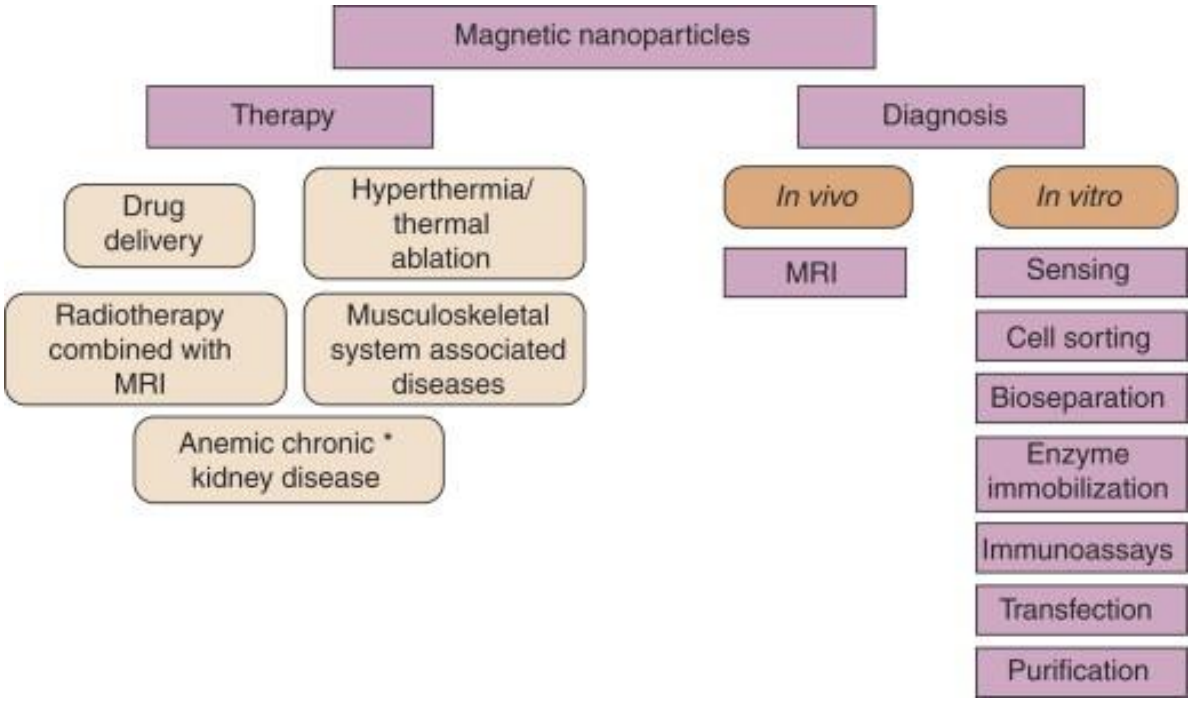

Figure 1.27 Classification (diagnosis and therapy) for biomedical applications of magnetic nanoparticles materials [53].

The main application of magnetic nanoparticles can be drug targeting and transport of drugs (by external magnetic fields) in the specific areas of the patients, the detection of tumor and a hyperthermic tumor treatment [54] by heating the magnetic particles (approximately to 42°C) by an alternating magnetic field [55, 56]. Diagnostic applications of magnetic nanoparticles include a contrast enhancer in nuclear magnetic resonance (NMR) spectroscopy and magnetic resonance imaging (MRI) [52], magnetic separation, magnetic immunoassays (widely used in the laboratory diagnosis of infectious diseases) etc.

Figure 1.27 shows the major bio-application areas of magnetic nanoparticles (Arruebo et al. 2007).

In general, the superconducting quantum interference device (SQUID), magnetic atomic force spectroscopy and resonance methods are used to measure intrinsic magnetic properties of nanoparticles. The giant magnetoresistance is other method recently using to detect and determine the properties of micro-nano magnetic particles. The detection the number of microbeads by utilizing the GMR sensor has been reported in [57].

1.5.4 Brief historical aspects of ferrofluid and their applications

The first magnetic fluid or magnetic liquid was obtained by an American, Solomon Stephen Papell in 1960 [58], as the product of mechanical grinding of magnetite particles in ball mills.

The ferrofluid consists of a fluid that contains ultra-fine magnetic or other particle compounds containing iron, nickel or cobalt with a particle size of 50 nanometers to a few micrometers, stabilized in a polar (water or organic solvent) and nonpolar (hydrocarbons and silicones) media, using surfactants or polymers. Magnetic fluids produce a strongly expressed black color in the fluid due to the presence in them of a highly dispersed magnetic phase of magnetite. Magnetic fluids are unique in that high turnover of particles is combined with high magnetization greater than that of ordinary liquids. Each particle is coated with a thin layer of protective membrane that prevents the adhesion of the particles to each other. The thermal motion of the liquid scatters them throughout the entire volume of the liquid [59]. Also magnetic fluids retain long term stability for many years and have a good flow in conjunction with their magnetic properties.

Methods for preparing magnetic fluids are varied; some are based on the combination of iron, nickel, and cobalt of hundreds of a micron size in mills, with arc or spark discharge, some – on the use of sophisticated equipment.

Today, magnetic fluids are used in various applications [60] of technology such as in the chemical industry (as magnetic lubricants, in the cooling systems), medicine (magnetic cell separation, cancer treatment, magnetic drug delivery and immunoassay), in mechanical engineering (in NASA research projects on the use of a ferromagnetic fluid in a closed ring as the basis for the stabilization system of spacecraft in space [61], and in the oil and the printing industry), electronic devices, mining industry and military (to seal the sealing and insulation gaps between the moving parts of machines, reduce friction).

Other significant usage of ferrofluids are in medicine. As we know anticancer drugs are harmful to healthy cells. But if you mix them with magnetic fluid and enter them into the blood the medicine becomes concentrated in the tumor without harming the body. You can also move the body enzymes. Magnetic magnetite particles are used to treat cancer (hyperthermia). This method of treatment is based on the fact that under the influence of an alternating magnetic field magnetite particles are heated and inhibit the growth of cancer cells [62].

Magnetic fluid can be used as a contrast agent for X-rays. Usually fluoroscopic diagnosis of gastrointestinal tract are based on gruel barium sulfate [63]. Another great bioapplication of magnetic fluids is in surgery [64]. If the permanent magnet is in the place where the surgeon has to make the cut, the cap of the magnetic fluid flows from the syringe into a vein or artery to clog impede the flow of blood after the cut. And finally, we want to mention another vital role of magnetic fluids, that of usage in orthopedics and traumatology where it is used to lubricate the joints (in lower limb prosthetics) [65].

1.6 Conclusion

The beginning of Chapter one contains a summary of the invention history of giant magnetoresistance (GMR) effect and explains the early experience of this effect on multilayers Fe/Cr antiferromagnetically-coupled (AFC) in 1988.

Afterwards, the comparison of the GMR sensor and other magnetic field sensors, relative to their power, price and ability to detect the magnetic field in several ranges has been shown. We have described the basic characteristics to understand the GMR effect in multilayers and presented the most important structures of giant magnetoresistance such as spin valve structure, current in plane (CIP) and current perpendicular to plane (CPP) structures, magnetic tunnel junction structure and giant magnetoimpedance (GMI) structure.

Furthermore, we have perused the behavior of all the magnetic materials while placed in a magnetic field or when the magnetic field is removed. To conclude, all materials can be classified into various categories according to their magnetic susceptibility.

At the end of this Chapter a short history and main applications of the magnetic fluid in several domains, particularly in medicine have been examined. Mainly, application of these materials in biomedicine represents hyperthermia treatment, magnetic targeted delivery, magnetic cell separation, magnetic resonance imaging (MRI) and etc.

Chapter 2 : Giant magnetoresistance sensor characterization

2.1 Introduction

A biosensor is a device for the detection or quantification of physical properties that combines a biological component with a physicochemical or physical detector component. Fabrication the biosensors on basic of the GMR effect is a new way, promising for detecting and measuring the biological molecules being magnetic or being labeled with magnetic beads or nanoparticles. The measuring principle is the electrical resistance variations of the GMR element due to a magnetic field in presence or absence of micro or nanoparticles.

This chapter deals more specifically with fabrication, and characterization of the GMR sensor types designed at Kanazawa University and provided to us by Professor Yamada for this work.

2.2 Structure and design of the giant magnetoresistance needle probe

2.2.1 First model of the GMR needle probe sensor

The giant magnetoresistance sensor is conditioned in a thin needle with two sensing elements of 75 µm×75 µm. They are placed at the top and the end of the needle and connected in a Wheatstone bridge configuration. A first model is showed on Figure 2.1.

This Wheatstone bridge configuration permits to measure voltage variations induced by magnetic field with removing of DC voltage part due to the GMR polarization. The resistances of the Wheatstone bridge should have values close to that of the GMR elements, in order to have the same DC value of voltage in Vref and Vout. This configuration allows to directly amplify (Vout−Vref) without necessity of a high pass filter for removing the DC component.

The length of the needle inserted into the cavity containing the ferrofluid sample is 3 cm with an approximate diameter of 300 µm. The needle is made of aluminum titanium carbide (AlTiC), a hard material and sintered material such as aluminum oxide (Al_2O_3) and titanium carbide (TiC).

Furthermore, for this type of GMR the maximum admissible current is 9.7 mA. The schematic of the sensor is presented in Figure 2.1.

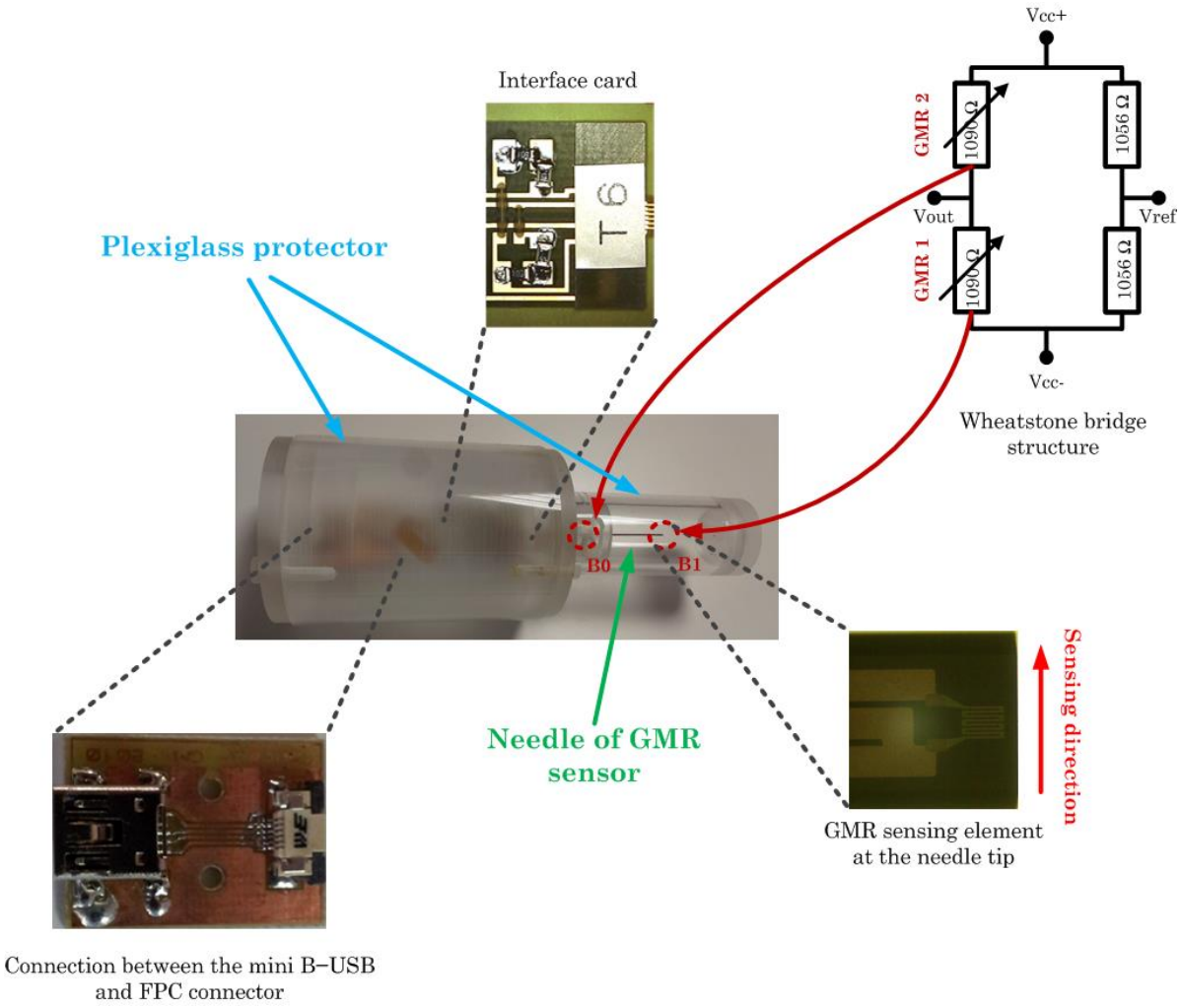

Figure 2.1 Schematic of first model of the GMR sensor.

The sensing elements change their resistances according to presence of the magnetic field, the first GMR measure the magnetic flux density (B_1) in the container of fluids and the second one determines the external magnetic flux density (B_0). The sensing direction of the GMR sensor (first model) is perpendicular to the needle, and this direction is very important for positioning the Helmholtz coil. In order to connect flexible printed circuit (FPC) connector and mini B−USB as shown in Figure 2.1, we have fabricated a small dimension Printed circuit board (PCB) as presented in Figure 2.2. Table 2.1 shows the pins connection of PCB board cart.

On one hand, the circuit and needle of the GMR sensor are maintained by the plexiglass to shield and protect from any impact or shock. On the other hand, the plexiglass cover does not cause modification of the magnetic field when sensor is placed at the center of the Helmholtz coil.

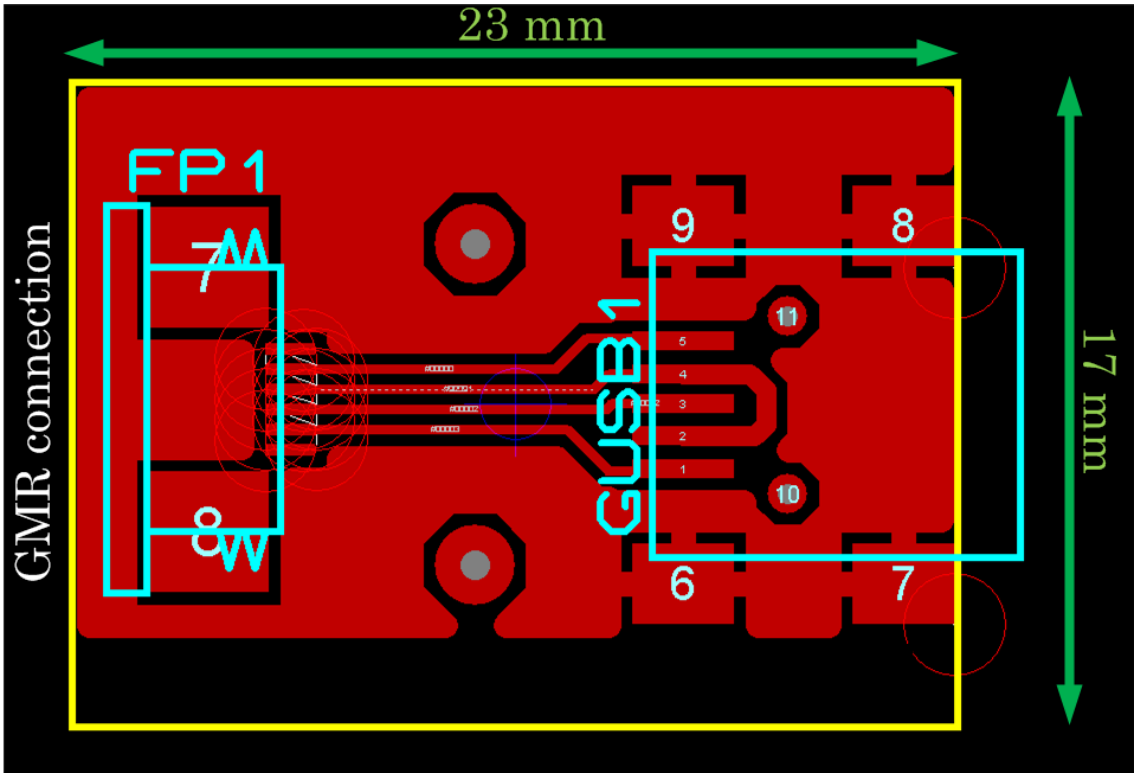

Figure 2.2 Schema of PCB card for connection the mini B−USB and FPC connector.

Table 2.1 Pins connection of mini B−USB and FPC connector.

Number of pin	FPC pins	Mini B USB pins
1	Not connected	Vref
2	Vcc_+	Vcc_-
3	Vcc_-	Vout
4	Vout	Vcc_-
5	Vref	Vcc_+
6	Not connected	GND

The GMR sensor is supplied with a mini B−USB interface which is located at the end of the sensor shield and connected to a DC power supply by an interface card (USB−A). The pin connection diagram for the mini B−USB of the GMR sensor and the USB−A of the interface card are shown in Table 2.2.

Table 2.2 The pin connection of Mini B-USB to USB-A of PCB cart.

Number of Pin	1	2	3	4	5
Mini B-USB	Vref	Vcc_-	Vout	Vcc_-	Vcc+
USB-A	Vref	Vcc_-	Vout	Vcc+	-

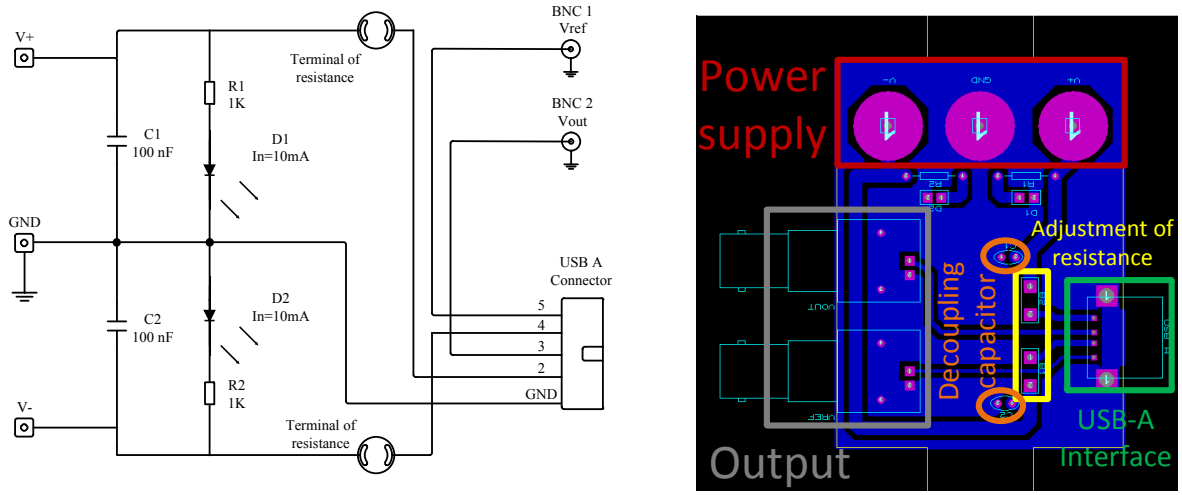

Figure 2.3 The schematic of connection cart between sensor and power supply.

The main role of the interface card is to control and protect the GMR sensor from an excessive electrical current passing through the GMR sensor. The circuit and layout of the connection card of the GMR sensor to the power supply is explained in Figure 2.3.

2.2.2 Second model of GMR needle probe sensor

A second model of the GMR sensor consists also on two main parts: a needle with four GMR elements instead of two as in GMR I and a Wheatstone bridge conditioning circuit.

The needle type SV−GMR sensor consists of four sensing elements: the first sensing element (GMR1) is at the tip of the needle and the other sensing elements (GMR2, GMR3 and GMR4) are at the end of the needle. All four sensing elements are connected in a Wheatstone bridge configuration.

As we mentioned previously for the first model GMR I, the first sensing element at the top of sensor is in contact with the magnetic liquid in the container (inside magnetic flux density B_1) and the other sensing elements are embedded to sense magnetic flux density (B_0) at the outside of the ferrofluid's cavity.

The needle length is 17 mm with a cross section 300×300 µm and the material used for fabrication is the same as for the first model. The sensing direction of GMR sensor is parallel to the needle. It should be noted that the maximum allowable current for this type of the GMR sensor is 5 mA.

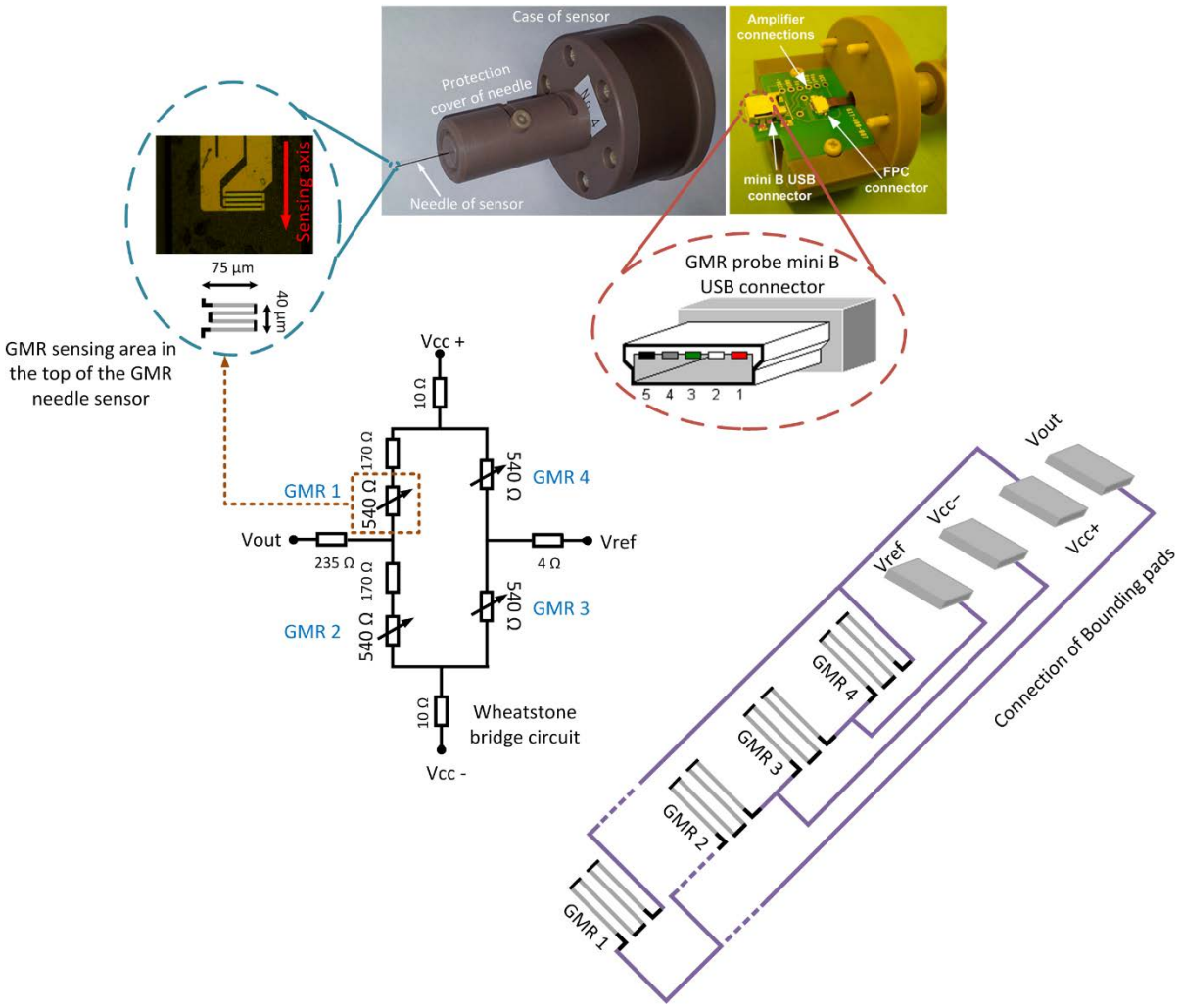

Figure 2.4 The design of the GMR needle probe and its components.

Wheatstone bridge is a four branch electric circuit composed of impedances (resistors, capacitors or inductors), designed by the relationship between components at the electrical equilibrium. The schematic of the GMR sensor with the Wheatstone bridge configuration is indicated in Figure 2.4. In the schematic of the Wheatstone bridge all 540 ohm resistances represent the four sensing elements and the rest of the resistances are used to model the electrical resistances of the connection paths.

2.3 Setup component of giant magnetoresistance needle probe

2.3.1 Uniform magnetic field generator

In our investigation Helmholtz coils are used to obtain a uniform magnetic field. Even this is a well-known magnetic source structure, we summarize here some technical details of the one designed in our laboratory.

In general, there are two identical circular coils connected in a series and spaced within a coil radius of each other (Figure 2.5). As the Helmholtz coil generates a more uniform magnetic field it is widely used for AC, DC or pulsed magnetic field, for the calibration of the sensors of magnetic induction, magnetization and demagnetization of permanent magnets, etc. Thus, the Helmholtz structure is very useful and has been proposed for use in biomedical research.

Magnetic flux density in the center of a Helmholtz coil can be calculated by the formula [66]:

$$B = \mu_0 \left(\frac{4}{5}\right)^{3/2} \frac{IN}{R} \tag{2. 1}$$

Where μ_0 is the permeability of free space, I is the coil current, N is the number of turns in each coil and R is coil radius.

The specification of the Helmholtz magnetic source that has been produced in our laboratory consists of two circular coils of twelve turns (tight winding) with the cabling wire (rigid copper stranded; 16 mm^2). Each coil is 0.52 meters diameter and the distance between the coils is equal to the coil radius (0.26 meters).

Finite element analysis software COMSOL 4.0a is used to calculate the value of the magnetic flux density (B) in whole and particularly in the midpoint of the Helmholtz coil. This analysis consists of several steps. First, two coils with diameter 0.52 meters were created in the geometry section. Second, an air sphere with radius 1 meter was selected. Third, the equation of external current density (Je) of X, Y, Z axes were putted in the section of magnetic field (mf) parameters. The Je for the Helmholtz coil can be determined by following expressions [67]:

$$\begin{array}{ll} \dfrac{-J_0 \times Z}{\sqrt{X^2 + Z^2}} & \text{X} \\ 0 & \text{Y} \\ \dfrac{J_0 \times X}{\sqrt{X^2 + Z^2}} & \text{Z} \end{array} \tag{2. 2}$$

and J_0 is:

$$J_0 = \frac{I}{A} \tag{2. 3}$$

where, I is the total current and A is the cross sectional area.

Fourth, in the model builder window a tetrahedral mesh (finer) was selected and finally we clicked on “compute” in study part in order to run the simulation.

The schematic of the Helmholtz coil (a) and the magnetic flux density along the X axis of coil (b) simulated by finite element software COMSOL 4.0a are presented in Figure 2.5.

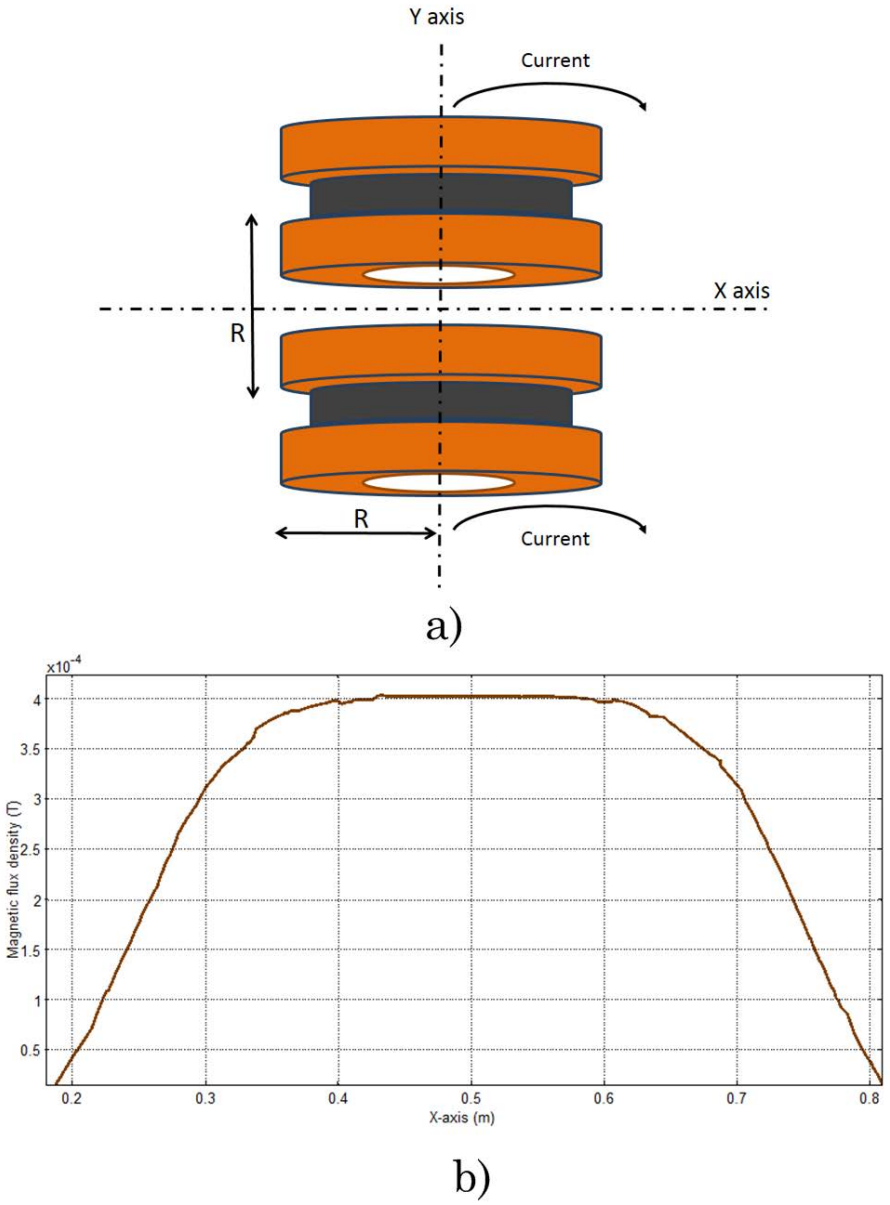

Figure 2.5 The Helmholtz coil structure (a), B (T) along the x-axis (b).

In order to verify the simulation results, an analytical method of magnetic flux density calculation was performed. This method and mathematical expressions of the calculation is developed by [68]. Figure 2.6 indicates the magnetic flux density distribution throughout the total area of Helmholtz coil. As it is well known the B field is more uniform in the center of

the coils. The analytical calculation of the magnetic flux density distribution for each contour along the X and Y axes is presented in Figure 2.7. In both methods (simulation in COMSOL and analytical calculation in MATLAB) the input current of coils is equal to 10 A. The results obtained are similar and confirm each other with an average error 3.23%.

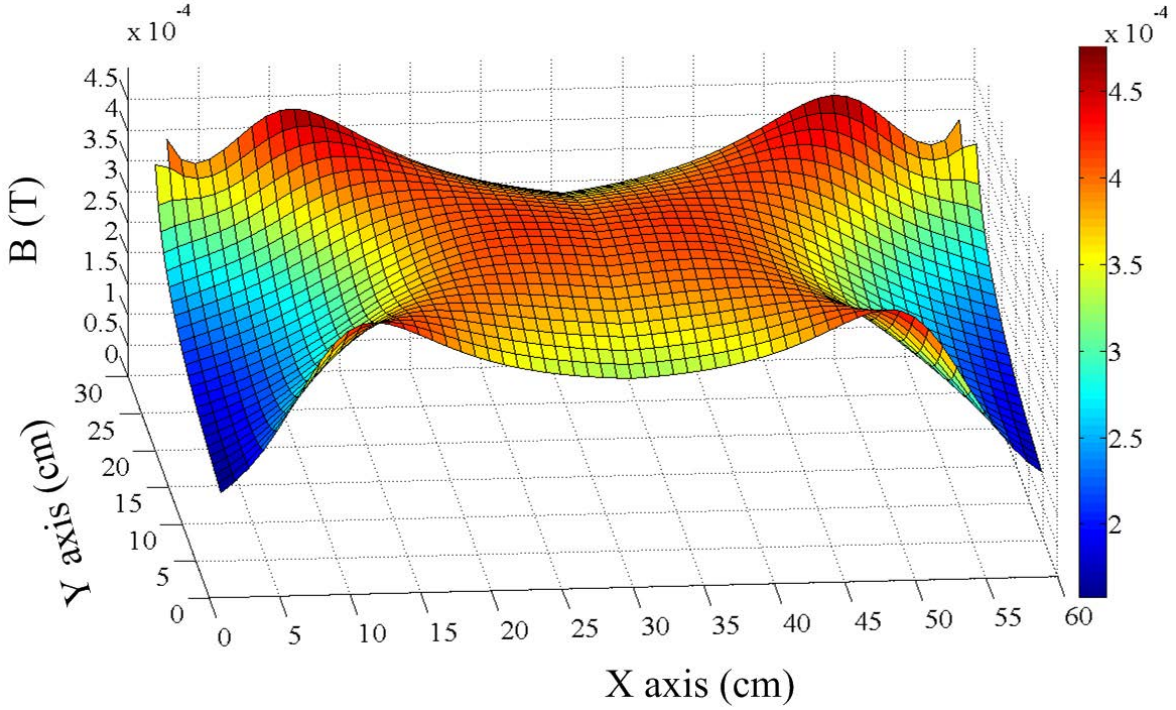

Figure 2.6 Distribution of magnetic flux density in Helmholtz coils.

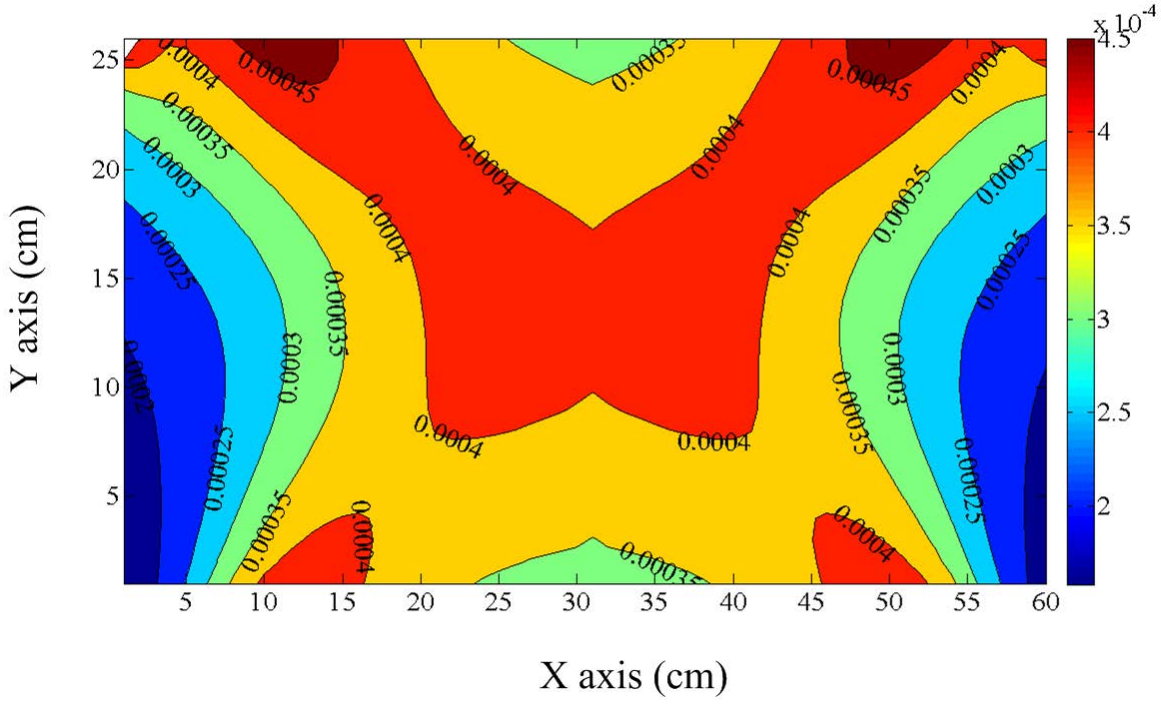

Figure 2.7 Analytical calculation the B distribution along the axes X and Y.

The coil is alimented by an amplifier (variable gain) through a two transformers in series (the choice depending on the frequency range of interest), the voltage induced in the secondary coil (Vs) and the primary coil (V_p) are related by:

$$\frac{V_S}{V_P} = \frac{N_S}{N_P} = \frac{I_P}{I_S} \tag{2. 4}$$

where the symbol (P) corresponds to the values related to the primary winding and the index (S) corresponds to the values for the secondary winding, *N* is the number of turns. The configurations (coils with or without matching transformer) for frequencies of 50/60 Hz and 10/50 kHz are shown in Figure 2.8 (a, b). First configuration has two transformers in series which permit to optimize the impedance adaptation by reducing the transformation ratio of 1/3. The second power supply configuration is a step-up transformer (ratio of 5:1) and this arrangement allows us to transmit 400 VA to Helmholtz coil.

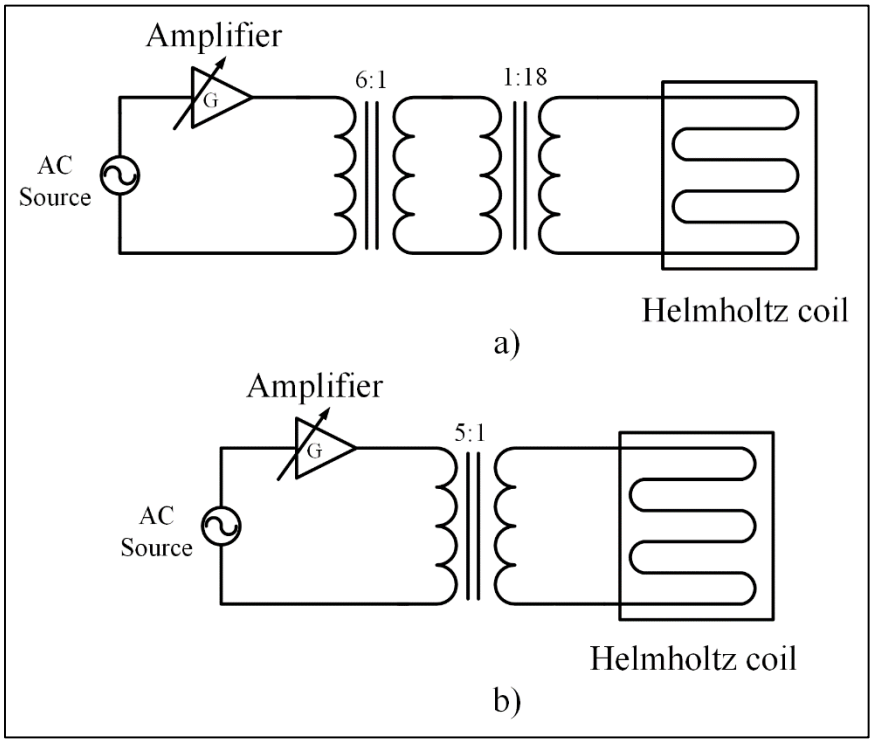

Figure 2.8 The power supplies schematic of the Helmholtz coil: 50/60 Hz (a) and 10/50 kHz (b).

Table 2.3 presents the maximum ranges of B (µT) and impedance calculation of the Helmholtz coil as a function of the frequency. In Figure 2.9 and Figure 2.10 the experimental results of the magnetic flux density (µT) as function of input voltage (V) at the frequencies 50, 60 Hz and 10, 50 kHz are introduced.

Table 2.3 Experimental characterization of the Helmholtz coil as a function of the frequency.

Frequency (Hz)	Impedance (Ω)	B (µT)	I (A)
50	0.096	3440	70
60	0.113	3440	70.1
10000	17.41	66	1.85
50000	64.2	42	1.35

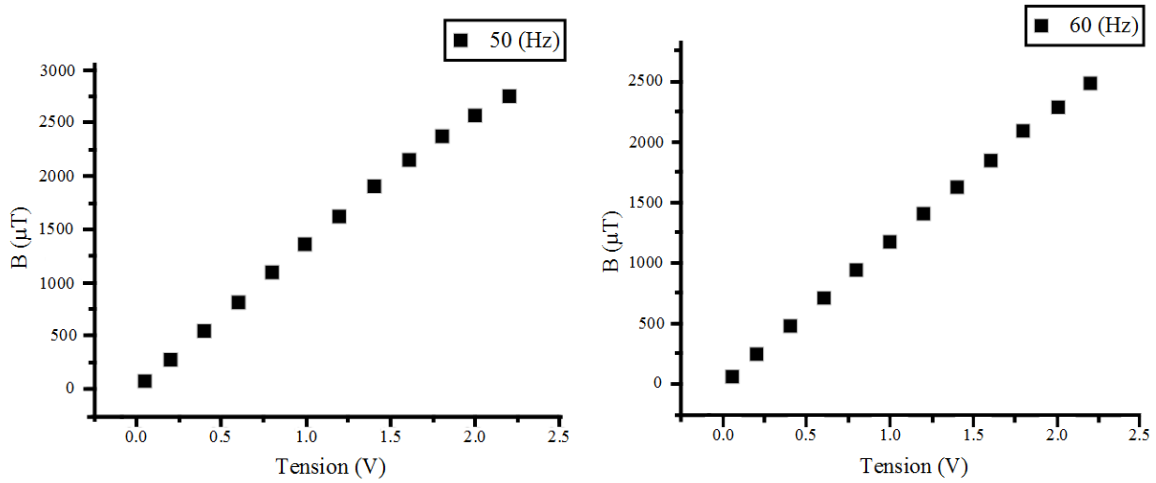

Figure 2.9 Measurement the magnetic flux density (µT) as a function of the input voltage applied to 50 and 60 Hz.

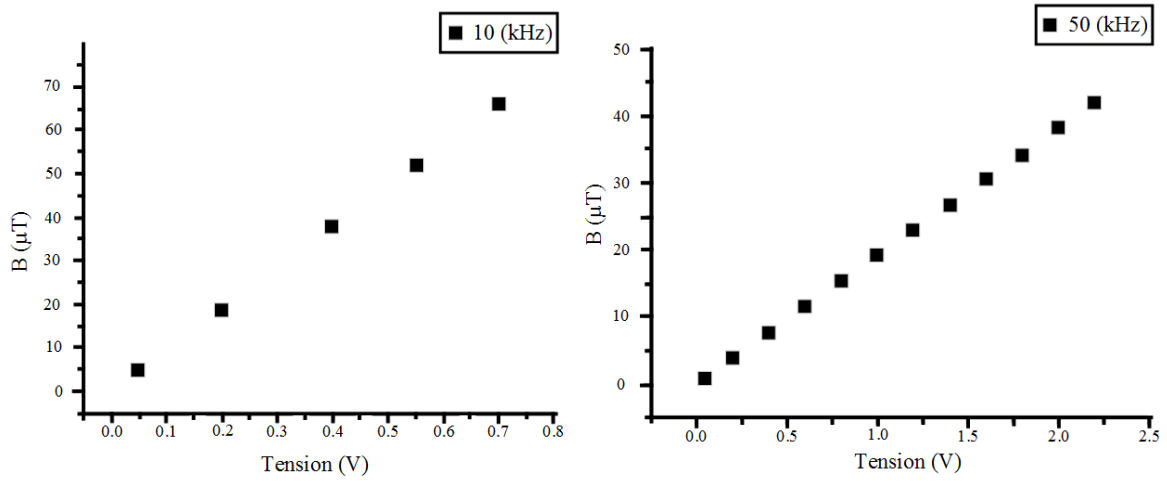

Figure 2.10 Measurement the magnetic flux density (µT) as a function of the input voltage applied to 10 and 50 kHz.

2.3.2 Displacement system

As noted in the previous part, the GMR sensor has a needle that could be inserted in the center of a sample cavity. In the testing process the needle being very fragil in one hand and to reduce the percentage of error rate for more accurate measurements on the other hand, the displacement system type RCP2-SA6C produced by Rosier company [69] was used,

controlled by controller PCON-CG-42PI. The associated software allows a backup of 512 preset positions. The displacement system permits changing of both X and Y axis positions of the Helmholtz coil according to the direction of sensing axis for each sensor. This system gives us more ability to carefully control the process of insertion of the GMR sensor needle and its cleaning in two positions. The specification of displacement system is shown in Table 2.4.

Table 2.4 Actuators specification of displacement system model RCP2-SA6C [69].

Item	Description
Material	Aluminum
Positioning repeatability	± 0.02 mm
Speed range	0.01 to 150 mm/s
Backlash	0.1 mm or less
Displacement range	100 mm
Safety	Brake power failure
Ambient operating temperature	0−40^{o}C

Displacement system is supported with 220 V AC to 24 V DC convertor via a protection relays. They permit to cut-off motor by keeping supply for controller and brake system to immediately lock the moving part in case of emergency button activation. The system can be reactivated after removing emergency button and pushing on/off button. Electrical schematic and control panel of this system are shown in Figure 2.11 (a) and (b).

There is an importance to measure the height between the displacement system and the Helmholtz coil for two axes. When moving the displacement system the magnetic flux density is perturbed. For this reason the simulation analysis with COMSOL 4.0a was used to estimate the appropriate height of the displacement system. Figure 2.12 presents the schematic of the displacement system of the GMR sensor.

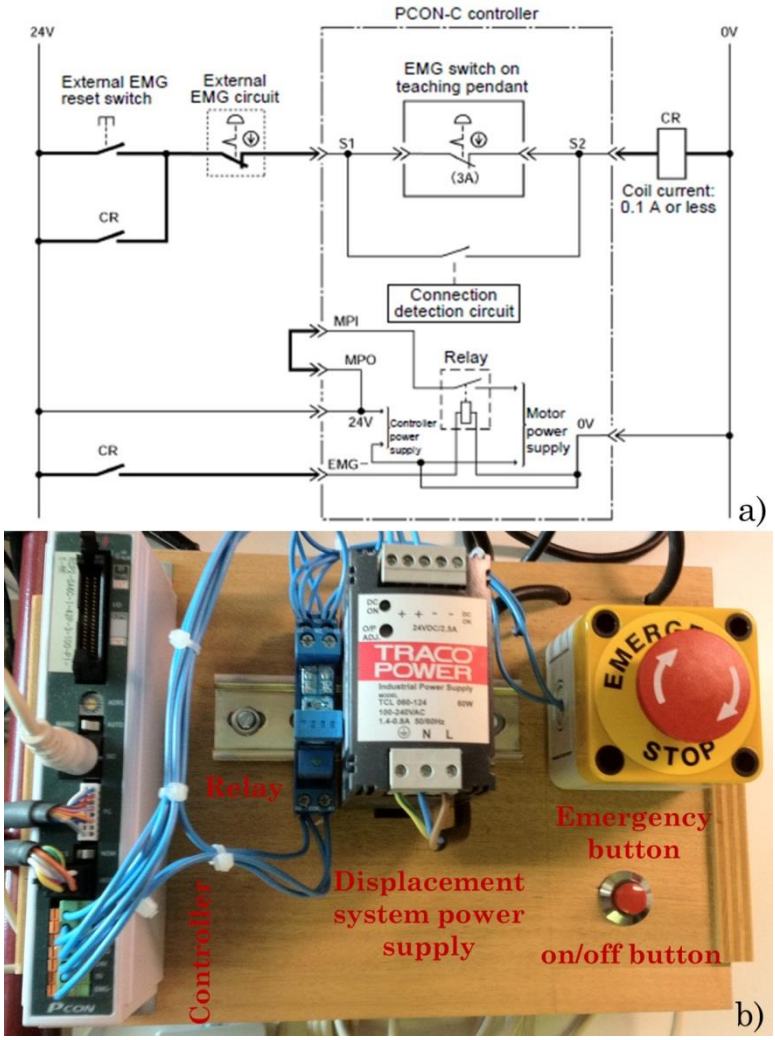

Figure 2.11 Electrical schematic (a) [69], control panel (b) of displacement system.

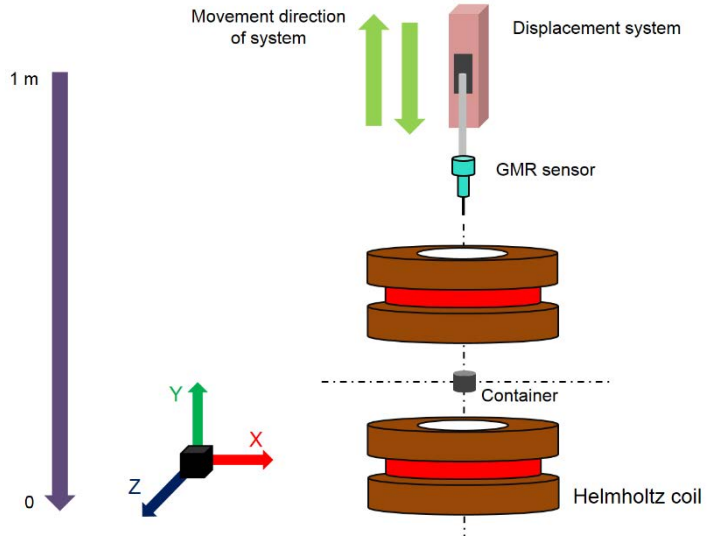

Figure 2.12 Positioning the displacement system of the GMR sensor.

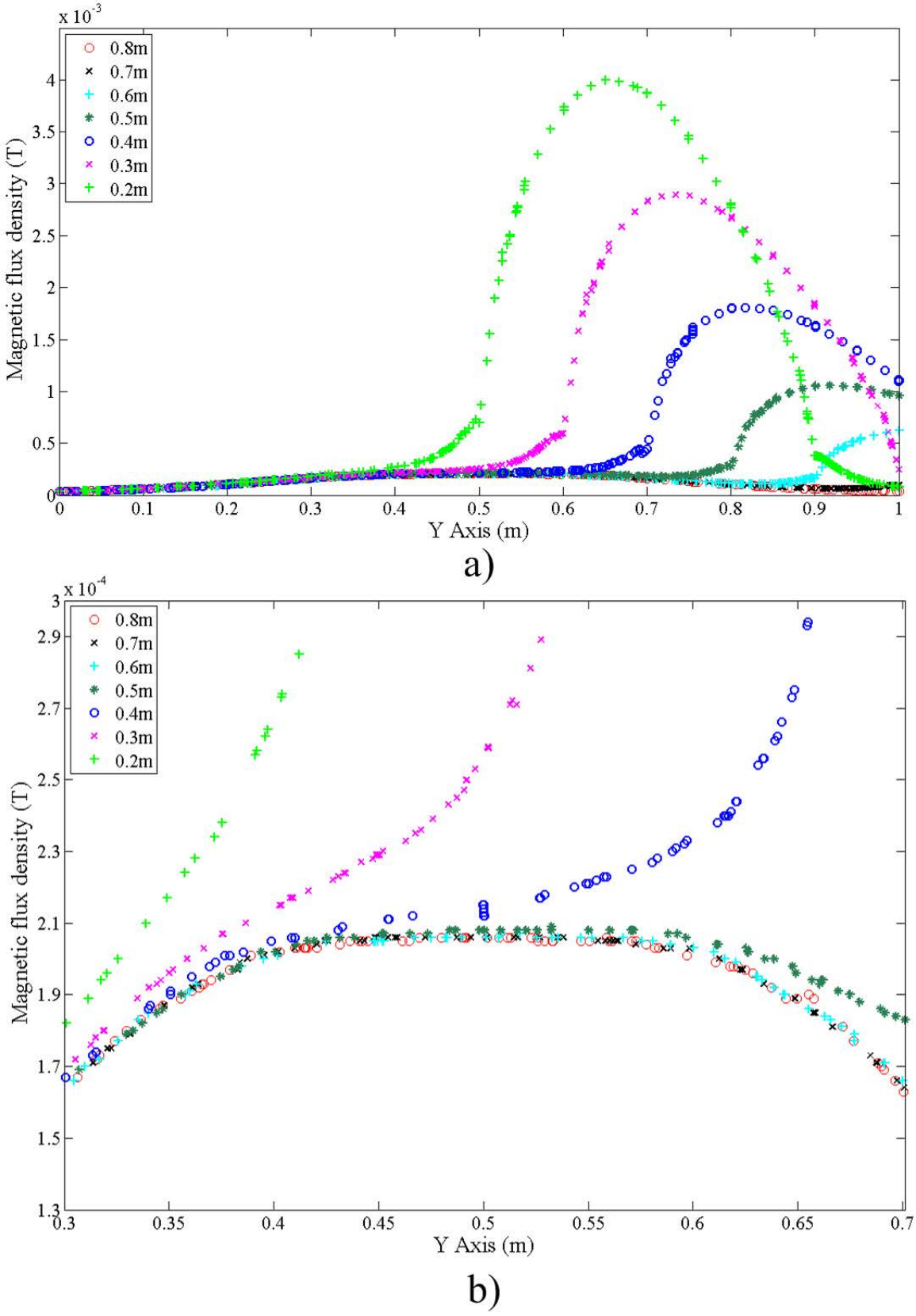

Figure 2.13 Changing the magnetic flux density according to the moving of the displacement system along the Y axis (a), the change of magnetic flux density in midpoint of the Helmholtz coil considering the system of the GMR sensor (b).

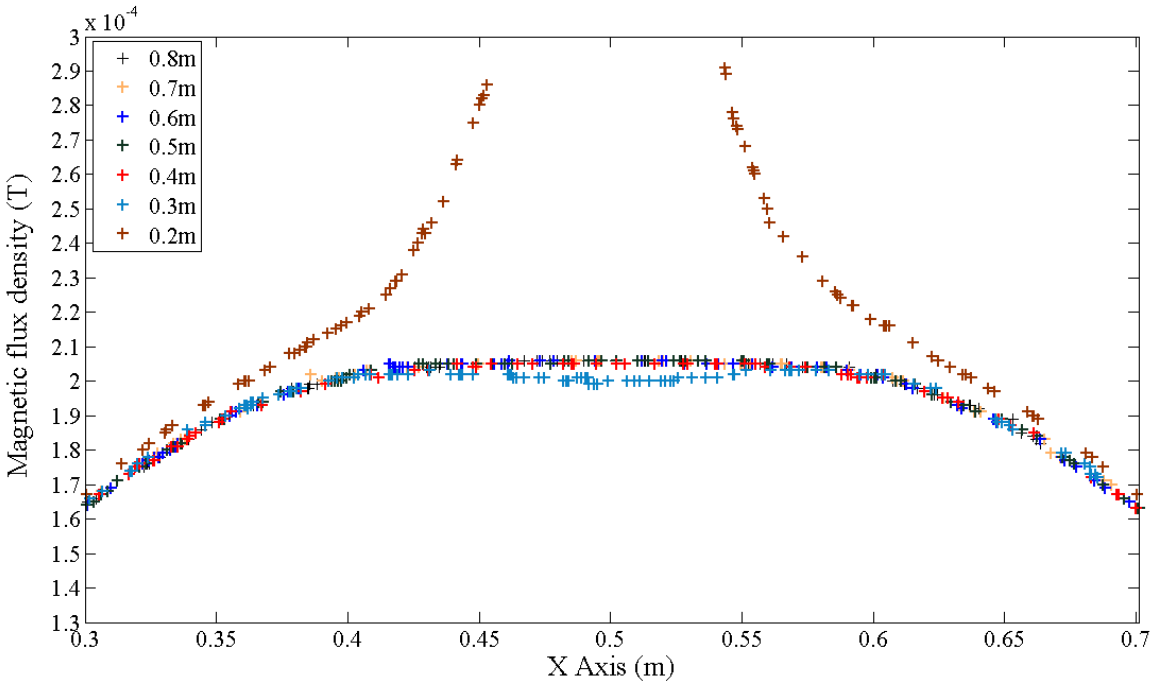

Figure 2.14 Changing the magnetic flux density (B) in center of the Helmholtz coil by changing the position of the displacement system along X axis.

We simulated a displacement system with the following dimensions: 0.4 height, 0.06 weight, 0.06 depth in meters and selected several heights ranged from 0.8 m to 0.2 m (around the midpoint of the Helmholtz coil).

Figure 2.13 (a), (b) indicates the simulation results obtained for the vertical position where as horizontal position is presented in Figure 2.14. Furthermore, the variation of magnetic flux density (%) as a function of displacement system's position is calculated and introduced in Figure 2.15 (a) and (b).

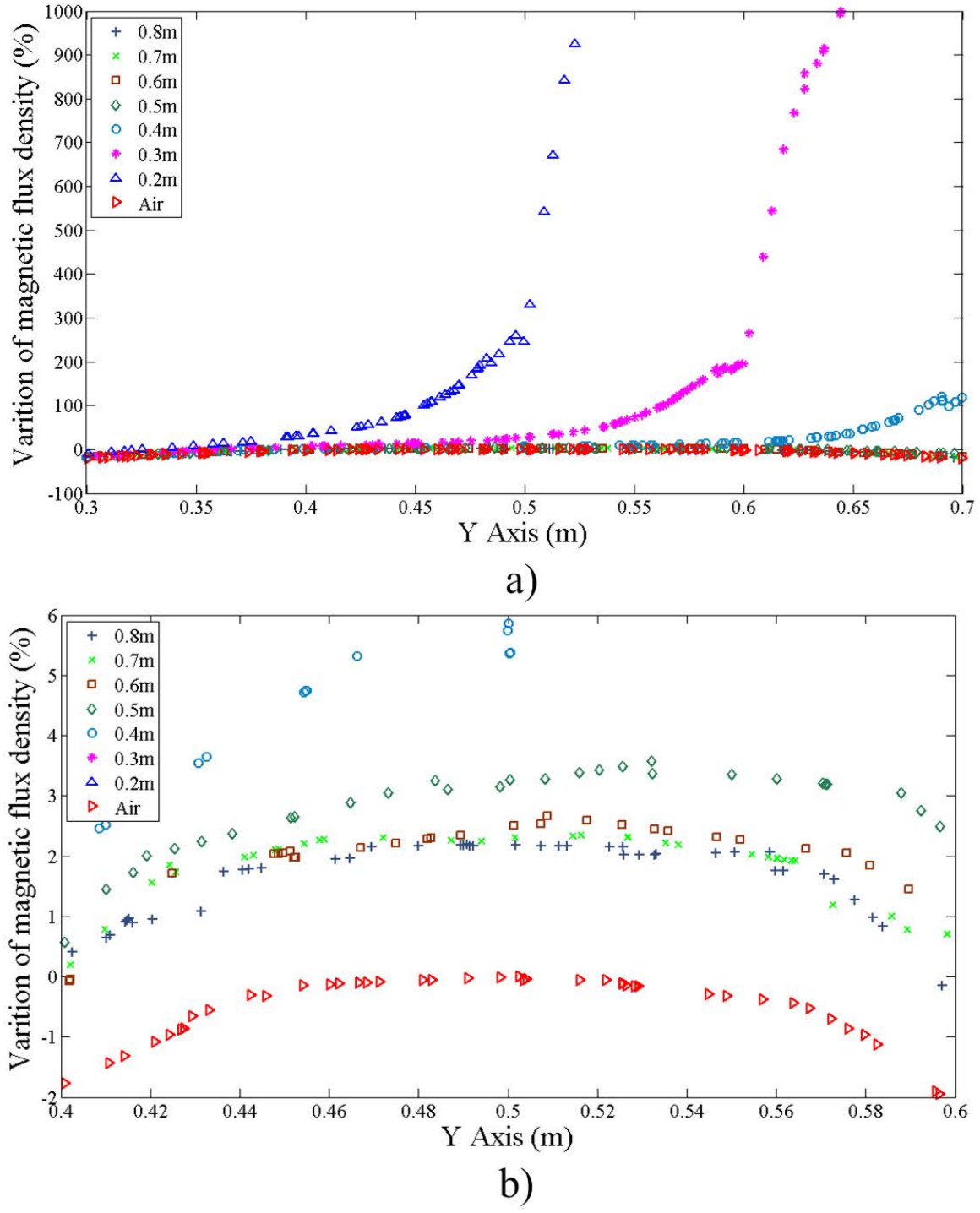

Figure 2.15 Calculation of the percentage error (%) of magnetic flux density variation as function of the system position along the Y axis (a), the variation of (B) % in the center of coil (b).

The results show that with the positioning system approaching the center of the coil, the uniformity of magnetic flux density is disturbed, and it is further seen in the vertical position compared with horizontal position of the Helmholtz coil. As shown in Figure 2.15 (b), the position of displacement system of the GMR sensor in the location 0.2 m and 0.3 m has

completely disrupted the uniformity of the magnetic field and for this reason we cannot observe it in this experiment. Due to this, the displacement system of sensor was placed at a distance 40 cm (approximately the point 0.74 m in the simulation) from the upper surface of the Helmholtz coil and the GMR sensor is connected to displacement system with a plexiglass rod.

2.3.3 Preamplifier and lock-in amplifier

The output signal of GMR senor is very weak; approximately in range of µV. Additional amplifier for the GMR sensor setup has been designed to decrease the output noise, to have a clear and strong signal in output of the sensor. For the setup, Analog Device AD 620b is selected and is connected to HF2IS Impedance Spectrometer (1 µHz−50 MHz), produced by Zurich Instruments Company. The gain of AD 620 is ranged from 1 to approximately 1000 times and depends on the choice of the gain resistors in pins 1 and 8 (Figure 2.16). The calculation formula of gain resistance (R_G) to change the gain value (G) of amplifier can be described as [70]:

$$R_G = \frac{49.9k\Omega}{G-1} \tag{2. 5}$$

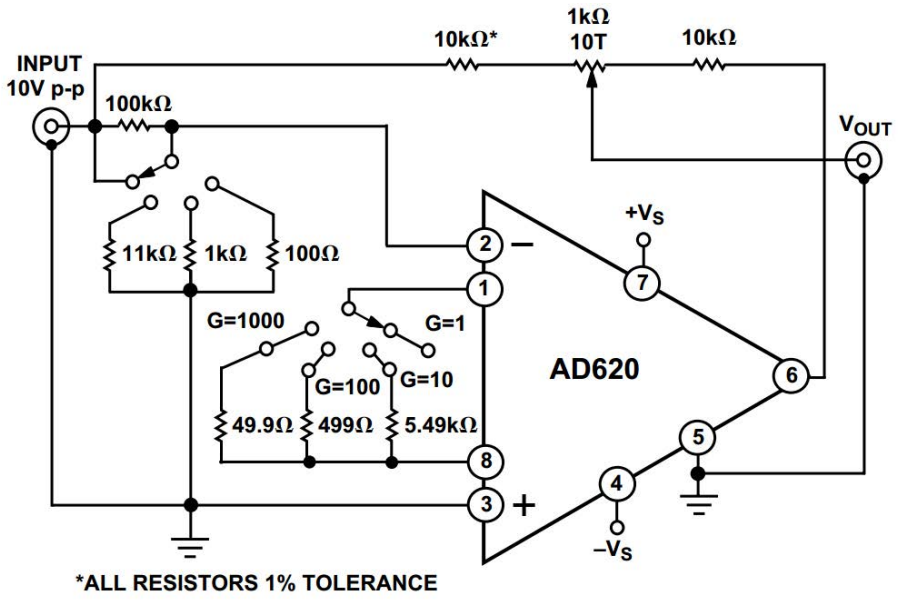

Figure 2.16 The pins schematic of the AD 620 [70].

It should be noted that maximum low offset voltage of the AD 620 is 50 µV and operating temperature ranges from −40ºC to +85ºC, voltage ranges from ±2.3 V to ±18 V. In the Figure 2.17 (a, b) the diagrams of gains and voltage noises according to frequency (Hz) are shown.

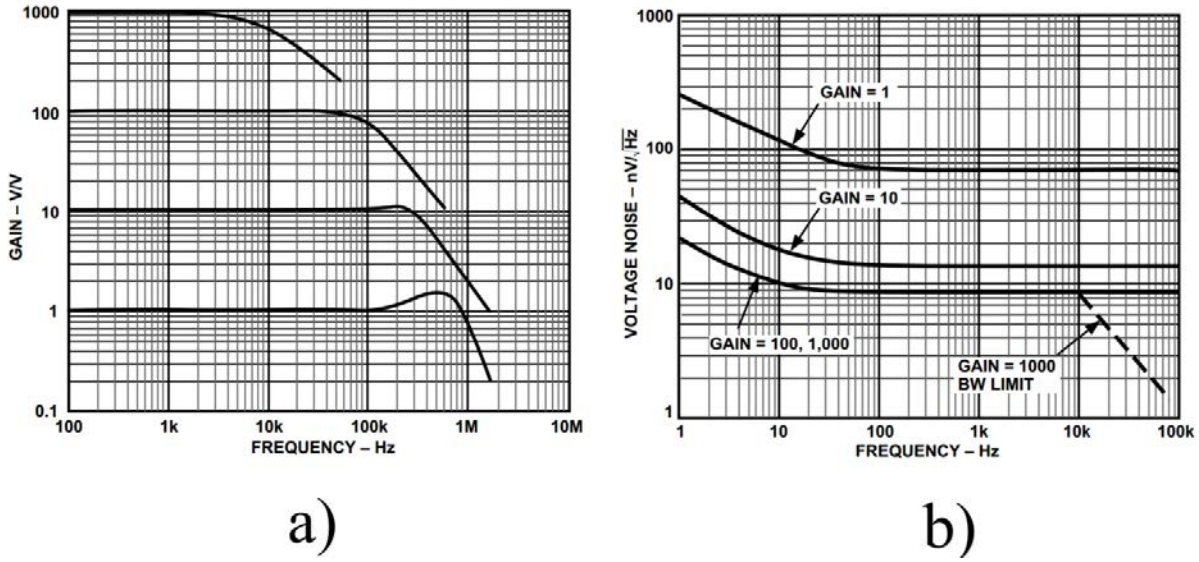

Figure 2.17 Typical characteristics of the Analog Device AD 620: Range of gain as a function of frequency (a); Voltage Noise Spectral Density depending on frequency for Gain = 1–1000 (b) [70].

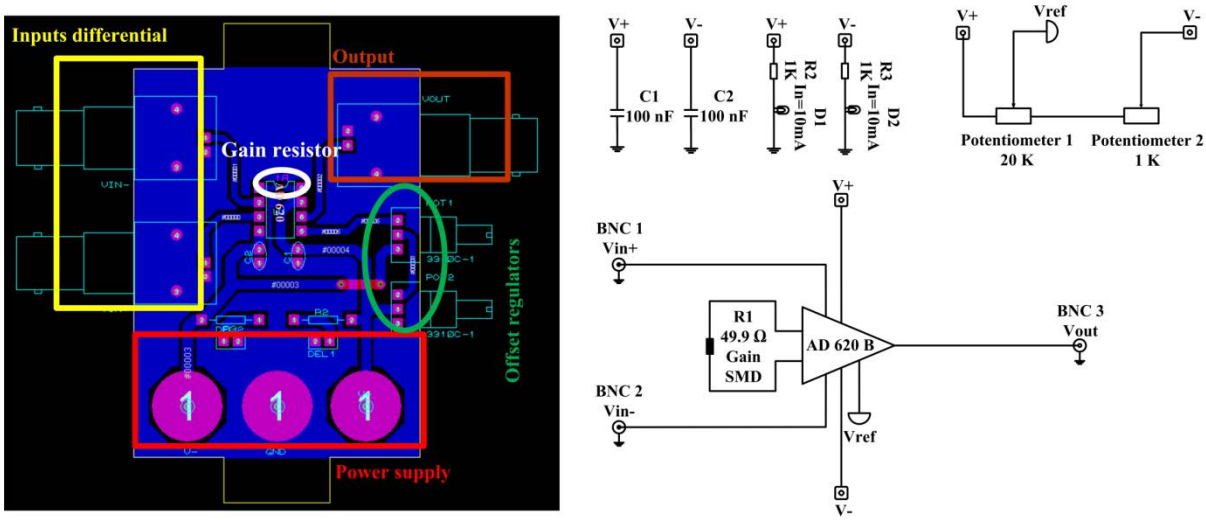

Figure 2.18 Design of preamplifier circuit.

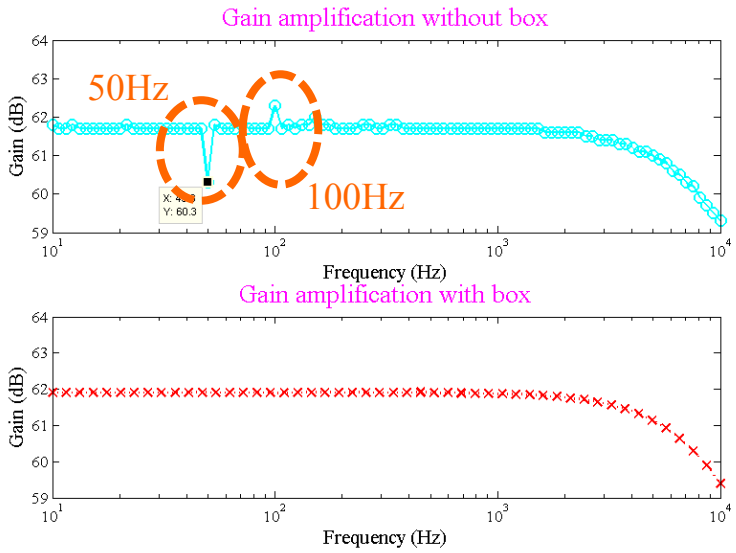

Figure 2.19 The amount of gain as a function of frequency.

The circuit design of the PCB of additional amplifier for the GMR sensor setup measurement is presented in Figure 2.18. To have a gain for the preamplifier of approximately 1000 times (60 dB) a resistance gain (R_G 49.9 Ω) is used. Furthermore, two potentiometers are used to control offset (one is for fine tuning of offset and second is for first approximate adjustment). Furthermore, we have enclosed the preamplifier into an aluminum box (98×64×36 mm) to enhance the electromagnetic compatibility of the electronic circuits, particularly at 50−60 Hz. The amplification gain's (dB) results, as function of the frequency ranged from 10 Hz to 10 kHz with and without the aluminum box, are presented in Figure 2.19. We observe from Figure 2.19 that a cutoff frequency (−3 dB) for AD 620 for gain range is approximately 10 kHz.

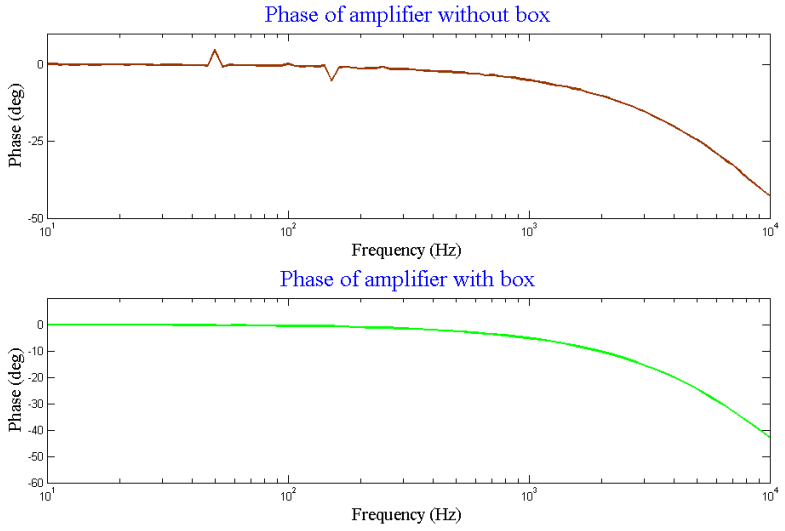

Figure 2.20 The Phase (deg) calculation with and without the aluminum box.

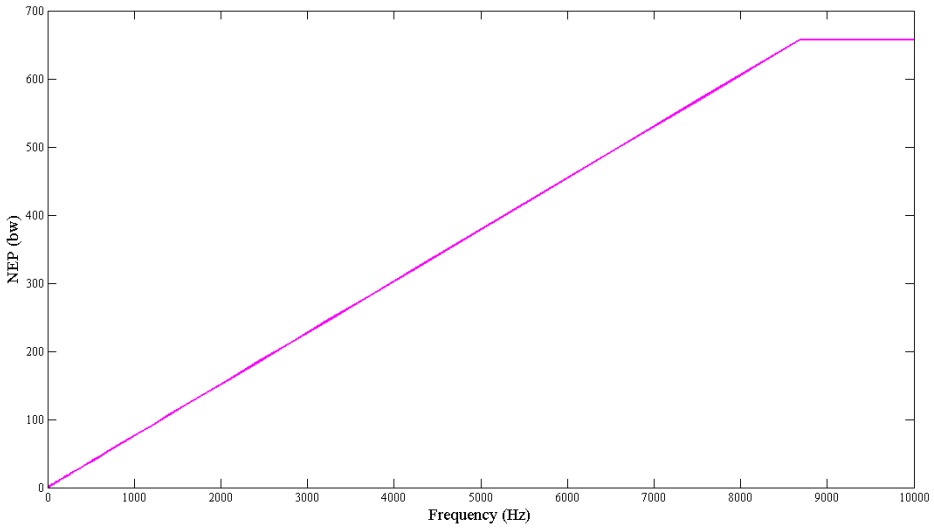

Figure 2.21 Noise equivalent power according to frequency (Hz).

Figure 2.20 shows the results of the phase (deg) of AD 620 that have been obtained with HF2IS Impedance Spectrometer.

The conclusion is that the AD 620 has a more stable gain, ranged until 1 kHz, and give an excellent support for our measurement setup.

Besides, the graphic of Noise Equivalent Power (NEP) as a function of frequency (until 10 kHz) is presented in Figure 2.21.

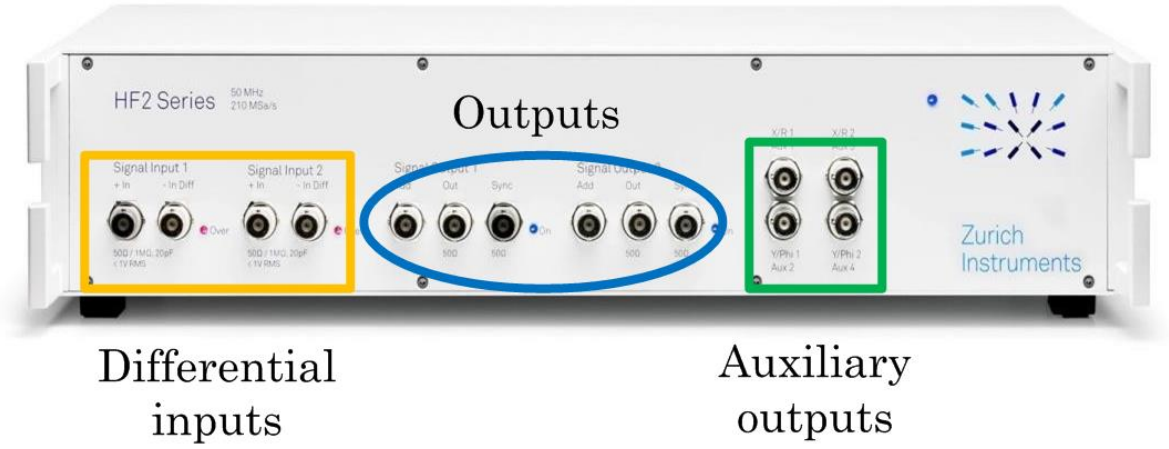

Figure 2.22 The schematic of the HF2IS Impedance Spectrometer.

The HF2IS Impedance Spectrometer has two different low noise frequency inputs and outputs, moreover the device has two other outputs (auxiliary). The schematic of the HF2IS Impedance Spectrometer (Zurich Instruments') is presented in Figure 2.22.

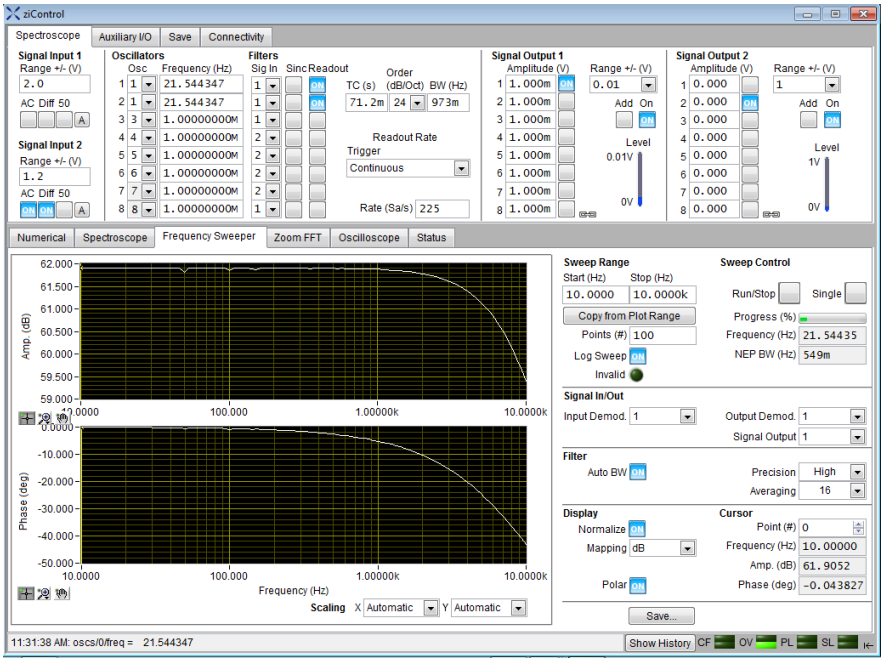

Figure 2.23 Interface program of the HF2IS Impedance Spectrometer.

Table 2.5 Technical specifications of the HF2IS Impedance Spectrometer [71].

Signal inputs frequency range	1 µHz - 50 MHz
Signal outputs frequency range	DC - 50 MHz
Input voltage noise	5 nV/√Hz
Input A/D conversion	14 bit, 210 MS/s
Input AC range	±1 mV to ±1.5 V
Filter slope (dB/Oct)	6, 12, 18, 24, 30, 36, 42, 48
Reference frequency resolution	0.7 µHz
Reference phase resolution	1.0 µ°

Due to two output signal generators, the alimented system of the Helmholtz coil can be directly generated without necessity of using the waveform generator. Some of the important specifications of the device HF2IS are shown in Table 2.5 [71] and an interface program of the HF2IS is presented in Figure 2.23. Furthermore, the HF2IS Impedance Spectrometer operates on the basis of a lock-in amplifier and can be used as impedance or lock-in amplifier. We use only the operation mode “lock-in”.

Summary of the principle of the digital lock-in amplifier

The output signal is generated internally by a frequency generator and then transmitted at the output, passing by a digital to analog converter, and an amplifier. It serves as a reference and excitation signal for the system to characterize. The system's response is then measured by means of the analog inputs. Each input is composed of an amplifier, an anti-aliasing filter with 50 MHz cutoff-frequency and an analog to digital converter.

The digital input and output signals are then multiplied and integrated. This action allows determining mathematically the gain and phasing shift between its two signals, while filtering out signals of other frequencies. The function diagram and additional features of the HF2IS Impedance Spectrometer are given in Annex 1.

Additional features of the amplifier:

- Each input can be used in single input or differential.
- Each output has an additional input, and a synchronization output.
- An ability to generate a multifrequency signal (up to 8 frequencies multiplexed).
- A spectrum analyzer with FFT (Fast Fourier Transform).
- A digital oscilloscope.

2.4 Characterization of the giant magnetoresistance sensors

2.4.1 GMRI sensor's characterization

2.4.1.A Determination of the sensitivity value for different magnetic flux densities between two GMR elements

As noted in previous part, this model of sensor has two sensing elements at the top and at the end of needle with 75 µm×75 µm dimensions for each GMR element.

The power supply is important part to safe each electronic equipment, therefore it is extremely important to realize this configuration carefully. The power supply configuration and the measurement setup of the GMR sensor is presented in Figure 2.24.

The Helmholtz coil is alimented by a variable gain amplifier through a two serial transformers, the amplifier stage produces a phase shift of the signal.

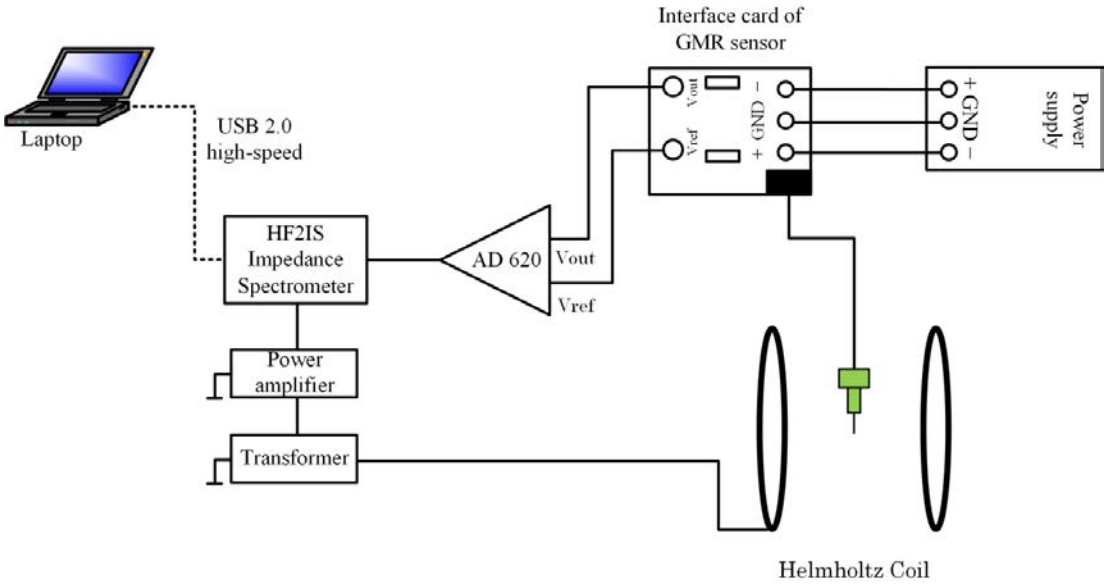

Figure 2.24 Measurement setup of the GMR sensor.

As shown in Figure 2.24, two PCB terminal blocks embedded into interface card of the GMR facilitate changing the value of circuit resistance and allow to find the appropriate amount of resistance, needed to protect the GMR sensor and to have the highest sensitivity.

In this experience, we have used different resistances in the interface card to find the maximum value of sensitivity and to protect the sensor. In other words, the resistances are added to adjust the bias current of a power sensor which fixed in ± 6 V for all GMR sensor types. The optimal experimental result was obtained for 809 Ω resistances (the value of resistances is measured with a LCR meter model HP 4284A). The schematic circuit of power supply of the GMR sensor with the two resistances is presented in Figure 2.25.

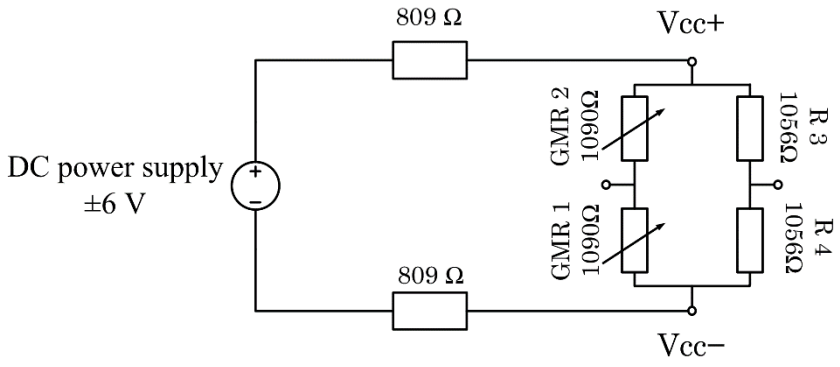

Figure 2.25 Power supply circuit by use two additional resistors.

The operating frequency of exciting field of the Helmholtz coil is 60 Hz and the input voltage generated with the HF2IS ranges from 1mV to 200 mV, the magnetic flux density (B) ranges from 1.3 µT to 252 µT.

The nonlinearity of this bridge circuit may be neglected due to the small range of variation of the resistance of the sensing element. The vérifaication this statement was made in the caratérisation part of the sensor.

The Fast Fourier Transform (FFT) of HF2IS allows determining the frequency of a discrete signal, representing the signal in the frequency domain. The GMR sensor output voltage (Vout−Vref) and FFT result are presented in Figure 2.26 (a) and (b).

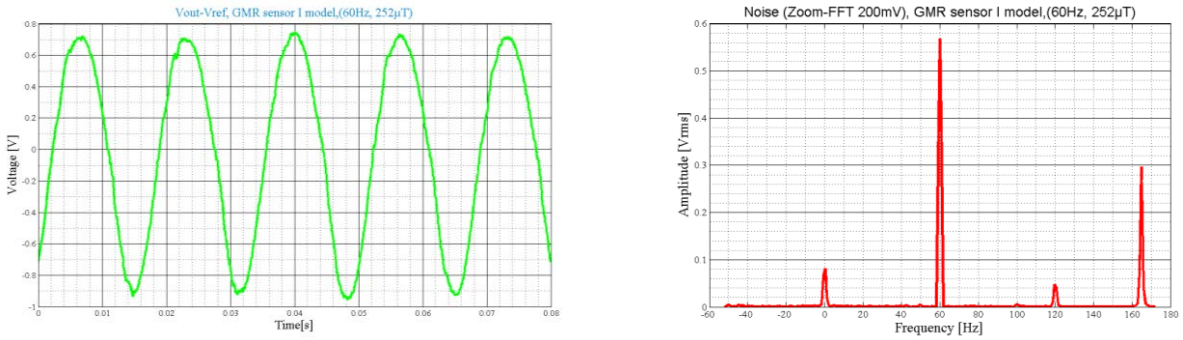

a) b)

Figure 2.26 The output voltage (V) of first model (a) and the FFT detection from (Vout−Vref) of the GMR sensor at 60 Hz (b).

We define the sensitivity of the GMR sensor is considering the output voltage (Vout−Vref) as a function of the total magnetic flux density (B) that affects both GMRs, we obtained results presented in Figure 2.27.

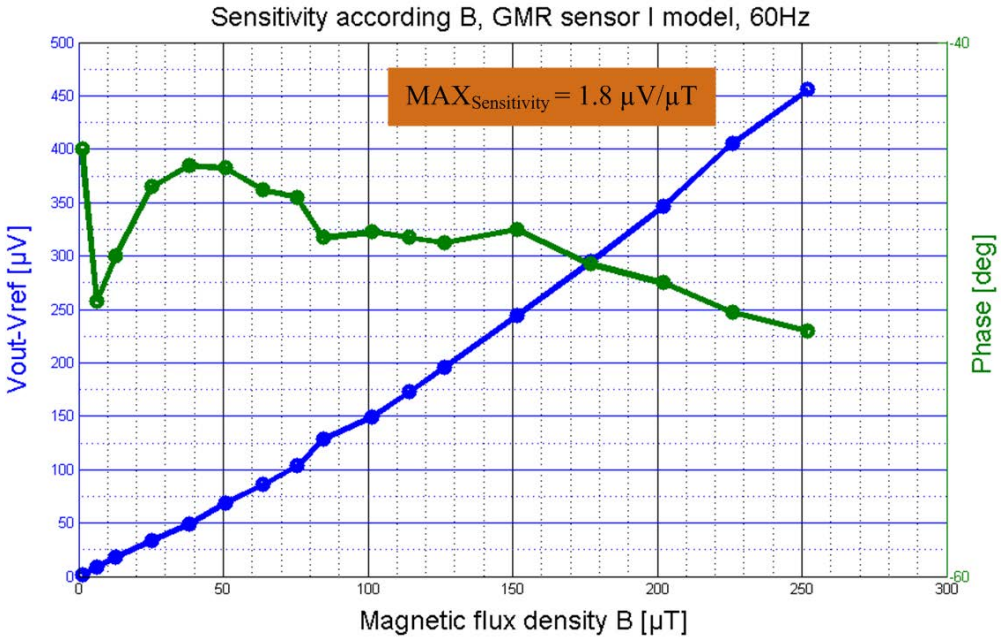

Figure 2.27 The output voltage (µV) and phase calculation (deg) with two resistors (809 Ω) as a function the total changes magnetic flux density B (µT).

The maximum value of sensitivity obtained from this step is 1.8 µV/µT, but this value is not correct, because the magnetic flux densities are different for each sensing element. To estimate the magnetic flux density (B_1 and B_0) for each GMR, we used the finite element analysis in software program Comsol 4.0. As shown in Figure 2.28, we have chosen two points, one is at the exactly midpoint (0, 0, 0) of Helmholtz coil where GMR 1 is placed and second point is 30 mm (30, 0, 0) upper than the first point (where GMR 2 is located) in X-axis. Furthermore, we have used other simulation method to confirm the results obtained with the first simulation (two points). At this stage, we have selected the strip with length 30 mm (proportional to the size of needle) in X-axis (Figure 2.29) to check the variation of magnetic flux density along the needle of the GMR sensor.

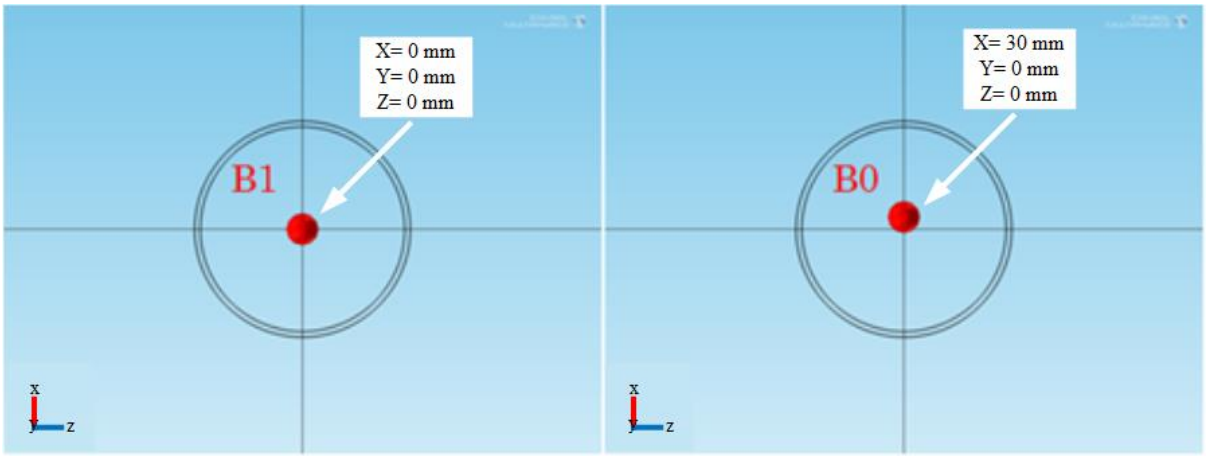

Figure 2.28 Calculation of the magnetic flux density for two points (B_1 and B_0).

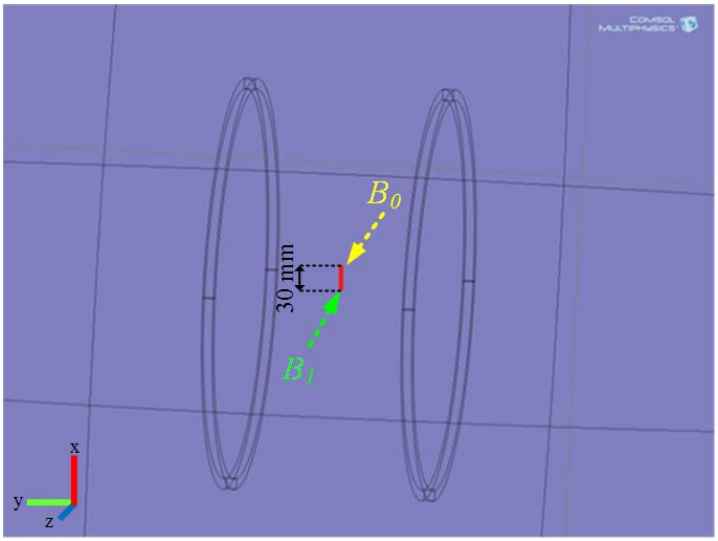

Figure 2.29 Calculation of the magnetic flux density (B) along the needle of sensor.

The results achieved with two simulation methods confirm each other. We observe from Figure 2.30 (a), that the results for different values of B (T) are linear along the sensor's

needle. But if one zoom the curve of each obtained result, we notice that they have the difference in magnetic field between two points, as shown in Figure 2.30 (b). The distance between the points B_0 and B_1 is very small compared to the size of the complete simulated system. The number of mesh between B_0 and B_1 is limited to 5 because of hardware limitations (an extremely fine mesh does not provide a good convergence during simulations).

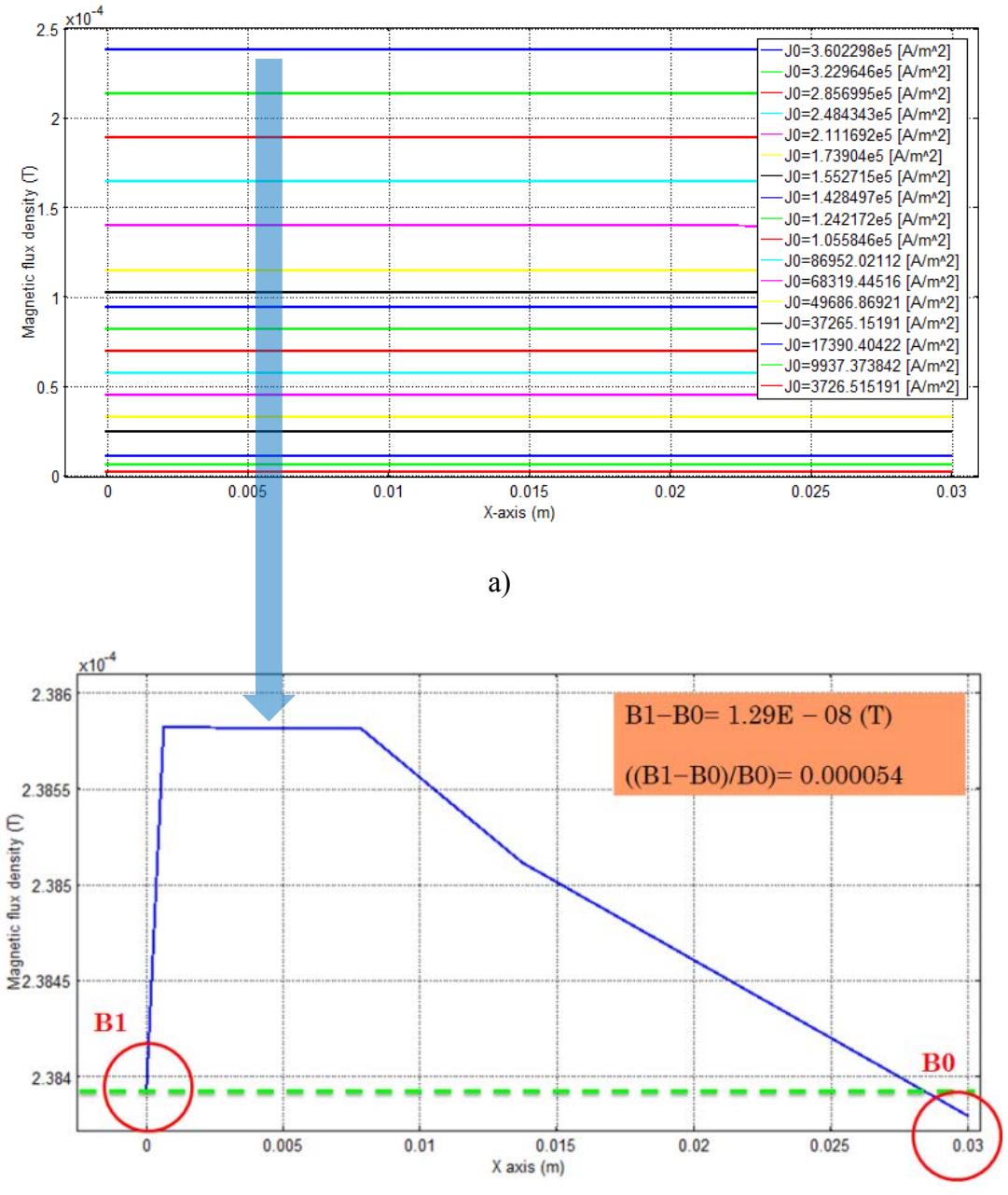

Figure 2.30 Distribution of the magnetic flux density (T) along the needle of sensor (a), zooming on a curve of the figure 2.30 (a) which presents the difference B between two GMR (b).

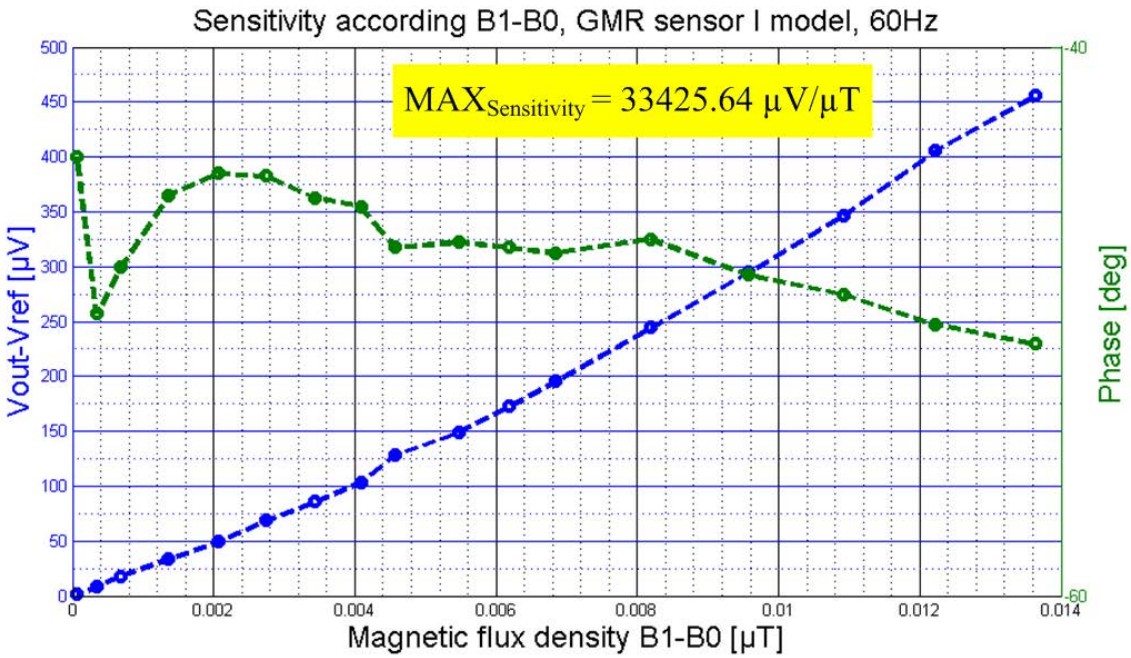

Figure 2.31 The output voltage result by GMR sensor I (µV) and phase calculation (deg) with two resistors (809 Ω) as a function of different magnetic flux density (µT) between two sensing elements GMR.

According to the different magnetic flux densities between two GMRs, one can observe in Figure 2.31 that the maximum value of sensitivity changes is noticeable and equal approximately to 33 426 µV/µT. The precision of the phase is very low, because the magnetic field is very small and the phase variation, perhaps, provokes incertitude's measuring device.

However, these results of sensitivity cannot be considered as final and exact ones, because the sensitivity should be in contact only with the one of the sensing elements for example for first GMR (B_1) that is placed at the top of the needle with magnetic flux density in the center of coils and second GMR (B_0) should stay completely out of magnetic field. In order to complete this task, we have designed and built smaller coils.

2.4.1.B Sensitivity's determination by individual variation of magnetic flux density for each GMR element

The main goal of this part is to characterize more accurately the GMRI sensor. For this reason and as explained in the previous part, we should create the uniform magnetic flux density only for one sensing element of the sensor. In order to complete the task, we have fabricated small Helmholtz coil that consists of two coils with 18 mm diameter and 9 wire turns. The technical data sheet of copper wire that was used for small coil is detailed in Table 2.6.

Table 2.6 Specification of wire's coil.

Reel Length	70 m
External Diameter	1 mm
Maximum Current	1.21 A
Conductor Material	Copper
Insulator Material	Polyurethane
Conductor Area	0.79 mm²

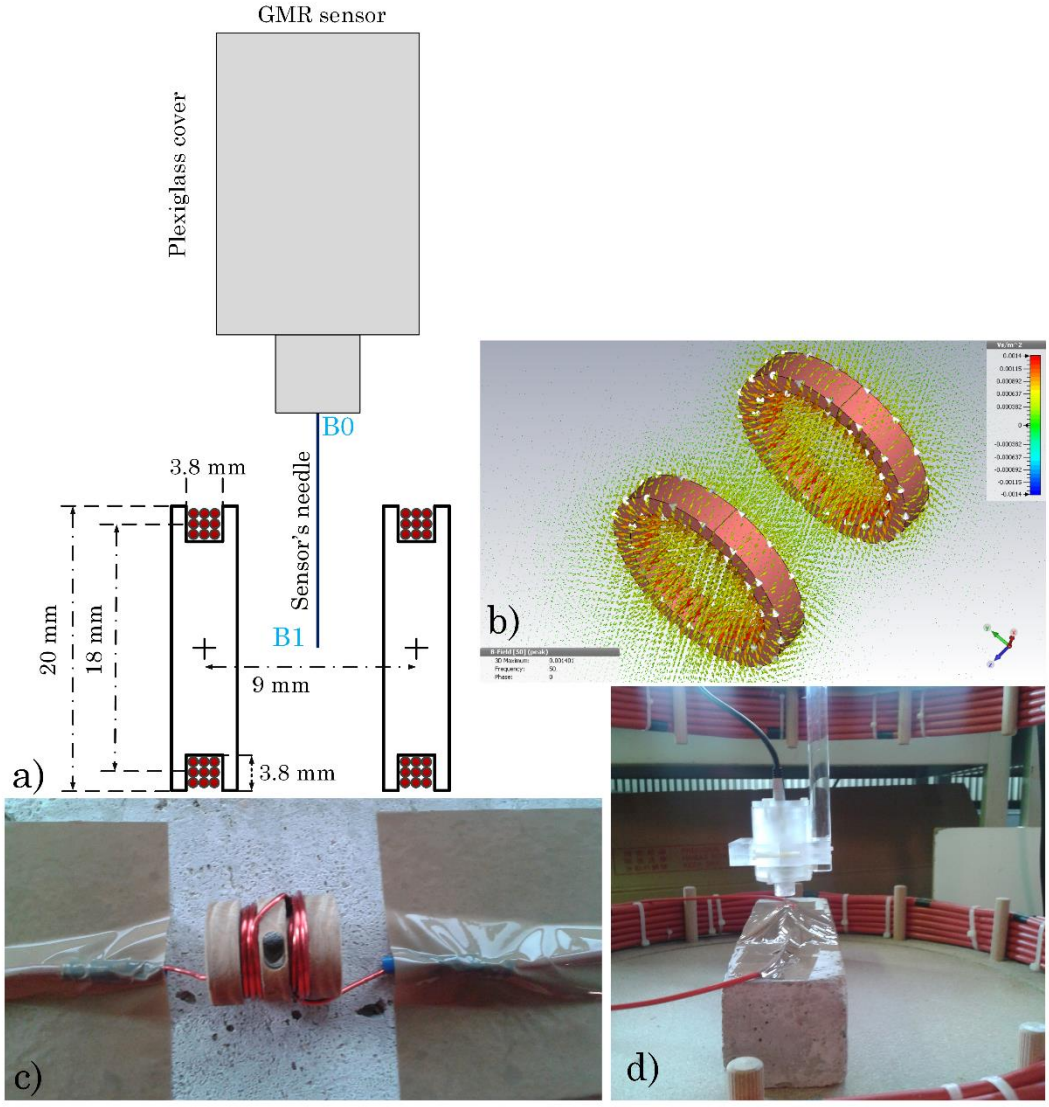

Figure 2.32 Schematic and actual images of small Helmholtz coil (a, c), uniform magnetic flux density simulated with CST (b), placing the sensor at center of coil (d).

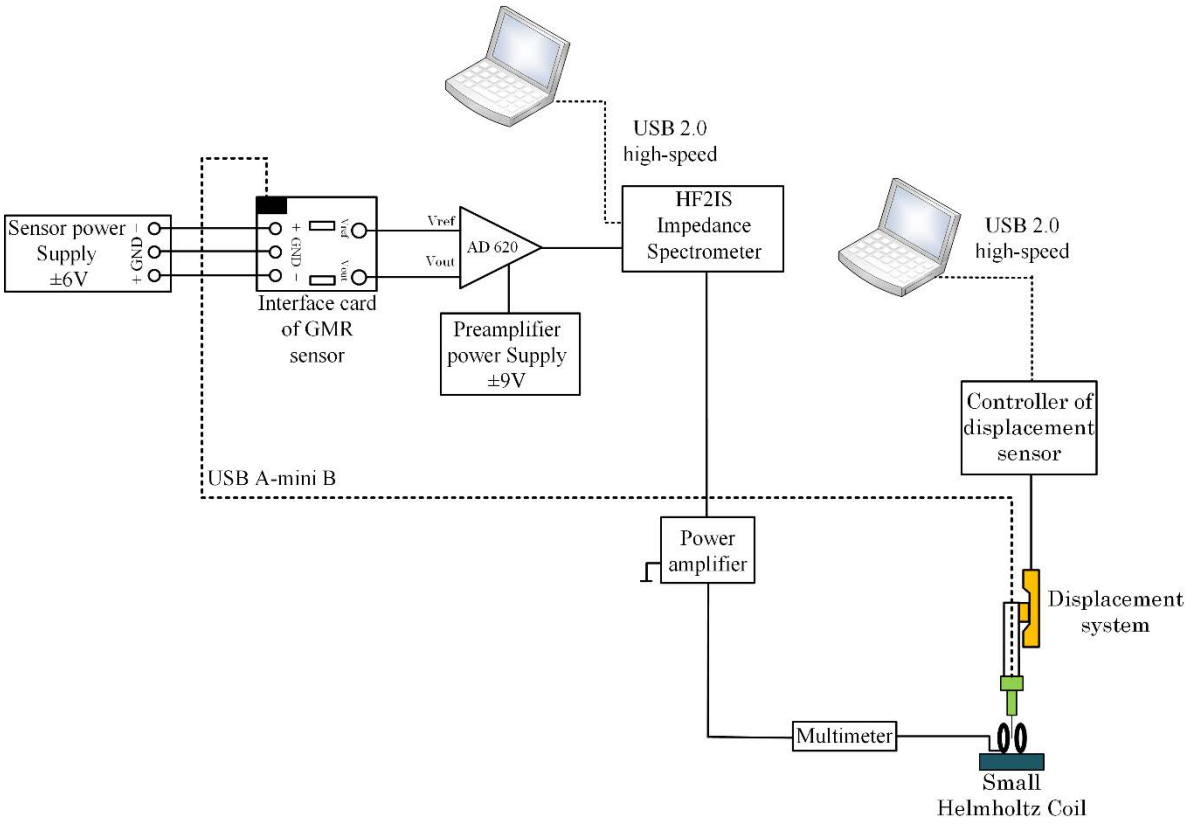

Figure 2.33 Measurement setup for sensor characterization.

The distance between two coils is sufficient to enter the needle's sensor. Thanks to the displacement system, we have the ability to insert the thin needle carefully and progressively at the center of the small Helmholtz coil which has the uniform magnetic field. Figure 2.32 (a) shows the small Helmholtz coil's structure. 3D simulation of uniform magnetic field distribution in the center of coils obtained by Computer Simulation Technology program (CST®) is presented in Figure 2.32 (b). An image of the coils when the needle sensor is inserted is presented in Figure 2.32 (c) and (d).

The experimental setup for the GMR characterization is presented in Figure 2.33. The measurement setup is controlled by two laptops, first to conduct the displacement system and second to control the HF2IS impedance Spectrometer as well as to store measurement data, obtained by the GMR sensor.

GMR sensor I is connected to DC power supply (±6 V) by a circuit interface. Differential signal (Vout−Vref) was supplied to the preamplifier AD 620 where output signal is strengthened approximately 1200 times (62 dB) and after submitted to HF2IS Impedance Spectrometer. The output data (Vrms, phases [deg]) of the GMR signal were recorded using HF2IS Impedance Spectrometer.

The small Helmholtz coil is powered by a variable gain amplifier with a signal generated by the spectrometer. The HF2IS Impedance Spectrometer allows to directly supply the Helmholtz coils through two output signal generators. Between power amplifier and the small Helmholtz coils we have put a multimeter to check the current in the coil in order to protect it. The operating frequency of exciting field of the Helmholtz coil is 60 Hz. By changing the value of input voltage (mV), the magnetic flux density (B) has been switched approximately from 5 µT to 410 µT. These results have been obtained by 3D gauss/teslameter 460 three-channel Hall effect (AC RMS accuracy is ±2% and AC frequency range is 10 Hz to 400 Hz ; Lakeshore company) [72].

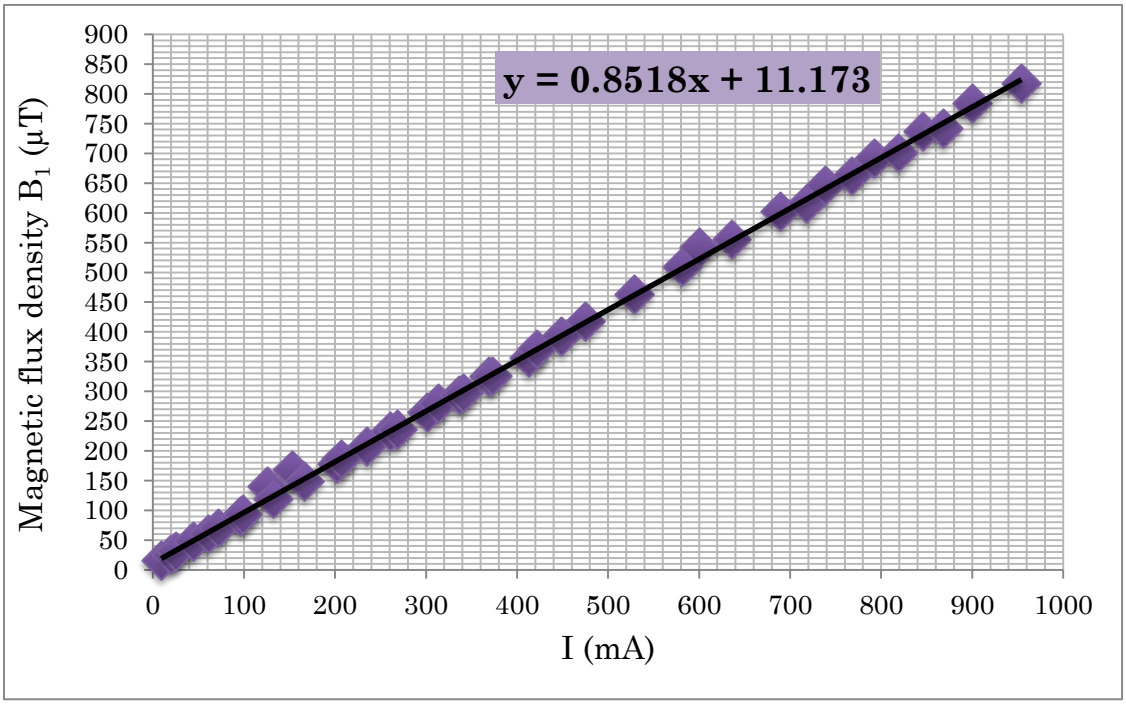

Figure 2.34 Measurement the magnetic flux density B_1 (µT) as a function of the input current (mA) applied to 60 Hz.

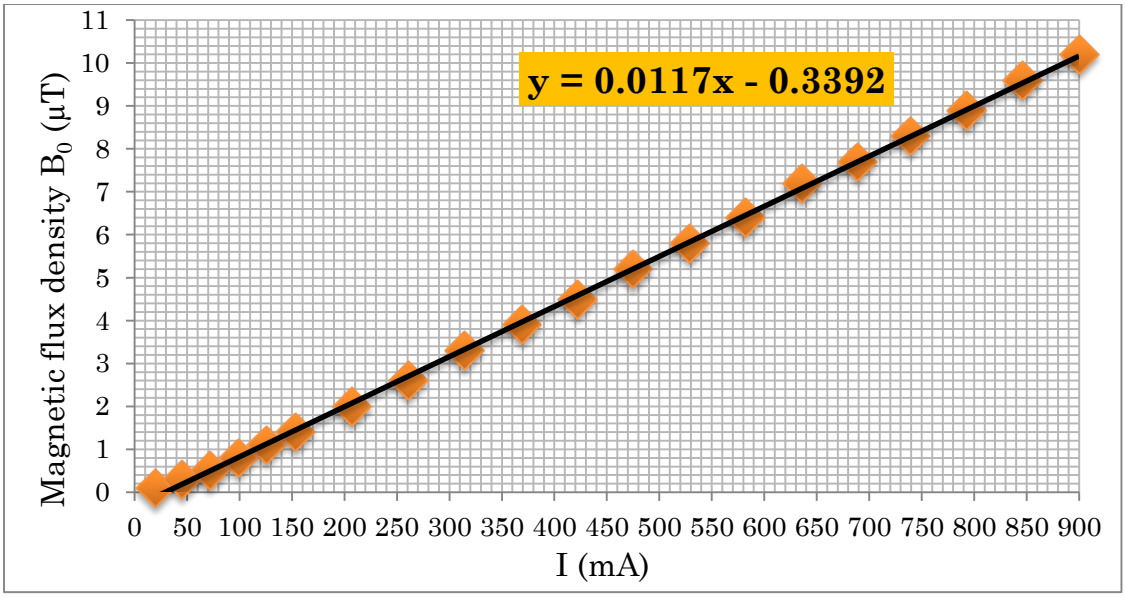

Figure 2.35 Measurement the magnetic flux density B_0 (µT) as a function of the input current (mA) applied to 60 Hz.

Figure 2.34 presents the experimental results obtained by gaussmeter of the magnetic flux density B_1 (µT) as a function of input current (mA) in center of small Helmholtz coil where the first sensing element has been placed. Furthermore, for more accurate calculation, a weak magnetic flux density (B_0) that influences second sensing element was measured with gaussmeter. In this method the gaussmeter probe is located at a distance of 30 mm (where second sensing element will be placed) from small Helmholtz coil's center, the measurement results of variation of B_0 as a function of current power supply are shown in Figure 2.35.

Different resistances values for the interface card of the GMR sensor have been tried in order to obtain the best sensitivity. It was found that the top choice to get high sensitivity is to use two additional 809 Ω resistors for a magnetic flux density equal approximately to 9 µT. Figure 2.36 presents the experimental results to find the best sensitivity values of the GMR needle probe sensor for different resistances.

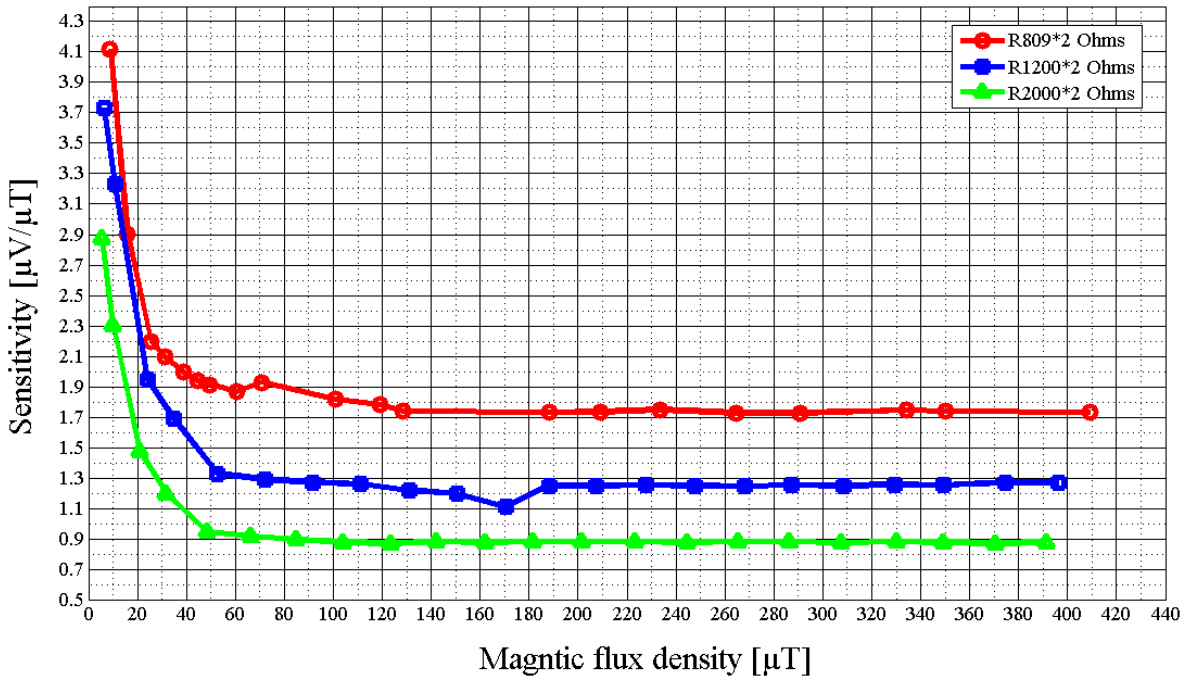

Figure 2.36 The relationship between sensitivity (µV/µT) and changes of the magnetic flux density (µT) by using several resistances in the interface card of the GMR sensor I.

Table 2.7 shows the experimental results attained with each resistance value, and presents the magnetic flux density (B_1-B_0) range to have the maximum sensitivity. The sensitivity curve of the sensor measured with two 809 Ohms resistances is presented in Figure 2.37.

Table 2.7 Experimental results achieved with different resistance values to characterize the GMR sensor I.

Resistor's value (Ω)	I_{in} Sensor (mA)	V_{in} Sensor (V)	Maximum sensitivity (µV/µT)	Magnetic flux density B_1-B_0 (µT)
2×2000	2.354	2.584	2.87	5.42
2×1200	3.430	3.766	3.73	6.25
2×809	4.418	4.851	4.12	8.87

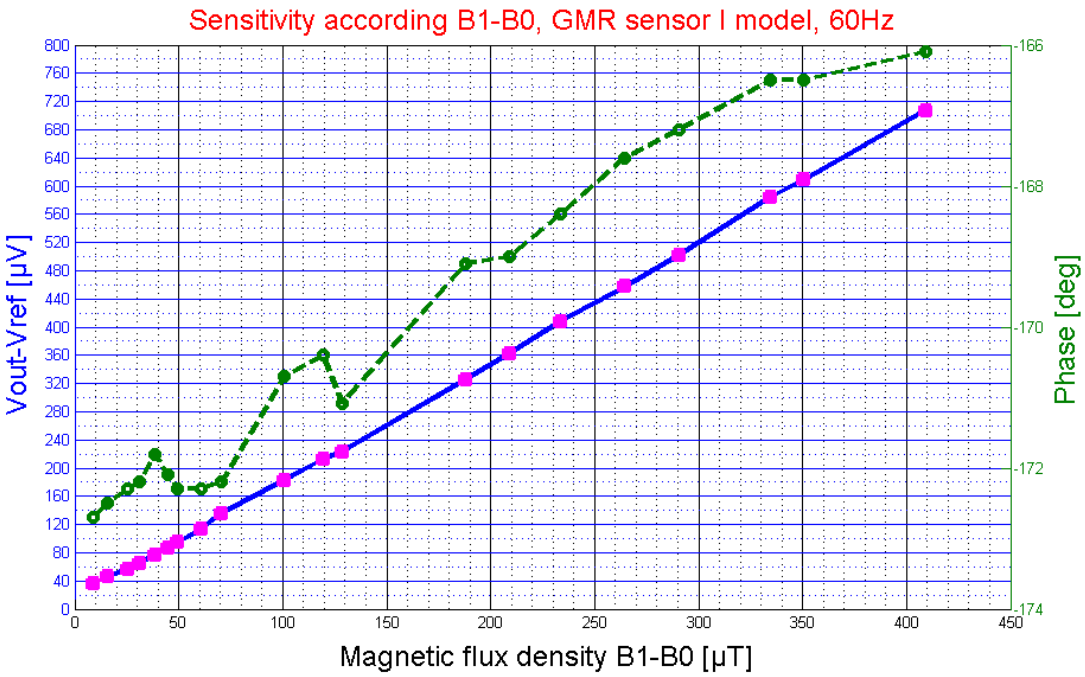

Figure 2.37 Output voltage (µV) and phase calculation (deg) with two resistors 809 Ω as a function of the total changes magnetic flux density B_1-B_0 (µT).

Measurement of the variation values of R in the Wheatstone bridge of the GMR sensor first model:

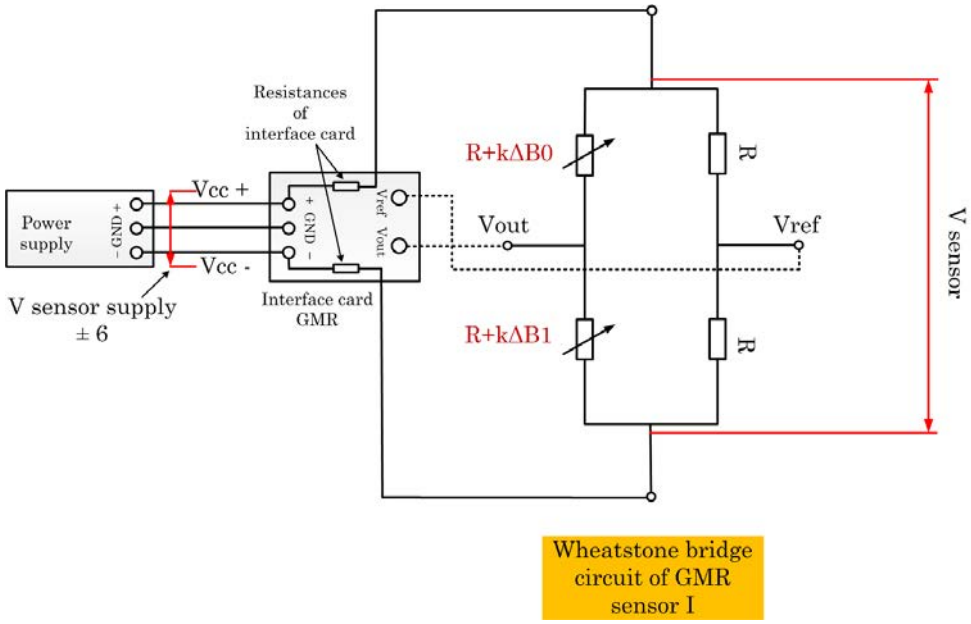

Figure 2.38 Electrical schematic and the Wheatstone bridge circuit of the GMR sensor I.

Figure 2.38 presents the connection schematic of the GMR sensor I. The total resistance value in the Wheatstone bridge of the GMR sensor is equal to 1098 Ohms. If we assume that the magnetic flux density for the second sensing element is absent (B_0=0), the output signal (Vout−Vref) of sensor can be determined by:

$$V_{out} - V_{ref} = V_{sensor} \times \frac{R + k\Delta B1}{2R + k\Delta B1} \tag{2. 6}$$

Where, k is a variation the sensing element in Ω/T.

$$V_{sensor} = \frac{V_{\sup} \times R_{total}}{R_{total} + R_{card}} \tag{2. 7}$$

Annex 2 presents the experimental results of variation values of R, ΔR as a function of the magnetic flux density and ΔR compared with R total of the sensor (resistance variation in %), considering the usage of different resistances in power supply card of the GMR sensor.

The nonlinearity of this bridge circuit may be neglected due to the small range of variation in the resistance of the sensing element. Verification of this assertion was performed in the characterization part of the sensor.

As shown in Figure 2.39, the results are proportional to the value of magnetic flux density's changes in current ranges used in this measurement. In this case, the variation of R depends on the variation of magnetic field and does not relate to resistor's value which is used in the interface card of the sensor.

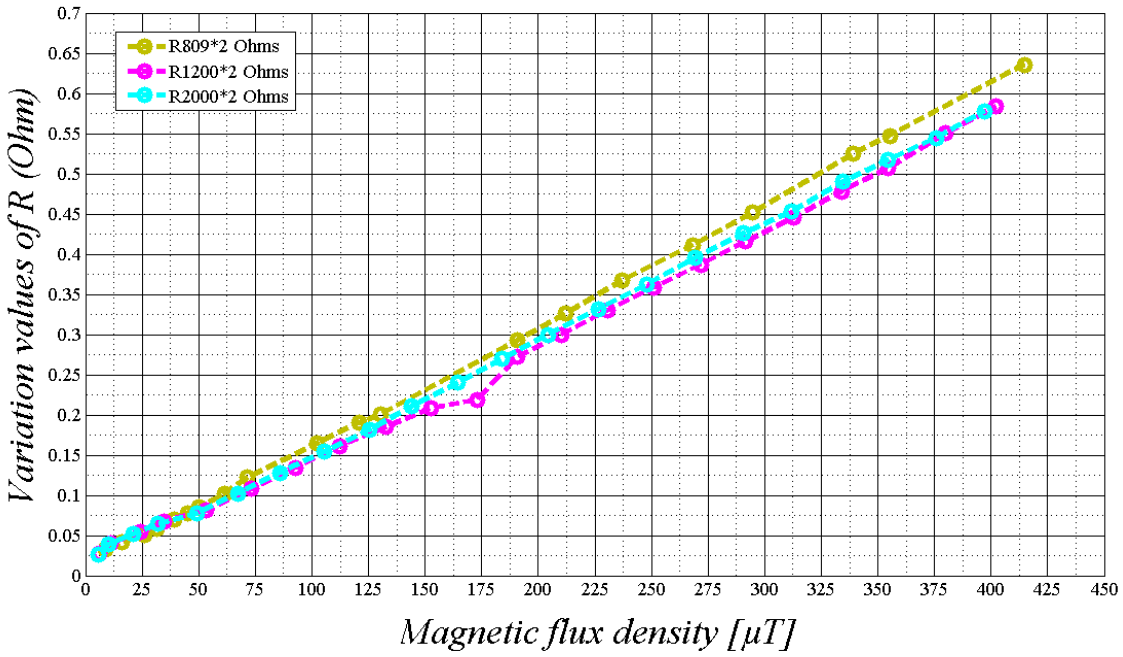

Figure 2.39 The values of ΔR according to magnetic flux density (µT).

Furthermore, according to the results, we conclude that the value of sensing element (GMR) sensitivity as a function of magnetic flux density (B) is equal approximately to 0.34 $\%mT^{-1}$.

2.4.2 Second GMR sensor's characterization

Figure 2.41 presents the measurement of the output signal variation of GMR sensor in X, Y and Z axes. While performing the measurement, the sensor was placed at the center of the Helmholtz coil, the GMR sensor was connected to circuit interface (see section 2.2.1) to prevent and control the current, passing in the GMR sensor (for GMR type two is I_{max}=5 mA).

Differential signal Vout−Vref was supplied to the HF2IS Impedance Spectrometer. The data (Vrms, phases [deg]) of the signal was recorded using an interface program of the HF2IS Impedance Spectrometer. Besides, by interface program of this instrument we can see the output signal of the GMR sensor in oscilloscope of program and detect the noises of signal (FFT).

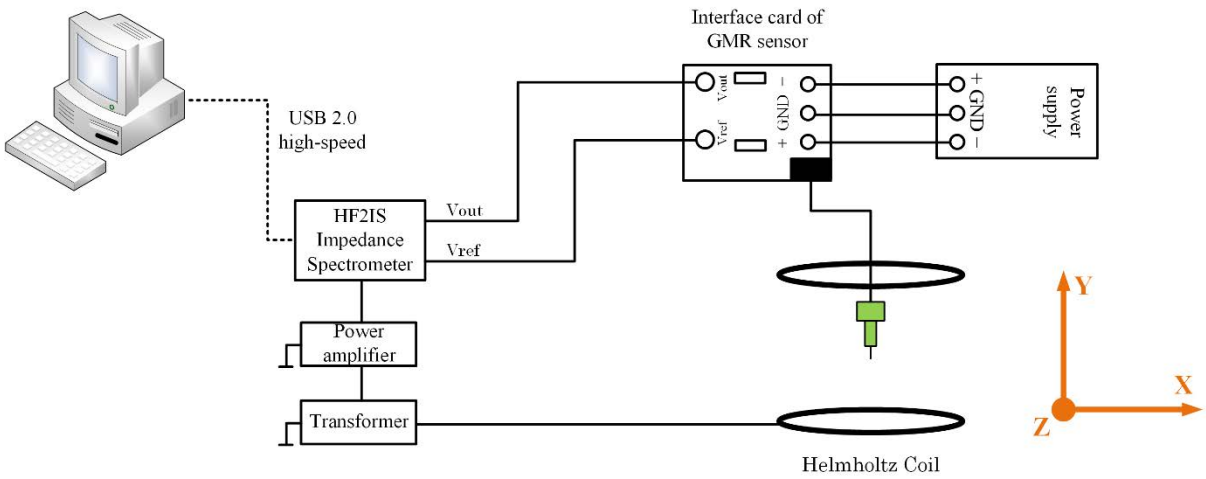

Figure 2.40 Measurement setup to characterize the GMR sensor.

The experiment frequency of exciting field of the Helmholtz coil is 60 Hz and the input voltage generated by the HF2IS Impedance Spectrometer is ranged from 5 mV to 200 mV. The magnetic flux density (B) was changed by varying the value of the input voltage (mV) approximately from 242 µT to 5.7 µT. These results have been obtained by using a field meter ESM-100 (Measuring range 1 nT–20 mT and 0.1 V/m−100 kV/m).

As explained earlier, the sensor output signals are very weak and the S/N ratio must be checked to verify the quality of the measurement. Figure 2.41 presents the output signal of the GMR sensor in X, Y, Z direction when sensor is placed in midpoint of the Helmholtz coil. The results obtained without lock-in filtering had visible parasite signals and offset in output of the GMR sensor. The lock-in filtering permits to eliminate the noising signals to obtain

good measurement of the GMR output signals. In Table 2.8 presents the output signal results (Figure 2.41), obtained with the GMR sensor in different positions of sensor.

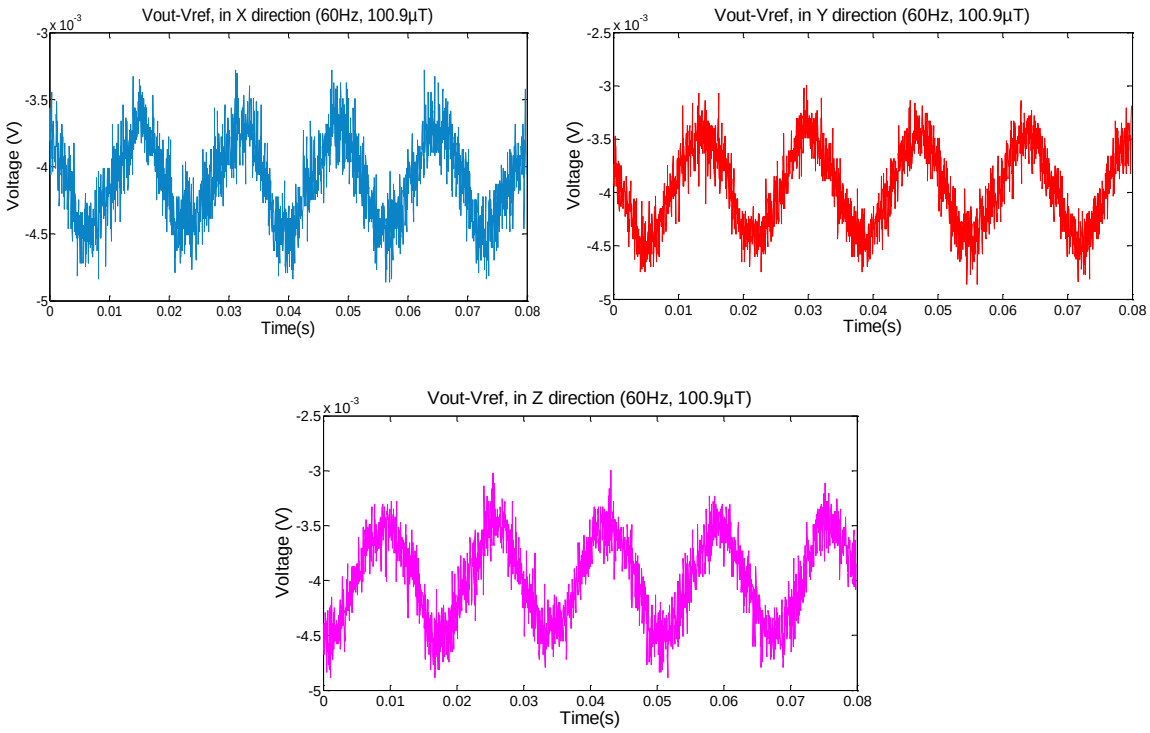

Figure 2.41 Output voltage (Vout−Vref) signals of the GMR sensor in direction (X, Y, Z) at a frequency 60 Hz with B= 100.9 µT.

Table 2.8 The output voltage of the GMR sensor in direction (X, Y, Z) at a frequency 60Hz.

Magnetic flux density (µT)	$V_{out}-V_{ref}$ (µV)	Phase (θ)	Direction of sensor
100.9	272	+125.5	X
100.9	340	+126.8	Y
100.9	362.8	+127.3	Z

Also as shown in the results, even using the HF2IS the output signals remain still associated with noise. Therefore, to improve signals, we have used the preamplifier AD 620 (the schematic is given in part 2.3.3) with gain approximately 1200 times (62 dB).

For all calculations with the GMR sensor or other type of biosensors, it is important to determine the value of sensitivity. Again, to find the best value of sensitivity, we used different resistances for the interface card of the GMR sensor. Furthermore, in order to calculate exactly the sensitivity of the sensor like it has been done in previous investigations, a uniform magnetic flux density (B_1) for the small Helmholtz coil should be created for first GMR element of the sensor.

We used the same setup as for the first model (see Figure 2.33) to characterize the GMR sensor, the difference is only the position of the small Helmholtz coil considering the sensitivity direction of the sensor model 2. The experimental results characterized the gain magnetoresistance needle probe show that to obtain the highest sensitivity of the GMR sensor only one resistance in circuit interface by value 2.128 kΩ should be used. Figure 2.42 shows the circuit schematic of sensor's power supply with one resistor (2.128 kΩ).

GMR sensor II is connected to DC power supply (±6 V) by circuit interface. Differential signal Vout−Vref was supplied to preamplifier AD 620 before to be applied to HF2IS Impedance Spectrometer. The output data of the GMR signal was recorded with interface program of the HF2IS Impedance Spectrometer.

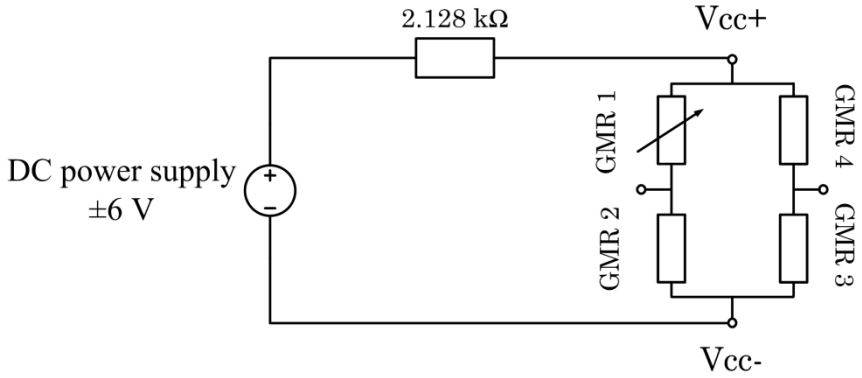

Figure 2.42 Power supply circuit with two additional resistors.

The small Helmholtz coil is supported by an amplifier (variable gain). Between power amplifier and small Helmholtz coil we have put a multimeter to check the passing current in coil and to protect its wire. The operating frequency of the exciting field of the Helmholtz coil is 75 Hz in order to be consistent with experiments made in chapter three by using Vibrating sample magnetometer's frequency. By changing the value of input voltage (mV), the magnetic flux density (B) has been switched approximately from 6 μT to 309 μT. These results have been obtained by 3D gauss/teslameter 460 three-channel Hall effect. Additionally, a weak magnetic flux density (B_0) that influences on the rest of sensing elements was measured with gauss/teslameter to increase the accuracy of calculations. We have placed the probe of teslameter at a distance of 17 mm from small Helmholtz coil's center to measure the variation of B_0.

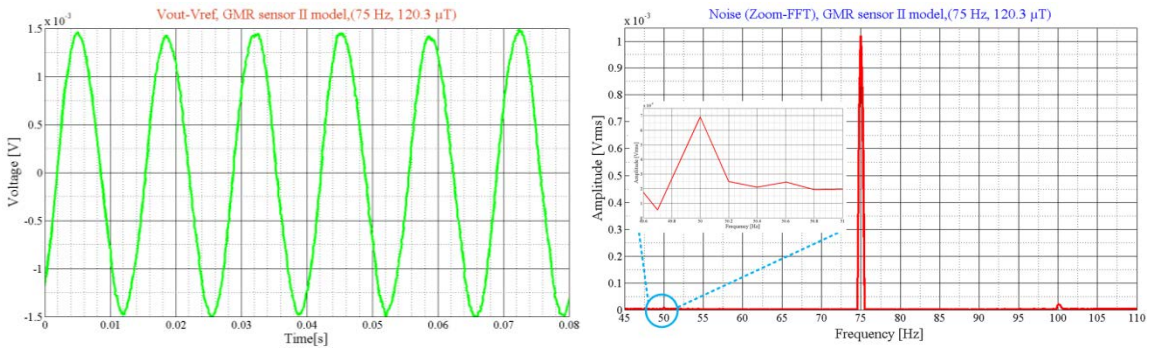

a) b)

Figure 2.43 The GMR sensor's output voltage (V) with 2.128 kΩ (a) and FFT detection from Vout−Vref of the GMR sensor for frequency 75 Hz (b).

Figure 2.43 (a, b) present the GMR sensor's output voltage (Vout−Vref) and FFT magnitude spectrum of the GMR sensor's output signal in frequency 75 Hz by one resistor (2.128 kΩ) in power supply circuit.

The experimental results for the sensitivity of the GMRII sensor with the use of several resistors are shown in Table 2.9.

Table 2.9 The experimental results obtained by the GMR sensor at a frequency 75 Hz with use the additional resistors in sensor's interface card.

Resistor's value (kΩ)	I_{in} Sensor (mA)	V_{in} Sensor (V)	Maximum sensitivity (µV/µT)	Magnetic flux density B_1-B_0 (µT)
1×2.128	4.37	2.68	8.51	130.23
1×2.710	3.61	2.21	3.5	226.23
2×2.148	2.44	1.50	2.53	270.83
2×1.190	4	2.46	3.65	208.62

As shown (Figure 2.44), the Vout−Vref (µV) is linear and proportional to change the value of magnetic flux density (µT).

The most appropriate way to obtain high sensitivity is to use one additional resistor in the interface card circuit by value 2.128 kΩ with magnetic flux density equal approximately to 130 µT. Figure 2.45 presents the experimental results to find the best sensitivity values of the GMR needle probe sensor with different resistances.

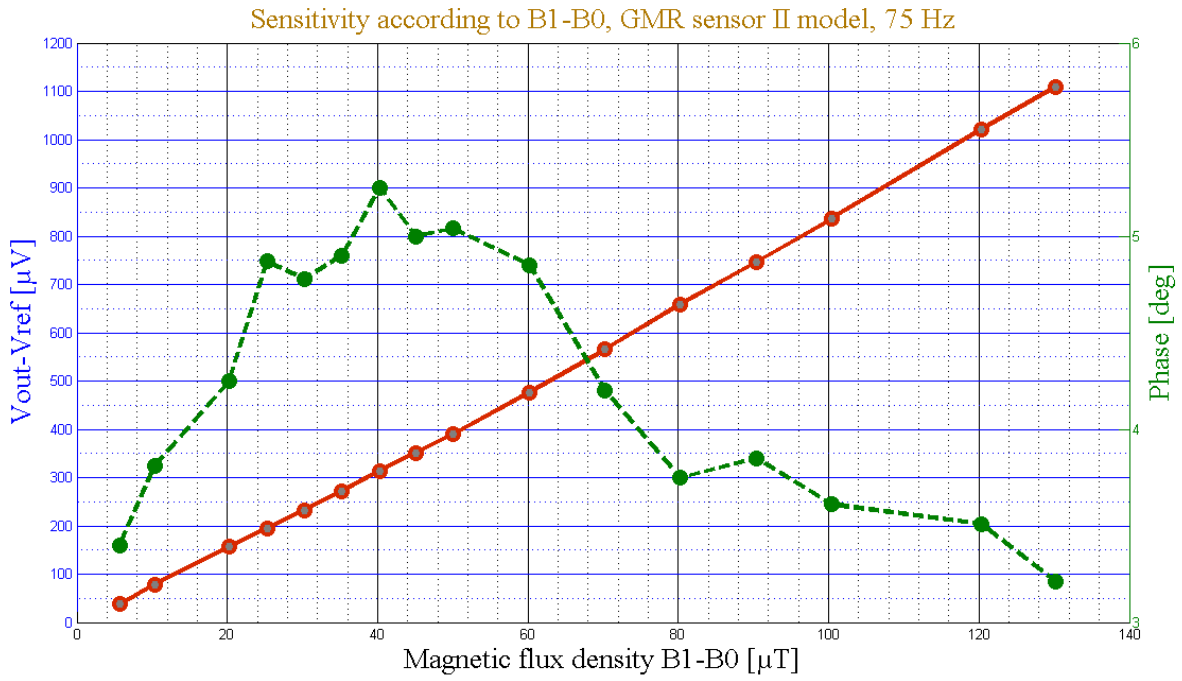

Figure 2.44 The output voltage results obtained by the probe GMR sensor (µV) and phase calculation (deg) with one resistor (2.128 KΩ) as a function of the changes in magnetic flux density (µT).

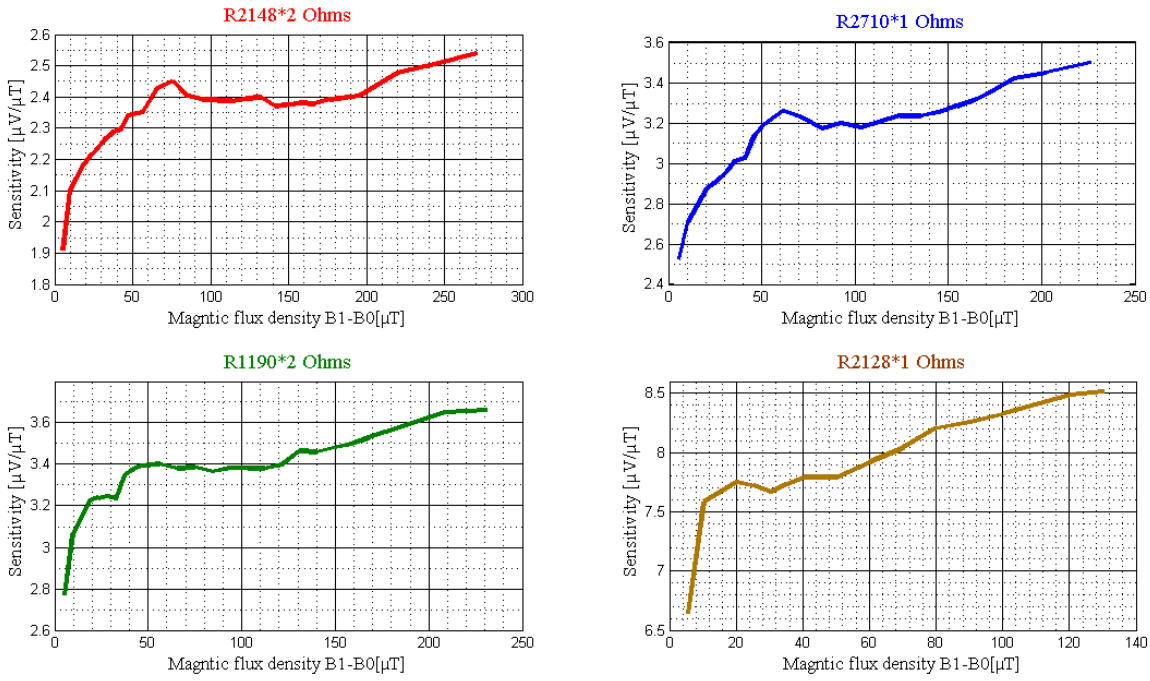

Figure 2.45 The relationship between sensitivity (µV/µT) and the magnetic flux density (µT) variations for different resistances values in the power supply card of the GMR sensor.

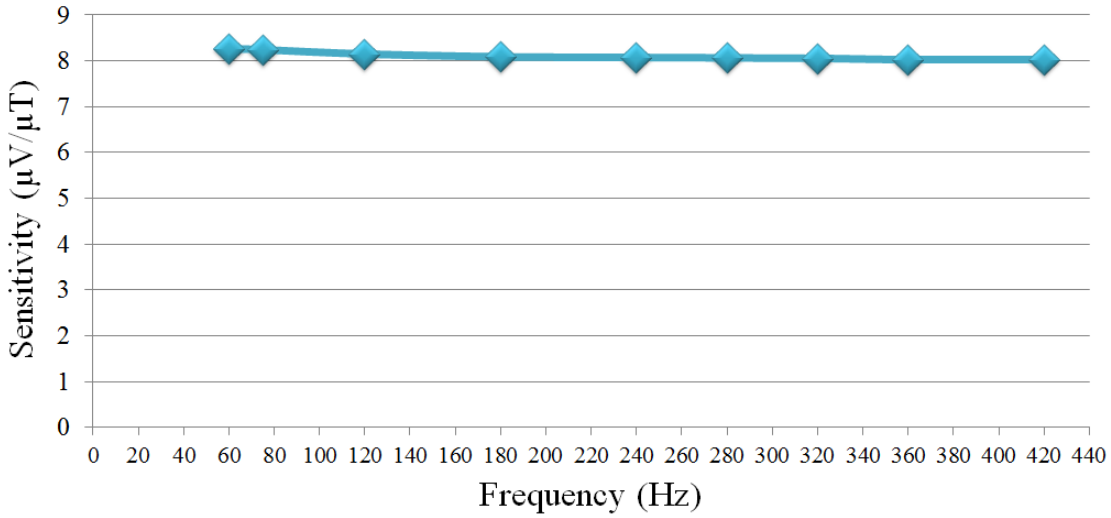

Figure 2.46 Experimental results obtained with GMR sensor to calculate the sensitivity as function of frequency (60 Hz − 420 Hz) with (B_1-B_0)= 87.6 µT.

Furthermore, the experimental results to determine the relationship between sensitivity as a function of frequency's changes have been done (see Figure 2.46). For this part of our measurements the value of magnetic flux density (B_1-B_0) was fixed at the level of 87.6 µT.

The results obtained by the GMR sensor demonstrate that the sensor's sensitivity in the different frequency range is constant. These experimental results have been done only until 420 Hz because of the frequency range limit of 3D gauss/teslameter 460 three-channel Hall effect device.

Variation of R in Wheatstone bridge of GMR sensor second model

As previously explained, the GMR needle type probe model two consists of four sensing elements, the first sensing element (GMR1) is at the tip of needle and the other sensing elements (3 GMRs) are at the end of needle, placed near the bonding pads. All sensing elements are connected to the Wheatstone bridge of the GMR sensor. The sensing elements at the tip and at the end of needle are equivalent to a potentiometer (ΔR+R) and they are used to detect the magnetic field (the sensing elements change the resistivity value once the magnetic field is present). It should be underlined that due to the low variations of the GMR sensing elements, we can consider global sensor's resistance as constant. The schematic of the GMRII sensor connection is presented in Figure 2.47.

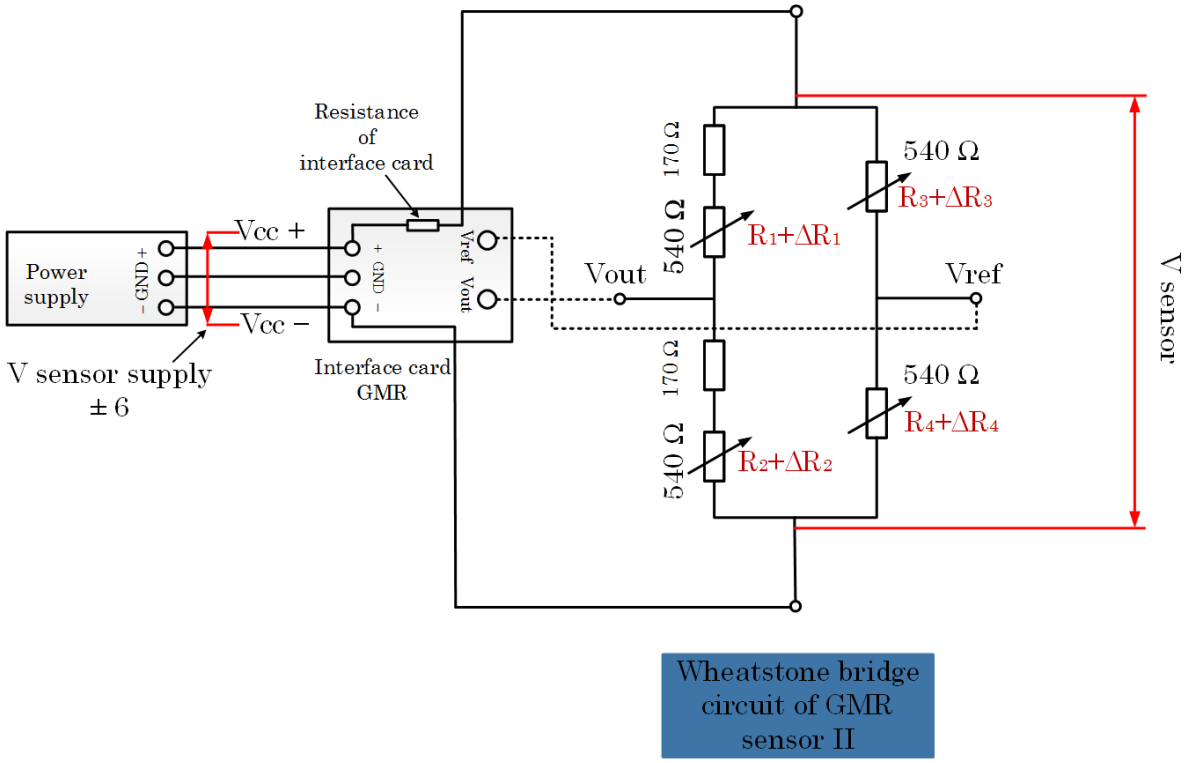

Figure 2.47 Schematic of the GMRII sensor (second model).

In this case the change of resistance in the Wheatstone bridge of the GMR sensor is described by the following expressions:

$$R_{GMR,i} = R_i + \Delta R_i \tag{2. 8}$$

$\Delta R_{2,3,4} = 0$, when magnetic flux density (B_0) =0

$$R_{total} = 613.44\Omega \tag{2. 9}$$

$$V_{ref} = \frac{V_{sensor} \times 540}{540 + 540} = \frac{V_{sensor}}{2} \tag{2. 10}$$

$$V_{out} = V_{sensor} \times \frac{170 + 540}{170 + 170 + 540 + R_{GMR}} = \frac{V_{sensor} \times 710}{R_{GMR} + 880} \tag{2. 11}$$

$$V_{measurement} = V_{out} - V_{ref} = V_{sensor} \times \frac{710}{R_{GMR} + 880} - \frac{V_{sensor}}{2} =$$
$$= V_{sensor} \times \left(\frac{710 \times 2 - R_{GMR} - 880}{880 \times 2 + 2R_{GMR}} \right) \Rightarrow \quad (2.\ 12)$$
$$V_{measurement} = V_{sensor} \times \left(\frac{540 - R_{GMR}}{1760 + 2R_{GMR}} \right)$$

R_{GMR} is thus determined from equation 2.13

$$R_{GMR} = \frac{540 \times V_{sensor} - 1760 \times V_{measurement}}{2V_{measurement} + V_{sensor}} \quad (2.\ 13)$$

When $V_{measurement}$ is equal to zero the R_{GMR} can be expressed as:

$$R_{GMR} = 540\Omega \quad (2.\ 14)$$

By using the one resistance in interface card of GMR sensor with value 2.128 kΩ the V_{sensor} can be estimated as:

$$V_{sensor} = \frac{V_{sup} \times R_{total}}{R_{total} + R_{card}} = 2.685\ \mathbf{V} \quad (2.\ 15)$$

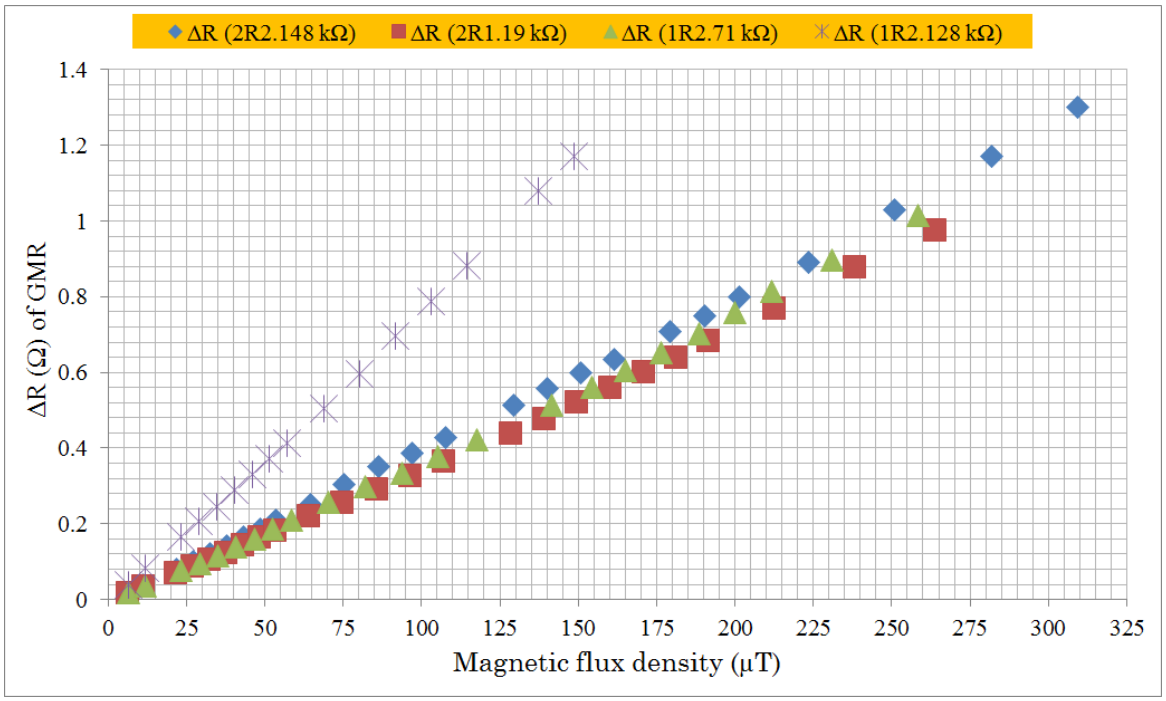

Figure 2.48 The values of ΔR according to magnetic flux density (μT) by several resistances in interface supply card of the GMR sensor.

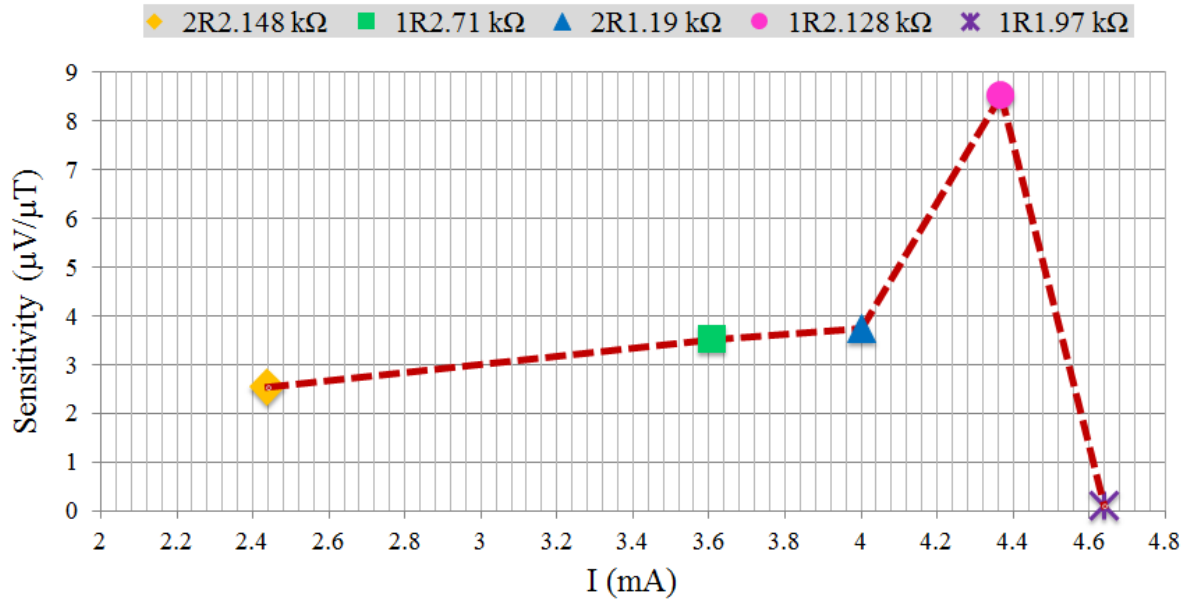

Figure 2.49 The relationship between sensor's sensitivity and its input current according to various resistances in interface supply card of the GMR sensor.

As it can be observed in the Figure 2.48, all results are proportional to the values of magnetic flux density. The exception is only resistance 2.128 kΩ where the sensitivity of sensor is around two times bigger than other resistances and sensor is near to saturation, whereas all other curves have similar slope. We can observe in Figure 2.49 that the sensitivity is proportional to the value of the bias current when it is less than approximately 4 mA. Beyond, and up to the maximum current is available by the GMR sensor (5mA). Furthermore, one can a sharp increase of the sensitivity for 4.37 mA (8.51 µV/µT) followed by a sudden attenuation for 4.64 mA (0.095 µV/µT).

Table 2.10 The Maximum GMR element sensitivity as function of magnetic flux density (B) obtained by GMR sensor II.

R (kΩ)	I (mA)	$\frac{\Delta R/R}{B}$ (mT^{-1})
2×2.148	2.44	0.779
1×2.710	3.61	0.727
2×1.190	4.00	0.685
1×2.128	4.37	1.459
1×1.970	4.64	0.661

This phenomenon can be explained by theoretical variation of R in a Wheatstone bridge of the GMR sensor that changes according to changing and presenting the magnetic flux density

in linear ranges. The different slope while using the resistance is equal to 2.128 kΩ due to the fact that bias current is out of the linear range. For each value of resistance (in interface card) the results of resistance variation of the sensor are approximately the same (Annex 3). Furthermore, according to the results obtained with the GMRII sensor, we conclude that the value of GMR element sensitivity as a function of B is approximately 0.71 $\%mT^{-1}$ for resistors in the linear part. The maximum of GMR element sensitivity (1.46 $\%mT^{-1}$) is reached for resistor 2.128 kΩ.

Table *2.10* presents these experimental results.

2.5 Structure and characterization of giant magnetoresistance sensor type III

Giant magnetoresistance sensor (GMR sensor) is fabricated on basis of GMR effect, in this effect the very thin layers (with thickness in a few nm) of ferromagnetic and non-magnetic alternately (parallel or an antiparallel) are repeated. The effect is observed if change an electrical resistance of the sample under the influence of a magnetic field. This effect exists when the resistance change does not exceed a few percent. But this slight change in resistance gives us a possibility to detect very weak magnetic field.

GMR's element GR01 is one of the elements which are fabricated by TDK® Company on the basis of GMR effect.

The GR01 consists on two GMR sensing elements placed in a mini chip. These two sensing elements are located oppositely one to each other (see Figure 2.51). This configuration of the two GMRs helps to increase sensitivity and to enhance the detection of the magnetic field in both directions. The mini chip has 3 pins connected to a power supply. The supplementary information of this chip and their components is confidential.

The GMR sensor type III has similar structure as shown for the GMR sensor type II, with difference that it is made up of a thicker needle if compared with the GMR sensor II.

The needle length of sensor is 30 mm, the GR01 is placed at the top of needle and connected in a Wheatstone half bridge configuration. This needle inserted in the cavity of magnetic liquid permit to measure their physical properties such as relative permeability (μ_r) and susceptibility (χ).

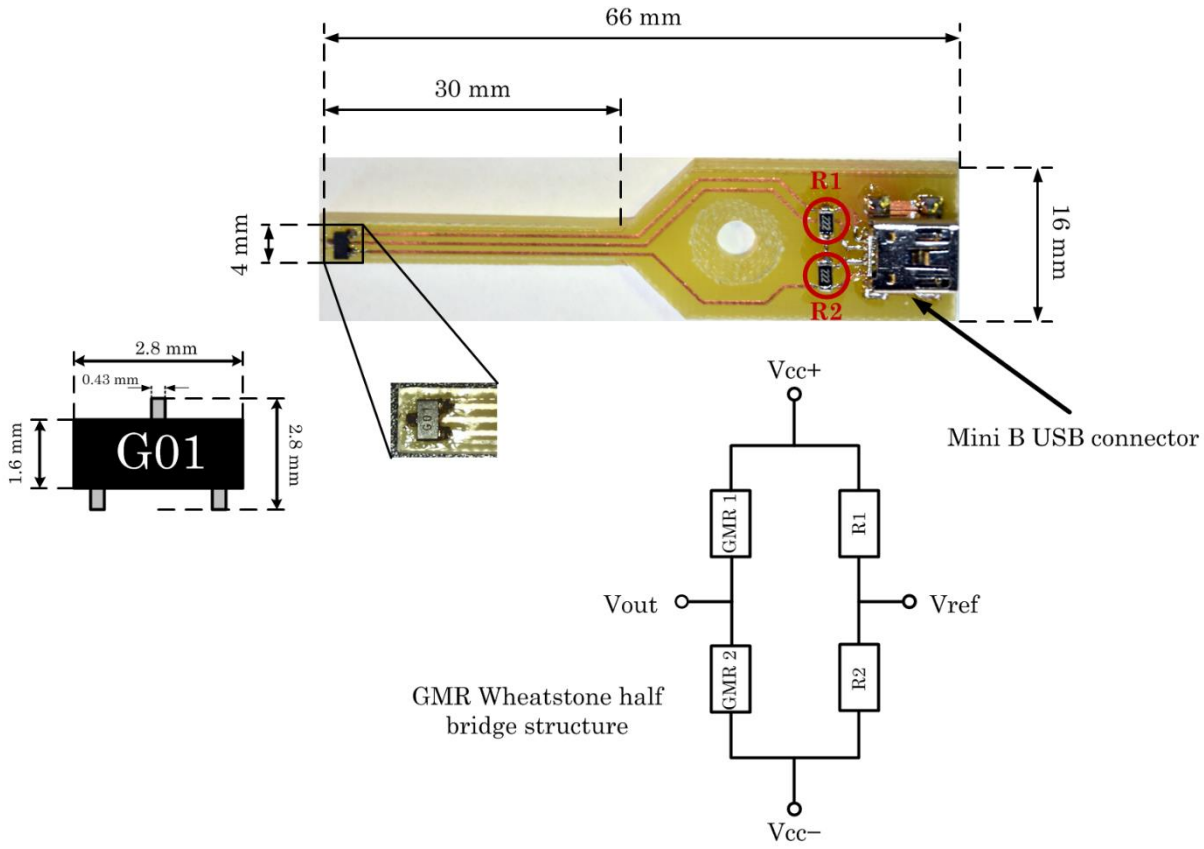

Figure 2.50 The design and components of the GMR sensor III.

The detection direction of the GMR sensor type III is collinear with the needle, this direction is important to position a Helmholtz coil. The schematic of the GMRIII sensor is presented in Figure 2.50.

The GMR sensor is supplied with a mini B USB that is placed at the end of the sensor and connected to DC power supply through an interface card. Furthermore, the maximum current of this type of the GMR sensor is 5 mA.

The pins details of the mini B−USB of the GMR sensor and references connection to G01 are presented in Table 2.11.

Table 2.11 Pins details of the mini B−USB.

Mini B USB Pins	Reference
1	Vref
2	Vcc_-
3	Vout
4	Vcc_-
5	Vcc_+

The Wheatstone bridge configuration of the GMR sensor permits to measure voltage variations induced by magnetic field with removing DC voltage part of GMR polarization. The resistance of the Wheatstone bridge should have approximately the same values as GMR elements, to have the same DC value of voltage in Vref and Vout. This configuration permits to directly amplify Vout−Vref without use of high pass filter for removing the DC component. The Wheatstone bridge configuration of the GMRIII sensor is shown in Figure 2.51.

The measurement setup is controlled by two laptops, one to conduct the displacement system and the second one to control the HF2IS impedance Spectrometer and to store measurement data, obtained by the GMR sensor.

The GMR sensor III through circuit interface card is connected to DC power supply (±6 V). Differential signal Vout−Vref (without any preamplifier) was submitted to a HF2IS Impedance Spectrometer. The output data (Vrms, phases [deg]) of GMR signal was recorded by interface program of HF2IS Impedance Spectrometer. The measurement setup for characterization of the GMRIII sensor is presented in Figure 2.52.

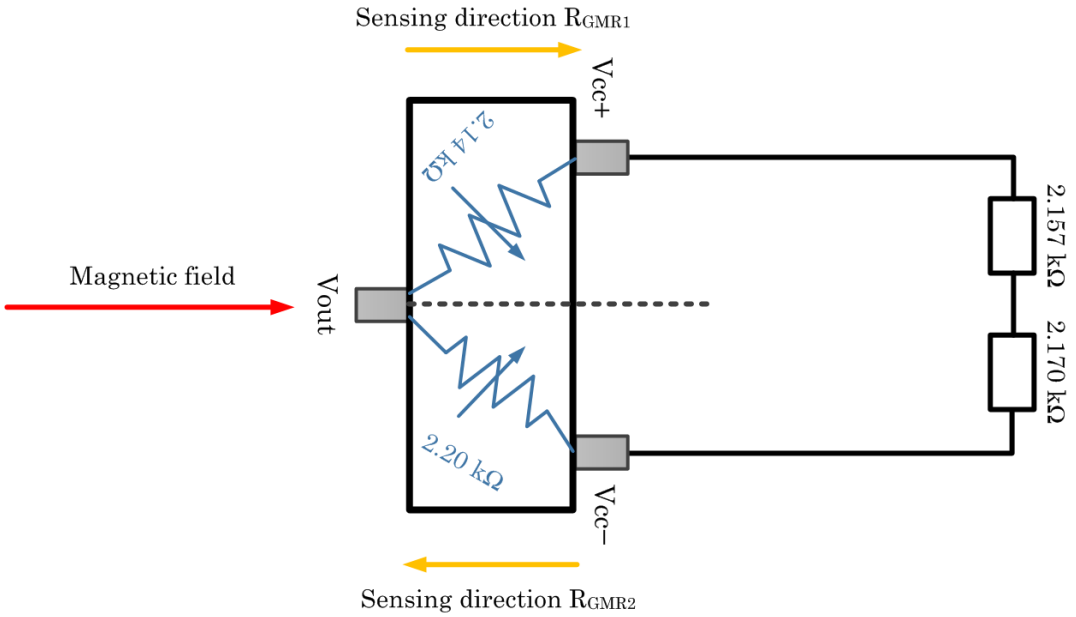

Figure 2.51 The Wheatstone bridge configuration of the GMR sensor type III.

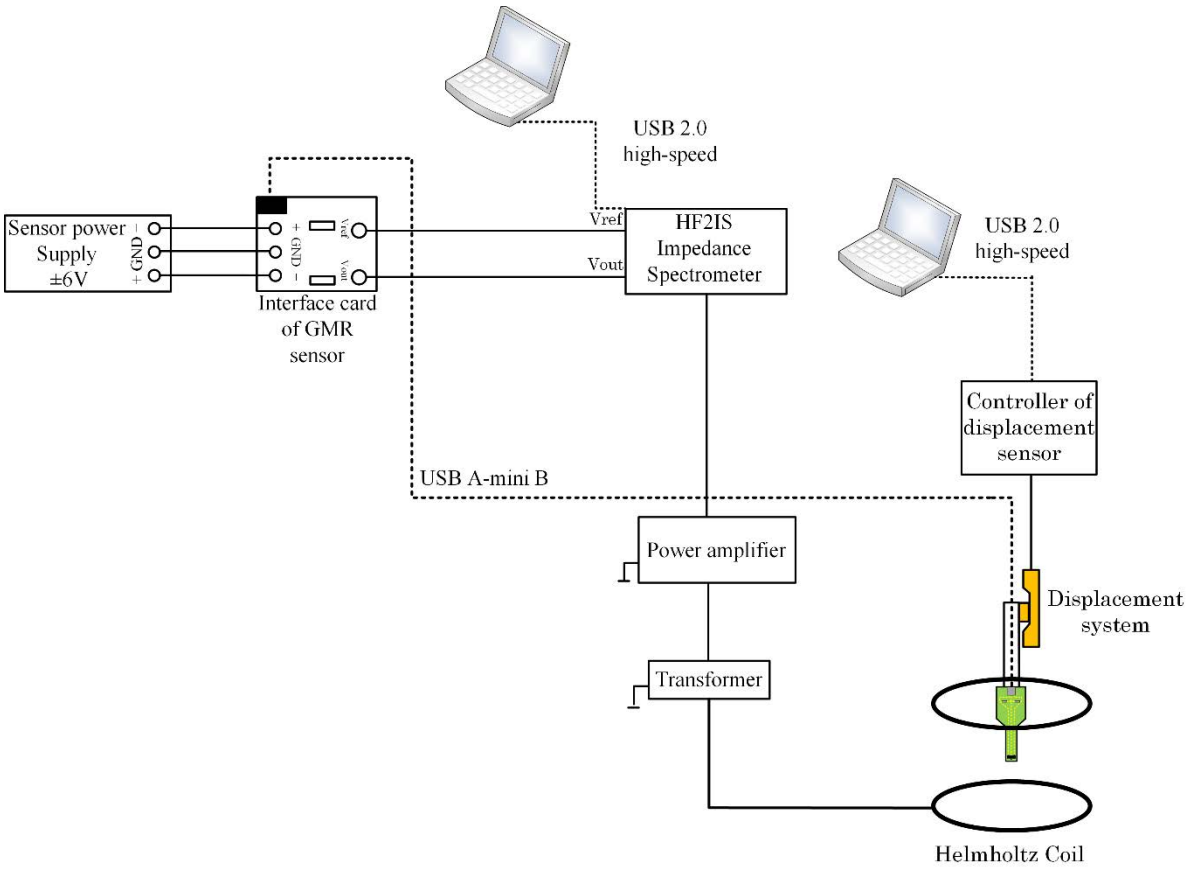

Figure 2.52 Measurement setup for characterize of the GMR sensor type III.

The Helmholtz coil is supplied by an amplifier. Due to the output signal generators of the HF2IS Impedance Spectrometer, we can directly generate the supply system of the Helmholtz coil without using a waveform generator. The experiment frequencies of exciting field of the Helmholtz coil are 60, 75 and 100 Hz. By changing the value of input voltage (mV), the magnetic flux density (B) has been changed. These results have been obtained by Teslameter for each value of magnetic flux density (B).

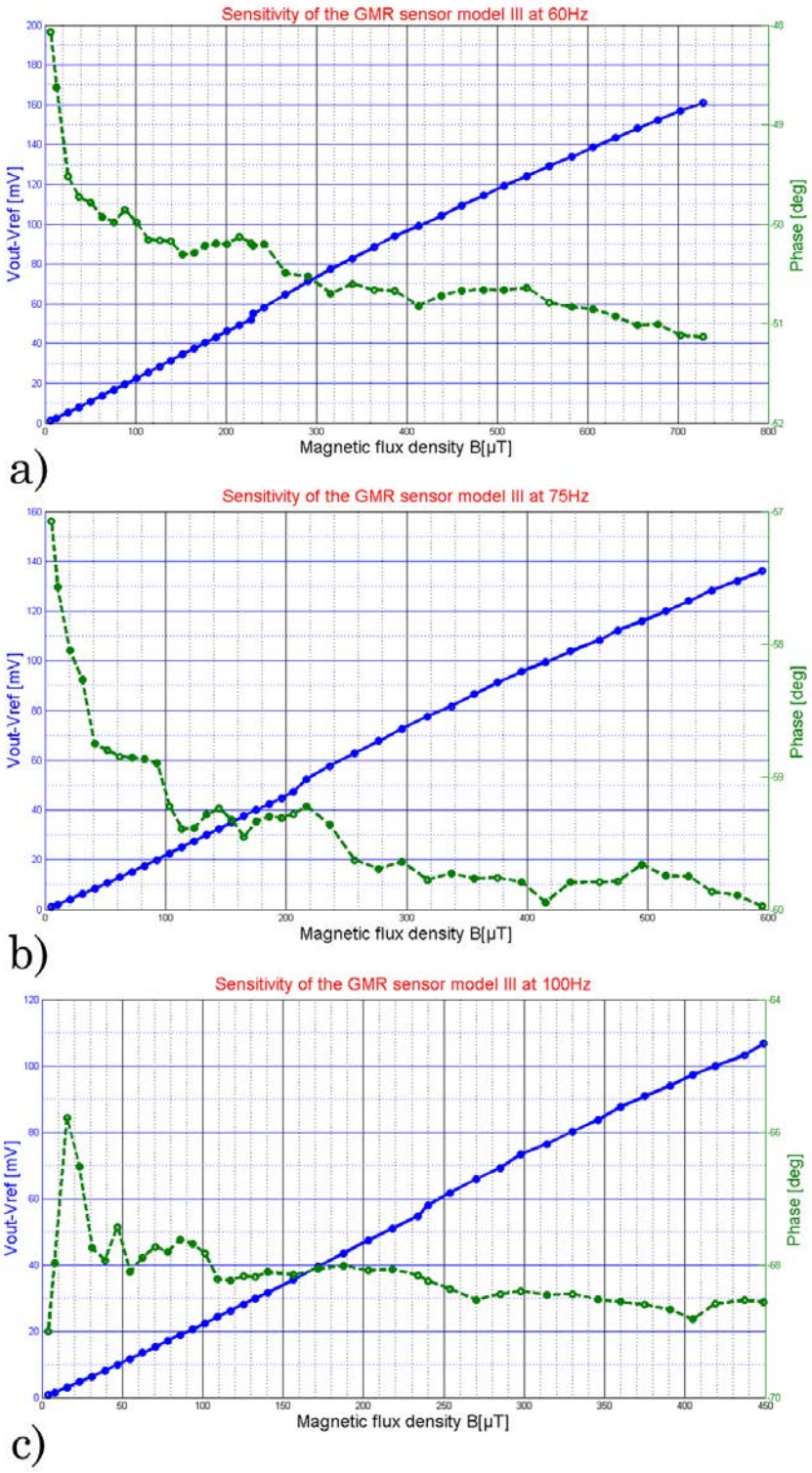

Figure 2.53 Experimental results of sensitivity obtained with the GMR sensor III at different frequencies of 60 (a), 75 (b) and 100 Hz (c).

Figure 2.53 (a), (b) and (c) show the sensitivity curve of GMRIII sensor with different frequencies. These results are linear and proportional to the magnetic flux density (µT) variations.

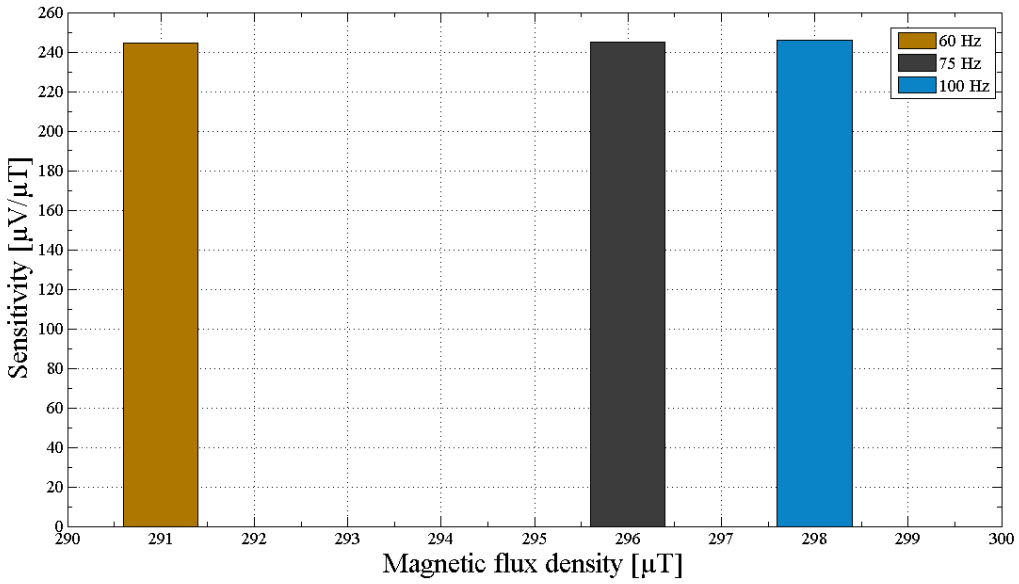

Figure 2.54 High value of sensitivity (µV/µT) as a function of B (µT) at f=60, 75, 100 Hz.

The high value of sensitivity as a function of magnetic flux density (µT) for different frequencies, obtained by GMRIII sensor model is presented in Figure 2.54. It can be concluded from the experimental results that the best sensitivities values (~ 245 µV/µT) are quite the same for the similar magnetic field values. Furthermore, this optimum value of the sensitivity is constant in the 50−100 Hz frequency range.

Measurement of the variation values of R in the Wheatstone bridge of the GMR sensor third model:

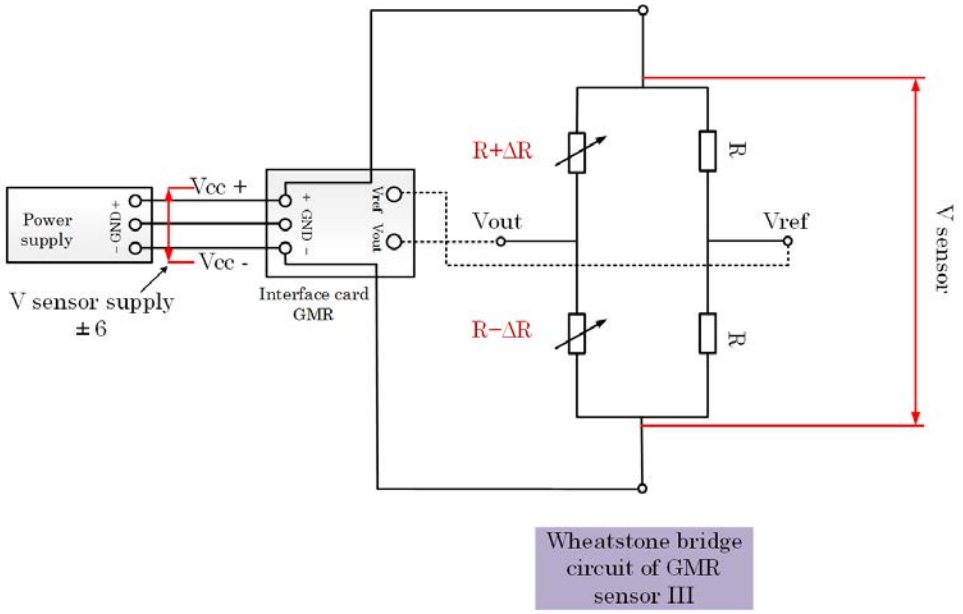

Figure 2.55 Electrical schematic and the Wheatstone bridge circuit of the GMR sensor model III.

The model of sensing elements is equivalent to two potentiometers (R+ΔR) and (R−ΔR). They depend on the direction of magnetic field, according to the magnetic field's direction, one of them is increasing and the other decreasing.

They are used to detect the exciting magnetic field inside containers. Figure 2.55 presents the schematic of the GMRIII sensor.

The total resistance value of both GMR elements is equal to 4340 Ohms. The variations of the resistance in the Wheatstone bridge of the GMRIII sensor is described by the following expression:

$$V_{measurmenet} = V_{out} - V_{ref} = \left(\frac{V_{sup}}{2} + \frac{V_{sup} \times \Delta R}{2R}\right) - \frac{V_{sup}}{2} \tag{2. 16}$$

After removing the DC component with HF2IS one obtain:

$$\begin{aligned} V_{measurmenet} &= \frac{V_{\sup}}{2R} \times \Delta R \\ \Rightarrow \Delta R &= \frac{V_{measurmenet} \times 2R}{V_{\sup}} \end{aligned} \tag{2. 17}$$

As shown in Figure 2.56, the results are proportional to changes the value of magnetic flux density.

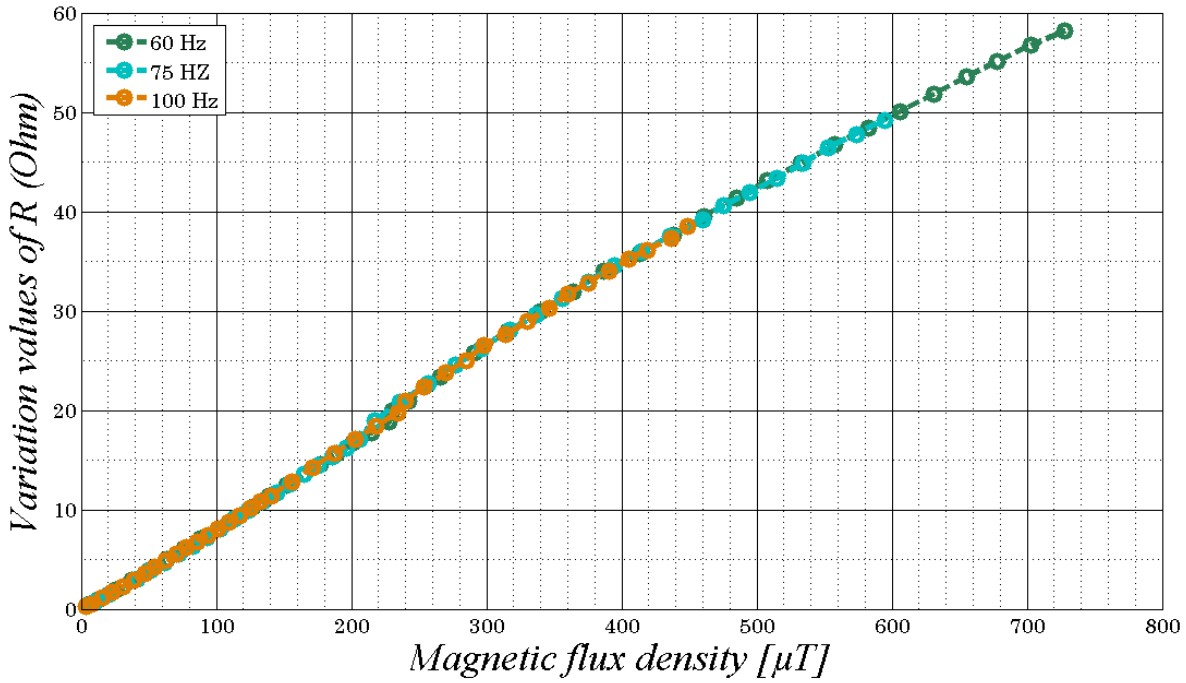

Figure 2.56 The variation (ΔR) of the GMR elements according to the magnetic flux density (B) at different frequencies.

Annex 4 presents the experimental results of variation values of R, ΔR as a function of changing the magnetic flux density and ΔR compared to R (total of sensor, resistance variation in %), considering the usage of different frequencies (60, 75, 100 Hz) in a power supply card of the sensor.

Furthermore, according to the results we can conclude that the value of the GMR sensing element sensitivity as a function of magnetic flux density (B) is equal to 4% mT^{-1}.

2.6 Conclusion

In this section we have presented the specifications and the design of three GMR sensors. The sensors have two basic parts: needle specifically designed to permit its insertion into midpoint of tiny ferrofluid's cavity. On the needle of each sensor the sensing elements are placed to measure the magnetic flux density inside and outside of magnetic fluid (as a reference). The second important part of the sensors is a Wheatstone bridge configuration to measure voltage variations induced by magnetic field, the DC voltage part of the GMR polarization being removed. This configuration is ideal for maximizing measurement sensitivity.

We have explained separately all parts of the GMR sensor's setup which include the following:

I. An interface card – to limit the current and protect the sensors from excessive electrical current,

II. A preamplifier – to boost output signal of sensors (except third sensor model),

III. A lock-in amplifier – to detect and measure the amplitude and phase in very small range of AC signals in the presence of high noise levels,

IV. A Helmholtz coil – to produce a fairly uniform magnetic field,

V. A displacement system – to protect the sensor's needle form any shock and moreover to control and reduce the percentage of error during the needle positioning in a center of sample's cavity.

At the end of this Chapter we have completed the process of sensor's characterization and the sensitivity of all sensors has been calculated. The experimental results achieved from this part are summarized below:

1) The maximum sensitivity of GMR sensor I is equal to 4.12 μV/μT with magnetic flux density about 9 μT. The value of the GMR element sensitivity as a function of magnetic flux density (B) is approximately 0.34% mT^{-1}.

2) A value 8.51 μV/μT for maximum sensitivity of sensor type II has been obtained. Furthermore, the value of GMR element sensitivity as a function of B is nearly 0.71% mT^{-1} for the first part (liner) and 1.46% mT^{-1} for the second part.

3) The highest value of sensitivity for model III in three frequencies (60, 75 and 100 Hz) is approximately 245 μV/μT and value of the GMR sensing element's sensitivity as a function of B is equal tentatively to 4% mT^{-1}.

According to sensitivity analysis results were obtained with three different GMR sensors, one can conclude that the GMRIII sensor has the highest sensitivity compared to the other types, due to its elements' dimensions, positions and also the Wheatstone bridge configuration.

Chapter 3 : Characterization of magnetic fluid properties by GMR sensors

3.1 Introduction

As discussed previously, magnetic properties of biological matter are widely investigated in the frame of nanomedicine research or nanoparticules applications. Spectroscopic variations of susceptibility or permeability could serve as support for new biomedical applications' development. Giant magnetoresistance sensors are particularly well suited to detect the magnetic particles because they provide high sensitivity and detection capability at micro-nanoscale.

Ferrofluids or magnetic liquids involve particles of magnetic materials such as iron, nickel and cobalt with extremely small size. They currently have a great importance in the mechanical industry, the military technology as well as in various medical applications.

In this work, the proposed GMR sensors can operate at various frequencies and at low magnetic field level.

Among the objectives of the third chapter, we present the measurement of magnetic properties such as relative permeability and susceptibility of magnetic fluids obtained with two different GMR sensors. To confirm the experimental results achieved with these sensors, we checked their performance with vibrating sample magnetometer (VSM) and also through theoretical calculations.

3.2 Experimental methodology of ferrofluid

3.2.1 Determination of the low-concentration of magnetic fluid

The shape of the magnetic nanoparticles is presumed to be cylindrical with a uniform distribution in the magnetic fluid. Magnetic nanoparticles show paramagnetic and diamagnetic behavior due to the level of relative permeability (μ_r), if relative permeability is more than 1, the magnetic nanoparticles is paramagnetic, if less than 1 it is diamagnetic [73].

Due to the possibility to measure the magnetic flux density by the GMR sensor, we can estimate the relative permeability (μ_r) of ferrofluid. The relationship between magnetic fluid volume density (D_V) measured as a percentage and magnetic fluid weight density (D_W) measured as a weight of ferrite per volume (mgFe/ml) is described by the following expression [74]:

$$D_W = \frac{\gamma_f \times D_V}{(1 - D_V) + \gamma_f \times D_V} \tag{3. 1}$$

Where γ_f is a specific gravity (ratio of density of a substance to the density of its reference substance) of magnetic bead [74].

From equation (3.1) the magnetic fluid volume density (D_V) is determined as [75]:

$$D_V = \frac{1}{\left[1+\left(\left(\frac{1}{D_W}\right)-1\right)\times\gamma_f\right]} \tag{3. 2}$$

When D_W<<1 the equation can be rewritten as [76]:

$$D_V = \frac{D_W}{\gamma_f} \tag{3. 3}$$

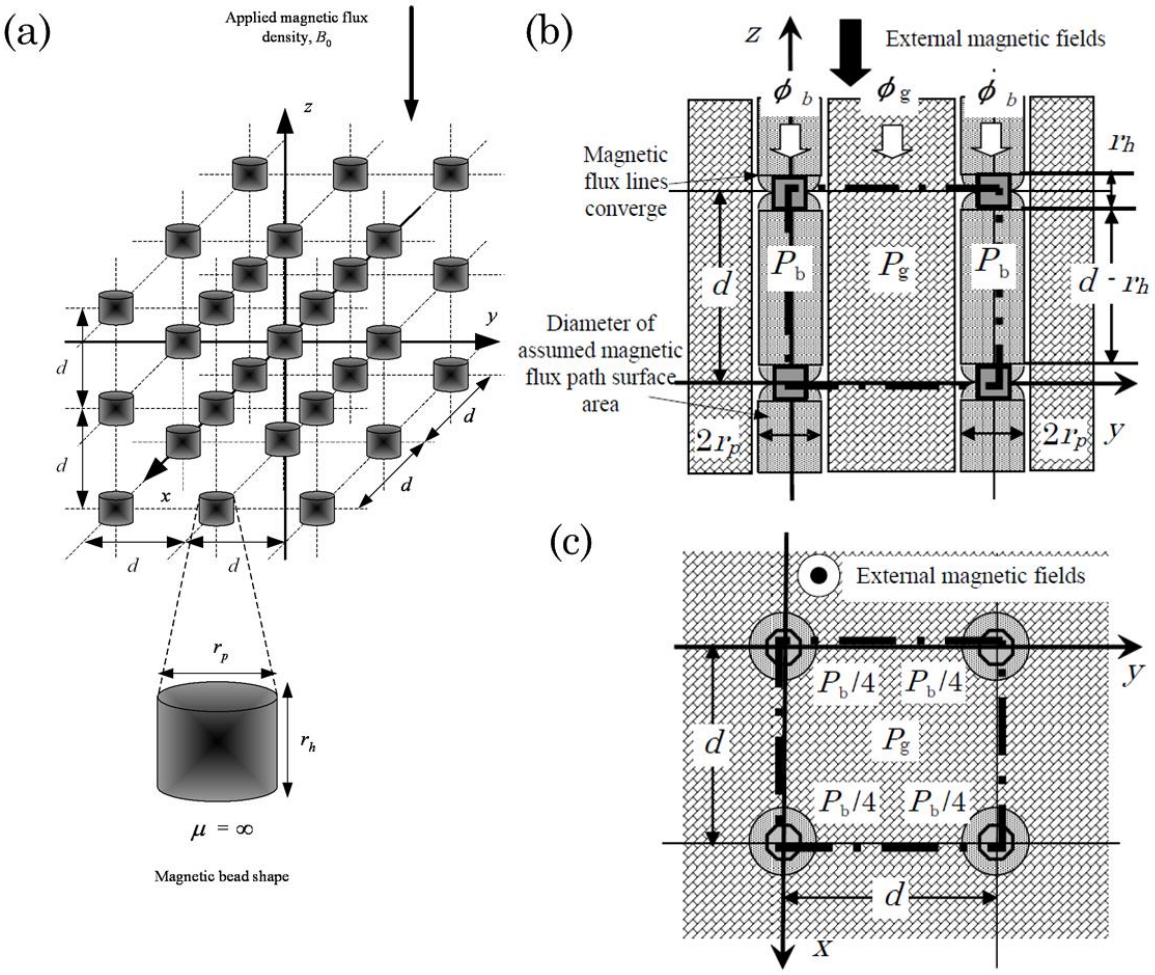

Figure 3.1 The magnetic model of nanoparticles (a), side view of magnetic path of a magnetic fluid in z−direction external magnetic field (b) and top view of magnetic circuit path (c) [75].

On one hand, it is supposed that the nanoparticles are uniformly spread inside the ferrofluid. On the other hand, the magnetic nanoparticles seem to be cylindrical form with equivalent height (rh) and diameter (rp) (see Figure 3.1.a)

Figure 3.1.b presents the side view of magnetic circuit path under the an external magnetic field, the top view of magnetic circuit path is presented in Figure 3.1.c [75, 77].

The permeance of magnetic path (P_b) through the magnetic particles or magnetic bead and permeance of magnetic path (P_g) through liquid may be computed from the following formulas [78]:

$$P_b = \frac{\mu_0\left(\pi r_p^2\right)}{\left(d - r_p\right)} \approx \frac{\mu_0\left(\pi r_p^2\right)}{d}\left(1 + \frac{r_p}{d}\right) \tag{3. 4}$$

$$p_g = \frac{\mu_0\left(d - \pi r_p^2\right)}{d} \tag{3. 5}$$

Where, πr_p^2 is a cross section for the magnetic flux ϕ_b, and $\left(d - \pi r_p^2\right)$ for the magnetic flux ϕ_g.

Taking into account equations (3.4-3.5), the permeance per unit volume can be rewritten as [75, 78]:

$$P = \frac{\mu S}{l} = \frac{\mu_0 \mu_r 1^2}{1} = \left(p_g + p_b\right)\frac{\left(1/d^2\right)}{\left(1/d\right)} \tag{3. 6}$$

Where l is a length and S is a surface of magnetic path.

The relative permeability (μ_r) of magnetic fluid can be determined from the expression [79]:

$$\mu_r = 1 + 4D_V \approx 1 + \frac{4D_W}{\gamma_f} \quad (D_W << 1) \tag{3. 7}$$

Given that the needle of the GMR sensor is injected into an ellipsoidal cavity, the GMR sensing area located at the tip of the needle is exposed to a magnetic flux density B_1 in center of cavity where the relative permeability is higher than 1, and the second sensing element located at end of the needle is exposed to a magnetic flux density B_0 outside of the cavity (μ_r=1) [73]. The magnetic fluid weight density can be calculated from the difference between the applied magnetic flux density outside (B_0) of the fluid filled cavity, and the magnetic flux density inside (B_1) of the fluid filled cavity.

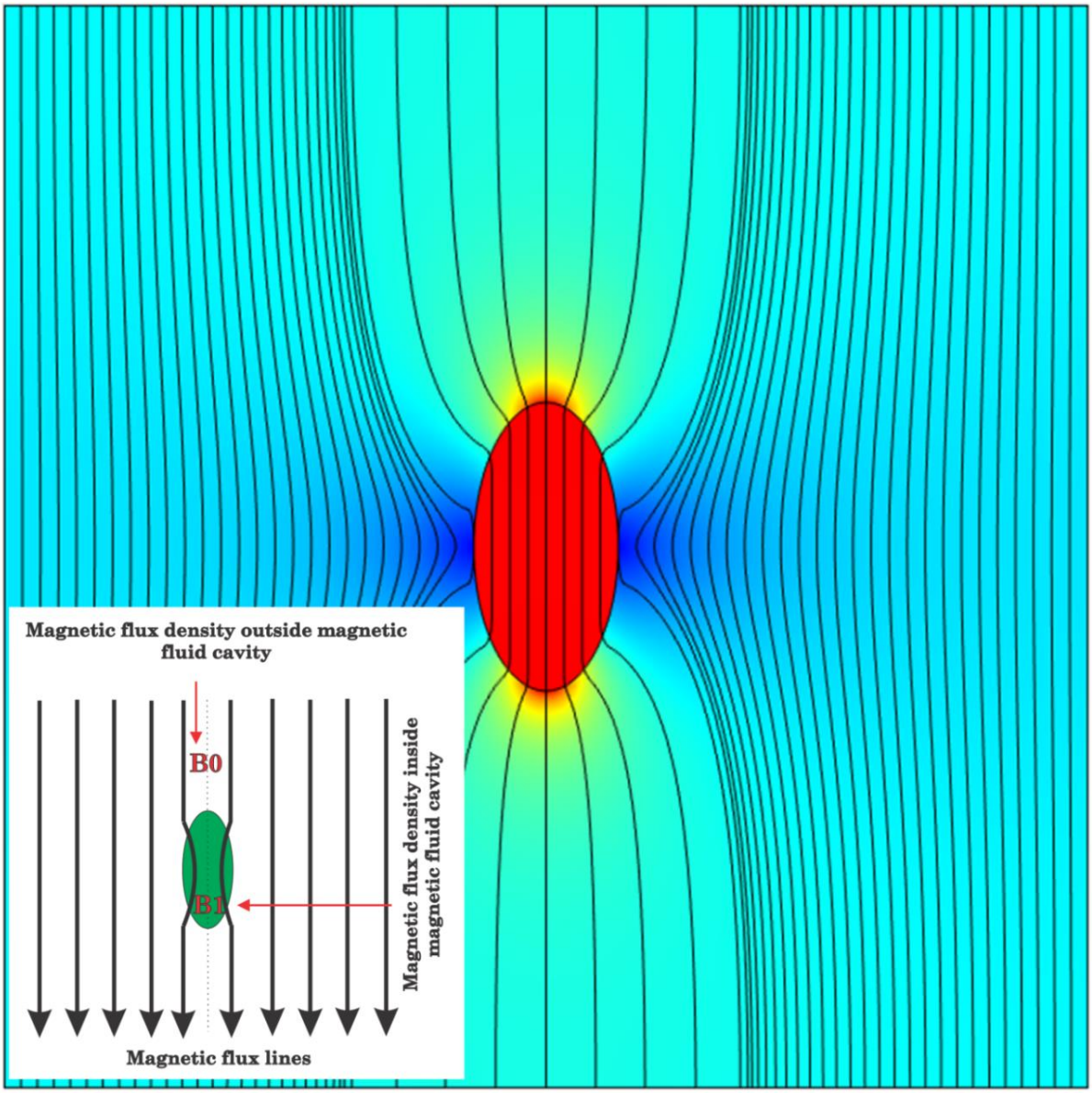

Figure 3.2 Distribution of magnetic flux density inside and outside of an ellipsoidal cavity.

Furthermore, the magnetic flux density is more concentrated in an ellipsoidal cavity and magnetic flux density (B_1) of each ferrofluid in the center of cavity depends and changes into magnetic fluid weight density (D_W).

The magnetic flux distribution inside and outside of an ellipsoidal cavity is presented in Figure 3.2. The relationship between changes magnetic flux density (δ) and magnetic fluid weight density (D_w) can be described by the following expression [80].

$$\delta = \frac{(B_1 - B_0)}{B_0} = \frac{C_d(1-N)D_w}{h_s\gamma_f} \quad (D_w << 1) \tag{3. 8}$$

Where B_0 is a magnetic flux density outside and B_1 is a magnetic flux density inside the cavity, C_d is a coefficient which is theoretically equal to 4 and practically in range between 3−4, N is a demagnetizing factor; in cylindrical shaped cavities S=1 (aspect ratios) , N=0.333 [81], and the space factor of cluster h_s is 0.523. The relationship of a relative susceptibility (χ^*) and a ratio of magnetic field measured by the GMR sensor is described by the following expression [82]:

$$\delta = \frac{(B_1 - B_0)}{B_0} = (1-N)\chi^*, \qquad \chi^* = \frac{\frac{(B_1 - B_0)}{B_0}}{(1-N)} \quad (\chi^* << 1) \tag{3. 9}$$

The demagnetizing factor (N) of a cavity depends on what is called the “aspect ratio” (S) (height/diameter) of cavity. This global factor represents the proportional relationship between the height and the diameter of a cylindrical container. For the thin and long cavity the demagnetizing factor is zero (N=0, S=∞) [81].

3.2.2 Preparation of different concentrations of ferrofluid and experimental setup

This part of my research was performed during summer 2011 under the leadership of Professor Yamada, at Division of Biological Measurement and Applications at Kanazawa University.

Several experiments were performed to prepare different magnetic fluids with several weight densities (D_w). A concentration of pure magnetic fluid (Fe_2O_3) with magnetic particle size 16 nm was made out of 40 % magnetic fluid and 60 % of distilled water. In this part, the ferrofluid is diluted by distilled water to achieve several magnetic fluids with weight density equal respectively to 1 %, 0.4 %, 0.3 % and 0.09 % (the volume density is 1:50, 1:120, 1:160, 1:600), as shown in Figure 3.3.

The 78.5 µl of magnetic fluid was poured to cylindrical shape cavity with dimension 5×4 mm by micro pipette. Then, the four ferrofluids were placed at the center of the Helmholtz coil, where the magnetic field is more uniform.

The experimental setup for the measurement is given on Figure 3.4. The needle-type GMR sensor permit the characterization of four samples (weight densities varying from 1 %, 0.4 %, 0.3 % to 0.09 %) of magnetic fluid when the Helmholtz coil is activated to generate an uniform magnetic field.

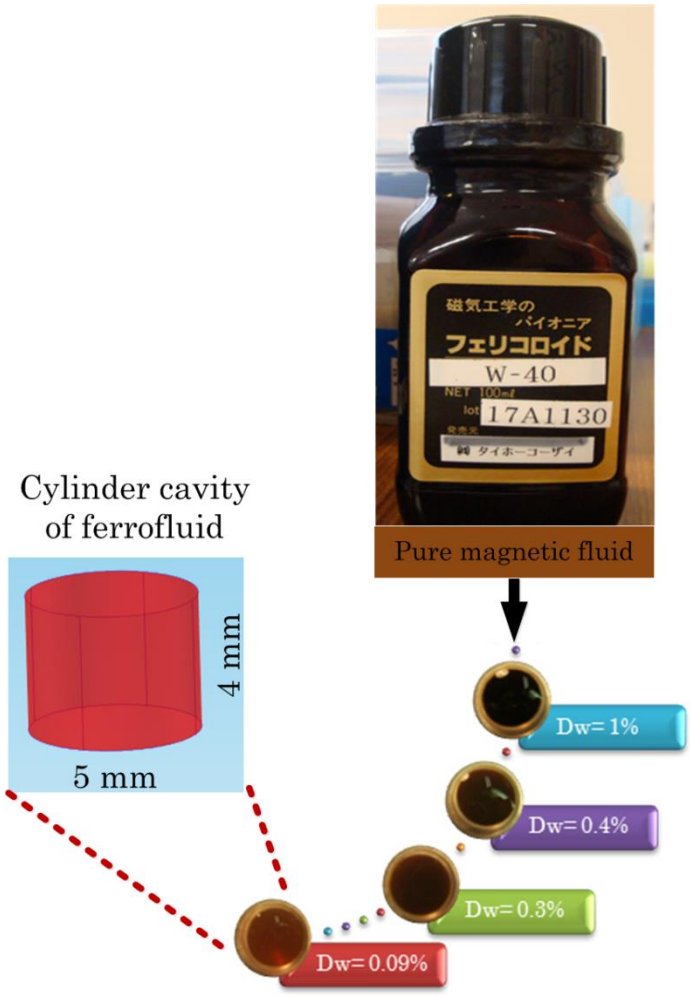

Figure 3.3 Top-view model of ferrofluid with different weight density.

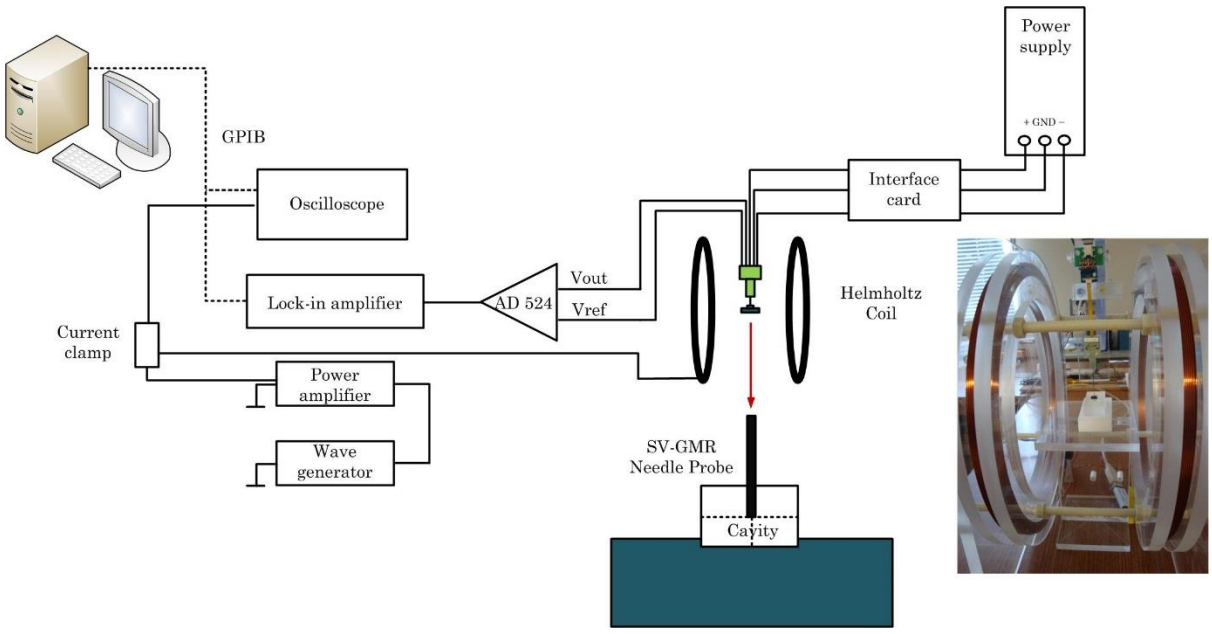

Figure 3.4 Measurement setup.

The needle type SV-GMR used in this study consists on two GMR sensing elements connected in a Wheatstone bridge configuration. Dimension of each sensing element is 150 µm per 150 µm. The length of the needle is equal to 3cm by cross section 300×300 µm. The sensor needle is inserted inside the ferrofluid at the center of its container. After the measurement of each ferrofluid, the needle of GMR sensor was cleaned carefully to reduce the errors.

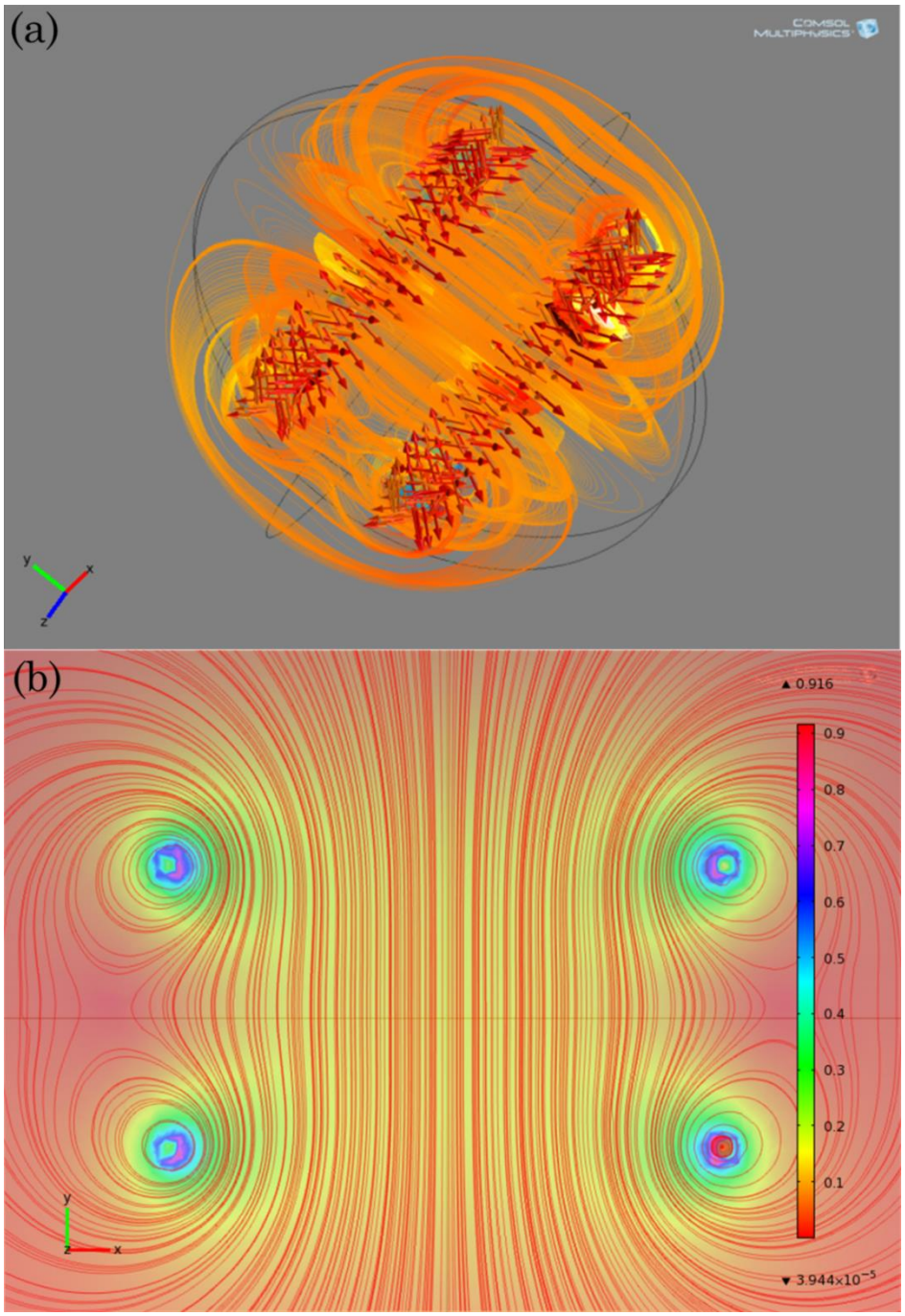

Figure 3.5 Magnetic flux density in total sphere of coils (a), distribution (B) at midpoint of the Helmholtz coil.

The Helmholtz coil used in this experiment consists of two circular coils with 106 turns, each coil is fabricated with diameter 0.25 meters and the distance between coils is equal to coil radii. It should be noted that the magnetic field range for measuring with SV-GMR sensor is within tens of nT to few mT.

One constraint before proceeding to experimental measurement of magnetic fluids is to set the appropriate value of the magnetic field in order to maintain sensor's safety. To solve this task, simulations using COMSOL® were done to determine the limit values of the magnetic field. The distribution of magnetic flux density (mT) inside the Helmholtz coil is shown in Figure 3.5 (a), and its uniformity is presented in Figure 3.5 (b).

Figure 3.6 shows the simulation plot and graphically represents different regions inside the coil.

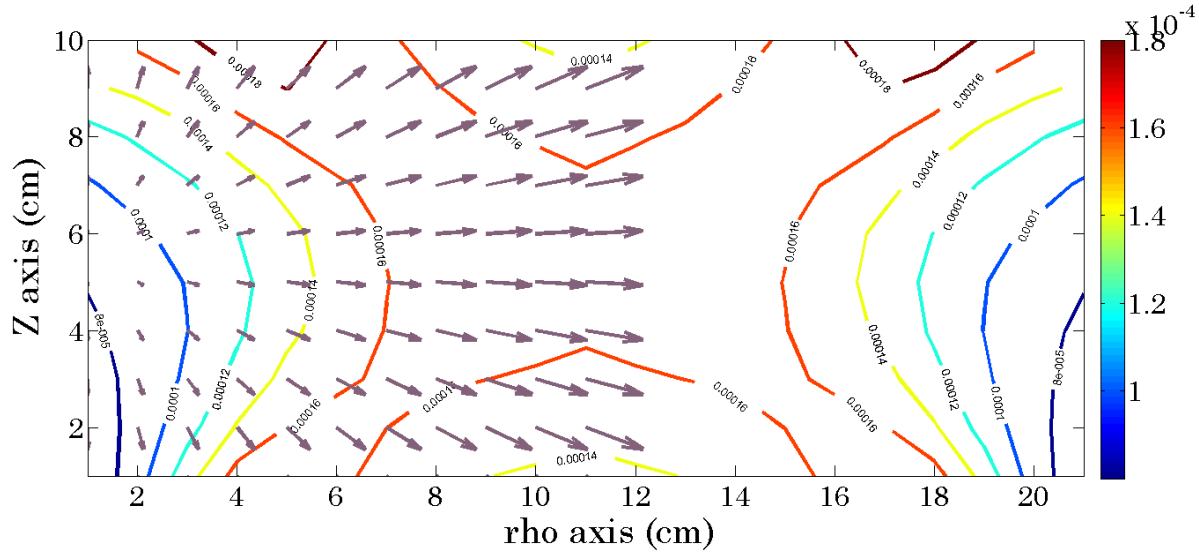

Figure 3.6 Distribution of magnetic flux density (B) in a sphere of the Helmholtz coil.

As for the previously described sensors, the electronic conditioning consists on a DC power source (±6 V) connected to the GMR sensor by an interface card, the output signal being amplified by an Analog Device AD 524 circuit with gain 40 dB. The differential signals Vout−Vref of the GMR sensor were applied to a multifunction digital Lock-in Amplifier (NF Li 5640). In order to reduce the percentage of errors of the GMR sensor, we have measured the signal amplitude, phase and frequency 5 times for each sample through MATLAB® program specifically for this lock-in amplifier. An average of the data was then deduced for each sample.

The Helmholtz coil is powered by a signal sinusoidal from the wave generator (Wave factory 1965 NF electronic instruments multifunction), the current amplitude of the Helmholtz coil is

observed by an oscilloscope (Iwatsu DS-8814 Bringo Oscilloscope). The operating frequency of the Helmholtz coil is 100 Hz, the input current of the coil is 200 mA, the magnetic field (H) is approximately 121 (A/m) and the magnetic flux density (B) is 153 µT.

3.2.3 Results obtained by vibrating sample magnetometer (VSM)

A Vibrating Sample Magnetometer (VSM) is a scientific instrument used to characterize DC magnetic properties of materials as a function of magnetic field, temperature and time. A VSM was invented by Simon Foner in Lincoln Laboratory in 1955 [83]. A VSM can be used to characterize magnetic liquids, powders or thin films. Magnetic moment and coercivity are among the properties that can be measured.

The measurement principle of the VSM is to determine the variation of a magnetic induction producing by a vertical oscillation of the sample through the coils. In this method the sample is placed under a uniform magnetic field.

The alternating magnetic field will cause an electric field in the pick-up coils (according to Faraday's law). The signals pick-up coils are detected by a synchronous detector. Furthermore, the VSM's frequency and amplitude are constant.

The VSM (model 3374−140), used in this experience, was produced by GMW Associates; the measurement setup of VSM and its dimensions are presented in Figure 3.7 (a) and (b). The typical specifications of this model are shown in Table 3.1.

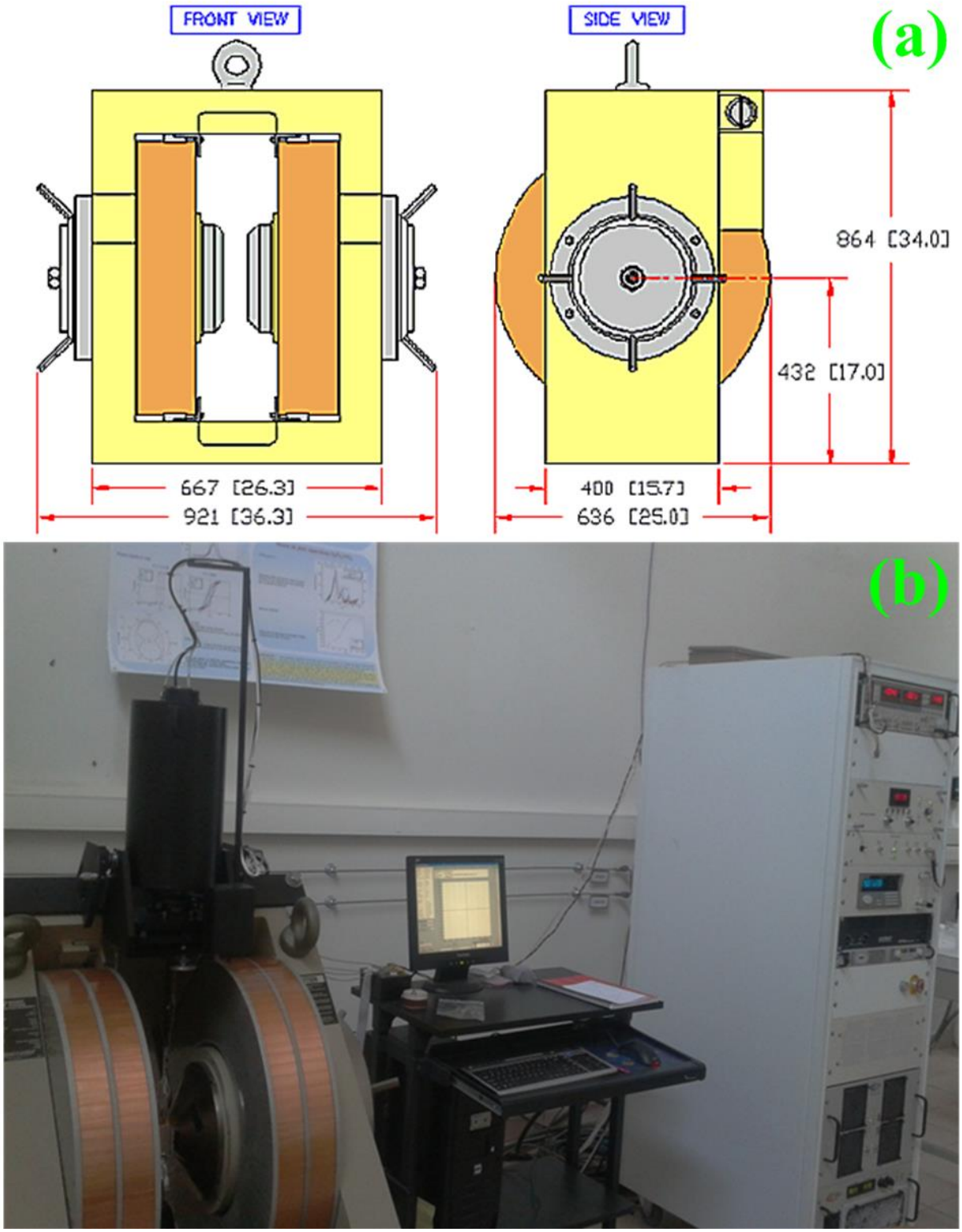

Figure 3.7 Dimensions (a) [84] and real image (b) of the VSM measurement setup.

Table 3.1 Main features of the VSM 3374-140 [84].

Dimensions	920 mm(W)×636 mm(D)×864 mm (H)
Pole Diameter	250 mm
Pole Gap	Variable from 0 to 160 mm
Field Readout Resolution	20 bit (1 µT up to 3.0 T field)
Max Power (air)	40 Amps, 22 Volts (0.88 kW)
Max Power (water)	140 Amps, 76 Volts (10.6 kW)
Self -Inductance	Approximately 80 mH
Frequency	75 Hz
Water Cooling	15 liters/min, 2.0 bar
Weight	1800 kg

In this part of our experiments we have used another ferrofluids, produced by Ferrotec Corporation to detect magnetic properties of liquid by the VSM. This ferrofluid consists of very small ferromagnetic particles with size about 10nm and with weight 56 g; key characteristics of this magnetic liquid are given in Table 3.2.

Table 3.2 Specific components of ferrofluid [85].

Magnetite	3−15% by volume
Oil soluble dispersant	6−30% by volume
Carrier liquid	55−91% by volume
Boling point	401−491 (°F)
Specific gravity	0.92 to 1.47
Appearance	Black liquid, mild odor

The pure ferrofluid have been mixed with distilled water, and we have prepared several concentrations (with different weight densities) such as 1:10, 1:50, 1:100, 1:200, 1:400 and 1:600. The different ferrofluids were poured in a glass flacon shown in Figure 3.8.

As explained in Chapter one, ferrofluids are dissolved in water or organic solvent (oil). This type of ferrofluid that we have used in this research is made from an oily solution and it is not well dissolved by distilled water. Furthermore, to reduce the amount of mixing errors, we have utilized a micropipette (Eppendorf Research® plus) with the volume range 20 to 200 µl and the errors specification are shown in Table 3.3.

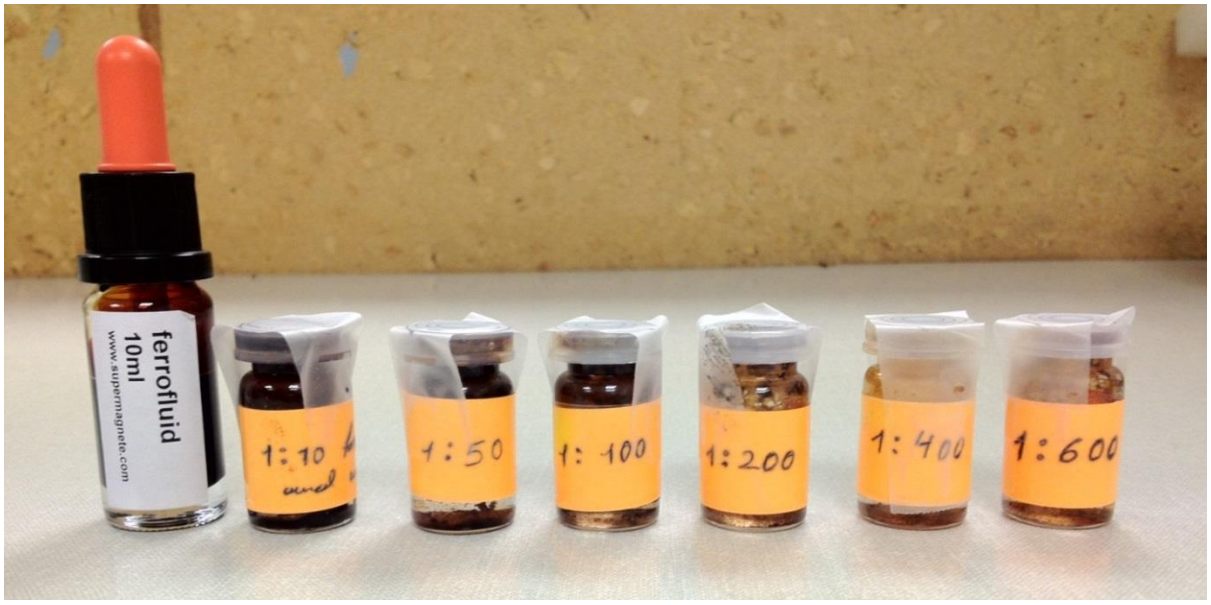

Figure 3.8 Ferrofluid at different concentrations.

Table 3.3 Errors information from a pipette [86].

Volume	Systematic error		Random error	
20 µL	±2.5%	±0.5 µL	±0.7%	±0.14 µL
100 µL	±1.0%	±1.0 µL	±0.3%	±0.3 µL
200 µL	±0.6%	±1.2 µL	±0.2%	±0.4 µL

Next, each ferrofluid was poured by pipette (45 µl) into the special cavity of VSM with dimension 6×3 mm (W and H). After turning on the VSM, it is necessary to choose the parameters of magnetic field ranges (in Oersted), angle of samples and step size of measure. A window menu of the controlling program is presented in Figure 3.9. The conversions factors between units are provided in Table 3.4.

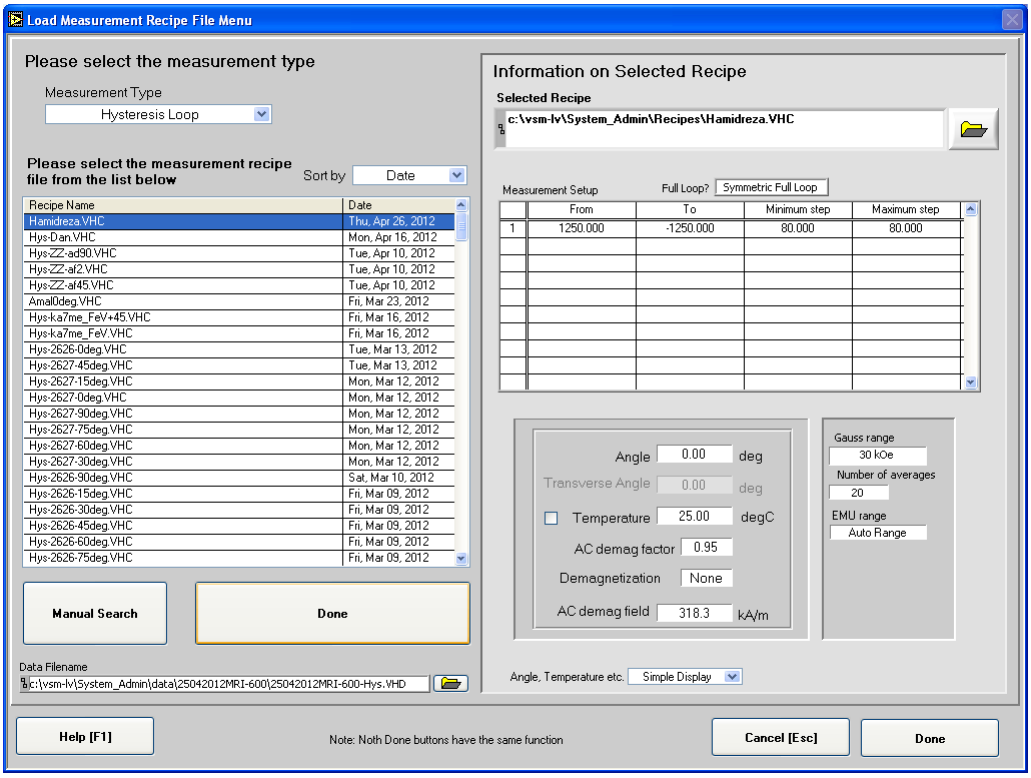

Figure 3.9 The VSM controlling program.

Table 3.4 Table of conversions of the units.

Units	CGS	SI & MKSA	Conversion factor CGS to SI
Magnetic field [H]	Oersted (Oe), Gb/cm	A/m	$10^3/4\pi$
Magnetic flux density [B]	gauss (G)	tesla (T), wb/m^2	10^{-4}
Magnetization [M]	emu/cm^3	A/m	10^3

After filling the different concentrations of magnetic liquid into the plastic container (cavity) with the pipette, we have closed the cap of cavity and covered it with Teflon tape very carefully in order to insure its sealing. In addition, to keep better the container on quartz rod, we have used the vacuum grease.

Next, the rod contains of ferrofluid have been placed in the center of the VSM, as shown in Figure 3.10.

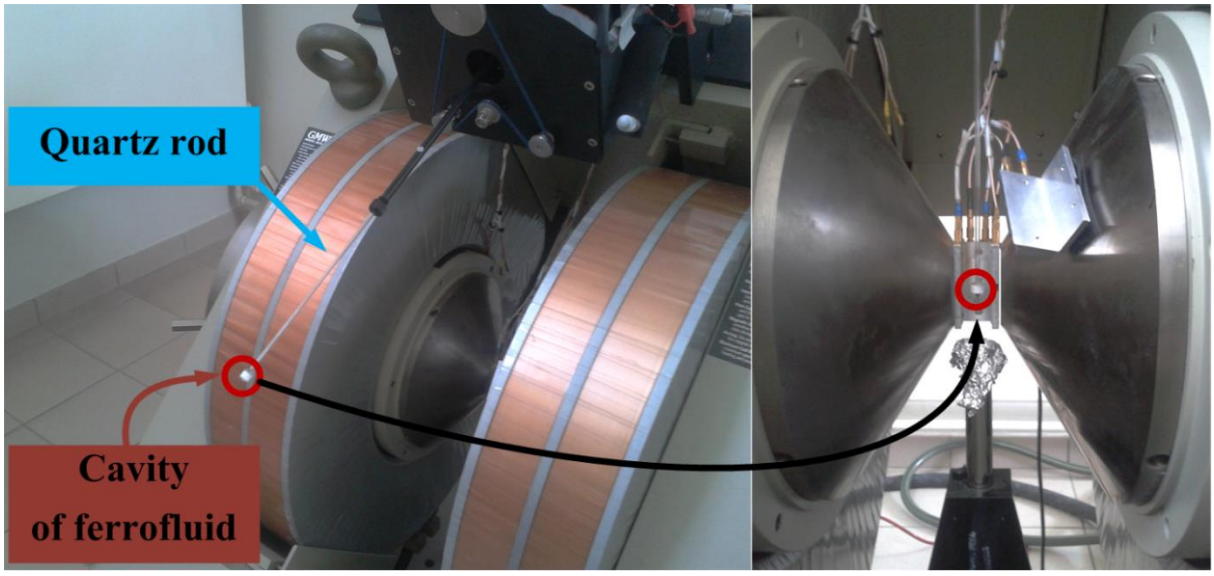

Figure 3.10 The placing of container of ferrofluid in center of the VSM.

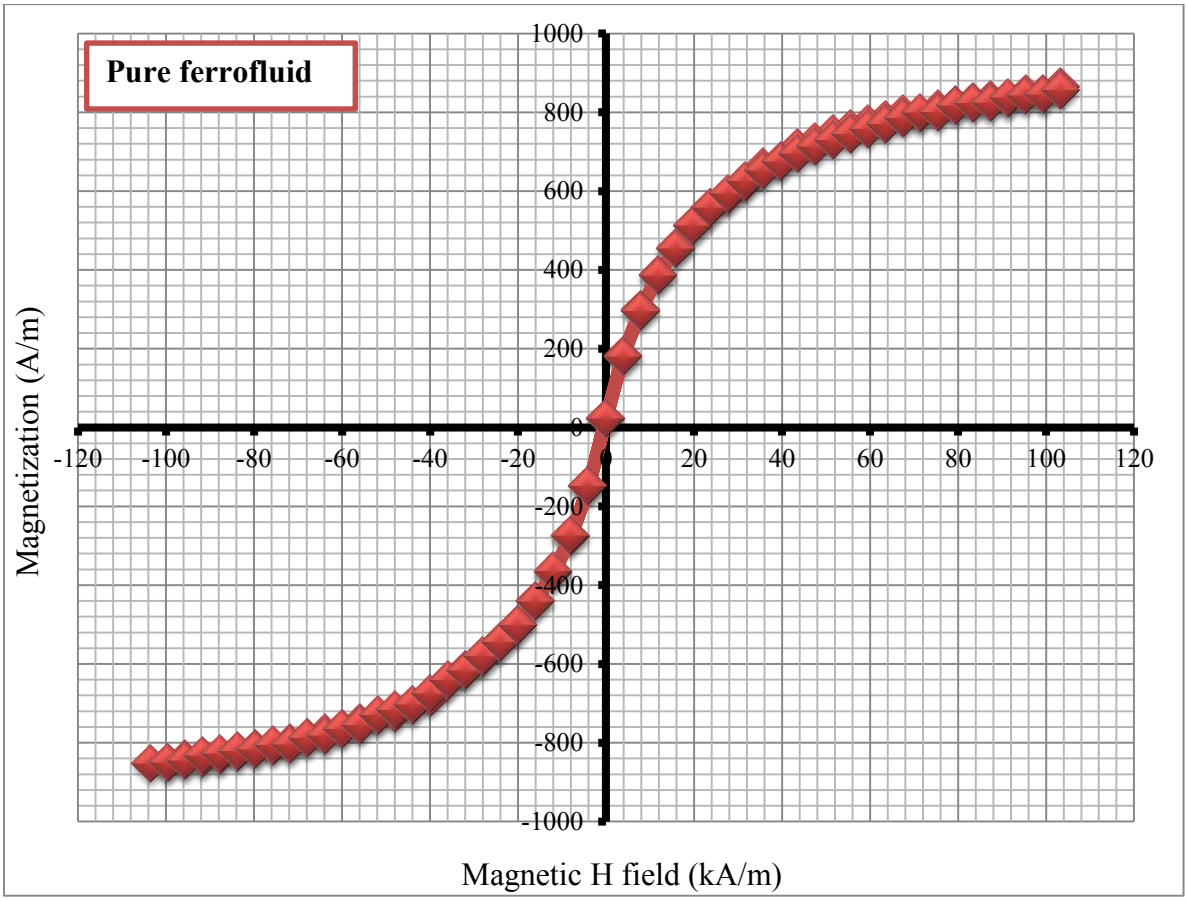

Figure 3.11 Magnetic hysteresis curve of pure ferrofluid.

The center of the VSM is the place where the magnetic field is the most uniform, thus allowing to implement highly accurate and reliable tests for all our measurements. The range of the magnetic field can increase up to 2.8 Tesla.

The sample was then placed in the center of the device. Next step is to run the VSM program to start the measurement. Moreover, sample vibration of the VSM helps to prevent precipitate while mixing the liquids (homogeneous mixture). Alternatively, the coils of the VSM are cooled during the experiment by cold water to avoid getting hot as very high currents flow in each coil.

Figure 3.11 presents the results for magnetic hysteresis obtained by the VSM for several concentrations in magnetic field (H) range from +100 to −100 (kA/m).

No hysteresis neither remanent magnetization is observed in the measured loop-cycle, this loop is typical of a paramagnetic or “superparamagnetic” material. If each magnetic nanoparticle is considered as one magnetic moment, the completely random organization at zero field leads to zero magnetization. Thus under an external magnetic field, the magnetic moments tends to align and a non-null magnetization appears that reaches saturation for an external field amplitude close to 100 kA/m.

Moreover, it is observed from Figure 3.12 that the magnetic fluid is diluted with distillated water, the overall magnetization at saturation decreases but the magnetization at saturation per magnetic fluid dose stays constant. This observation confirms that the magnetization originates from non-interacting particles.

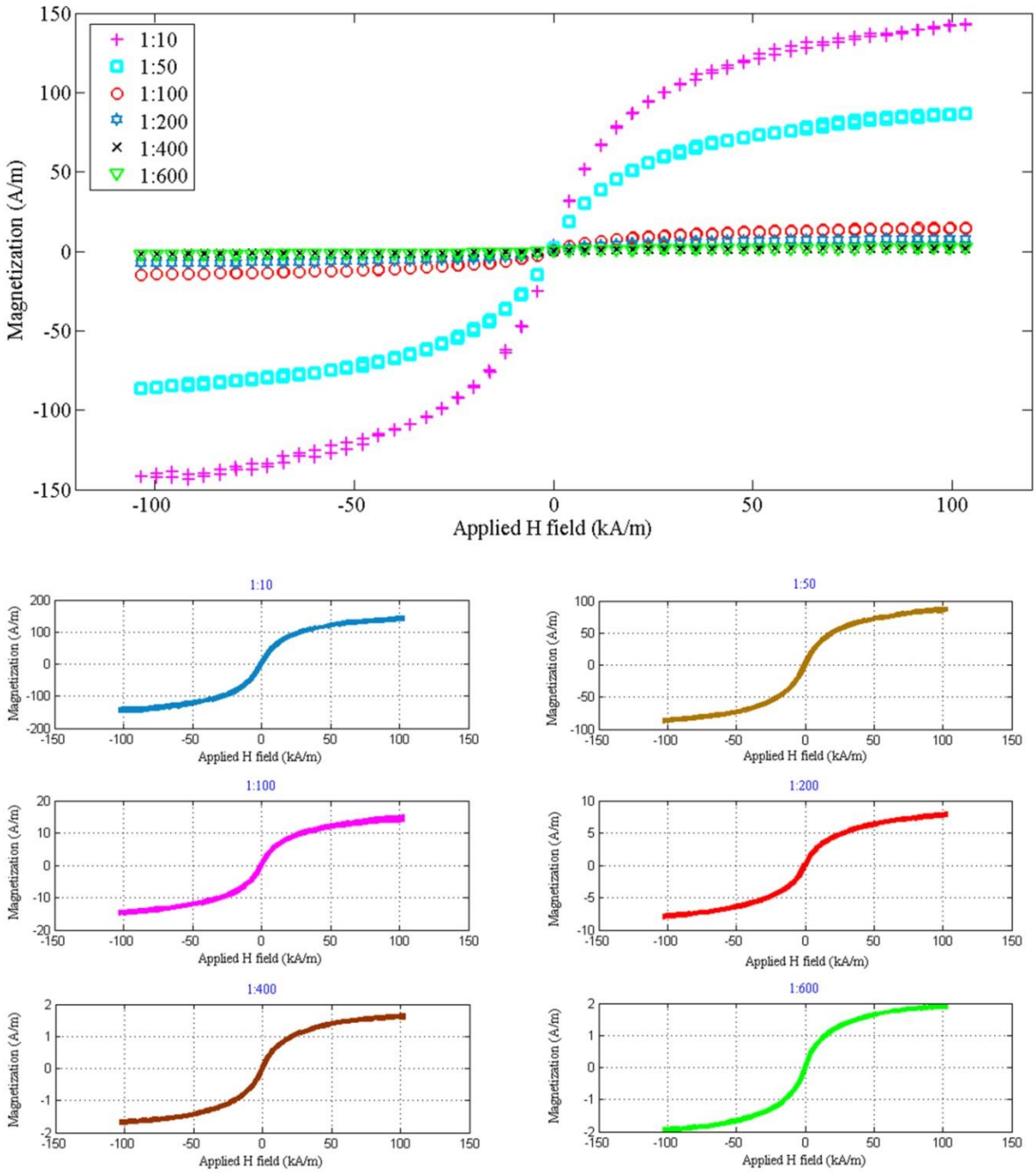

Figure 3.12 Hysteresis curve of fluids obtained from pure ferrofluid.

Magnetic susceptibility reaches particularly high values in ferromagnetic material and, therefore, the magnetic susceptibility of ferromagnetic materials depends on Magnetization (M) as a function of magnetic field (H).

The derivative of magnetization (dM) and magnetic field strength (dH) permit to determine the initial magnetic susceptibility and is given by following equation:

$$\chi_i = \frac{dM}{dH} \tag{3. 10}$$

The relative permeability (μ_r) can also be calculated from the equation 1.13.

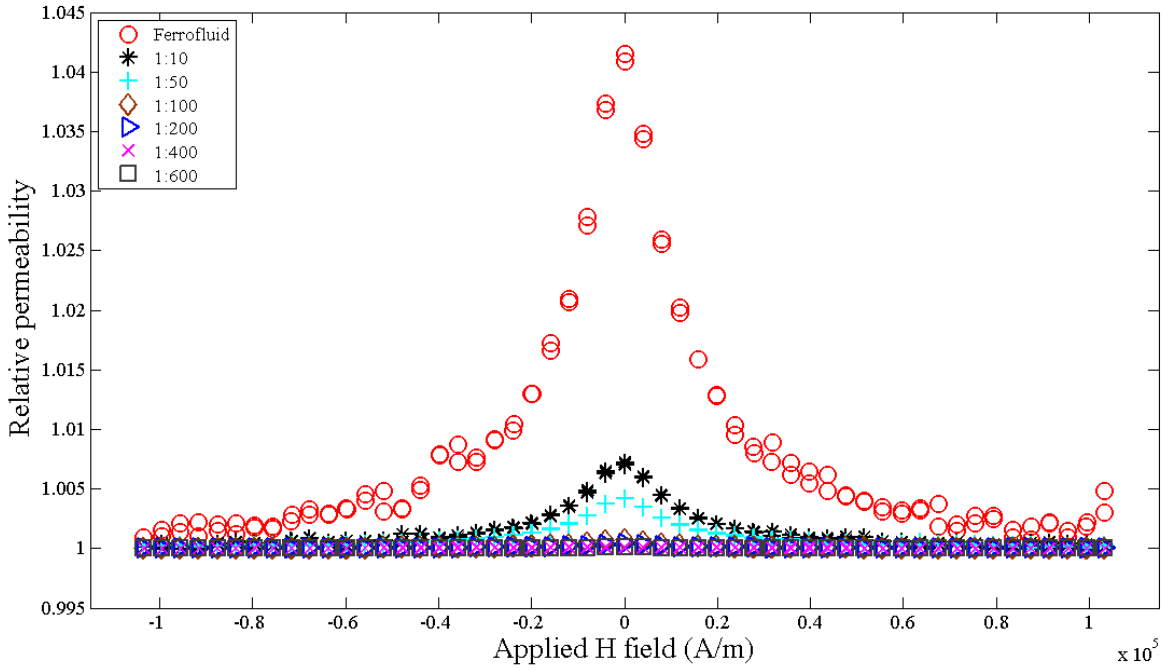

Figure 3.13 Initial relative permeability (μ_{ri}) as a function of an applied field (A/m).

In Figure 3.13 and Figure 3.14 we present the experimental results of the initial relative permeability (μ_{ri}) and the initial magnetic susceptibility (χ_i) obtained by the VSM.

We have used the equation (3.10) to calculate these parameters (μ_{ri} and χ_i) according to the magnetic hysteresis curves for each dilution.

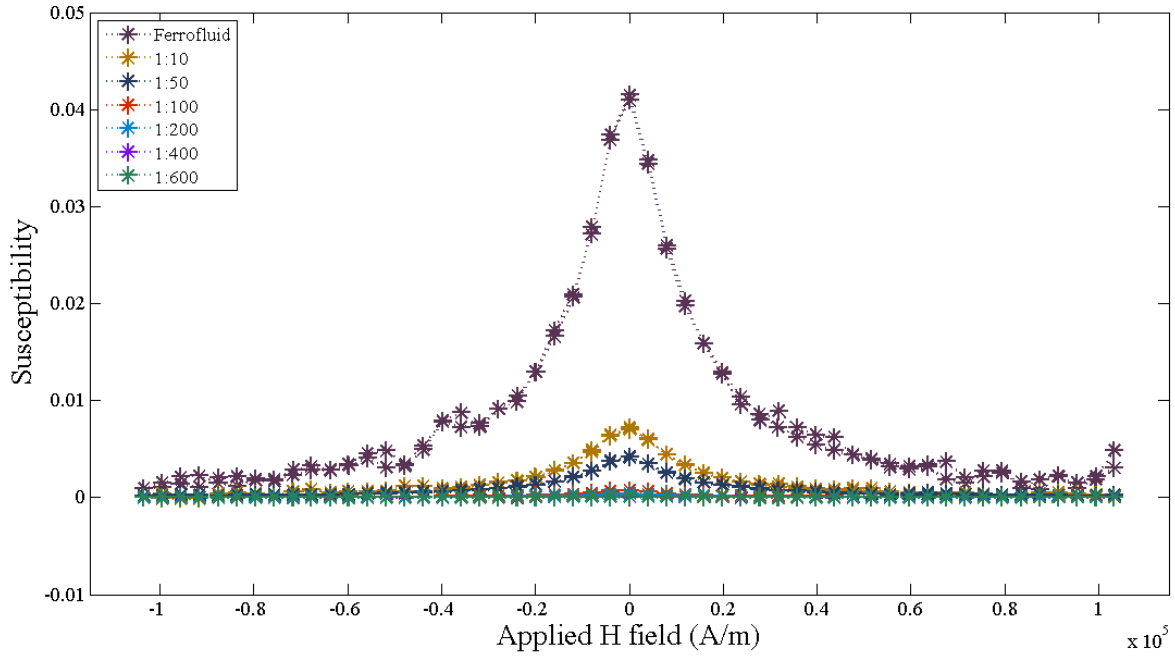

Figure 3.14 Initial magnetic susceptibility χ_i as a function of an applied field (A/m).

One can note that the large value of magnetic susceptibility (χ) corresponds and is related to strongly magnetic materials. In the weak applied field limit, a magnetization is linear with the external magnetic field and magnetic susceptibility (χ) is defined by the relationship [87]:

$$\chi = \frac{M}{H} = \frac{\pi}{18} \times \frac{\mu_0 \phi M_d^2 d^3}{kT} \qquad (3.\ 11)$$

Where, ϕ is a volume section of magnetic solid to carrier liquid, M_d is a magnetic domain magnetization of the major magnetic particles part and equal volume (V) over the magnetic moment (m), d is a diameter of the magnetic particle, $k=1.38\times10^{-23}$ (J/K) is a Boltzmann's constant and T is a temperature in Kelvin.

The results of susceptibility and relative permeability obtained from equations (3.11) and (1.13) are presented in Figure 3.15 and Figure 3.16. These results show a good correlation and they confirm those obtained by using two equations 3.10 and 3.11.

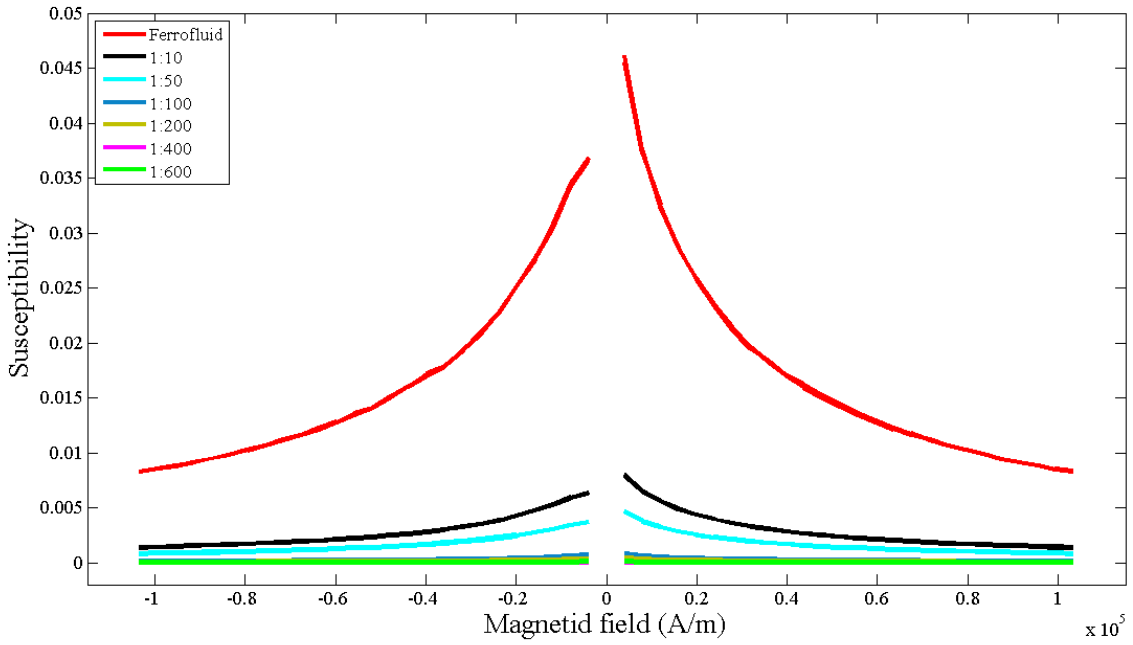

Figure 3.15 Magnetic susceptibility (χ) as a function of an applied field (A/m).

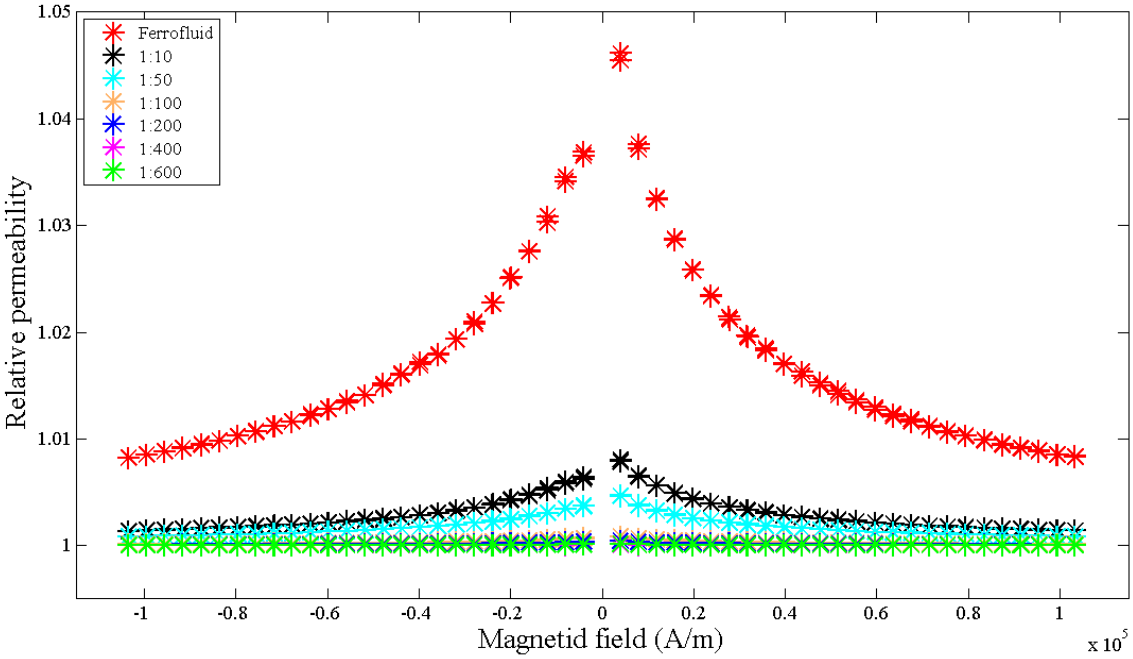

Figure 3.16 Relative permeability (μ_r) as a function of an applied field (A/m).

3.2.4 Comparison of results obtained by the GMR sensor and by the VSM

In this section we present the experimental results for each magnetic fluid with different weight density, and the measurement setup of the GMR sensor. The results from the GMR sensor are compared with those obtained with the VSM. The Figure 3.17 presents the relationship between the output signal from the GMR sensor and the weight density (1.10 %, 0.41 %, 0.36 % and 0.097 %).

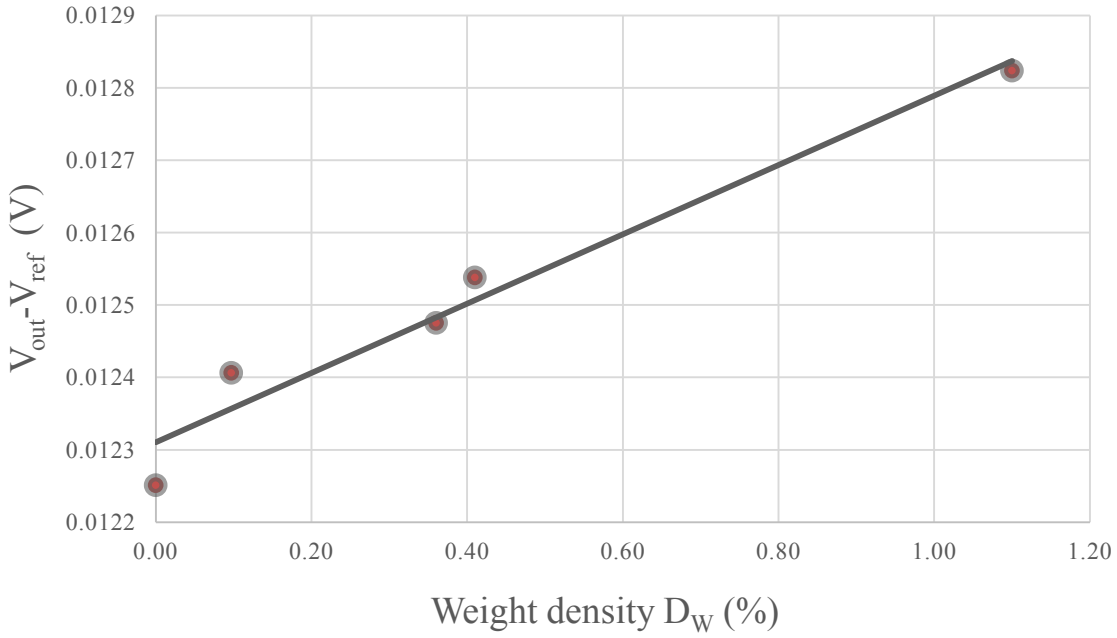

Figure 3.17 The relationship between the output signal from the GMR sensor and the weight density (D_W %).

The VSM refers to a technique for measuring magnetic fields and can be used to determine the magnetic properties of substances and materials in the laboratory and experimental devices.

The ratio between relative permeability (μ_r) and the susceptibility (χ) depending (linearly) on different range of weight densities (D_w %) obtained by the needle type GMR sensor are compared with the results achieved from the VSM (see Figure 3.18). According to equation 3.7, it can be noticed from the results that μ_r and χ are proportional to D_w and the results of the GMR sensor and the VSM confirm each other. The average error for μ_r results between both experimental methods was estimated around 0.08%.

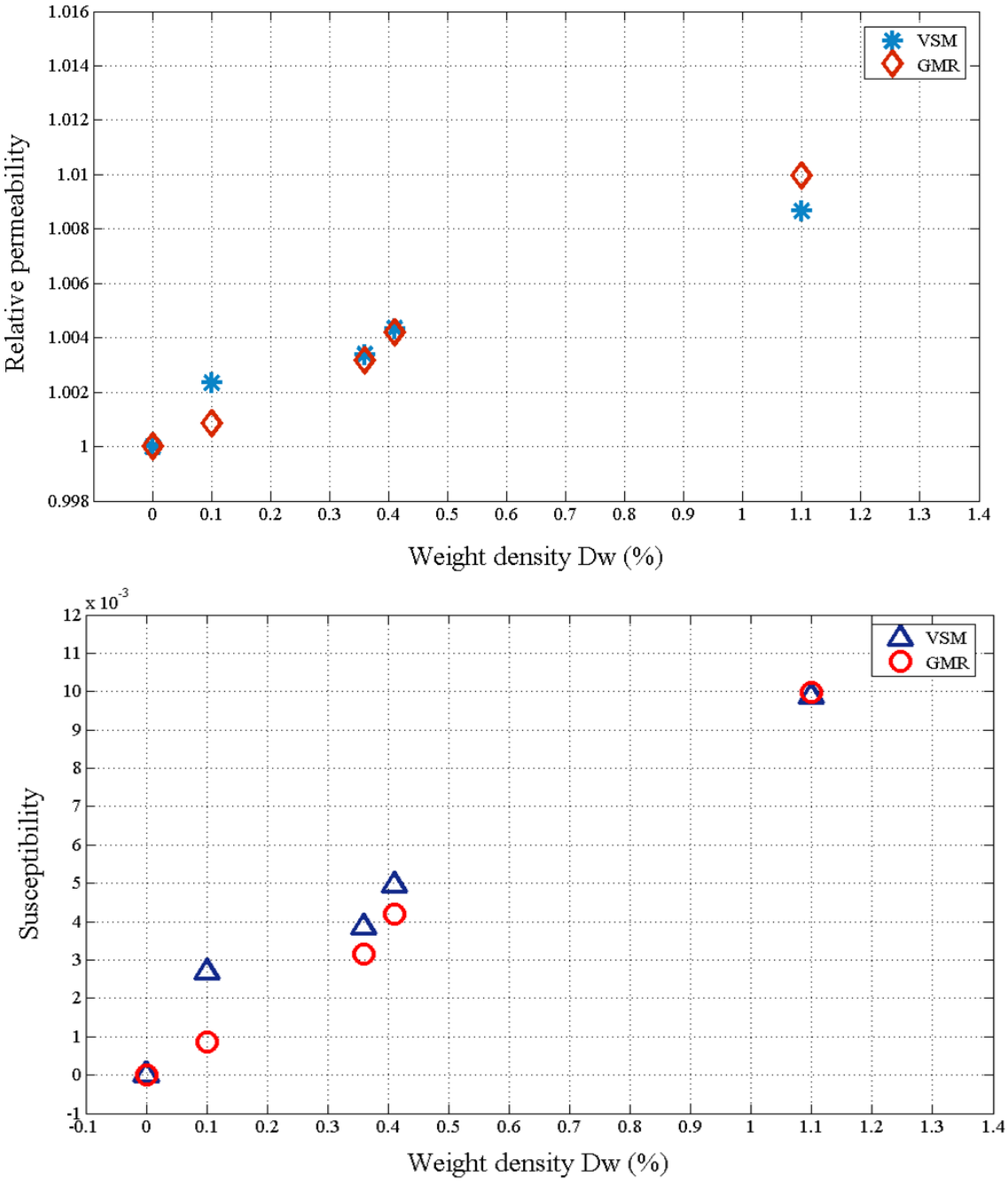

Figure 3.18 The experimental results of relative permeability and susceptibility according to several weight densities (%) of ferrofluid.

The GMR needle probe was used to estimate the D_w of the magnetic fluid, by measuring the applied magnetics flux density outside (B_0=152.5 μT) and the magnetic flux density inside (B_1) of cavities.

The demagnetizing factor (N) depends on the shape ratio of the cavity (S). In our case, in this experiment it has cylindrical shaped cavities with S=1 and demagnetizing factor (N) is equal to 0.333.

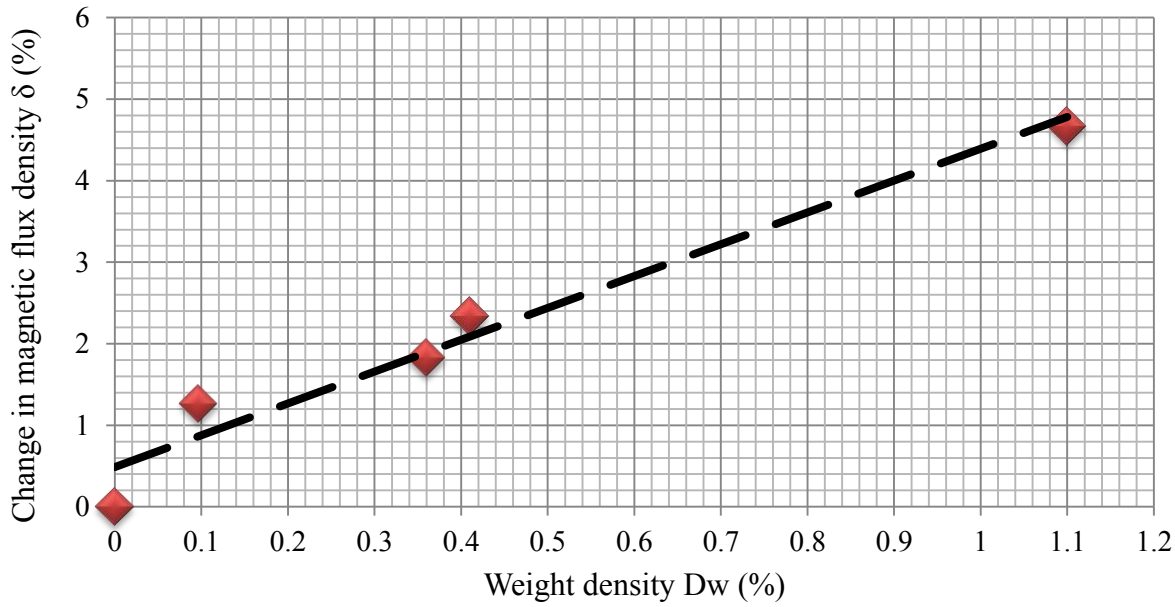

Figure 3.19 The change of magnetic fluid density (δ %) with different weight densities (D_w %).

According to equation 3.8 we have calculated the relationship between the changes of the magnetic flux density (δ %) and the magnetic fluid weight density (D_w %). The experimental results (Figure 3.19) are performed to estimate magnetic flux density by changing the value of weight density. The results are linear and proportional to change of weight density.

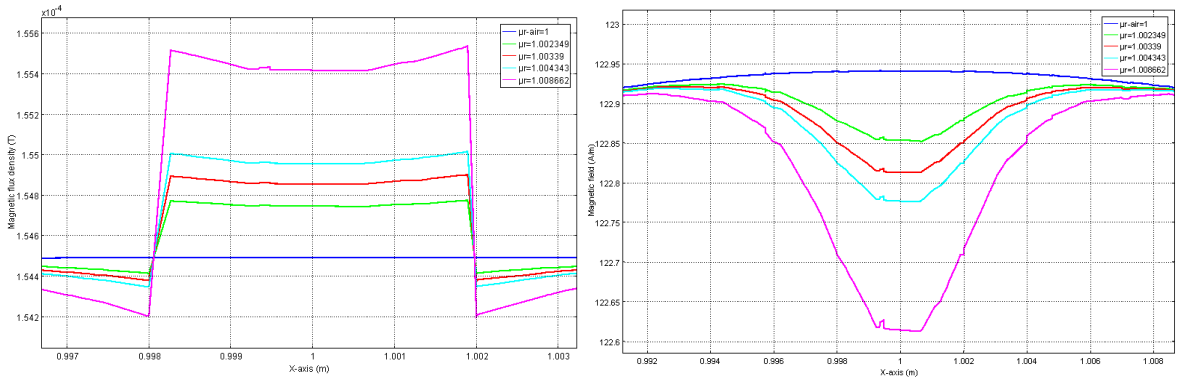

a) b)

Figure 3.20 Variations of the curve of magnetic flux density (a) and magnetic field (b) in midpoint of the Helmholtz coil by presence the different ferrofluids (μr up than μr−air).

Figure 3.20 a and b presents the value of relative permeability for each ferrofluid (different D_W %) estimated by the GMR sensor as a function of the magnetic flux density (T) and magnetic field (A/m). These results have been simulated by COMSOL 4.0a. In the center of Helmholtz coil where a magnetic flux density 154.5 μT is created, placed a glass cavity (5×4 mm). Changing the concentration of a magnetic fluid in a glass flacon, we have examined its

behavior in a magnetic field. A tetrahedral fine is chosen for Helmholtz coil and a tetrahedral extra fine for glass cavity.

The peak of the curves (where the cavity of ferrofluid is placed) was deformed (see Figure 3.20). We explain this according to the equation 3.12. For each material that has the relative permeability more than μr-air, the magnetic flux density (B) increases and the magnetic field (H) respectively decreases and vice versa.

$$\begin{aligned} &H = \frac{B}{\mu_0 \mu_r} \\ &if\ \mu_r > \mu_{rair}, H \downarrow B \uparrow; \\ &if\ \mu_r < \mu_{rair}, H \uparrow B \downarrow . \end{aligned} \tag{3. 12}$$

3.3 Estimation of magnetic fluid weight density and relative permeability and susceptibility of magnetic fluid-D

3.3.1 Specifications of magnetic fluid-D

A magnetic fluid-D (MAG-D) is a specific magnetic resonance imaging (MRI) contrast that contains an aqueous dispersion of a large number of superparamagnetic iron oxide nanoparticles with hydrodynamic diameters of 100−200 nm [88]. The magnetic fluid-D is produced by Chemicell Company and it can be injected as an intravenous injection or IV, to reduce the time dissemination and immediate imaging of the liver.

The fluid MAG-D is also applied in other applications such as in cell separation and magnetic drug targeting. Magnetic cell separation is widely utilized and very inexpensive method to separate different types of cells. The magnetic beads used in this method represent a mix of a magnetic iron oxide polymer in the range from 10 nm to 10 μm [89]. Magnetic drug targeting is a transportation of drugs to target tissue place with aid and use of an external magnetic field toward a tumor [90]. Table 3.5 presents the product information of the fluid MAG-D.

Table 3.5 The specification of the fluid MAG-D [88].

Volume	1.5 ml	
Size of particles	100 nm	200 nm
Number of Particles	1.8×10^{15}/g	2.2×10^{14}/g
Weight of Volume	25 mg/ml	
Density of each particle (Magnetite)	5.17 g/cm^3	
Magnetic core	Magnetite (Fe_3O_4)	
Color	Brown	

The microscopic image of the fluid MAG-D with diameter equal to 200 nm is shown on Figure 3.21. This photo is obtained with an optical microscope with 1000 times zoom.

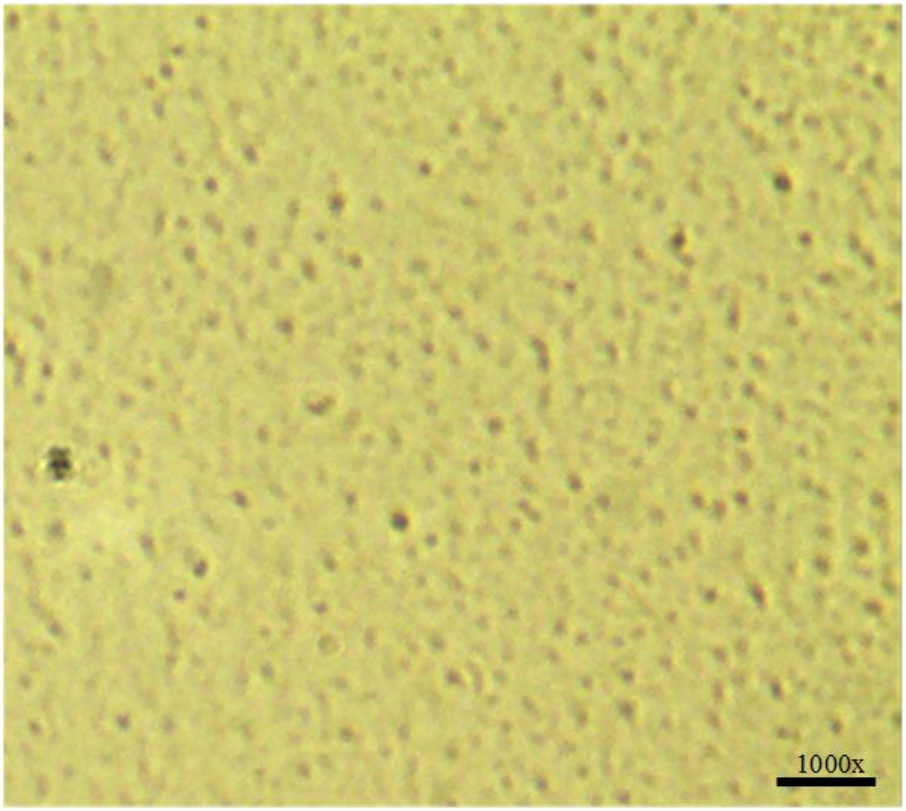

Figure 3.21 The fluid MAG-D (200 nm in diameter).

3.3.2 Preparation of different concentrations of fluid MAG-D

Based on the fluid MAG-D (200 nm) we have prepared several concentrations of different weight densities (D_W) by mixing it with distilled water, this, order to measure the magnetic fluid parameters such as relative permeability and susceptibility of different dilutions with the

GMR sensor. As we noted about this fluid, it's particles are superparamagnetic and have a magnetite core ($Fe_3O_4 = Fe^{II}(Fe^{III})_2O_4$).

The weight density and volume density of pure fluid MAG-D can be determined from the equations 3.1 and 3.2.

We have stocked several concentrations such as 1:1, 1:3, 1:6, 1:10, 1:20 and 1:40 from the pure fluid MAG-D. The amount of weight densities and volume densities for all concentrations have been calculated and are presented in Table 3.6.

Table 3.6 Weight and volume density details of different concentrations of fluid MAG-D.

Sample	Weight density (Dw)	Volume density (Dv)
Pure	0.02451	0.00484
1:1	0.01238	0.00242
1:3	0.00622	0.00121
1:6	0.00356	0.00069
1:10	0.00227	0.00044
1:20	0.00119	0.00023
1:40	0.00061	0.00012

Figure 3.22 presents the hysteresis curves of pure fluid MAG-D and other solutions, these results were obtained with a VSM (model 3374−140). In this experience 20 µl of each magnetic fluid was poured by micro pipette into the special VSM's cavity. It is observed from Figure 3.22 that the magnetization of the fluid has perceptibly reduced with decreasing the dilution when compared to primary solute (pure fluid MAG-D).

The results for diluted magnetic fluid obtained with the VSM are in concordance with the by theoretical calculations. In this method we assume that the results for each diluted solution are deduced as prorata from the results for the initial pure fluid-D by multiplication each diluted solution to the degree of dilution to obtain the same result as pure fluid-D. This approach is important to ensure the accuracy and correctness of concentrations prepared from the fluid MAG-D. As shown in Figure 3.23, the results are close and confirm each other.

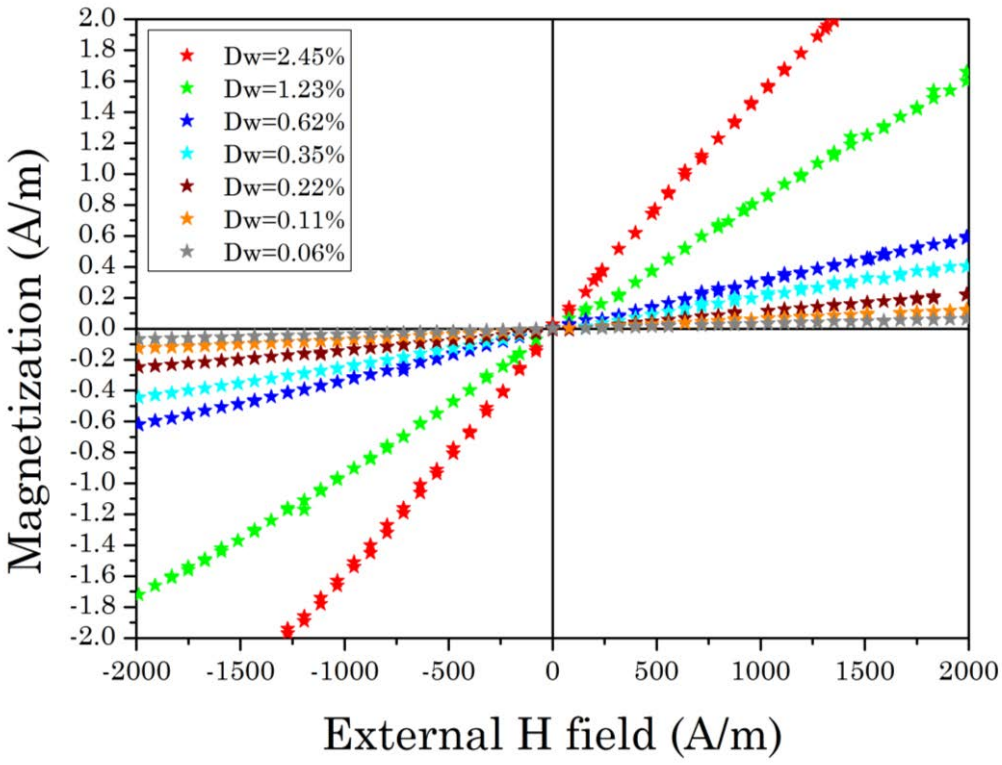

Figure 3.22 The hysteresis curves of fluid MAG-D's concentrations.

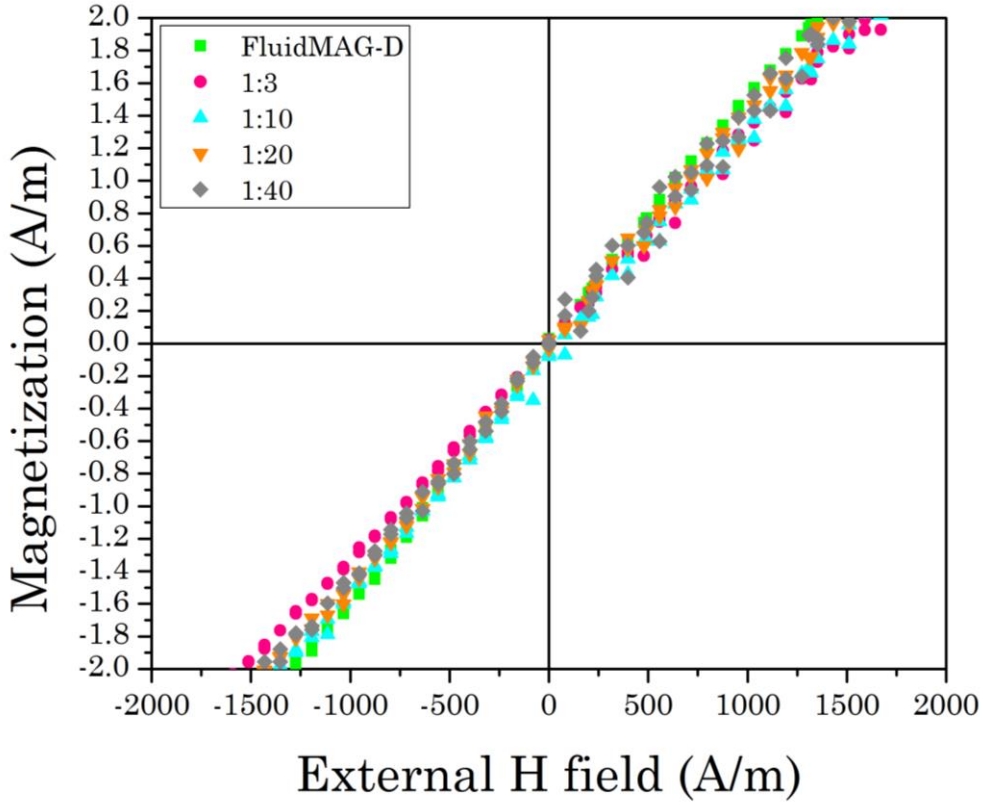

Figure 3.23 Confirmation the results of different concentrations with use the VSM's data.

3.3.3 Experimental measurement setup and method

The main goal of this experiment is to measure and to determine the basic magnetic properties of fluid MAG-D such as relative permeability and susceptibility. For this purpose we have prepared the measurement setup, presented in Figure 3.24.

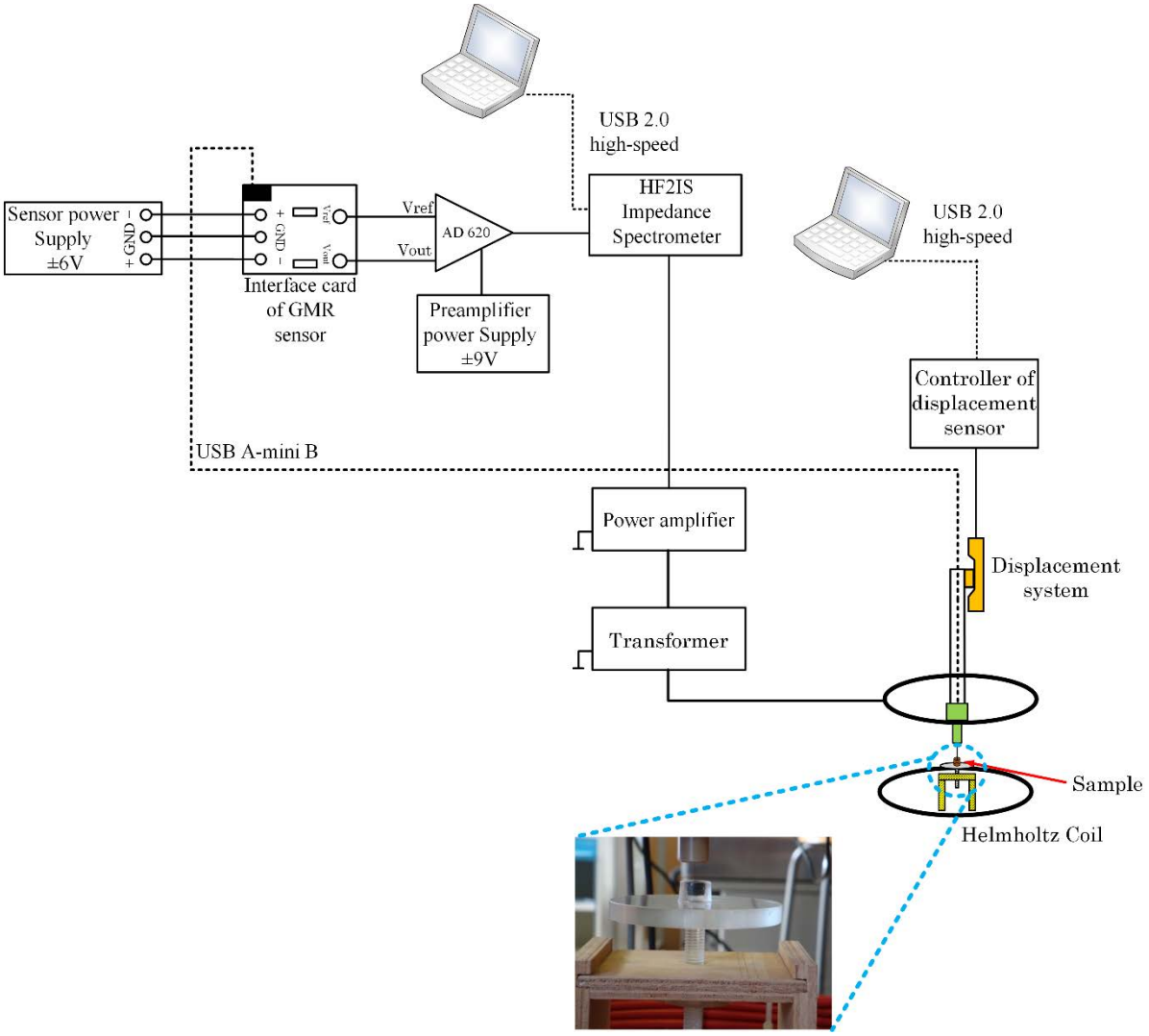

Figure 3.24 Schematic of measurement setup used to characterize the magnetic properties of ferrofluid MAG-D 200 nm.

Like in the previous experiments the setup consists of two main parts:

1. The measurement part based on a GMR sensor with high detection capability.
2. The Helmholtz coil setup, to generate a uniform magnetic field.

The second model of the GMR sensor was used in this research. Supplementary details of the sensor specification and the sensitivity analysis of this model are described in Chapter 2. The characterization of sensor is performed before each measurement in order to increase the accuracy of analysis.

The GMR sensor is connected to DC power supply (±6 V) by circuit interface where the resistance is placed to prevent the current. The differential signal Vout−Vref was supplied to preamplifier AD 620, where output signal was strengthened approximately by 1200 times (62 dB). The preamplifier AD 620 is fed by another power supply (±9 V). After that the signal has strengthened by AD 620 and has sent to HF2IS Impedance Spectrometer to get and record the output data (Vrms, phases) of the GMR signal by interface program of the HF2IS Impedance Spectrometer.

The operating frequency of the Helmholtz coil is 75 Hz and the input signal generated by the HF2IS Impedance Spectrometer is equal to 180 mV. The value of magnetic flux density (B) produced in the center of Helmholtz coil is 185.7 µT.

To provide protection of the needle against any shock, we have used the previously described (see Chapter 2) displacement system.

The measurement setup is controlled by two laptops, one to drive the displacement system and the other to control the HF2IS Impedance Spectrometer for data storage.

In the first step, the needle's sensor was precautionary placed at the center of the Helmholtz coil to record the data of the sensor without the magnetic fluid (only air). This data is utilized to calculate the magnetic flux density variations (see the equation 3.8) for different concentrations. In a second step, the 450 µl of pure fluid MAG-D was poured to cylindrical shape cavity with dimension 8×8 mm by micro pipette. The cavity is placed at the center of the Helmholtz coil. Then, the needle's sensor was inserted very carefully in the midpoint of the cavity. After each measurement, the needle of the GMR sensor was warily get out from the magnetic liquid's cavity and cleaned very carefully by distillated water and soft sponge in order to reduce the percentage of testing errors.

This measurement method was utilized for the other fluids with different concentrations (weight densities varying from 2.45 %, 1.23 %, 0.62 %, 0.35 % to 0.22 %).

Additionally, we should point out that the cavity was produced by a substance named Polydimethylsiloxane (PDMS).

3.3.4 Analysis of the GMR sensor's results and comparison of experimental and theoretical results

In this part we present the experimental results obtained by the first model of the GMR sensor. We have calculated by applying the results to equation 3.8 the relationship between

the magnetic flux density variations (δ %) and the magnetic fluid weight density (Dw %) for all magnetic fluid's low-concentrations. The experimental results are linear and proportional to changes of weight density (see Figure 3.25).

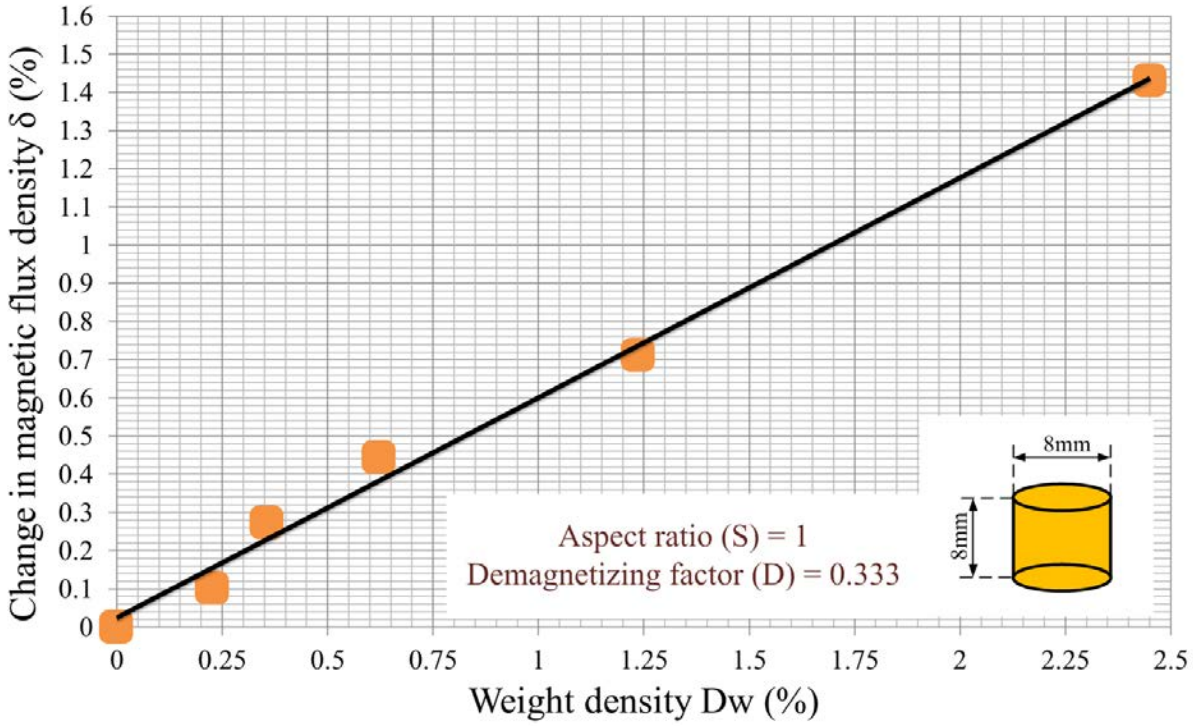

Figure 3.25 Estimating the changes in magnetic flux density with different weight densities.

The demagnetizing factor (N) for an ellipsoid cavity depends on the aspect ratio (S) of the cavity. According to the dimensional relation (height/diameter), we have calculated the aspect ratio of each ellipsoid cavity. For a cylindrical shaped cavity, the aspect ratio is equal to 1 and the demagnetizing factor corresponds to 0.333.

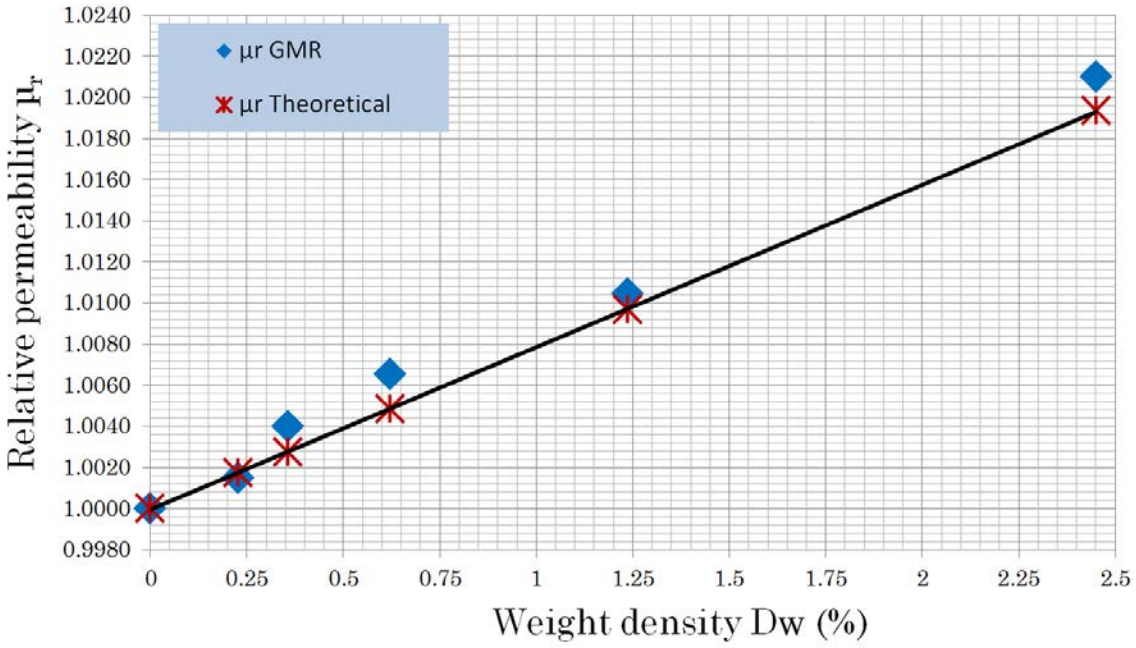

Figure 3.26 Experimental results of the relative permeability (μ_r) as a function of different weight densities Dw (%) and comparison with the theoretical results.

The experimental results of relationship between relative permeability depending on several fluid MAG-D weight densities obtained by needle type GMR sensor are presented in Figure 3.26. To confirm these findings, we have compared the experimental and theoretical results according to equation 3.7. It can be seen that theoretical and experimental results have a good agreement with an average error of 0.11%.

3.4 Conclusion

The beginning of this part explains theoretical method for magnetic fluid weight density (D_W) and magnetic fluid volume density (D_V) calculations for different concentrations. In the next parts, we have presented the analytical way to estimate the magnetic flux density (δ) relative permeability (μ_r) and susceptibility (χ) according to different concentrations (several magnetic fluid weight densities).

We have prepared the different concentrations from two magnetic liquids. They differ in size, number and density of particles. Then, we have measured their magnetic properties such as relative permeability (μ_r) and susceptibility (χ) by using our GMR sensors.

In order to confirm the experimental results of first liquid obtained by GMR sensor, we have utilized the vibrating sample magnetometer (VSM). For second ferrofluid (fluid MAG-D) the experimental results have been compared with theoretical results. In both comparisons the results are similar and confirm each other with an average error 0.08% for the first ferrofluid's results and off 0.11% for the second ferrofluid's results.

Chapter 4 : Detection of Escherichia coli by a GMR sensor

4.1 Introduction

Bacteria are the earliest group of organisms of the biological life. The first bacteria probably appeared about 3.5-4 billion years ago.

It was only during the 17th century that Anton van Leeuwenhoek, a Dutch scientist and father of microscopy, was the first who observed bacteria. He also developed and improved a microscope with a magnification of 270 times.

Most bacteria are colorless and do not produce pigments, only a few are painted in purple or green. But many bacteria colonies have a bright color, which is caused by the release of the colored substance in the environment or pigmented cells.

The first part of chapter focuses on bacterial cells, particularly on Escherichia coli. We explain about one of the deadliest and most famous called Escherichia coli O157:H7 and related illnesses.

In a second step, we propose to detect a magnetic marker by GMR sensor. These beads are widely used to separate the Escherichia coli O157:H7 from food, feed, water and etc. Characterization of the magnetic properties involved in this interaction between the bacteria and its marker is another aim of this chapter.

4.2 Summary of Escherichia coli

4.2.1 Definition of Escherichia coli

In the warm blooded (endotherms) intestine, friendly bacteria exist together with harmful ones, the optimal content which is necessary for the full process of gastrointestinal tract. One of the representatives of these bacteria is Escherichia coli (E. coli). It is recognized that E. coli is widely spread in nature, animals and humans, living in the intestine and it is required for normal body functioning.

E. coli has many strains, most of which belong to the natural human intestinal microflora, helping to prevent the development of harmful microorganisms and involving into the process of the synthesis of vitamins B and K [91]. However, some of its variants can lead to severe poisoning and to certain diseases such as intestinal dysbiosis, colibacillosis, etc. Furthermore, with long-term use of antibiotics a human's bacterial balance is disturbed and E. coli could perish, causing the development of intestinal dysbiosis. In addition to human and animal intestines, the bacteria can live in polluted water and soil.

The E. coli was discovered in 1885 by German bacteriologist Theodor Escherich [92]. E. coli is a gram-negative rod-shaped bacterium of the family enterobacteriaceae and it is classified as a prokaryotic. The cells of prokaryotes, which bacteria include, unlike eukaryotes, have a relatively simple structure. In prokaryotic cell, organized nucleuses are absent and hence it has DNA floating in the liquid (cytoplasm) center of the cell. It contains only one chromosome, which is not separated from the rest of the cell membrane, and lies directly in the cytoplasm. Since the bacterial chromosome contains very little protein and a DNA strand, it can only be conditionally called chromosome [93]. Unlike prokaryote which has a circular DNA, DNA of eukaryotic is linear. The schematic of prokaryotic and eukaryotic cells is shown in Figure 4.1.

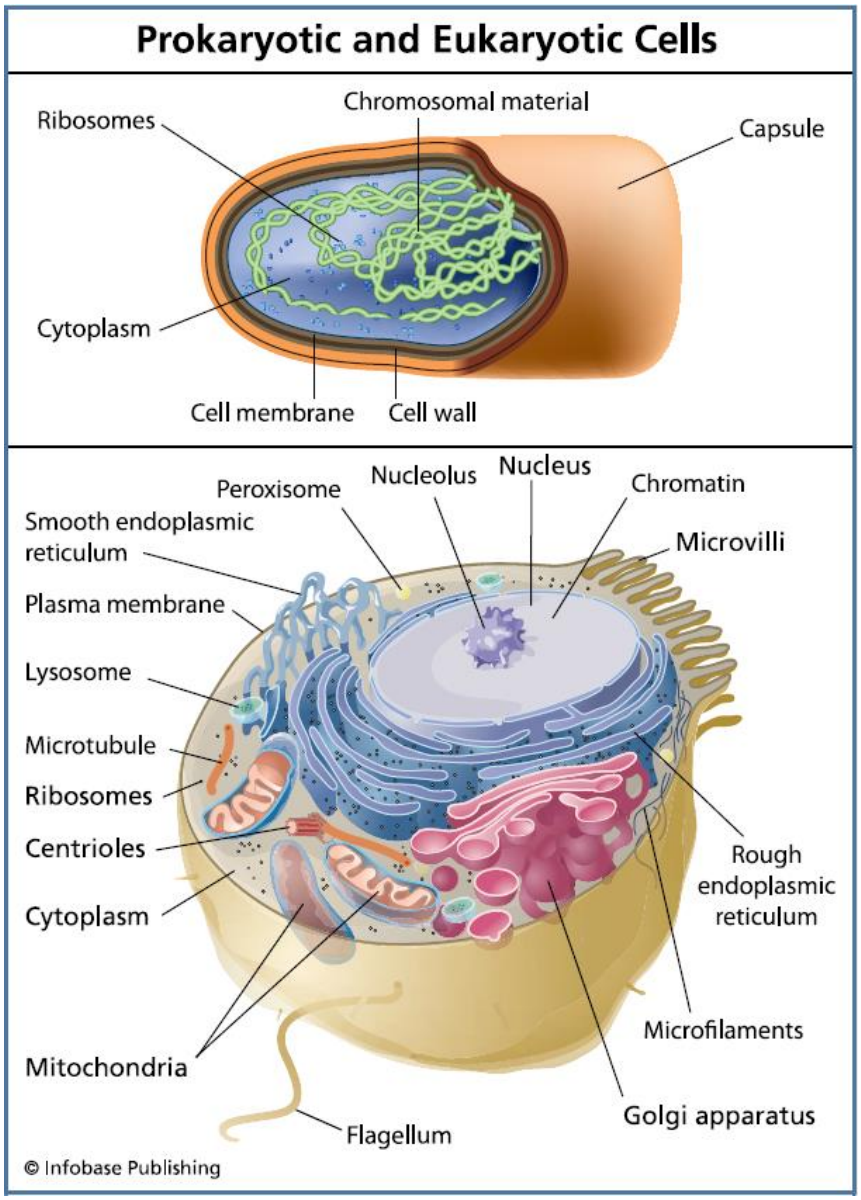

Figure 4.1 The structure of prokaryotic cell (top) and eukaryotic cell (bottom) [94].

The cytoplasm of prokaryotes if compared with the cytoplasm of eukaryotic cells is much poorer in composite structures. Moreover, prokaryotic cells like eukaryotic cells have many ribosomes, but the eukaryotic cell's ribosomes are larger and more complicated [95].

Table 4.1 Principal differences between prokaryotic cells and eukaryotic cells [96, 97].

Characteristic	Prokaryotic cell	Eukaryotic cell
Size of cell	Typically 0.2-2.0µm in diameter	Typically 10-100 µm in diameter
Example	Bacteria and Archaea	Animals and Plants
Nucleus	Absent	Present
Membrane-enclosed organelles	Absent	Present; examples include lysosomes, Golgi complex, endoplasmic reticulum, mitochondria & chloroplasts
Flagella	Consist of two protein building blocks	Complex; consist of multiple microtubules
Cell wall	Usually present; chemically complex	Only in plant cells and fungi (chemically simpler)
Plasma membrane with steroid	Usually no	Yes
Cytoplasm	No cytosketeton or cytoplasmic streaming	Cytoskeleton; cytoplasmic streaming
Ribosomes	Smaller	Larger
Cell division	Binary fission	Mitosis
Number of chromosomes	One, but not true chromosome	More than one
Sexual reproduction	No meiosis; transfer of DNA fragments only (conjugation)	Involves meiosis

Prokaryotic cells, as well as eukaryotic cells, are covered with the plasma membrane, which is located on top of the cell membrane or mucous capsule. Despite of its relative simplicity, prokaryotes are typically independent cells. Table 4.1 presents the major differences between prokaryotic and eukaryotic cells.

Strains flagella of bacteria are able to move around. Flagella can only be considered by an electronic microscope. The bacterial cells are arranged in different ways according to the number and position of its flagella [98, 99]:

A. Atrichous are devoid of flagella or hair (such as Lactobacillus and Pasteurella);
B. Monotrichous have a single flagellum (such as Caulobacter and Vibrio cholerae);
C. Amphitrichous have flagellum at both poles of the cell (Spirillum serpens);
D. Cephalotrichous have more than one flagella attached at one end (pseudomonas fluorescens);
E. Lophotrichous bunches of flagella present on one pole of the bacterium (Pseudomonas, Chromatium, Bartonella bacilliformis);
F. Peritrichous have a large number of flagella, which are located across the surface of cells (E.coli and Erwinia).

Various arrangements of bacterial flagella are presented in Figure 4.2.

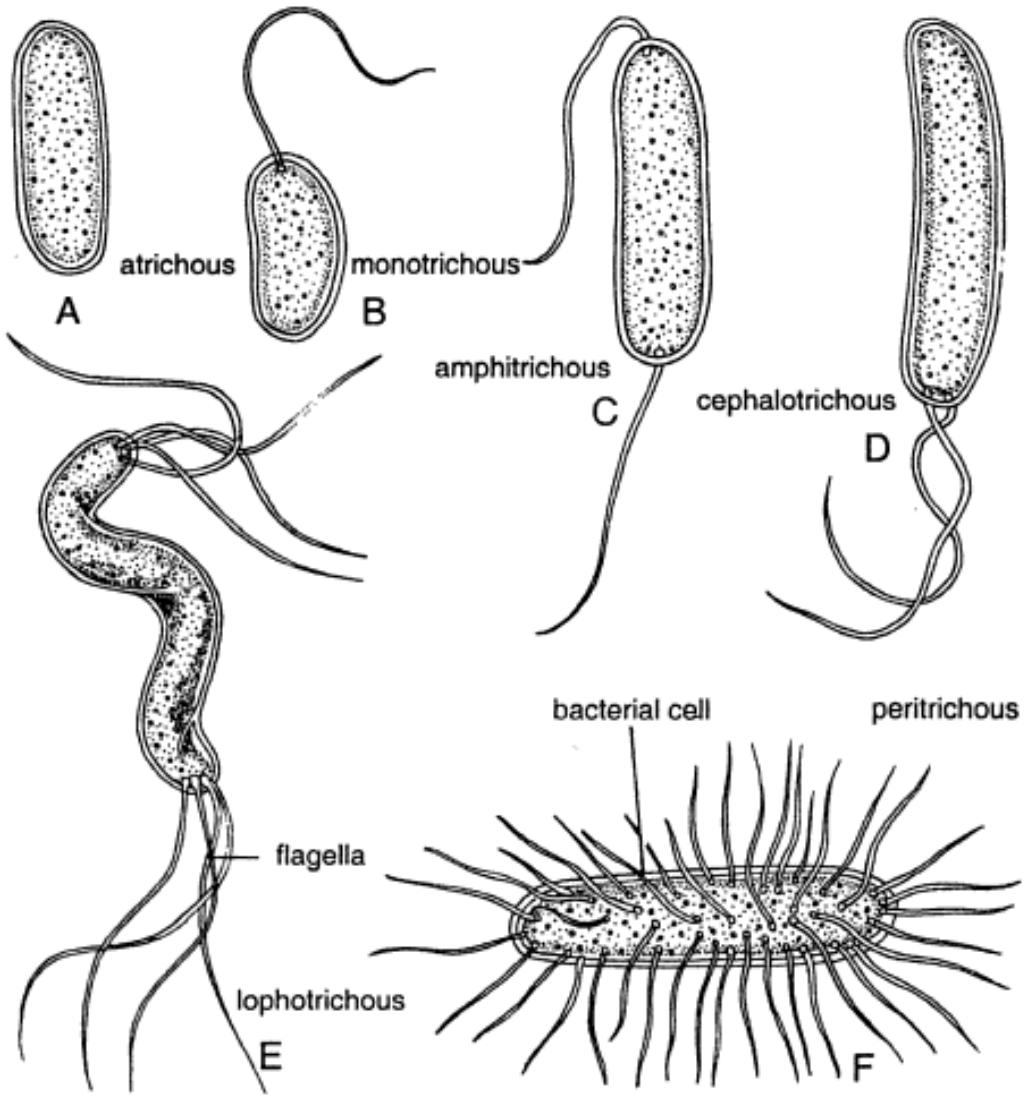

Figure 4.2 The different schemes of bacterial flagella's arrangement [98].

4.2.2 Specification of E. coli

The size of this bacteria as shown in Figure 4.3 is very small around 0.5 μm in diameter and 2−3 μm in long and in cell volume is approximately 0.6–0.7 μm^3 [100] rod shaped or similar to a stick with square ends.

Escherichia coli can inhabit on a wide variety of substrates. Under anaerobic conditions, E. coli generates as a waste product: lactate, succinate, ethanol, acetate and carbon dioxide. Often during this process molecular hydrogen is formed which interferes the above metabolites' creation. Accordingly, E. coli often coexists with microorganisms that consume hydrogen - for example, methanogens or bacteria in order to regenerate sulfate [101].

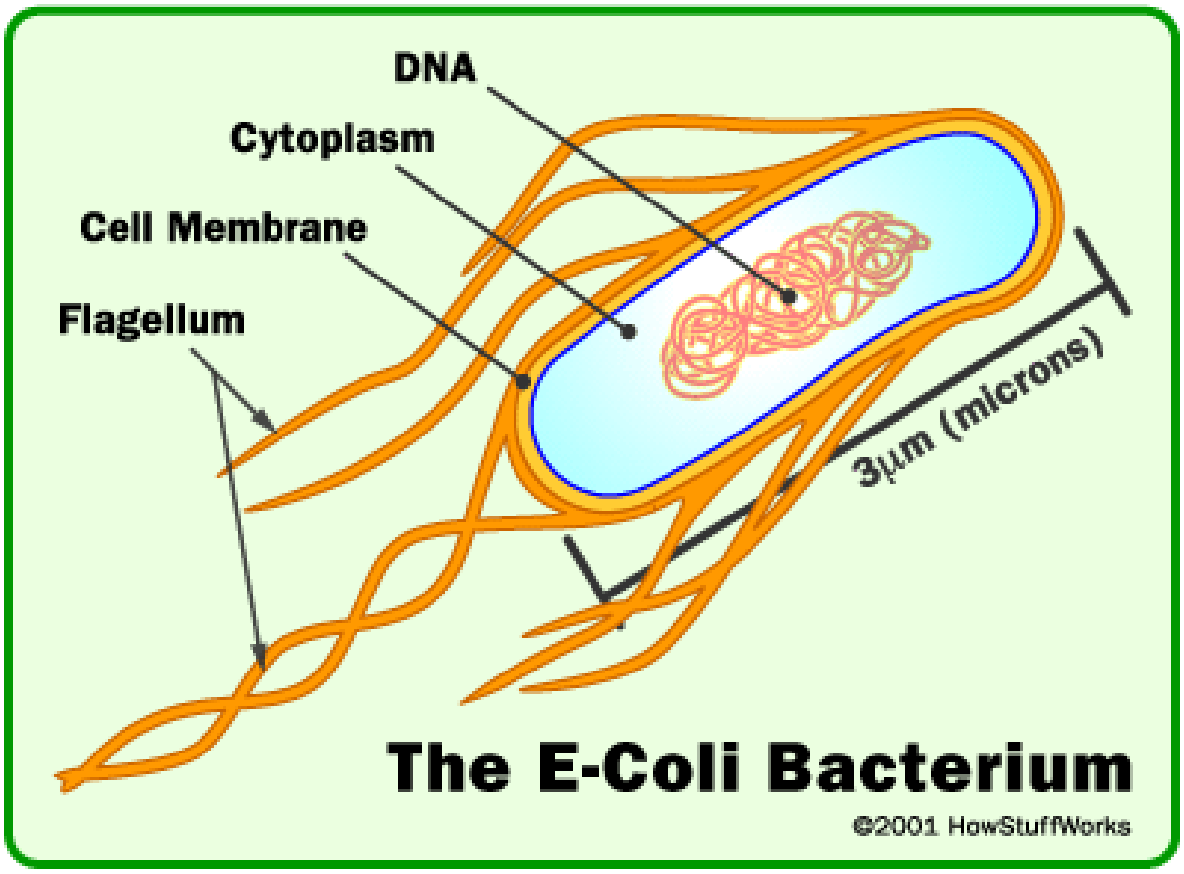

Figure 4.3 E. coli bacteria [102].

Optimal growth of E. coli is achieved at 37°C, some strains can share at temperature up to 49°C [103]. Growth can be stimulated by aerobic or anaerobic respiration, different pairs of oxidizing and reducing agents, including the oxidation of pyruvate, hydrogen, amino acids, and oxygen reduction, nitrate, etc.

The process of reproduction in bacteria can be explained that by increasing of the prokaryotic cells, consistent increasing of the number of chemical components, of which bacteria is built, occurs. The growth is a result of a coordinated set of biosynthetic processes under strict regulatory control. Furthermore, the growth of the cells is not limited.

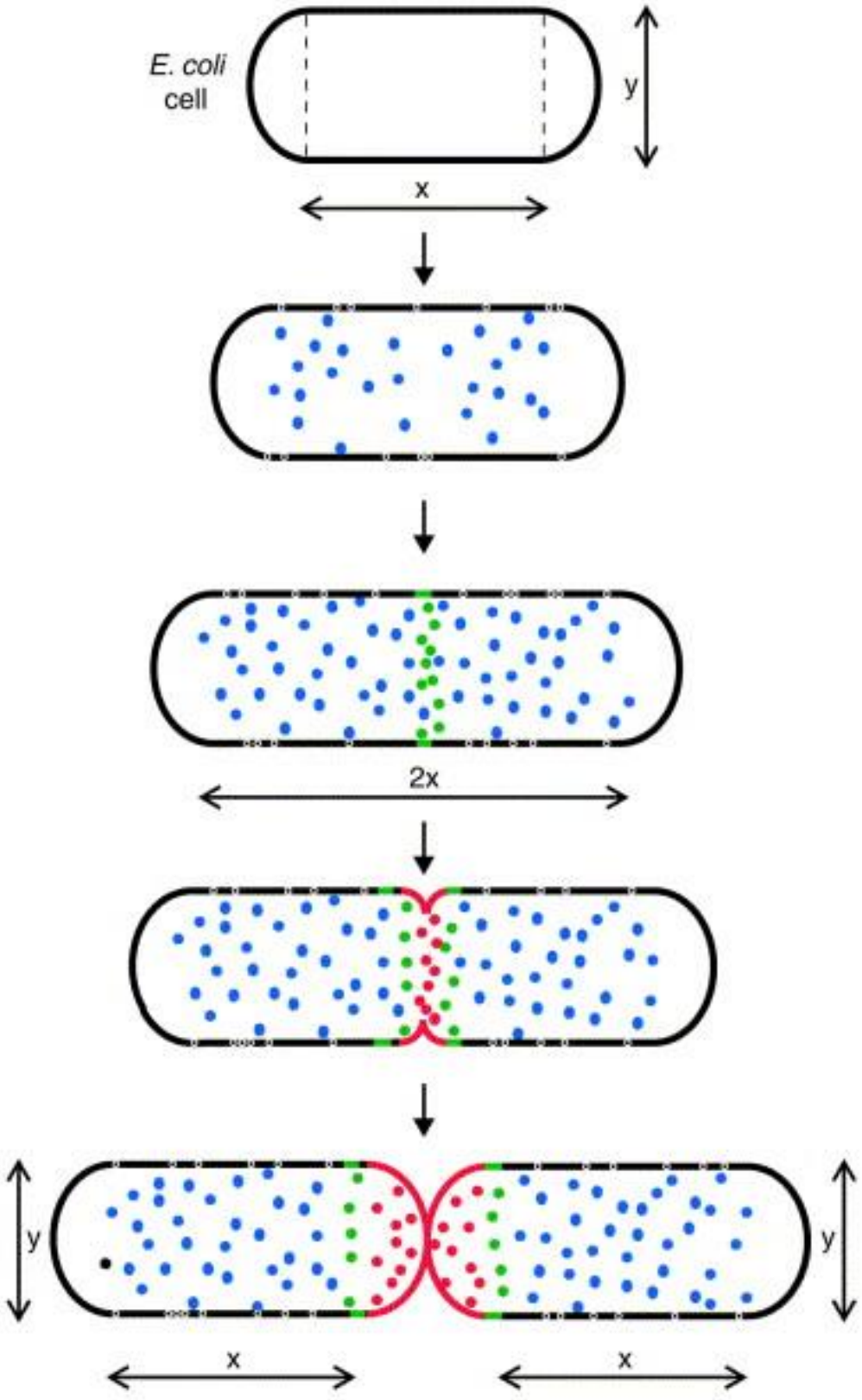

Figure 4.4 The general process of binary fission in E. coli [104].

Vast majority of prokaryotes are characterized by homolographic binary cross-division, leading to the formation of two identical cells. With this method of division there is

symmetry with respect to the longitudinal and transverse axis. The majority of gram-positive eubacteria and filamentous cyanobacteria cell division occurs through the synthesis of the transverse partitions, running from the periphery to the center [105]. Therefore, in the middle of the cell there is a ring invagination, accompanied by the formation of different mesosomes [106]. They are formed in a transverse tab divider, and they are actively involved in the synthesis of peptidoglycan and other cell wall's components.

In E. coli, constriction appears in place of division (midcell) and gradually increasing inward curvature of the cytoplasmic membrane and cell wall. Furthermore, in midcell of E. coli the coordinated action of different proteins (about 10) is required to divide [107]. Synthesis of a new cell wall can occur in several places, or only in the zone of transverse walls. Figure 4.4 presents binary fission diagram of E. coli, as observed from this image the cell maintains its diameter Y during the division. The E. coli bacteria can copy itself very quickly around each 20 minutes [108].

4.2.3 Diseases caused by Escherichia coli

More than half of the diseases caused by Escherichia coli are urinary tract infection, other common infections are originating from the liver and bile ducts of the abdominal cavity, skin and lungs. Occasionally, E. coli atrium is indistinguishable in patients with bacteremia, however it can be detected neoplastic or hematological diseases [109].

Invasive and toxigenic E. coli strains provokes diarrhea in children and adults. Enterohemorrhagic Escherichia coli (EHEC) causes significant morbidity and mortality worldwide, it is a subset of pathogenic E. coli which induces life threatening hemorrhagic colitis and hemolytic uremic syndrome (HUS) [110, 111]. Especially, the cases in small children and an elderly are very difficult and heavy.

Infection caused by EHEC is usually occurs by the fecal-oral route by eating contaminated meat, milk, vegetables, etc.

Ingestion of even small amounts of these bacteria can cause serious illness. Transmission from person to person usually can be seen in kindergartens or nurseries, within families, mental health facilities, etc.

Some strains type of E. coli such as E. coli O157:H7 and E. coli O104:H21 synthesize potentially deadly toxins.

The E. coli O157:H7 is a serotype of E.coli that has the ability to produce toxins such as Shiga toxins or verotoxins [112]. Although most strains of the E. coli are natural inhabitants of the intestines of animals, the strain O157: H7 causes severe damage of the epithelium and endothelium of the large intestine. The E. coli O157: H7 is found in the intestines of healthy animals, which are the reservoir of infection.

The E. coli O157: H7 causes bloody diarrhea and also referred as EHEC [94], which became famous in 1990 by a deadly outbreak associated with ground beef.

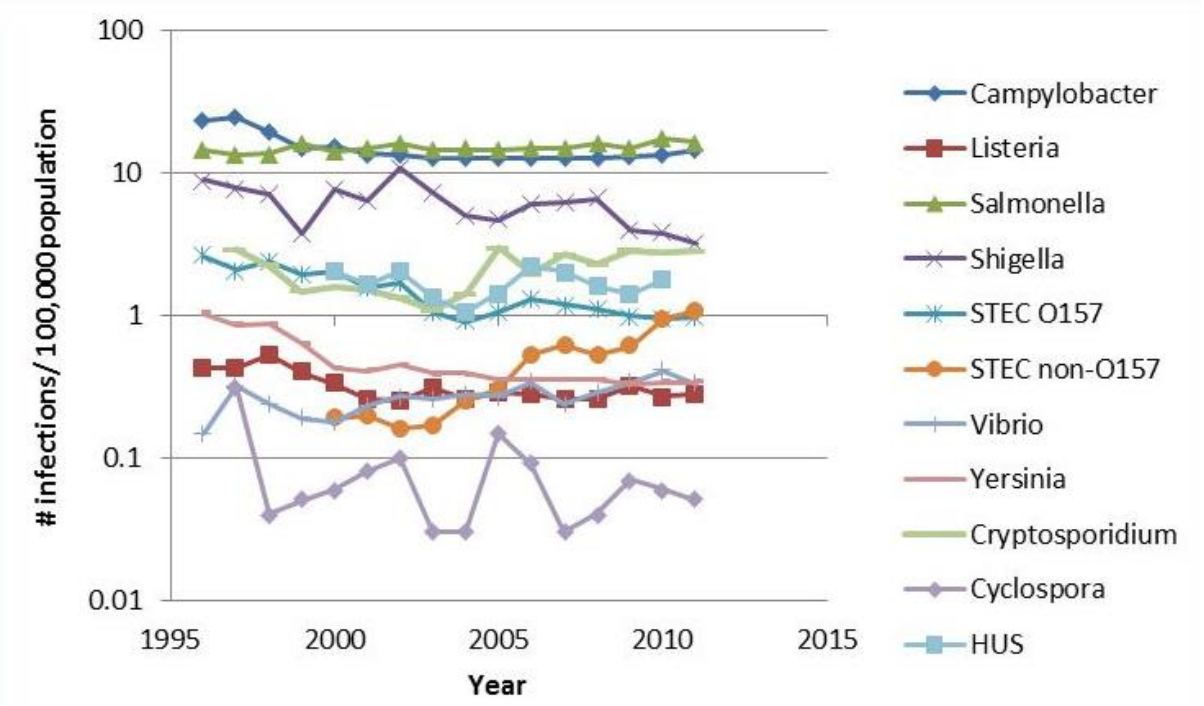

Figure 4.5 The number of foodborne disease cases in the United States between 1996 and 2011 [113].

Since the first outbreak, and to date, there were a significant number of cases of infection associated mainly with the consumption of beef, raw milk, etc. Figure 4.5 shows the number of cases of foodborne illness from 1996 to 2011 in USA. Furthermore, it has been underlined that the Shiga toxin-producing Escherichia coli (STEC) plays an important role in these statistics.

4.3 Detection of Escherichia coli O157:H7 by magnetic beads

4.3.1 A brief description of Dynabeads Max E. coli O157

As we have noted before, Escherichia coli O157:H7 is a toxin producing bacteria (like verotoxins or Shiga toxins); the main reservoir for E. coli O157:H7 is contaminated water and food, animal or their environment and feces of infected humans or animals. It causes

several foodborne and waterborne diseases such as stomach cramps, bloody diarrhea, nausea, vomiting. In most dramatic cases E. coli O157:H7 may provoke patient's death. Therefore using rapid and accurate methods for detecting the E. coli O157:H7 is very important in medical diagnostics.

Dynabeads® MAX E. Coli O157 is a biomagnetic marker which has been produced from uniform size of superparamagnetic spherical particles. These magnetic beads provide the rapid selective separation of E. coli O157:H7 from food, feed, water and environmental samples by applying a magnetic field [114].

This product is designed and fabricated by Life Technologies Company and offered in two different contents [114].

- 1ml of Dynabeads with 16 ml of 10 X buffer to dilute (see Figure 4.6),
- 5 ml of Dynabeads with 80 ml of 10 X buffer.

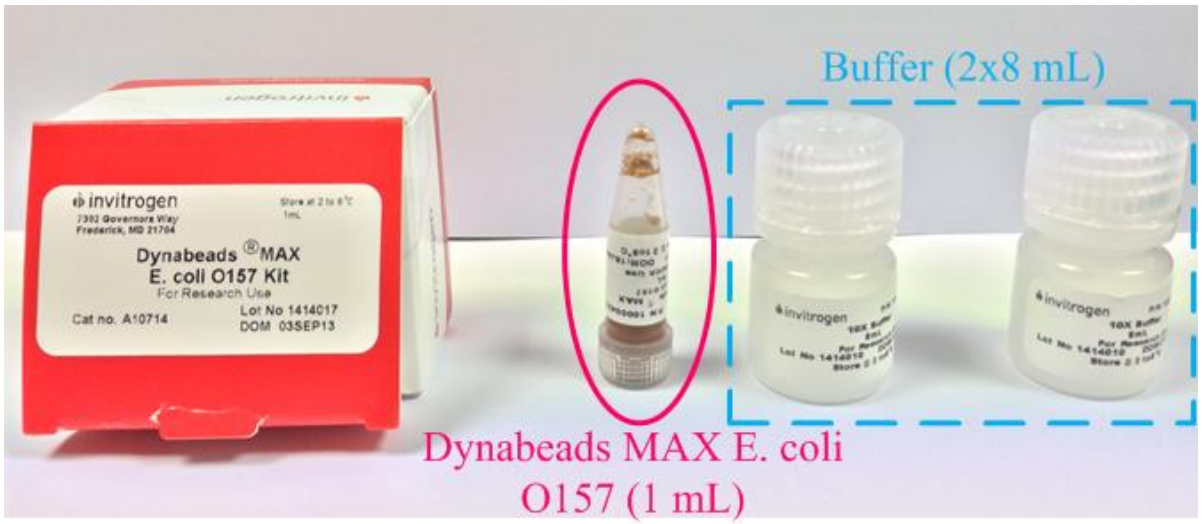

Figure 4.6 Pictures of Dynabeads MAX E. coli O157 and buffers.

We should point out that the major specifications of Dynabeads such as particle's weight density, size, number and magnetic core material of beads are confidential information. The Life Technology Company does not share these datasheets with their customers. For this reason, it would not be possible for us to calculate and determine theoretically the weight density (D_W), volume density (D_V) and also relative permeability (μ_r) and susceptibility (χ). Therefore, we were just able to measure these parameters (μ_r, χ) experimentally.

A trinocular microscope Realux LABO2 was used to get sight of the particles of Dynabeads. This microscope consists of four focusing objectives 4X, 10X, 40X and 100X (combined with 10X eyepiece). Additionally, in order to observe and save the movements of beads a

CMOS camera 3 Megapixel on the third eye (objectives) is fixed. The real image of optical microscope and the microscopic image of Dynabeads are shown in Figure 4.7(a) and (b). As presented in Figure 4.7 (b), the diameter of each particle is 1 µm. This image was obtained by focusing objective 1000X.

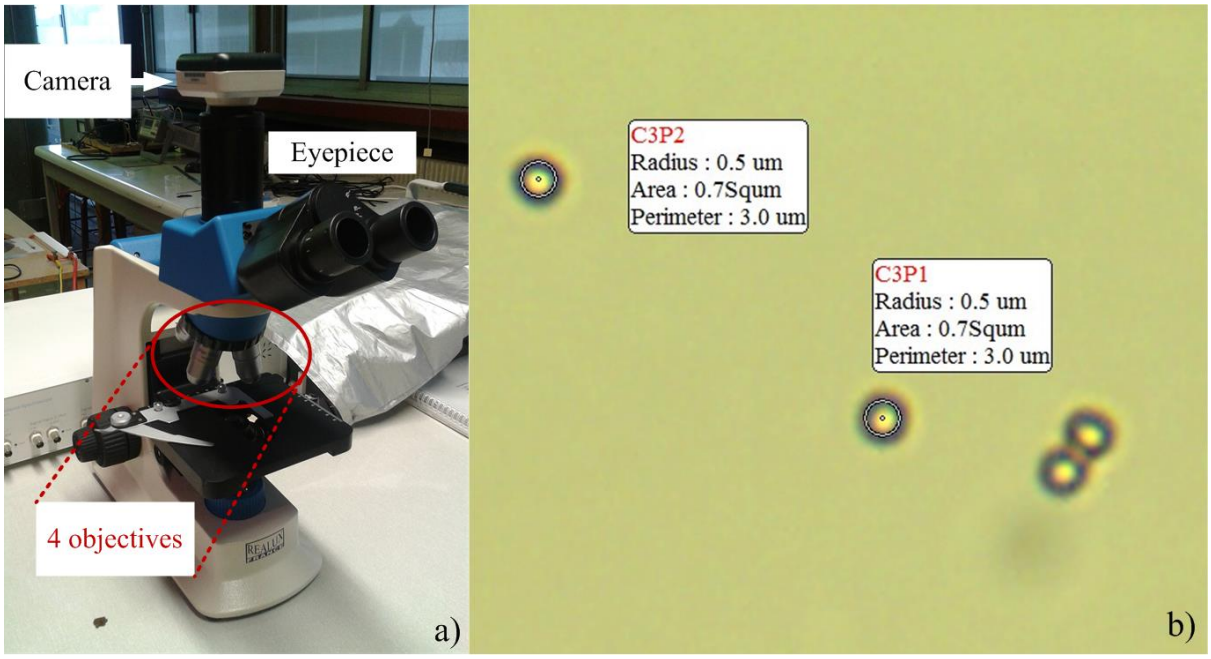

Figure 4.7 *Picture of microscope (a), the E. coli's marker under optical microscope (b).*

Additionally, it was interesting to make pH analysis to recognize the acid or base of the Dynabeds marker and Fluid MAG-D. For this purpose, the pH meter model HI 98103 was employed. This pH meter consists of a LCD to read the pH data and a screw-type connector pH electrode model HI 1270 with dimensions 80 mm×8 mm (see Figure 4.8). The pH meter's specifications are also presented in Table 4.2.

Figure 4.8 The pH meter and its pH electrode.

Table 4.2 Specifications of pH meter HI 98103[115].

Range	0.00 to 14.00 pH
Resolution	0.01 pH
Accuracy	±0.2 pH
Calibration	manual, 2 points
Electrode	HI 1270 (included)
Battery Type / Life	1.5V (2) / approximately 3000 hours of continuous use
Environment	0 to 50°C (32 to 122°F); RH max 95%
Dimensions	66 x 50 x 25 mm (2.6 x 2.0 x 1.0") - without probe
Weight	50 g (1.8 oz.) without probe

The pH meters must be calibrated before measurement the pH of samples. A two-point manual calibration was performed with using pH 7.01 and pH 4.01 buffer solutions. The image of two buffers to calibrate the pH meter is presented in Figure 4.9.

Figure 4.9 The pH 7.01 and 4.01 buffer solutions.

After the calibration, we have diluted the pure solution of Dynabeads with the 10 X buffer in order to obtain four different concentrations (1:1, 1:4, 1:8 and 1:16). For example, to prepare the 1:16 concentration, the 30 µL of Dynabeads marker was mixed with 480 µL of 10 X buffer (pH is equal to 6.24). Moreover, like Dynabeads four concentrations 1:1, 1:4, 1:8 and 1:16 form pure fluid MAG-D (200 nm) were confected. These samples were achieved by mixing the Fluid MAG-D and distilled water as a buffer with pH 5.43 (at room temperature). The micro pipette was used to obtain the exact concentration of each sample.

In general, buffer is a solution which can be added to moderate amounts of acid or base without significant change (approximately ±1) of its pH (acidity or alkalinity). Typically an acid buffer is made of a mixture of a weak acid and its conjugate base and similarly an alkaline buffer consists of a weak base and its conjugate acid [116].

Table 4.3 demonstrates the pH values of two pure ferrofluids (Dynabeads and MAG-D) and their solutions were diluted by buffers (10 X buffer and distilled water). We can conclude from these consequences that the buffer's behavior depends on the acidic or basic properties of the first material. Hence, the pH of pure Dynabeads is 7.48 and it is a basic substance, the 10 X buffer plays an acidic role and conversely it can be seen in Fluid MAG-D. In this case the Fluid MAG-D is an acid substance and after reducing the concentration by distilled water, the buffer plays a basic role.

Table 4.3 The pHs measurement of Dynabeads and fluid MAG-D solutions.

	Dynabeads MAX E. coli O157	Fluid MAG-D (200 nm)
Concentration of solutions	pH (10 X buffer)	pH (distilled water)
Pure	7.48	6.81
1:1	6.72	7.18
1:4	6.49	7.26
1:8	6.44	7.54
1:16	6.27	8.22

4.3.2 Experimental methods for estimation the magnetic properties of Dynabeads

a) First test:

The third model of the GMR sensor was utilized for this experience. The GMRIII sensor's sensitivity is equal to 245 (µV/µT), the other complementary details of the GMR sensor and the sensitivity analysis of this model were defined in Chapter 2.

At the beginning, the chip of the GMR sensor was located at the center of the Helmholtz coil by the positioning system to record the data of the sensor (Vrms and phase) without the presence of Dynabeads E. coli marker. As also explained on Chapter 2 the differential signal Vout−Vref was supplied directly to the HF2IS Impedance Spectrometer to record the output data (Vrms, phases) of the GMR signal by interface program of the HF2IS Impedance Spectrometer. Figure 4.10 presents the experimental setup to measure the magnetic properties of Dynabeads marker.

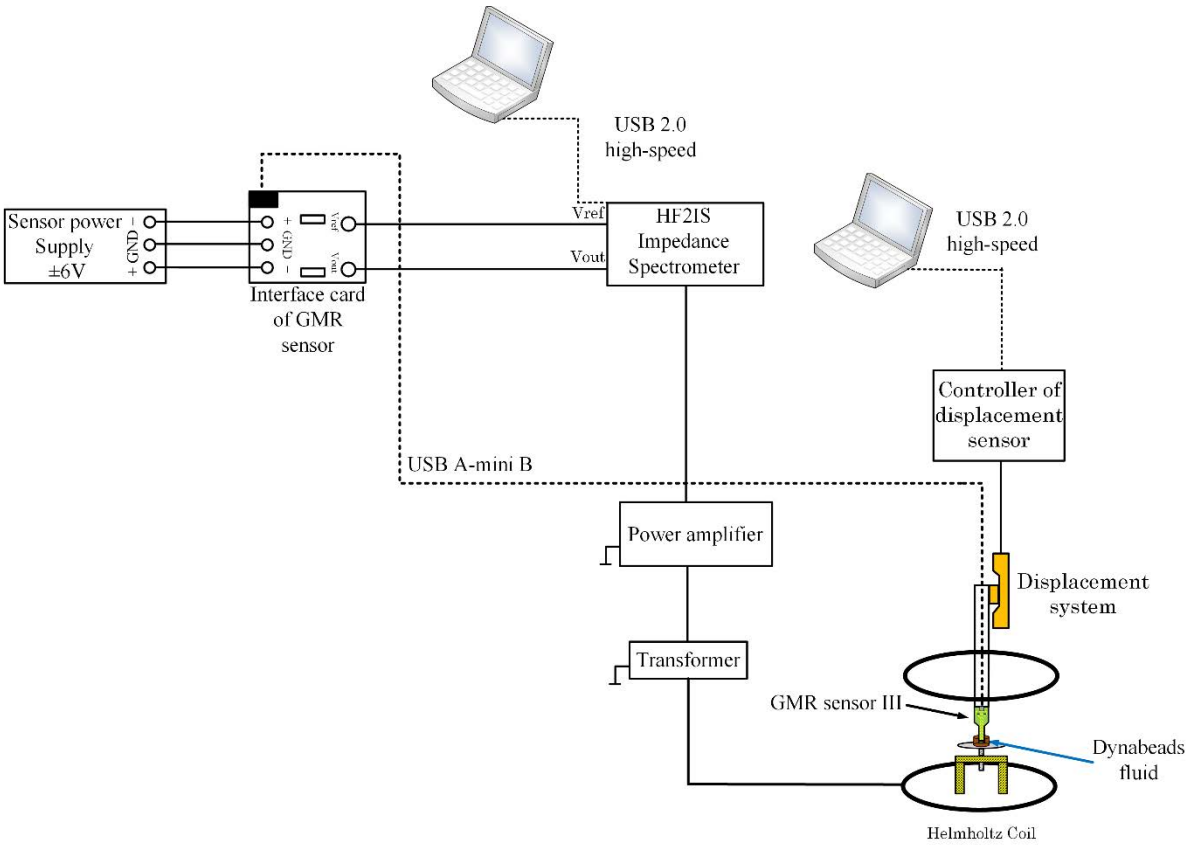

Figure 4.10 Schematic of measurement setup organized to estimate the magnetic properties of Dynabeads.

The frequency of the Helmholtz coil is fixed at 75 Hz and the input voltage generated by the HF2IS Impedance Spectrometer is equal to 340 mV. Furthermore, the value of magnetic flux density (B) produced in the center of Helmholtz coil is measured by field meter ESM-100 and is equal to 208 µT. We should underline that the Helmholtz coil is alimented by a variable gain amplifier through a step-down transformer (45-1000 Hz) which allows us to transmit 150 VA to Helmholtz coil. The alimented system of the Helmholtz coil for frequencies from 45 Hz to 1 kHz is shown on Figure 4.11 (a) and the experimental results of magnetic flux density B (µT) as a function of Helmholtz coil input amplitude Vrms (mV) at frequency 75 Hz are presented on Figure 4.11 (b).

In the next step, we have poured the 350 µl of Dynabeads pure to cylindrical shape cavity with dimension 8×8 mm by micro pipette. The cavity containing E. coli marker is placed under a uniform magnetic flux density in the center of the Helmholtz coil. Then, the GMR sensor III is inserted carefully in the midpoint of sample's cavity where the magnetic flux density is greatest.

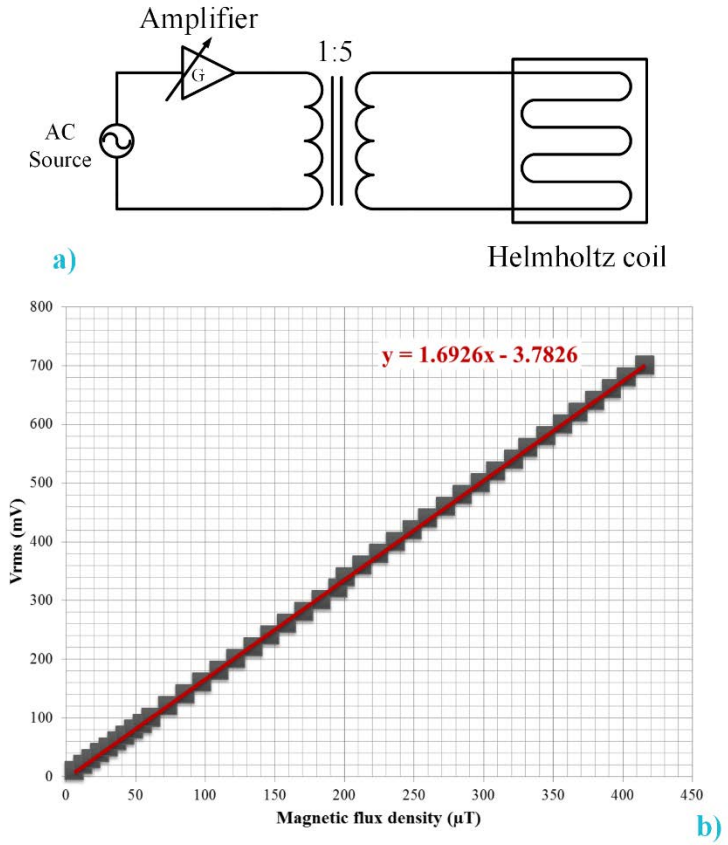

Figure 4.11 Helmholtz coil and its supply for operating in the frequency range 45-1000 Hz (a), measured magnetic flux density (µT) as a function of signal amplitude (Vrms) applied at 75 Hz (b).

When the GMR sensor III was placed completely in the center of cavity's sample (Figure 4.12 (b)), time was recorded and we started to register the GMR sensor's data. After approximately 20 seconds the sensor had a short circuit as observed in Figure 4.12 (c). This short circuit happened because of the corrosive material which has been dissolved in the Dynabeads solution.

Figure 4.12 (a), (b) and (c) indicate the GMR sensor's condition in three positions before, during and after the measurement with Dynabeads sample.

One should note that in order to protect printed circuit boards of sensor, it has been varnished three times by an electrolube clear protective lacquer against humidity and environmental attack. The corrosive material destroyed the protection layers and all wire connections between the chip and the mini B-USB connection.

In conclusion, this first test failed and we had to find solutions to avoid these electrochemical and corrosion problems.

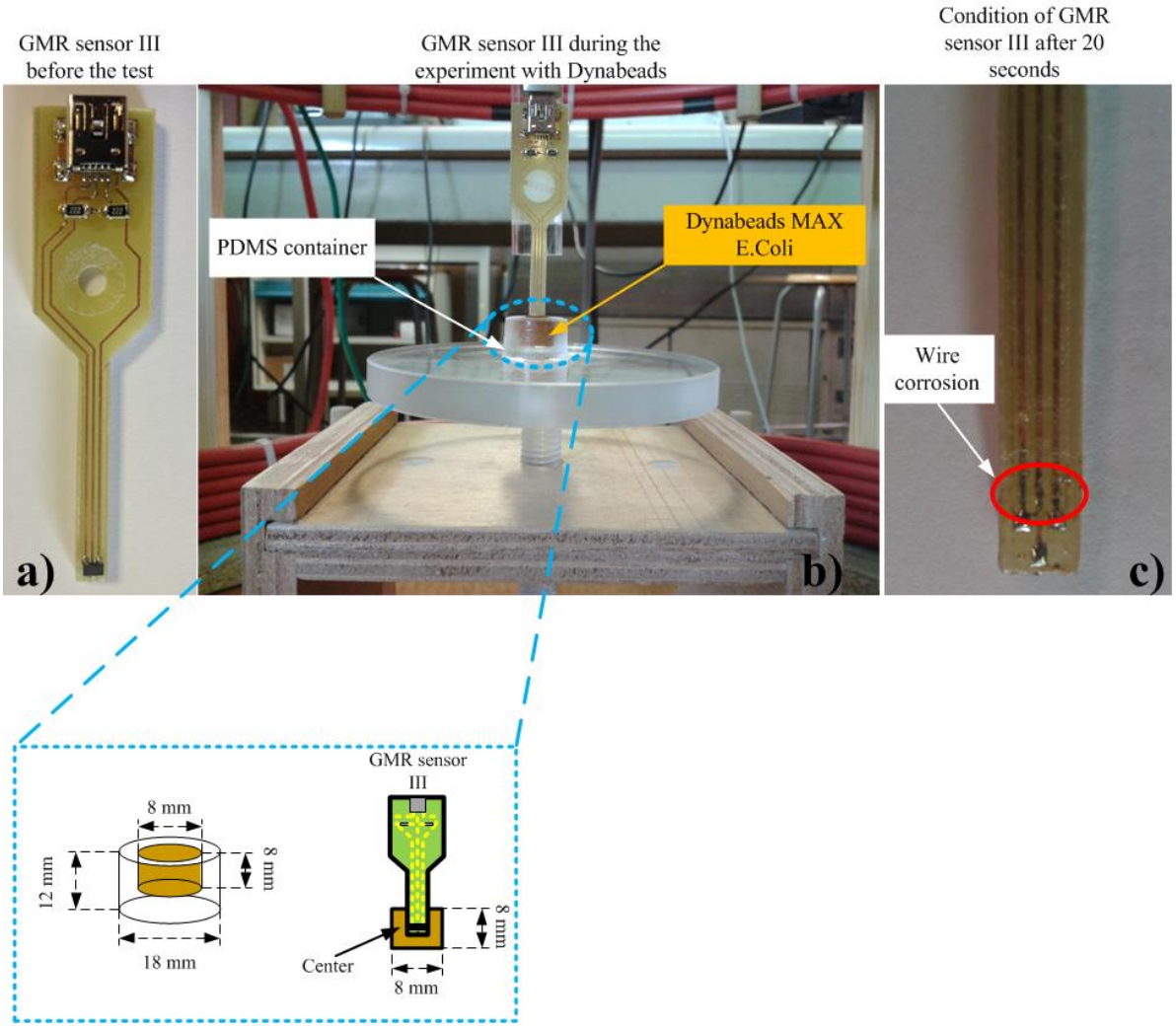

Figure 4.12 The GMR sensor type III status before the test (a), at the time of measuring (b) and after the experiment by Dynabeads (c).

b) Second test:

In this test we have completed several steps to analyze the Dynabeads marker. These steps are discussed below:

i. Re-preparation of GMR sensor printed circuit board (PCB)

ii. Protection of GMR sensor III by Polydimethylsiloxane (PDMS)

Polydimethylsiloxane (PDMS) is a chemical compound and a manufactured polymer. PDMS has the lowest value of the freezing point of all the known polymers. Due to its biocompatibility, it is extensively used in the fields of microfluidic, medicine, cosmetic, electrical insulation an etc. The main advantages of this substance are:

- ✓ Non-toxicity;
- ✓ Inert;

- ✓ Good compatibility;
- ✓ Hydrophobic;
- ✓ Easy to mold and unmold;
- ✓ Non-flammable;
- ✓ Transparent.

On one hand and as mentioned, the PDMS is applicable to protect and insulate electrical circuits. On the other hand, in the previous first test the PDMS cavity of E. coli's marker have not been seen any modifications such as corrosion, rupture or deformation. We have decided to guard the GMR sensor's circuit board by PDMS substance.

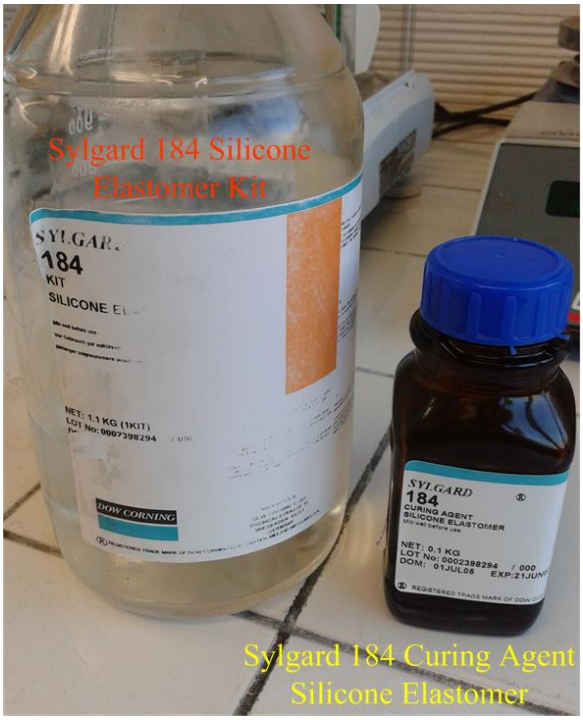

Figure 4.13 Picture of Silicone Elastomer substances.

PDMS is making by mixing well a ten parts of Sylgard 184 Silicone Elastomer Kit and one part of Sylgard 184 Curing Agent Silicone Elastomer (10:1). Figure 4.13 presents the real image of two silicones. Next step is to eliminate the bubbles included in PDMS by using a vacuum pump. Then, the PDMS was poured to the sample mold. Finally, waiting until the PDMS will be hardened or it is needed to bake the PDMS in the oven for approximately 1 hour (depends on the temperature selected).

To protect the GMR sensor we have designed and fabricated a plexiglass mold. In the mold's center we have created a channel by dimension 30×4.6×3.2 (mm) which corresponds to the needle size of GMR sensor III (Figure 4.14 (a)). As shown in Figure 4.14 (b) the PDMS was

poured to the mold's channel and the sensor's needle was simultaneously placed inside. The sensor was fixed via displacement system in the mold for more than 24 hours. Finally, the GMR sensor was removed from the mold very carefully (Figure 4.14 (c)).

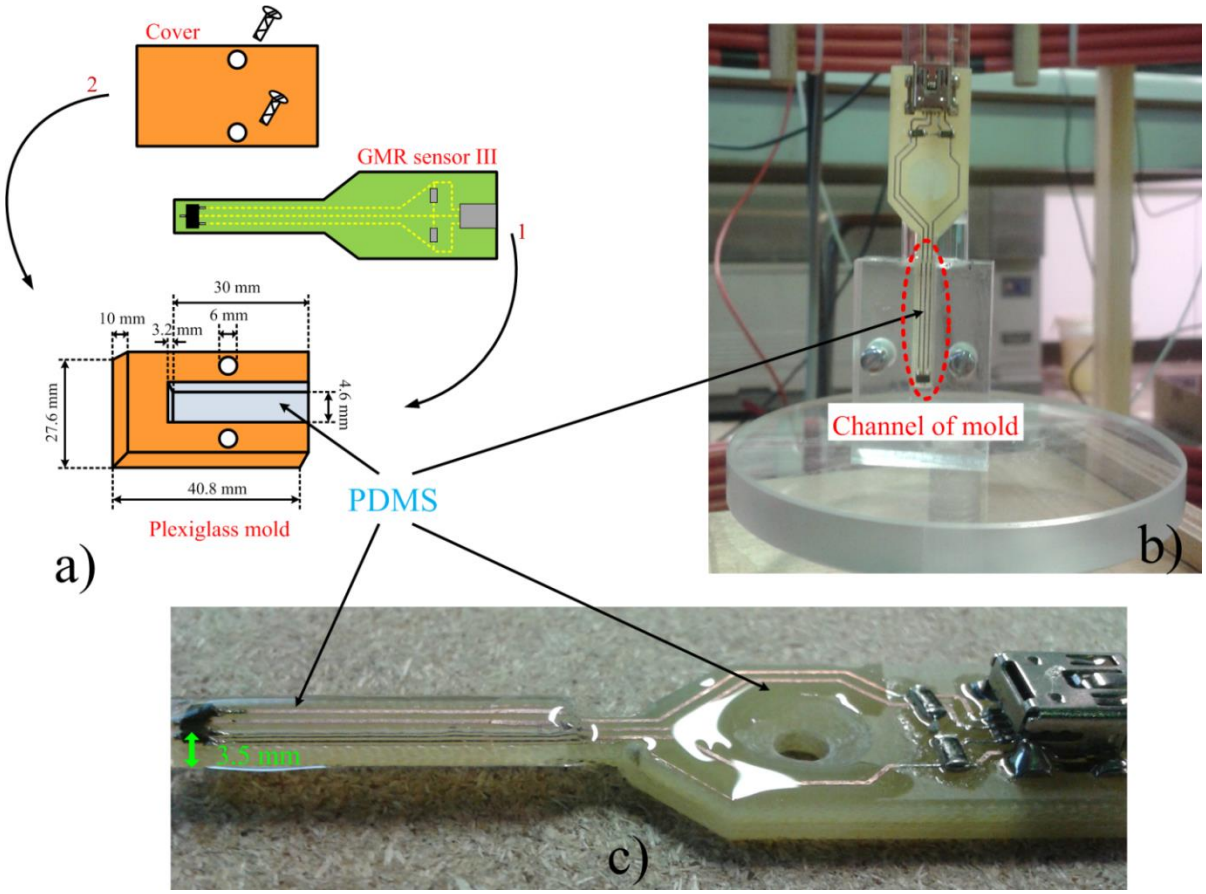

Figure 4.14 The insulation steps of GMR sensor: preparation of plexiglass mold (a), sensor's positing in the channel of mold (b), GMR sensor III with protective PDMS layers (c).

In the first step, the GMR sensor III is placed via displacement system in the center of Helmholtz coil to measure the data (air) of the sensor. The operating frequency of the Helmholtz coil is 75 Hz and the input voltage generated by the HF2IS Impedance Spectrometer is 350 mV, the magnetic flux density produced in the center of Helmholtz coil is equal to 212 µT. Figure 4.15 (a) and (b) presents the output voltage (Vout−Vref) and FFT result of GMR sensor III.

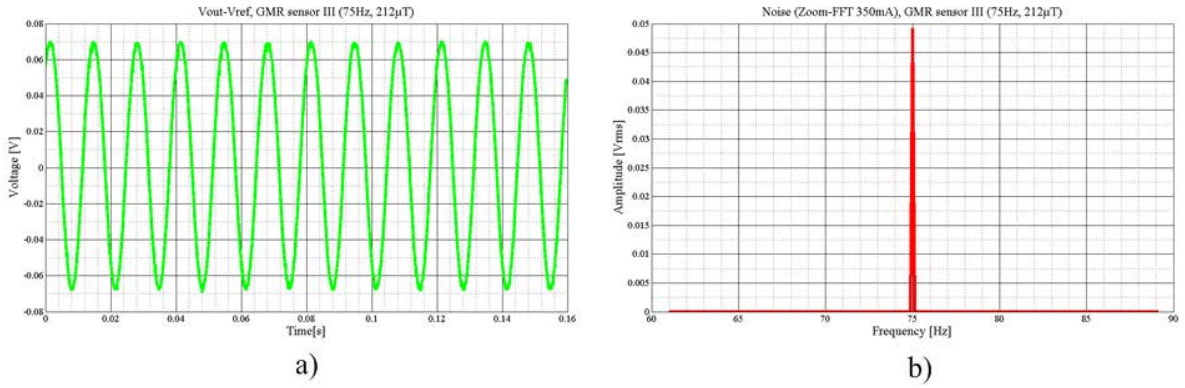

Figure 4.15 The output voltage (V) of GMR sensor (a) and the FFT detection from Vout−Vref of the GMR sensor for frequency 75 Hz (b).

In the second step, the pure Dynabeads solution along with four different concentrations 1:1, 1:4, 1:8 and 1:16 are poured (350 μL) in the cavity with dimension Ø8 mm ×8 mm (demagnetizing factor is 0.333) and each sample are placed in the center of Helmholtz coil respectively. It should be noted that the insulation layers of PDMS which posited whole of GMR sensor showed a good resistance against corrosion and measurement processes were successful.

Due to the interface program of HF2IS Impedance Spectrometer the sensor's data (Vrms and phase) for each sample are recorded 64 times and averaged. Additionally, the measurement of each concentration was repeated at least three times to ensure the accuracy of the results.

After each measurement the PDMS protection and insulation layers of sensor and also cavity were rinsed very carefully by distillated water and were dehumidified by soft sponge minimum two times in order to reduce the risk of errors by contamination.

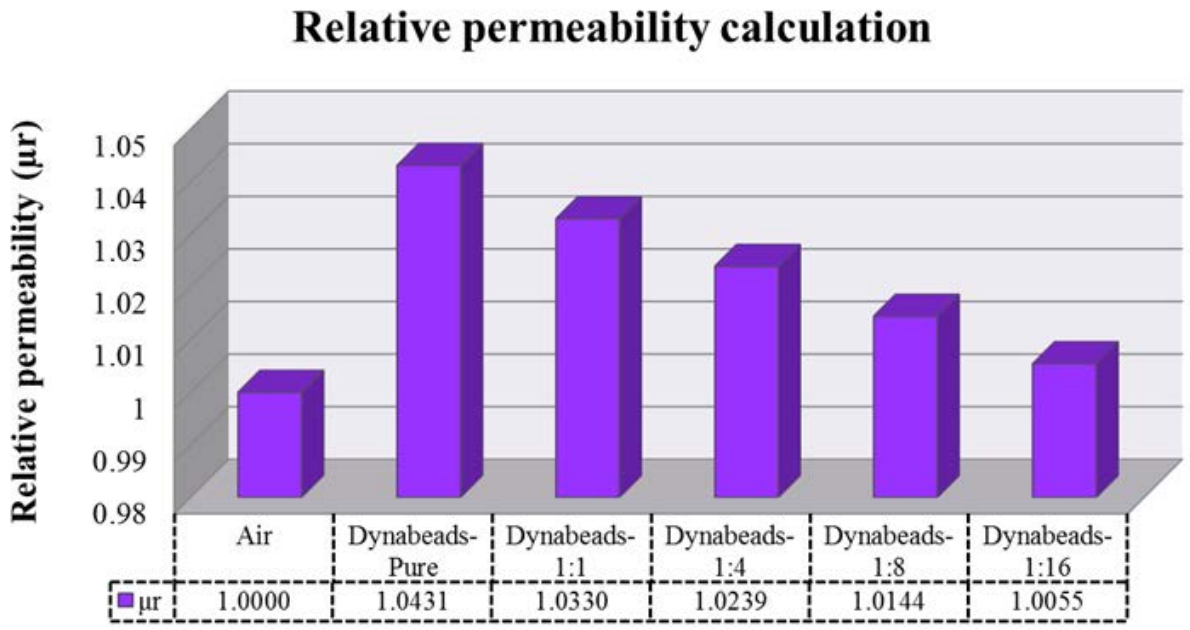

Figure 4.16 Relationship between relative permeability (μ_r) and different magnetic fluid concentrations.

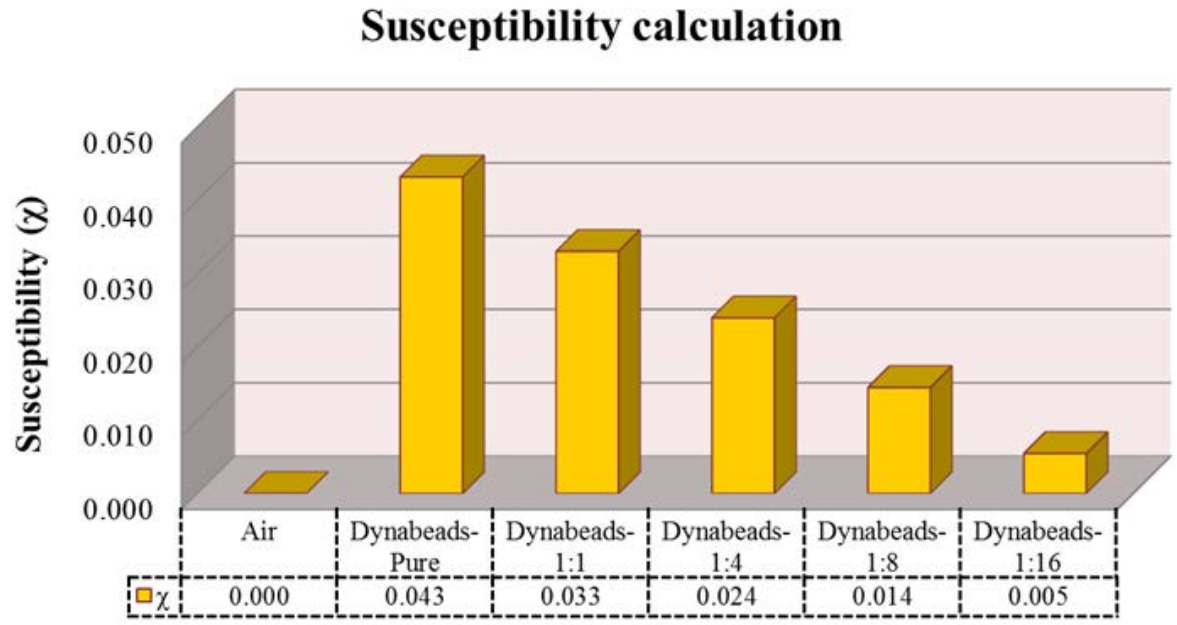

Figure 4.17 Relationship between susceptibility (χ) and different magnetic fluid concentrations.

Eventually, we have investigated the magnetic properties of Dynabeads MAX E. Coli O157 marker and the experimental results of relative permeability (μ_r) and susceptibility (χ) as a function of several concentrations (pure, 1:1, 1:4, 1:8, 1:16) are displayed in Figure 4.16 and Figure 4.17. It can be seen that the relative permeability and susceptibility are proportional to the amount of dilutions.

iii. Preparation of different experimental cavities

Last step of setup preparation was to build the different size of cavities in PDMS. We have fabricated four molds by Teflon and Nylon materials to obtain two different aspect ratios (S) and demagnetizing factors (N). Two cylindrical containers of dimensions Ø6 × 12 mm and Ø7 × 14 mm were selected for S = 2, N = 0.172 and the other two cylindrical cavities Ø8 × 8 mm and Ø7 × 7 mm to obtain S = 1, N = 0.333. Several sizes of cavities and their molds are indicated in Figure 4.18.

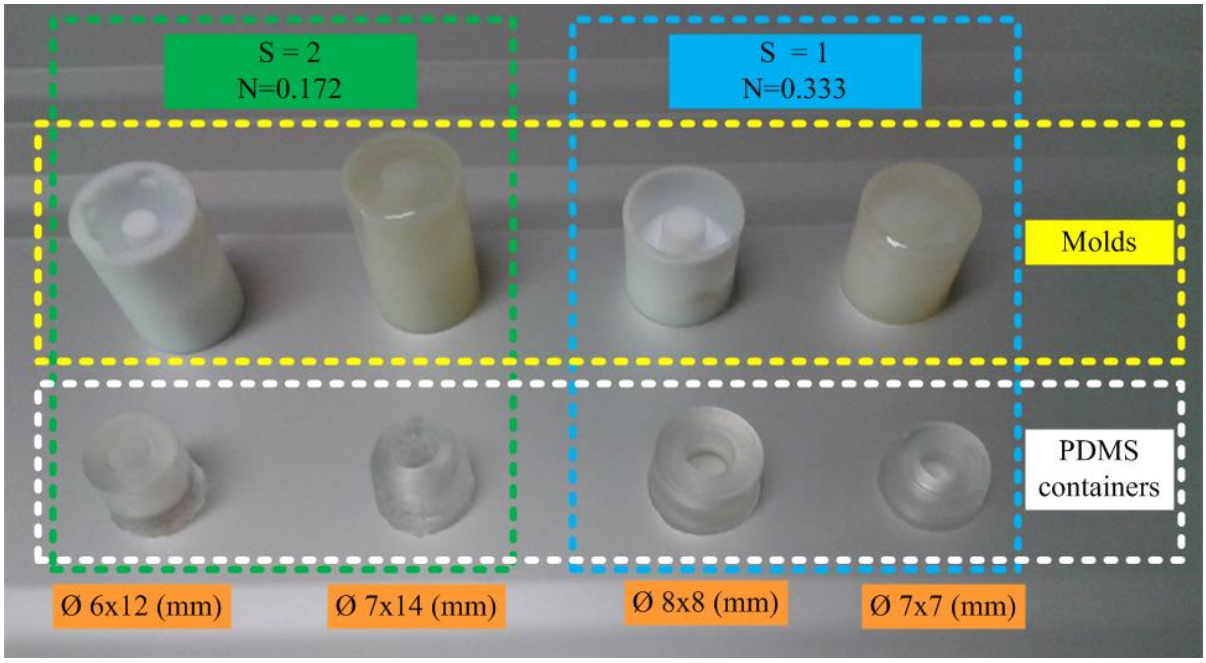

Figure 4.18 The schematic of four dissimilar size molds and PDMS containers.

We have poured the PDMS substance in all four cylindrical molds in order to obtain specific cavity sizes. After one day the PDMS cavities became hard enough to be removed from their molds.

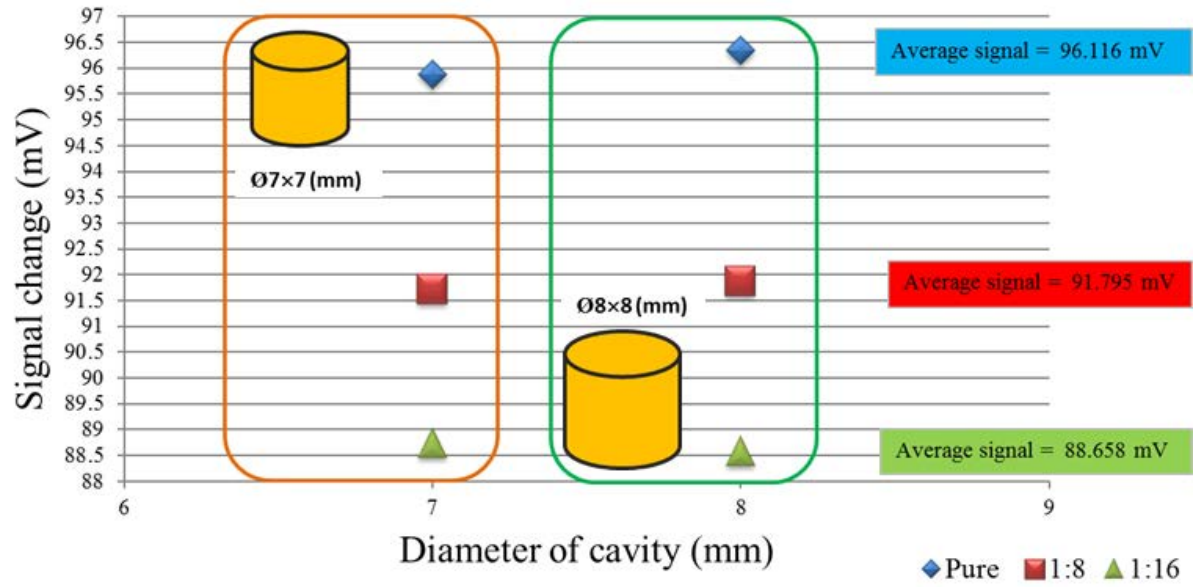

Figure 4.19 Signal changes measured in the cavities with S = 1, N = 0.333.

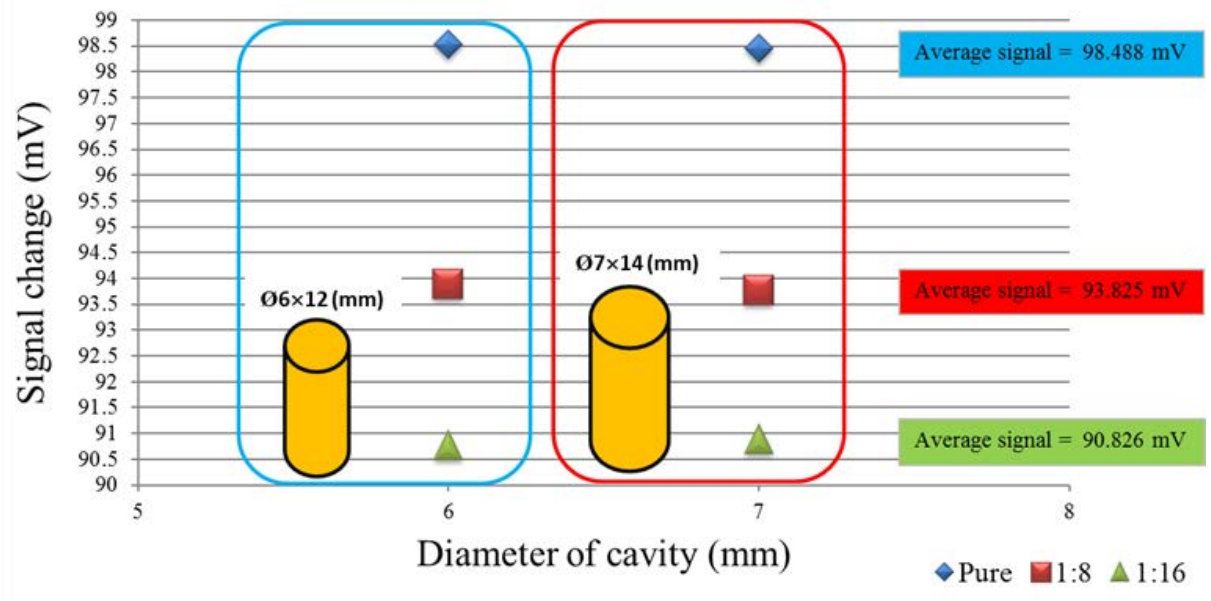

Figure 4.20 Signal changes measured in the cavities with S = 2, N = 0.172.

In this experiment three solutions of Dynabeads fluid (pure, 1:8 and 1:16) were tested in the four cylindrical cavities with sizes Ø7 mm × 14 mm, Ø6 mm × 12 mm, Ø8 mm × 8 mm, Ø7 mm × 7 mm. Like before a uniform magnetic flux density was generated by Helmholtz's coils. Their operating frequency was selected at 75 Hz and the input voltage was generated by the HF2IS Impedance Spectrometer at 690 mV. All samples were positioned in the center of Helmholtz coil which has a uniform magnetic flux density 400 µT and the GMR sensor III was located gradually in to the sample's container thanks to displacement system.

Figure 4.19 and Figure 4.20 present the experimental results of the signal variations as a function of the cavity's S and the N parameters. From obtained answers it can been seen that the signal changes do not show a dramatic modifications between sample cavities which have the same parameters of S and the N. In other words, the signal variations just depend on the amount of weight density (D_W) of solution and cavity's dimensions do not play significant role. Additionally, the phase variations for each sample were examined and be founded identical and equal to 118 deg.

4.4 Conclusion

The first part of Chapter 4 includes brief resume of a very popular group of bacteria called Escherichia coli (E. coli). We have studied main specifications of E. coli and process of its reproduction. In following, we have focused on the E. coli O157:H7 as a pathogenic bacterium that produces toxins such as *Shiga toxins* or *verotoxins* and causes an outbreak or epidemic disease through urine and stool of patients.

In the second part of this Chapter we have presented a magnetic marker (Dynabeads MAX E. Coli O157) in order to rapidly detect and separate the E. coli O157:H7 from contaminated environments. The good capability and the high sensitivity of GMR sensor III allow us to sense accurately these superparamagnetic beads even at low concentrations. After solving the sensor insulation problem by using polydimethylsiloxane (PDMS), we have determined and measured the relative permeability (μ_r) and susceptibility (χ) of several concentrations prepared from pure Dynabeads fluid. Additionally, we have examined the signal changes of concentrations in the various containers with similar aspect ratios and demagnetizing factors.

General conclusion

The main objective of this thesis was to investigate a novel and innovative measurement method to calculate and estimate the magnetic properties of ferrofluids and magnetic beads such as relative permeability and susceptibility by dint of the GMR sensors. This goal represents particular scientific and practical interest as magnetic liquids are widely used in several applications and particularly in applications of biomedicine such as hyperthermia treatment, magnetic cell separation, creation of magnetic drugs, etc. Furthermore, we have also investigated the use the GMR sensor rapidly, conveniently and easily detect bacteria such E. coli O157:H7 marked by magnetic nanoparticles.

To accomplish the principal target of the thesis, we have identified some additional sub-goals and fulfilled them:

First, we have introduced three new types of magnetic sensors produced on the basis of the giant magnetoresistance effect. Two of them have been completely designed and developed at Kanazawa University (Professor Yamada). The interest of these sensors is their packaging inside a very thin needle with few μm of diameter. The third sensor with different sensitivity has been manufactured on the base of a chip provided by our partner at Kanazawa University and conditioned in our laboratory.

Second, an experimental measurement setup to characterize the sensors and measure the physical properties of micro-nano particles have been described. The setup consists of Helmholtz coils with two different sizes to produce a uniform magnetic field in their center. Different circuit cards were designed such as an interface card to protect each GMR sensor from an excessive electrical current passing through and a preamplifier in order to amplify the sensor's output signal. A positioning system and its control panel have been used to reduce the positioning errors and to avoid any shock on the fragile needle of the sensor.

Third, we have completed the characterization process of each sensor to determine the sensor's sensitivity as a function of magnetic flux density (B). The sensitivity is a main parameter to characterize and classify the ability of the sensor; the highest sensitivity leads to more accurate and proper measurement of magnetic properties of ferrofluids at low concentrations and in a feeble magnetic field.

Fourth, we have presented the theoretical equations to calculate the weight and volume density of different ferrofluid's concentrations and moreover the theoretical formulas of the changes magnetic flux density, relative permeability and susceptibility detection have been introduced.

Fifth, we have shown another measurement way by virtue of a vibrating sample magnetometer (VSM). The vibration of this device helps to prevent settling magnetic fluid down, providing the clarity of measurement. The VSM is utilized not only to study the magnetic properties of ferrofluids but to measure thin film, powders, etc.

Sixth, we have fabricated Teflon and Nylon molds with different shapes to prepare cavities with different size ratio. They are made of polydimethylsiloxane (PDMS) substance which is biocompatible and resistant to corrosion and fouling. We have studied the changes of sample's signal related to the cavity sizes.

At the end of this research, we should point out that the proposed method of magnetic measurement by dint of the GMR sensor permits increasing the speed, preciseness and comfort if compared with other similar equipment like SQUID or VSM due to sensor's tiny size, appropriate sensitivity and possibility of measurement in a weak magnetic field. Moreover, it is necessary to underline that the usage of GMR sensor proposed in this thesis, gives another advantage that other equipment is lack of, such as performing the experiments at several frequencies.

References

[1] M. N. Baibich, J. M. Broto, A. Fert, F. N. Van Dau, F. Petroff, P. Etienne, G. Creuzet, A. Friederich, and J. Chazelas, "Giant Magnetoresistance of (001)Fe/(001)Cr Magnetic Superlattices," *Physical Review Letters,* vol. 61, pp. 2472-2475, 1988.

[2] E. Y. Tsymbal and D. G. Pettifor, "Perspectives of giant magnetoresistance," in *Solid State Physics, Vol 56*. vol. 56, H. Ehrenreich and F. Spaepen, Eds., ed, 2001, pp. 113-237.

[3] S. S. P. Parkin, N. More, and K. P. Roche, "Oscillations in exchange coupling and magnetoresistance in metallic superlattice structures: Co/Ru, Co/Cr, and Fe/Cr," *Physical Review Letters,* vol. 64, pp. 2304-2307, 1990.

[4] R. W. Schneider and C. H. Smith. (September 1, 1999). *Low Magnetic Field Sensing with GMR Sensors, Part 1: The Theory of Solid-State Magnetic Sensing*.

[5] M. J. Caruso, T. Bratland, C. H. Smith, and R. Schneider, "A New Perspective on Magnetic Field Sensing," *Sensors,* vol. 15, pp. 34–46, 1998.

[6] F. H. Ramli Ramli, Khairurrijal Khairurrijal and Mitra Djamal, "GMR Biosensors for Clinical Diagnostics," in *Biosensors for Health, Environment and Biosecurity*, P. A. Serra, Ed., ed, 19 July 2011

[7] A. Emmanuel, "Étude théorique de la structure et de la stabilité des alliages GeMn dans le cadre de la spintronique," PhD thesis, Université de Grenoble, 2010.

[8] M. Gottwald, "Nouveaux systèmes modèles à aimantation perpendiculaire pour l'étude des effets de transfert de spin," PhD thesis, Université Henri Poincaré, 2011.

[9] A. Korkin and F. Rosei, *Nanoelectronics and Photonics: From Atoms to Materials, Devices, and Architectures*: Books24x7.com, 2008.

[10] A. Johnson, "Spin Valve Systems for Angle Sensor Applications," Dr.-Ing., Fachbereich Material- und Geowissenschaften der Technischen Universität Darmstadt genehmigte, 2004.

[11] C. Vouille, A. Barthelemy, F. E. Mpondo, A. Fert, P. A. Schroeder, S. Y. Hsu, A. Reilly, and R. Loloee, "Microscopic mechanisms of giant magnetoresistance," *Physical Review B,* vol. 60, pp. 6710-6722, Sep 1999.

[12] A. P. Guimarães, *Principles of Nanomagnetism*: Springer, 2009.

[13] A. Fert, A. Barthelemy, P. Etienne, S. Lequien, R. Loloee, D. K. Lottis, D. H. Mosca, F. Petroff, W. P. Pratt, and P. A. Schroeder, "MAGNETIC MULTILAYERS - OSCILLATORY INTERLAYER EXCHANGE AND GIANT MAGNETORESISTANCE," *Journal of Magnetism and Magnetic Materials,* vol. 104, pp. 1712-1716, Feb 1992.

[14] S. Tumański, *Thin Film Magnetoresistive Sensors*: Institute of Phyiscs Pub, 8 juin 2001.

[15] J. G. Zhu and Y. F. Zheng, "Characteristics of AP bias in spin valve memory elements," *Ieee Transactions on Magnetics,* vol. 34, pp. 1063-1065, Jul 1998.

[16] J. C. S. Kools, "Exchange-biased spin-valves for magnetic storage," *Ieee Transactions on Magnetics,* vol. 32, pp. 3165-3184, Jul 1996.

[17] R. L. White, "GIANT MAGNETORESISTANCE - A PRIMER," *Ieee Transactions on Magnetics,* vol. 28, pp. 2482-2487, Sep 1992.

[18] Y. F. Zheng and J. G. Zhu, "Micromagnetics of spin valve memory cells," *Ieee Transactions on Magnetics,* vol. 32, pp. 4237-4239, Sep 1996.

[19] Y. A. Danilov, E. S. Demidov, Y. N. Drosdov, V. P. Lesnikov, V. V. Podolskii, M. V. Sapozhnikov, and A. P. Kasatkin, "Ferromagnetism in epitaxial layers of gallium and indium antimonides and indium arsenide supersaturated by manganese impurity," *Journal of Magnetism and Magnetic Materials,* vol. 300, pp. E24-E27, May 2006.

[20] J. J. Miles and M. R. Parker, "Micromagnetic modelling of spin valve and GMR read heads," *Ieee Transactions on Magnetics,* vol. 32, pp. 4597-4602, Sep 1996.

[21] M. Pannetier, C. Fermon, G. Le Goff, J. Simola, E. Kerr, and J. M. D. Coey, "Noise in small magnetic systems - applications to very sensitive magnetoresistive sensors," *Journal of Magnetism and Magnetic Materials,* vol. 290, pp. 1158-1160, Apr 2005.

[22] B. A. Gurney, V. S. Speriosu, D. R. Wilhoit, H. Lefakis, R. E. Fontana, D. E. Heim, and M. Dovek, "Can spin valves be reliably deposited for magnetic recording applications?," *Journal of Applied Physics,* vol. 81, pp. 3998-4003, Apr 1997.

[23] A. F. M. Nor, E. W. Hill, and M. R. Parker, "Geometry effects on low frequency noise in giant magnetoresistance (GMR) sensors," *Ieee Transactions on Magnetics,* vol. 34, pp. 1327-1329, Jul 1998.

[24] J. K. Spong, V. S. Speriosu, R. E. Fontana, M. M. Dovek, and T. L. Hylton, "Giant magnetoresistive spin valve bridge sensor," *Ieee Transactions on Magnetics,* vol. 32, pp. 366-371, Mar 1996.

[25] Z. R. TADISINA, "PERPENDICULAR MAGNETIC ANISOTROPY MATERIALS FOR REDUCED CURRENT SWITCHING DEVICES," PhD thesis, University of Alabama, 2010.

[26] Baibich M N, Broto J M, and Fertetal A, *Phys. Rev. Lett,* vol. 61, p. 2472, 1988.

[27] T. Valet and A. Fert, "CLASSICAL-THEORY OF PERPENDICULAR GIANT MAGNETORESISTANCE IN MAGNETIC MULTILAYERS," *Journal of Magnetism and Magnetic Materials,* vol. 121, pp. 378-382, Mar 1993.

[28] T. Valet and A. Fert, "Theory of the perpendicular magnetoresistance in magnetic multilayers," *Physical Review B,* vol. 48, p. 7099, 1993.

[29] M. A. M. Gijs and G. E. W. Bauer, "Perpendicular giant magnetoresistance of magnetic multilayers," *Advances in Physics,* vol. 46, pp. 285-445, May-Aug 1997.

[30] N. A. M. research. (4 October 2010). *Electronic, magnetic and superconducting materials (http://www.nature.com/am/journal/v3/n1/full/am20112a.html)*.

[31] K. Mohri, T. Kohzawa, K. Kawashima, H. Yoshida, and L. V. Panina, "MAGNETOINDUCTIVE EFFECT (MI EFFECT) IN AMORPHOUS WIRES," *Ieee Transactions on Magnetics,* vol. 28, pp. 3150-3152, Sep 1992.

[32] L. Kraus, "Theory of giant magneto-impedance in the planar conductor with uniaxial magnetic anisotropy," *Journal of Magnetism and Magnetic Materials,* vol. 195, pp. 764-778, Jun 1999.

[33] L. V. Panina, K. Mohri, T. Uchiyama, M. Noda, and K. Bushida, "Giant magneto-impedance in Co-rich amorphous wires and films," *Magnetics, IEEE Transactions on,* vol. 31, pp. 1249-1260, 1995.

[34] A. BORGE, "GIANT MAGNETO-IMPEDANCE EFFECT IN THIN FILM LAYERED STRUCTURES," PhD thesis, University of Central Florida, 2005.

[35] С. В. ВОНСОВСКИЙ and Я. С. ШУР, *ФЕРРОМАГНЕТИЗМ*. Москва-Ленинград, 1948.

[36] J. P. Srivastava, *Elements of Solid State Physics*: Prentice-Hall of India, 2006.

[37] U. J. Fourier, *Magnetism: Fundamentals*: Springer, 2004.

[38] *Xam Idea Physics (Class XII)*, 7 ed. New Delhi: Vk Global Publications Pvt Ltd.

[39] K. Yano, *Synthesis and Characterization of Ferromagnetic Nanoparticles*: University of Texas at Arlington, 2007.

[40] K. C. Singh, *Basic Physics*: Prentice-Hall Of India Pvt. Ltd., 2009.

[41] S. BUZID, "DETECTION MAGNETIQUE DE MATERIAUX ENTERRES," PhD thesis, Université de Reims Champagne Ardenne, Septembre 2009.

[42] A. Aharoni, *Introduction to the Theory of Ferromagnetism*: Oxford University Press, USA; 2 edition, March 15, 2001.

[43] C. Chevassu, in *ELECTROMAGNETISME POUR L'ÉLECTROTECHNIQUE*, ed, 2006.

[44] P. S. Dhogal, *BASIC ELECTRICAL ENGINEERING* vol. 1: McGraw-Hill Education (India) Pvt Ltd, 2001.

[45] http://www.electronenergy.com/magnetic-design/magnetic-design.htm.

[46] Q. A. Pankhurst, J. Connolly, S. K. Jones, and J. Dobson, "Applications of magnetic nanoparticles in biomedicine," *Journal of Physics D-Applied Physics,* vol. 36, pp. R167-R181, Jul 2003.

[47] S. Chikazumi, *Physics of Ferromagnetism 2e*: Oxford University Press, USA, 2009.

[48] H. Alloul and S. Lyle, *Introduction to the Physics of Electrons in Solids*: Springer, 2010.

[49] W. Lowrie, *Fundamentals of Geophysics*: Cambridge University Press, 2007.

[50] S. P. Gubin, Y. A. Koksharov, G. B. Khomutov, and G. Y. Yurkov, "Magnetic nanoparticles: Preparation methods, structure and properties," *Uspekhi Khimii,* vol. 74, pp. 539-574, 2005.

[51] T. Hyeon, "Chemical synthesis of magnetic nanoparticles," *Chemical Communications,* pp. 927-934, 2003.

[52] V. K. Varadan, D. L. F. Chen, and J. Xie, *Nanomedicine: Design and Applications of Magnetic Nanomaterials, Nanosensors and Nanosystems*: Wiley, 2008.

[53] M. Arruebo, R. Fernandez-Pacheco, M. R. Ibarra, and J. Santamaria, "Magnetic nanoparticles for drug delivery," *Nano Today,* vol. 2, pp. 22-32, Jun 2007.

[54] R. Hergt, W. Andra, C. G. d'Ambly, I. Hilger, W. A. Kaiser, U. Richter, and H. G. Schmidt, "Physical limits of hyperthermia using magnetite fine particles," *Ieee Transactions on Magnetics,* vol. 34, pp. 3745-3754, Sep 1998.

[55] T. Kobayashi, "Cancer hyperthermia using magnetic nanoparticles," *Biotechnology Journal,* vol. 6, pp. 1342-1347, Nov 2011.

[56] A. C. Silva, T. R. Oliveira, J. B. Mamani, S. M. F. Malheiros, L. Malavolta, L. F. Pavon, T. T. Sibov, E. Amaro, A. Tannus, E. L. G. Vidoto, M. J. Martins, R. S. Santos, and L. F. Gamarra, "Application of hyperthermia induced by superparamagnetic iron oxide nanoparticles in glioma treatment," *International Journal of Nanomedicine,* vol. 6, pp. 591-603, 2011.

[57] J. Rife, M. Miller, P. Sheehan, C. Tamanaha, M. Tondra, and L. Whitman, "Design and performance of GMR sensors for the detection of magnetic microbeads in biosensors," *Sensors and Actuators A: Physical,* vol. 107, pp. 209-218, 2003.

[58] S. S. Papell, "LOW VISCOSITY MAGNETIC FLUID OBTAINED BY THE COLLOIDAL SUSPENSION OF MAGNETIC PARTICLES " USA Patent, Nov 2, 1965.

[59] S. Odenbach, *Ferrofluids: Magnetically Controllable Fluids and Their Applications*: Springer, 2010.

[60] C. Scherer and A. M. F. Neto, "Ferrofluids: Properties and applications," *Brazilian Journal of Physics,* vol. 35, pp. 718-727, Sep 2005.

[61] http://ru.wikipedia.org/wiki/Ферромагнитная_жидкость.

[62] C. P. Gooneratne, S. C. Mukhopadhyay, and S. Yamada, "Electromagnetic field computation of GMR sensor for hyperthermia based cancer treatment," presented at the Applied Electromagnetics Conference (AEMC), Kolkata, 14-16 Dec. 2009.

[63] В. М. Нестеренко, Ю. Д. Апросин, and В. М. Шлимак, " по применению магнитных жидкостей в биологии и медицине," presented at the III Всесоюзн, Сухуми, 1989.

[64] W. Yu and H. Q. Xie, "A Review on Nanofluids: Preparation, Stability Mechanisms, and Applications," *Journal of Nanomaterials,* 2012.

[65] В. В. Коварда and А. К. Марчук, "О возможности применения продукции нанотехнологий (магнитных жидкостей и МРС) в травматологии и ортопедии для повышения конкурентоспособности протезно-ортопедических изделий," *Молодой ученый,* vol. 6, pp. 169-173, 2012.

[66] Э. Парселл, *Электричество и магнетизм: Берклеевский курс физики : Учеб. пособие для вузов по напр. 510000 "Естественные науки и математика", 550000 "Технические науки", 540000 "Педагогические науки"*: Лань, 2005.

[67] http://lme.elmat.pub.ro/~florin/student/MINF/course_files/helmholtz.pdf.

[68] D. J. DeTroye and R. J. Chase, "The Calculation and Measurement of Helmholtz Coil Fields," 1994.

[69] "ROSIER Mécatronique (www.rosier.fr)."

[70] *AD 620 (http://www.analog.com/en/index.html)*.

[71] Z. Instruments, "HF2IS Impedance Spectrometer (http://www.zhinst.com/products/hf2is)."

[72] Lakeshore. *http://www.lakeshore.com/products/gaussmeters/model-460-3-channel-gaussmeter/Pages/Overview.aspx*.

[73] H. Shirzadfar, R. Haraszczuk, M. Nadi, S. Yamada, and D. Kourtiche, "Detecting and Estimating Magnetic Fluid Properties by a Needle- Type GMR Sensor," in *Nanomaterials: Application & Properties*, Crimea, Ukraine, 2012.

[74] C. GOONERATNE, A. ŁEKAWA, M. IWAHARA, M. KAKIKAWA, and S. YAMADA, "Estimation of Low Concentration Magnetic Fluid Weight Density and Detection inside an Artificial Medium Using a Novel GMR Sensor," *Sensors & Transducers Journal,* vol. 90, pp. 27-38, April 2008.

[75] S. Yamada, K. Chomsuwan, S. C. Mukhopadhyay, M. Iwahara, M. Kakikawa, and I. Nagano, "Detection of Magnetic Fluid Volume Density with a GMR Sensor," *Journal of Magnetics Society of Japan,* vol. 31(2), pp. 44-47, 2007.

[76] C. P. Gooneratne, S. C. Mukhopadhyay, and S. Yamada, "An SV-GMR Needle Sensor-Based Estimation of Volume Density of Magnetic Fluid inside Human Body," *Journal of Sensors,* vol. 2008, 2008.

[77] P. Gooneratne C, M. Kakikawa, M. Iwahara, and S. Yamada, "GMR Sensor Application in Detecting and Estimating Magnetic Fluid Weight Density inside Various Size Tumors," *Journal of the Magnetics Society of Japan,* vol. 33, pp. 175-178, 2009/05/01 2009.

[78] R. G. Haraszczuk, "Studies on Frequency Domain Characteristics of Magnetic Markers Employing Needle Type Probe with Giant Magnetoresistance Sensor," PhD thesis, Kanazawa University, June 2011.

[79] Sotoshi Yamada, Chinthaka. P. Gooneratne, and M. Kakikawa, "Low-Invasive Detection of Magnetic Particles inside Human Body," *K-INET Kanazawa University,* vol. 21, pp. 140 - 145, 2009.

[80] C. P. Gooneratne, M. Kakikawa, T. Ueno, and S. Yamada, "Measurement of Minute Changes in Magnetic Flux Density by Means of a Novel GMR Needle Probe for Application in Hyperthermia Therapy," *Journal of the Magnetics Society of Japan,* vol. 34, pp. 119-122, 2010.

[81] D. X. Chen, J. A. Brug, and R. B. Goldfarb, "DEMAGNETIZING FACTORS FOR CYLINDERS," *Ieee Transactions on Magnetics,* vol. 27, pp. 3601-3619, Jul 1991.

[82] R. Haraszczuk, M. Kakikawa, T. Ueno, S. Yamada, and M. Nadi, "Spectroscopic Susceptibility Measurements of Magnetic Markers by SV-GMR Needle Probe," *Journal of the Magnetics Society of Japan,* vol. 35, 2011.

[83] L. M. Surhone, M. T. Tennoe, and S. F. Henssonow, *Vibrating Sample Magnetometer*: VDM Publishing, 2010.

[84] G. Associates. *GMW Dipole Electromagnet -250mm-3474 (http://www.gmw.com/electromagnets/dipole/3474/3474_Specs.html)*.

[85] Ferrotec. *(http://www.ferrotec.com/)*.

[86] *Eppendorf (http://www.eppendorf.com/int/index.php?l=1)*.
[87] W. Huang, J. M. Wu, W. Guo, R. Li, and L. Y. Cui, "Initial susceptibility and viscosity properties of low concentration epsilon-Fe-3 N based magnetic fluid," *Nanoscale Research Letters,* vol. 2, pp. 155-160, Mar 2007.
[88] http://www.chemicell.com/products/Magnetic_Nanoparticle/Magnetic_Nanoparticles.html.
[89] http://www.scribd.com/doc/7214596/Cell-Separation.
[90] C. Alexiou, W. Arnold, R. J. Klein, F. G. Parak, P. Hulin, C. Bergemann, W. Erhardt, S. Wagenpfeil, and A. S. Luebbe, "Locoregional cancer treatment with magnetic drug targeting," *Cancer research,* vol. 60, pp. 6641-6648, 2000.
[91] R. Bentley and R. Meganathan, "Biosynthesis of vitamin K (menaquinone) in bacteria," *Microbiology and Molecular Biology Reviews,* vol. 46(3), pp. 241-280, September 1982.
[92] M. J. Waites, N. L. Morgan, J. S. Rockey, and G. Higton, *Industrial Microbiology: An Introduction*: Wiley, 2009.
[93] G. Karp, *Cell and Molecular Biology: Concepts and Experiments*: John Wiley & Sons, 2009.
[94] S. D. Manning, I. E. Alcamo, and D. L. Heymann, *Escherichia Coli Infections*: Facts On File, Incorporated, 2009.
[95] http://www.cod.edu/people/faculty/fancher/prokeuk.htm.
[96] http://www.diffen.com/difference/Eukaryotic_Cell_vs_Prokaryotic_Cell.
[97] http://www.life.umd.edu/classroom/bsci424/BSCI223WebSiteFiles/ProkaryoticvsEukaryotic.htm.
[98] *Text Book Of Botany Diversity Of Microbes And Cryptogams*: Rajpal And Sons Publishing.
[99] C. B. Rosdahl and M. T. Kowalski, *Textbook of Basic Nursing, 9e*: Wolter Kluwer Health/Lippincott Williams & Wilkins, 2008.
[100] H. E. Kubitschek, "Cell volume increase in Escherichia coli after shifts to richer media," *Microbiology and Molecular Biology Reviews,* vol. 172(1), pp. 94-101, January 1990
[101] M. T. Madigan and J. M. Martinko, *Brock Biology of Microorganisms*: Pearson Prentice Hall, 2006.
[102] *HowStuffWorks http://science.howstuffworks.com/life/evolution/evolution4.htm*.
[103] S. Ishii and U. o. Minnesota, *Sources and Impacts of Indigenous Escherichia Coli in Soils from a Lake Superior Watershed*: University of Minnesota, 2007.
[104] W. Vollmer and J. V. Holtje, "Morphogenesis of Escherichia coli," *Current Opinion in Microbiology,* vol. 4, pp. 625-633, 2001.
[105] M. Schaechter, *Desk Encyclopedia of Microbiology*: Elsevier Science, 2010.
[106] *http://preuniversity.grkraj.org/html/2_CELL_DIVISION.htm*.
[107] S. Arends and D. S. Weiss, "Inhibiting cell division in Escherichia coli has little if any effect on gene expression," *Journal of bacteriology,* vol. 186, pp. 880-884, 2004.
[108] M. Schaechter, N. C. Engleberg, V. J. DiRita, and T. Dermody, *Schaechter's Mechanisms of Microbial Disease*: Lippincott Williams & Wilkins, 2007.
[109] "Diseases and epidemics (http://hainanwel.com/forum/viewtopic.php?f=419&t=837)."
[110] A. G. Torres, *Pathogenic Escherichia Coli in Latin America*: Bentham Science Publishers, 2010.
[111] http://www.cfsph.iastate.edu/Factsheets/pdfs/e_coli.pdf.
[112] P. M. Fratamico, A. K. Bhunia, and J. L. Smith, *Foodborne Pathogens: Microbiology And Molecular Biology*: Caister Academic Press, 2005.
[113] http://leavittpartners.com/2012/08/jensen-farms-outbreak-causes-us-to-miss-healthy-people-goals-and-other-foodnet-facts/.
[114] http://www.lifetechnologies.com/order/catalog/product/A10714.
[115] http://www.hannainst.com/usa/prods2.cfm?id=040003&ProdCode=HI%2098103.
[116] http://en.wikipedia.org/wiki/Buffer_solution.

ANNEX 1: Supplementary information of HF2IS Impedance Spectrometer

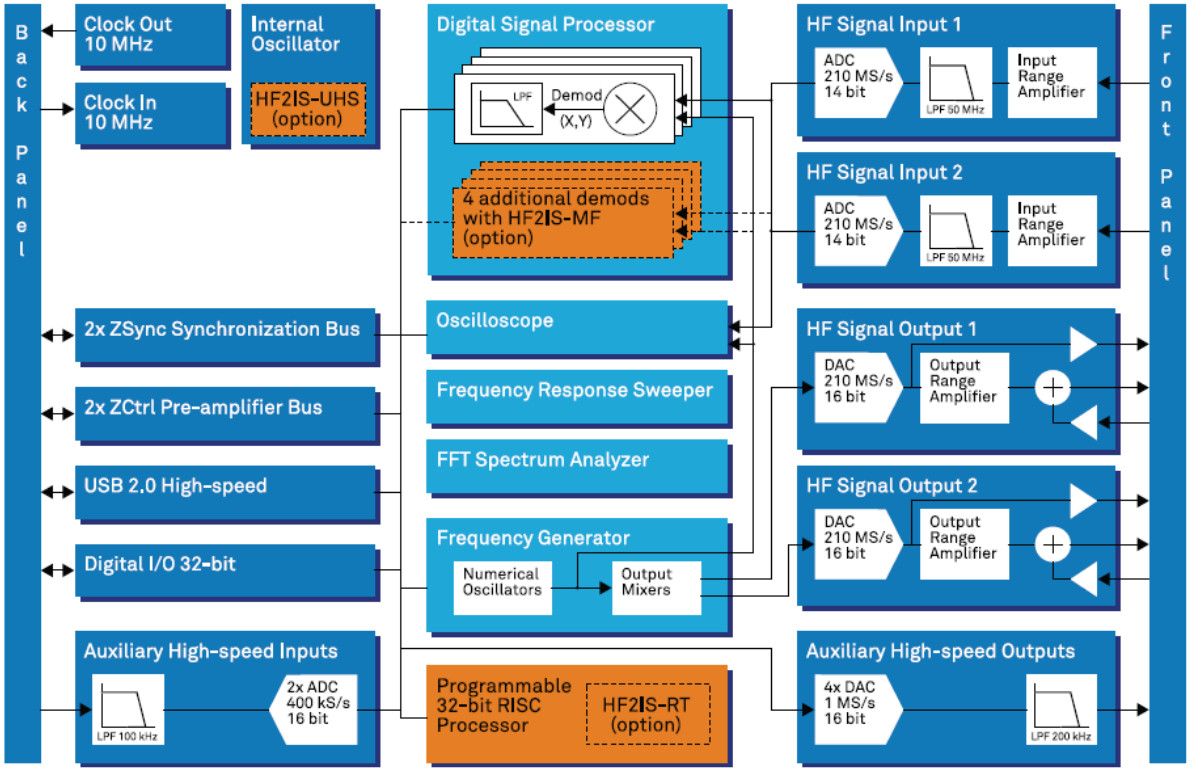

Schematic diagram of internal functioning of the HF2IS [71].

The specifications of HF2IS [71]:

	HF Analog Input
analog bandwidth	1 µHz - 50 MHz
input impedance	50 Ω or 1 MΩ || 20 pF
input noise voltage	5 nV/√Hz above 10 kHz
impedance range	100 mΩ - 10 GΩ
input range	±3.3 V
input AC range	±1.5 V (with DC coupling)
A/D conversion	14 bit, 210 MS/s
	HF Analog Output
analog bandwidth	DC - 50 MHz
operating ranges	±10 mV, ±100 mV, ±1 V, ±10 V
signal adder	±10 V, DC - 50 MHz bandwidth
output range	100 mA (max, 50 Ω output
D/A conversion	16 bit, 210 MS/s
	Demodulator & Reference
number of demodulators	4 dual-phase (8 with HF2IS-MF option)
output sample rate	on USB: up to 460 kS/s
	on Auxiliary outputs: 1 MS/s
filter time constant	1 µs - 500 s
filter bandwidth	80 µHz - 220 kHz

filter slope	6, 12, 18, 24, 30, 36, 42, 48 dB/Oct
X, Y, R, Theta	64-bit full range
reference frequency resolution	0.7 µHz
reference phase angle resolution	1.0 µ°

Auxiliary Signals

high-speed outputs	4 channels, ±10 V, amplitude, phase, frequency, X/Y, or user defined
D/A converter	16 bit, 1 MS/s
D/A analog bandwidth	200 kHz
high-speed inputs	2 channels, ±10 V
A/D converter	16 bit, 400 kS/s
A/D analog bandwidth	100 kHz

Other Interfaces

host connection	USB 2.0 high-speed, 480 Mbit/s
pre-amplifier control bus	ZCtrl proprietary bus to control external pre-amplifiers
synchronization bus	ZSync proprietary bus to locally interconnect ZI instruments
digital I/O	32 bit, general purpose

General

dimensions	45 x 35 x 10 cm (19" rack)
weight	6.2 kg
power supply	110-120 V, 220-240 V, 50/60 Hz
operating temperature	+5 °C to +40 °C
internal oscillator output	sine, ±1 V, 10 MHz
internal oscillator stability	30 ppm, check for HF2IS-UHS Ultra-high Stability option
PC operating systems	32-bit and 64-bit version of Windows XP, Vista, Windows 7, Linux

ANNEX 2: Measurement ΔR of the GMR sensor model I:

B (μT)	R=2×809 Ω			B (μT)	R=2×1200 Ω			B (μT)	R=2×2000 Ω		
	ΔR_{GMR} (Ω)	$\Delta R_{GMR}/B$ (Ω/mT)	$\Delta R/R$ (%)		ΔR_{GMR} (Ω)	$\Delta R_{GMR}/B$ (Ω/mT)	$\Delta R/R$ (%)		ΔR_{GMR} (Ω)	$\Delta R_{GMR}/B$ (Ω/mT)	$\Delta R/R$ (%)
8.94	0.033	3.67	0.0030	6.33	0.027	4.26	0.0025	5.49	0.026	4.79	0.0024
16.05	0.042	2.59	0.0038	10.97	0.041	3.69	0.0037	10.13	0.039	3.84	0.0036
25.86	0.050	1.95	0.0046	24.28	0.054	2.23	0.0050	21.08	0.052	2.46	0.0048
31.52	0.059	1.86	0.0054	34.89	0.068	1.94	0.0062	32.10	0.064	2.01	0.0059
39.18	0.069	1.77	0.0064	53.44	0.081	1.51	0.0074	49.13	0.077	1.57	0.0071
45.15	0.078	1.72	0.0071	73.25	0.108	1.48	0.0099	67.29	0.102	1.52	0.0094
50.26	0.085	1.69	0.0078	92.85	0.135	1.45	0.0123	86.03	0.128	1.49	0.0118
61.33	0.101	1.65	0.0093	112.44	0.162	1.44	0.0148	105.62	0.154	1.46	0.0141
71.55	0.122	1.71	0.0112	132.88	0.185	1.39	0.0170	125.21	0.181	1.45	0.0166
102.22	0.165	1.61	0.0151	152.47	0.208	1.36	0.0191	143.95	0.211	1.46	0.0193
120.96	0.191	1.58	0.0175	172.92	0.219	1.26	0.0201	164.40	0.240	1.46	0.0220
130.33	0.201	1.54	0.0184	190.80	0.272	1.43	0.0250	183.99	0.269	1.46	0.0247
190.80	0.293	1.53	0.0269	210.39	0.300	1.42	0.0275	204.43	0.300	1.47	0.0275
212.10	0.326	1.54	0.0299	230.84	0.330	1.43	0.0303	226.58	0.332	1.46	0.0304
236.80	0.367	1.55	0.0337	251.28	0.359	1.43	0.0329	247.87	0.362	1.46	0.0332
268.32	0.411	1.53	0.0377	271.72	0.387	1.42	0.0355	269.17	0.395	1.47	0.0362
294.72	0.452	1.53	0.0414	291.32	0.416	1.43	0.0382	290.46	0.426	1.47	0.0391
339.02	0.525	1.55	0.0482	312.61	0.445	1.42	0.0409	311.76	0.453	1.45	0.0416
355.20	0.547	1.54	0.0502	333.91	0.478	1.43	0.0439	334.76	0.490	1.46	0.0449
414.83	0.636	1.53	0.0583	354.35	0.507	1.43	0.0465	354.35	0.517	1.45	0.0474
				379.90	0.550	1.44	0.0505	375.64	0.544	1.44	0.0499
				402.05	0.584	1.45	0.0535	396.94	0.578	1.45	0.0530

Calculation the variable resistance of sensor's sensing element.

ANNEX 3: Measurement ΔR of the GMR sensor model II:

B (μT)	R_{int} =1×2.128 kΩ			B (μT)	R_{int} =1×2.71 kΩ			B (μT)	R_{int}=2×2.148 kΩ			B (μT)	R_{int}=2×1.19 kΩ		
	ΔR (Ω)	ΔR/B (Ω/mT)	ΔR/R (%)		ΔR (Ω)	ΔR/B (Ω/mT)	ΔR/R (%)		ΔR (Ω)	ΔR/B (Ω/mT)	ΔR/R (%)		ΔR (Ω)	ΔR/B (Ω/mT)	ΔR/R (%)
6.4	0.03	6.15	0.007	6.4	0.01	2.83	0.003	6.12	0.01	3.17	0.003	6.05	0.01	2.8	0.003
11.8	0.08	7.02	0.015	11.8	0.03	3.04	0.006	11.1	0.03	3.48	0.007	11	0.03	3.1	0.006
23.1	0.16	7.17	0.03	23.3	0.07	3.22	0.013	21.8	0.07	3.62	0.014	21.5	0.07	3.26	0.013
28.8	0.20	7.15	0.038	29.2	0.09	3.26	0.017	27.1	0.09	3.67	0.018	26.8	0.08	3.27	0.016
34.5	0.24	7.1	0.045	35.1	0.11	3.31	0.021	32.5	0.12	3.71	0.022	32.1	0.1	3.28	0.019
40.2	0.28	7.16	0.053	40.9	0.13	3.38	0.025	37.9	0.14	3.76	0.026	37.5	0.12	3.27	0.022
45.9	0.33	7.21	0.061	46.8	0.15	3.39	0.029	43.2	0.16	3.79	0.03	42.8	0.14	3.38	0.026
51.4	0.37	7.21	0.068	52.4	0.18	3.52	0.034	48.6	0.18	3.80	0.034	48.1	0.16	3.41	0.03
57.1	0.41	7.21	0.076	58.4	0.2	3.58	0.038	53.7	0.2	3.88	0.038	53.3	0.18	3.43	0.033
68.7	0.50	7.33	0.093	70.2	0.25	3.66	0.047	64.6	0.25	3.89	0.046	64	0.22	3.43	0.04
80.2	0.59	7.44	0.11	82	0.29	3.62	0.055	75.4	0.3	4.02	0.056	74.7	0.25	3.41	0.047
91.6	0.69	7.6	0.128	93.8	0.33	3.56	0.061	86.3	0.35	4.06	0.065	85.5	0.29	3.42	0.054
103.1	0.78	7.64	0.146	105.2	0.37	3.59	0.07	97.1	0.38	3.98	0.071	96.2	0.32	3.4	0.06
114.6	0.88	7.7	0.163	117.8	0.42	3.57	0.077	107.8	0.42	3.96	0.079	106.9	0.36	3.42	0.067
137.3	1.07	7.85	0.199	141.5	0.51	3.63	0.095	129.5	0.51	3.95	0.094	128.2	0.43	3.41	0.081
148.6	1.17	7.88	0.217	154.2	0.56	3.63	0.103	140.2	0.55	3.97	0.103	138.8	0.47	3.43	0.088
				165.1	0.6	3.65	0.111	150.9	0.6	3.97	0.111	149.4	0.52	3.5	0.096
				176.6	0.65	3.68	0.12	161.5	0.63	3.93	0.117	160	0.55	3.49	0.103
				188.5	0.70	3.72	0.13	179.1	0.7	3.94	0.13	170.6	0.6	3.51	0.111
				200.1	0.75	3.78	0.14	190.4	0.75	3.94	0.139	181.1	0.64	3.53	0.118
				211.7	0.81	3.84	0.15	201.5	0.79	3.96	0.147	191.5	0.68	3.56	0.126
				231	0.89	3.87	0.165	223.3	0.89	3.98	0.164	212.3	0.76	3.62	0.142
				258.2	1.01	3.93	0.187	250.9	1.03	4.10	0.19	238.1	0.87	3.68	0.162
								282	1.17	4.15	0.217	263.6	0.97	3.7	0.18
								309.2	1.3	4.2	0.24				

Calculation the variable resistance of sensor's sensing element.

ANNEX 4: Measurement ΔR of the GMR sensor model III:

B (μT)	f=60Hz			B (μT)	f=75Hz			B (μT)	f=100z		
	ΔR_{GMR} (Ω)	$\Delta R_{GMR}/B$ (Ω/mT)	ΔR/R (%)		ΔR_{GMR} (Ω)	$\Delta R_{GMR}/B$ (Ω/mT)	ΔR/R (%)		ΔR_{GMR} (Ω)	$\Delta R_{GMR}/B$ (Ω/mT)	ΔR/R (%)
6.34	0.45	71.56	0.020	5.16	0.34	67.17	0.015	3.96	0.25	64.74	0.011
12.68	0.92	72.77	0.042	10.32	0.71	69.32	0.032	7.91	0.54	68.41	0.024
25.3	1.89	74.89	0.087	20.6	1.46	71.28	0.067	15.65	1.11	71.02	0.051
37.9	2.90	76.66	0.133	31	2.24	72.49	0.103	23.3	1.68	72.50	0.077
50.7	3.94	77.75	0.181	41.3	3.03	73.59	0.140	31.2	2.27	73.06	0.105
63.4	4.98	78.68	0.229	51.5	3.85	74.82	0.177	39.1	2.89	73.94	0.133
76	6.05	79.69	0.279	61.9	4.67	75.50	0.215	46.8	3.54	75.71	0.163
88.4	7.06	79.91	0.325	72.2	5.49	76.14	0.253	54.5	4.19	77.05	0.193
101	8.10	80.25	0.373	82.5	6.34	76.91	0.292	62.6	4.86	77.68	0.224
114	9.19	80.65	0.423	92.8	7.16	77.25	0.330	70.6	5.49	77.89	0.253
126.8	10.28	81.12	0.474	103.2	8.12	78.76	0.374	78.2	6.16	78.77	0.283
138.9	11.36	81.79	0.523	113.5	9.07	79.92	0.418	85.9	6.80	79.22	0.313
151.8	12.46	82.13	0.574	123.8	9.95	80.39	0.458	93.8	7.39	78.84	0.340
164.9	13.54	82.13	0.624	134.1	10.86	80.99	0.500	101.4	8.07	79.63	0.372
177.1	14.58	82.38	0.672	144.4	11.73	81.29	0.540	109.2	8.77	80.35	0.404
189.5	15.61	82.40	0.719	154.8	12.62	81.58	0.581	117.2	9.42	80.43	0.434
201	16.71	83.14	0.770	165.1	13.61	82.45	0.627	125.3	10.14	80.96	0.467
215	17.75	82.58	0.818	175.3	14.46	82.51	0.666	132.7	10.80	81.39	0.497
228	18.80	82.47	0.866	185.7	15.30	82.42	0.705	140.6	11.41	81.20	0.526
230	19.90	86.55	0.917	196.1	16.19	82.60	0.746	148.6	-	-	-
242	20.97	86.65	0.966	206	17.11	83.06	0.788	156.4	12.82	81.99	0.590
266	23.33	87.73	1.075	217	18.93	87.24	0.872	171.7	14.26	83.06	0.657
291	25.71	88.36	1.185	236	20.84	88.32	0.960	187.6	15.70	83.73	0.723
316	27.98	88.55	1.289	257	22.72	88.44	1.047	203	17.13	84.41	0.789
340	29.92	88.01	1.379	277	24.51	88.49	1.129	218	18.40	84.42	0.848
364	31.97	87.83	1.473	296	26.24	88.66	1.209	234	19.75	84.43	0.910
387	33.98	87.82	1.566	317	28.03	88.43	1.291	240	20.96	87.34	0.966
413	35.81	86.71	1.650	337	29.56	87.72	1.362	254	22.32	87.88	1.028
438	37.63	85.92	1.734	356	31.27	87.86	1.441	270	23.79	88.14	1.096
461	39.55	85.80	1.822	375	32.96	87.89	1.518	285	25.03	87.84	1.153
485	41.37	85.31	1.906	395	34.57	87.53	1.593	298	26.50	88.946	1.221
508	43.13	84.90	1.987	415	35.96	86.65	1.657	314	27.63	88.01	1.273
533	44.87	84.18	2.067	436	37.55	86.12	1.730	330	28.96	87.77	1.334
558	46.71	83.71	2.152	460	39.15	85.11	1.804	346	30.25	87.44	1.394
583	48.41	83.05	2.231	475	40.57	85.41	1.869	360	31.70	88.05	1.460
606	50.08	82.64	2.308	495	41.88	84.60	1.929	375	32.84	87.59	1.513
631	51.82	82.12	2.388	515	43.35	84.17	1.997	391	34.01	86.98	1.567
655	53.52	81.72	2.466	534	44.86	84.01	2.067	405	35.18	86.86	1.621
678	55.08	81.24	2.538	553	46.38	83.88	2.137	419	36.13	86.24	1.665
703	56.77	80.76	2.616	574	47.77	83.23	2.201	437	37.30	85.36	1.719
728	58.16	79.89	2.680	595	49.20	82.70	2.267	449	38.56	85.88	1.777

Calculation the variable resistance of sensor's sensing element.

Conception et réalisation d'un biocapteur à GMR pour la caractérisation de milieux biologiques

L'objectif de cette thèse est de développer des bio-capteurs à base de magnétorésistance géante (GMR), ainsi que l'électronique de conditionnement associée, en vue de caractériser magnétiquement des ferrofluides biologiques. Ce travail a été réalisé en collaboration avec le Pr Sotoshi YAMADA de l'Institut « Nature and Environmental Technology» de l'Université de Kanazawa.

La première partie porte sur l'état de l'art et les méthodes de mesures des propriétés magnétiques des ferrofluides et la physique de l'effet GMR.

La deuxième partie concerne la mise en place d'un dispositif de mesure pour déterminer et caractériser la valeur de la sensibilité de chaque capteur. Cette sensibilité est une caractéristique cruciale pour toute application biomédicale. Sa connaissance et son optimisation permettent d'envisager des mesures précises et justes des propriétés magnétiques des ferrofluides notamment à bas niveau de signal.

La troisième partie, également expérimentale, décrit les mesures de la perméabilité relative (μ_r) et de la susceptibilité (χ) de fluides magnétiques (ferrofluides) par des capteurs GMR I, II. En outre, afin de confirmer les résultats expérimentaux obtenus avec ces capteurs, nous les avons comparés à ceux obtenus avec d'autres méthodes comme la magnétométrie à échantillon vibrant (VSM) ou à des calculs théoriques.

Le quatrième et dernier chapitre présente les résultats expérimentaux de la perméabilité relative et de la susceptibilité d'un marqueur magnétique permettant la détection de la bactérie pathogène Escherichia coli O157: H7.

Mots clefs : Biocapteur, GMR, biomédical, ferrofluide, caractérisation magnétique.

Design and evaluation of a GMR-biosensor for magnetic characterization of biological medium

The intent of this thesis is to develop bio-sensors based on giant magnetoresistance (GMR) and the associated conditioning electronics, to characterize magnetically organic ferrofluids. This work was done in collaboration with Pr Sotoshi YAMADA of the Institute "Nature and Environmental Technology" at the University of Kanazawa.

The first part focuses on the state of the art and the methods for magnetic properties measurements of ferrofluids and the description of the GMR effect.

The second part concerns the introduction of a measuring device to determine and characterize the value of the sensitivity of each sensor. This sensitivity is a crucial parameter for any biomedical application. Its knowledge allows optimization of sensors ability to measure very low magnetic parameters of ferrofluids very precisely.

The third experimental part describes measurements of relative permeability (μ_r) and susceptibility (χ) of magnetic ferrofluids with GMR sensors I, II. In addition, to confirm the experimental results obtained with these sensors, we have compared them to those obtained with other methods such as vibrating sample magnetometer (VSM) or by theoretical calculations.

The fourth and last chapter presents the experimental results of the relative permeability and susceptibility of a magnetic marker used to detect pathogenic bacteria (Escherichia coli O157: H7).

Keywords: Biosensor, GMR, biomedical, ferrofluid, magnetic characterization.